



City Research Online

City, University of London Institutional Repository

Citation: Papadopoulos, Konstantinos (2015). Flow effect on thrombus formation in stenosed coronary arteries: a computational study. (Unpublished Doctoral thesis, City University London)

This is the accepted version of the paper.

This version of the publication may differ from the final published version.

Permanent repository link: <https://openaccess.city.ac.uk/id/eprint/13497/>

Link to published version:

Copyright: City Research Online aims to make research outputs of City, University of London available to a wider audience. Copyright and Moral Rights remain with the author(s) and/or copyright holders. URLs from City Research Online may be freely distributed and linked to.

Reuse: Copies of full items can be used for personal research or study, educational, or not-for-profit purposes without prior permission or charge. Provided that the authors, title and full bibliographic details are credited, a hyperlink and/or URL is given for the original metadata page and the content is not changed in any way.

City Research Online:

<http://openaccess.city.ac.uk/>

publications@city.ac.uk



CITY UNIVERSITY
LONDON

+

Flow effect on thrombus formation in stenosed coronary arteries

A Computational study

Konstantinos P. Papadopoulos

April 2015

Thesis submitted for the fulfilments of the requirements for the Degree of
Doctor of Philosophy of City University of London



**CITY UNIVERSITY
LONDON**

CityLibrary
Your space
Your resources
Your library

**THE FOLLOWING PARTS OF THIS THESIS HAVE BEEN REDACTED
FOR COPYRIGHT REASONS:**

Page 19: Fig 1-1: Image of acute coronary syndromes.

Page 21: Fig 1-3: Image of revascularization.

Page 21: Fig 1-4: Image of coronary bypass.

TABLE OF CONTENTS

Chapter 1 Introduction.....	19
1.1 Coronary artery disease: impact and complications	19
1.2 Risk factors, symptoms and treatment	21
1.3 The role of geometry.....	24
1.4 The influence of flow.....	26
1.5 Blood flow and thrombus formation.....	27
1.6 Basis and aims of this work.....	28
Chapter 2 Literature review.....	31
2.1 Blood flow and blood flow simulations.....	31
2.1.1 Blood rheology	31
2.1.2 Geometry reconstruction	36
2.1.3 Inlet and outlet boundary conditions.....	39
2.1.4 Indicative results.....	43
2.2 Coagulation and thrombus formation	48
2.3 Thrombus formation- The process	48
2.4 Simulations of thrombus formation	53
2.4.1 Models for the coagulation process.....	53
2.4.2 Models for platelet aggregation and deposition	57
2.4.3 Integrated models of thrombus formation	60
Chapter 3 The simplified thrombus model.....	64
3.1 Introduction.....	64
3.2 Perfusion chamber.....	64

3.3 Exploiting the results of thrombin generation assay	66
3.4 Structure of thrombin generation sub-model	68
3.5 Calibration based on TGA parameters.....	72
3.6 Results of thrombin sub-model.....	76
3.7 Variation of the model parameters.....	85
3.8 Platelet adhesion sub-model	89
3.9 Initial estimation of reaction rate constants.....	91
3.10 The fine tuning of the platelet sub-model	94
3.11 Introducing the coagulation activation index (CAI).....	97
3.12 Coupling of the coagulation model with flow simulations	98
3.13 Overview of the model	104
3.14 Some details on simulations and programming.....	109
Chapter 4 Flow simulations	113
4.1 Introduction.....	113
4.2 Geometry reconstruction.....	Error! Bookmark not defined.
4.3 Governing Equations.....	120
4.4 Boundary conditions.....	120
4.5 Inlet and outlet for the normal LAD model.....	122
4.6 Inlet and outlet for stenosed LAD models.....	125
4.7 Processing of simulations results.....	130
4.8 Results.....	132
4.9 Velocity field.....	132
4.10 TAWSS.....	135

4.11 OSI and RRT	139
4.12 Coagulation activation index (CAI)	142
4.13 Grouping of the results.....	143
Chapter 5 Applying the thrombus model to realistic geometries	148
5.1 Method of application.....	148
5.2 Results.....	150
5.3 35% stenosis	153
5.4 50% stenosis	156
5.5 70% stenosis	159
5.6 Comments.....	162
Chapter 6 Overview, conclusions and future work	166
6.1 Thrombus modelling.....	166
6.1.1 Overview of model development	166
6.1.2 Discussion and suggestions for future work on coagulation model.....	171
6.2 Flow simulations and risk factors	173
6.2.1 Overview of simulation results	173
6.2.2 Suggestion for improvement of flow based assessment method	174
6.3 Thrombus model under transient flow conditions	176
References	181

TABLE OF FIGURES

Figure 1-1: The different cases of ACS. (Image taken from http://www.nottingham.ac.uk/nursing/practice/resources/cardiology/acs/arteries.php)	19
Figure 1-2: Thrombus formation in occluded coronary after rapture of the plaque (left) and stable stenosis without thrombotic complications (right).(images: M.H. Davidson, American Journal of Managed care)	20
Figure 1-3: Revascularization with the use of catheter and stent (PCI).Image taken from: http://www.birlaheart.org/Research/clinical_research.html	21
Figure 1-4: Coronary bypass. Vessel grafts connect the aorta with a point distal the stenosis. Image taken from: http://uvahealth.com/services/heart/treatment/14782	21
Figure 1-5: Left coronary trees of different patients (same view). Note the significant variation of the shape of the coronary arterial tree between different individuals.....	24
Figure 1-6: Schematic representation of shear rate	26
Figure 1-7: (a) Fibrin mesh as depicted by scanning electron microscopy Image: http://www.leeds.ac.uk/light/research/cdr/mechanisms_of_thrombosis.html (left) (b) Scanning electron microscopy image of fibrin mesh (blue) with trapped platelets (purple) and red blood cells (red)Image: <i>Yuri Veklich and John W. Weisel, University of Pennsylvania School of Medicine</i> (right)	27
Figure 2-1: Characteristics of blood: Non-Newtonian (Baskut et al 2003). Bloods rheological behaviour becomes Newtonian above a level of shear stress. The exact value of the threshold is under discussion but in arterial flow condition the average shear is definitely above the threshold.	31
Figure 2-2: Axial distribution of platelet concentration. Values are normalized using the bulk platelet concentration (E.C. Eckstein 1991 [66]).	33
Figure 2-3: WSS along a stream-wise line in a right coronary geometry with the use of different models for blood viscosity for steady state simulation [80]. There are differences in the exact values but the distribution is very similar	34
Figure 2-4:Image from conventional coronary angiography and the resulting reconstructed geometry (images from Chen et al 2005 [91]). Note the very small pressure drop values among the inlet and the outlets of the branches.	36
Figure 2-5: Methods for modelling the motion of the vessel network. Left: use of 5 different images from angiography corresponding to five different instances of the inlet waveform. The method uses the exact position of each point of the network (Theodorakakos et al 2008). Right: Use of a curvature-versus-time function for the modelling of the motion of coronary vessels (Prosi et al 2004).....	37
Figure 2-6: Non dimensional (maximum values set to 1) wave forms for the inlet pressure (Westerhoff et al 2006) on the coronary network (aortic pressure) and the inlet mass flow rate Q (Levi 2001) for non stenosed vessel. The two quantities are obviously out of phase as the inlet is severely influenced by the motion of the heart muscle.	39
Figure 2-7: Schematic representation of the three element Windkessel model.	41

Figure 2-8: WSS distribution along a line in a single branch coronary model for two different types of inlet waveforms. The distribution is almost identical and there is an almost constant difference between them (Myers et al 2001 [101])44

Figure 2-9: WSS distribution in different coronary models with bifurcations for a normal (left) and a stenosed (right) case [86]. The differences in geometry lead to much higher values of WSS for the vessel with CAD. Although the view angle is different it is clear that the values of WSS are approximately three times higher in the right image.....46

Figure 2-11: The cell based model for blood coagulation, image from K.P. Papadopoulos et al 2014 [142] inspired from the work of Smith 2009 [126]. The different steps of the process (initiation, amplification and propagation) occur at different sites. The arrows show how the processes are lumped in a smaller number of reactions in the developed phenomenological model (Chapter 3)52

Figure 2-12: Lagrangian simulation of platelet aggregation in a tube of 50 μ m diameter and 500 μ m length (Pivkin et al 2006)58

Figure 2-13: Indicative results of a discrete cell model (Fogelson et al 2007). Discrete cell models are used mainly in two dimensional studies and for small computational domains. The method is applied for computational domain smaller than typical coronary dimensions (here two orders of magnitude smaller)61

Figure 2-14: Three dimensional simulation of fibrin concentration on vessel wall. Simulation of coagulation in rigid wall tube (D=6.2mm, L=31mm) using a fully developed velocity profile (Bondar and Sequeira 2007)63

Figure 3-1: Variation of the temporal evolution of thrombin generation for different individuals [132]66

Figure 3-2: Typical thrombogram curve and the main parameters of the test (image from J.J. van Veen et al [189]).....66

Figure 3-3: Schematic of the reduced version of the cell based model of coagulation I shown in Figure 2-11 that was used for the development of the thrombin sub-model.68

Figure 3-4: Time step independence test for the thrombin sub-model. For time-step values below 0.5s the results coincide.76

Figure 3-5: Curve matching the typical TGA parameters C1 and the curve that matches thrombin generation for low platelet concentration C8.79

Figure 3-6: Fitting of cases with added phospholipids in the absence of inhibitors. Triggering substance is r-TF:VIIa79

Figure 3-7: Adjustment of the model in order to reproduce a specific TGA curve. Experimental results from Hemker et al [198].....80

Figure 3-8: Simulated thrombin generation curves for different platelet concentrations, C5-C7 and the typical curve C1. Values of the reaction rate constants are identical for cases C5 to C780

Figure 3-9: Simulation of thrombin generation for cases of haemophilia. In order for the equations to reproduce pathological cases the reaction rate constants have been significantly modified compared to

their values with the use of the equations of Table 3-4.	81
Figure 3-10: Effect of the sampling frequency to the resulting curve after automated curve fitting on the results.	82
Figure 3-11: The geometry used for adjusting the platelet deposition sub-model and a cut of the computational grid showing the dense cells of the boundary layer. The contour of the velocity profile corresponds to the case PLA1; the other cases had identical velocity profiles but the values of the velocity magnitudes were scaled according to the flow rate at the inlet.	94
Figure 3-12: Platelet deposition on de-endothelized vessel segments. Computational results against experimental for the PLA1 case.	96
Figure 3-13: Platelet deposition for cases PLA2 and PLA3. The introduction of shear dependent platelet aggregation rate captures the aggregation rate, but the model fails to reproduce the reduction of the quantity of aggregated platelets. However this occurs approximately 600sec after initiation, while the maximum simulation time for the realistic models was 480s.	96
Figure 3-14: Geometric and flow characteristics for cases SA and SB. Note that in both cases the entrance length (upstream the reacting area) is sufficiently long for the development of velocity profile, which was identical with the velocity profile at the outlet.	101
Figure 3-15: Comparison between the sub-threshold and the above-threshold cases. The X sign indicate the logarithm (base 10) of average thrombin concentration in the specific points, divided by the threshold thrombin concentration, while in the contours it is depicting the distribution of actual thrombin concentration in kg/kg. This distribution pf thrombin concentration is after 300s of perfusion.	102
Figure 4-1: (left) Typical image from X-ray angiography and (right) the centrelines of the main branch and the side branches used for the averaged LAD model.	113
Figure 4-2: The data used for the construction of the average LAD model and the modifications on the tapering.	114
Figure 4-3: The sites of the stenotic lesions on the initial geometry and the model with maximum stenosis (90%) for each of three groups tested.	115
Figure 4-4: Boundary layers near the wall surface as seen at the inlet of the computational domain.	117
Figure 4-5: The denser grid at the areas of main interest (bifurcations and stenotic lesions) is shown	117
Figure 4-6: Curves for the model without stenosis and the model with maximum stenosis (90%). The grid points for the intermediate models were obtained directly (without constructing new mesh) by interpolating the coordinates of the two extreme states.	118
Figure 4-7: Symmetric stenosis (Case STABLE with 50% of stenosis)	119
Figure 4-8: Eccentric stenosis (Case MI2 with 50% stenosis)	119
Figure 4-9: Factors determining the coronary flow. As it can be seen, the 'operating' pressure and the resulting flow rate are out of phase. The flow is mainly determined by the intramyocardial pressure, exerted on the coronary vessel network due to contraction. The vessels are coloured according to the intra-myocardial pressure [214] (blue is 0 red is 8kPa) at a random instance of the cardiac cycle.	121

Figure 4-10: Mass flow rate inlet waveform for the healthy LAD model inlet. Waveforms for the six outlets are identically shaped but scaled according to the f_i fraction factors..... 122

Figure 4-11: The distribution of the WSS on the walls of the healthy LAD model. For most part of the geometry, the WSS is between 1.5 and 2 Pa, confirming the assumption used for determining mass flow rates at the outlets. 123

Figure 4-12: The pressure waveforms used as inlet and outlet pressure for the whole coronary network. ..126

Figure 4-13: Simplified representation of the electrical circuit equivalent of the system considered for the extraction of the boundary conditions. 126

Figure 4-14: Normalized average mass flow for the inlet, the side branches distal and proximal to the peak of the stenosis. Results were similar for the three groups. 129

Figure 4-15: Normalized waveforms of mass flow for the inlet and the side branches distal and proximal to the stenosis. Side branches proximal to the stenosis exhibit sharper variations of flow rate. 129

Figure 4-16: Recirculation zones downstream the stenotic lesion. Magenta-coloured streamlines indicate that part of the flow from the vortex area ends up in the side branch mainly in MI1 cases. Vortex stream-wise length is considerably larger for MI1 and MI2 models. All snapshots correspond to the same instance of the pulse. 133

Figure 4-17: Time averaged velocity profiles downstream of the stenotic lesion. Note that a small difference in the location of the stenosis (<3mm, less than 20% of the total length of the whole lesion) as it is between MI1 and MI2, changes significantly the location of the areas with inversed average flow velocity..... 134

Figure 4-18: Distribution of time averaged wall shear stress for all geometry groups. Note that for groups MI1 and MI2 there are areas with high TAWSS after the stenotic lesion. 136

Figure 4-19: Spatial distribution of OSI for the models with 50% and 70% of stenosis. 139

Figure 4-20: Contours of RRT. For great degrees of stenosis the areas with high RRT values are moved downstream. MI1 and MI2 have larger areas with high RRT, and in MI2 models there is also an area with high RRT in the side branch after the stenosis. 140

Figure 4-21: Surface of the vessel wall with OSI and RRT above certain values. The areas with high RRT and OSI are definitively higher for MI2 and MI1 geometries compared to STABLE for the same degree of stenosis, but the change of these values is mainly determined by the degree of stenosis rather than the exact location of the stenotic lesion. 141

Figure 4-22: The variation of CAI for all groups and degrees of stenosis. 143

Figure 5-1: The discrete steps used for the application of the thrombus model, shown on the mass flow rate pulse corresponding to the healthy model. The resulting flow rate pulse that was used is described by the dashed lines. 148

Figure 5-2: The defined reacting boundary (RED) for all the geometries on which the model was applied. The images are in the same scale. The reacting area has the same stream-wise length for all models, approximately 6mm while the middle is at the point of maximum stenosis..... 149

Figure 5-3: The different temporal evolution of the process for different distributions of wall shear rate (WSR) with the time (T_p) and the amount of bound activated platelets ($AP^{(b)}$) required for downstream propagation. It is clear that the cases with low values of WSR do not require the presence of bound activated platelets (additional surface bound activity) for downstream propagation. 151

Figure 5-4: Temporal evolution of thrombin concentration near the vessel wall within two minute time interval after the downstream propagation. 153

Figure 5-5: Temporal evolution of thrombin generation/inhibition rate near the vessel wall within two minute time interval after the downstream propagation. 153

Figure 5-6: The distribution of thrombin concentration for the three models with 35% stenosis, 1 minute after the downstream propagation. While in MI1 and STABLE models there is a large area with above threshold values for thrombin concentration in the MI2 models high thrombin concentration is localized in a specific site..... 154

Figure 5-7: The spatial distribution of the rate of change of [IIa] one and two minutes after the downstream propagation for 35% stenosis. In all cases the rate of production decreases and it is interesting that for the MI2 geometry the areas with high production rate coincide with those of high concentration. 155

Figure 5-8: Temporal evolution of thrombin concentration near the vessel wall during two minutes after the downstream propagation for models with 50% stenosis. The three geometries have similar images. 157

Figure 5-9: Temporal evolution of thrombin generation/ inhibition rate near the vessel wall during two minutes after the downstream propagation. There is an increase of the inhibition rate for MI1 and STABLE while MI2 exhibits very small values. 157

Figure 5-10: The distribution of thrombin concentration for the three models with 50% stenosis, 1 minute after the downstream propagation. While in MI1 and STABLE models there is a large area with above threshold values for thrombin concentration in the MI2 models high thrombin concentration is localized in a specific site..... 158

Figure 5-11: Thrombin production rate for 50% stenosis. The rate of production for the MI2 model is significantly increased near the reacting site while there is not increased inhibition rate downstream. 158

Figure 5-12: Temporal evolution of thrombin concentration near the vessel wall during two minutes after the downstream propagation..... 160

Figure 5-13: Temporal evolution of thrombin generation/ inhibition rate near the vessel wall during two minutes after the downstream propagation..... 160

Figure 5-14: The distribution of thrombin concentration for the three models with 70% stenosis, 1 minute after the downstream propagation. While in STABLE model there is a large area with above threshold values for thrombin concentration in the MI1 and MI2 models high thrombin concentration is localized in a specific sites..... 160

Figure 5-15: Thrombin production rate distribution for the models with 70% stenosis. In MI1 and MI2 models thrombin production is localised in specific sites that do not change with time. In STABLE model the

area with high thrombin production rate is larger and changes with time. 161

Figure 6-1: (left) The variation of prothrombin concentration. The snapshot is from STABLE model with 35% stenosis, and one of the moments with lowest [II] concentration yet the maximum variation is approximately 0.5%. (right) The variation of resting platelet concentration. The case is different compared to prothrombin as in some areas the concentration falls to the 25% of its initial value. 171

Figure 6-2: MI1 (orange) and MI2 (gray) models with 20% degree of stenosis. The differences between the two geometries are hard to distinguish and although these two models are supposed to be classified in different groups it is doubtful if a performed-from-scratch geometrical classification would make that distinction. The flow fields however have noticeable differences, as shown in chapter 4. 175

LIST OF TABLES

Table 2-1: Localization of some of the enzymatic activations of the coagulation process [126, 132]	50
Table 2-2: Different ways for simplified modelling of enzymatic biochemical reactions. The specific way used in every case depends on the type of the reaction, the desired accuracy and the available data.	54
Table 3-1: Typical values for the 4 main parameters of TGA test	67
Table 3-2: The source terms for each substance of the thrombin sub-model, for zero dimensional simulations	69
Table 3-3: The values of the model's constants and parameters that were used as a starting point for the calibration and the fine tuning of the model	70
Table 3-4: Set of equations for tuning thrombin sub-model to reproduce the results of a specific TGA with the use of the four main parameters of TGA	75
Table 3-5: Brief description of the different cases simulated with appropriate modification of the model constants.....	77
Table 3-6: The experimental TGA parameters for all the cases used for the model testing and calibration and the resulting numerical ones	78
Table 3-7: The variation of the reaction rate constants during the process of fitting the model to the different cases. In cases 2 and 3 there is no inhibitors in the experimental procedures and in cases 5-7, used to test the function of the model for different platelet concentrations the reaction rate constants were fixed.	86
Table 3-8: Source terms for the four different states considered in the platelet aggregation sub-model: <i>SRP_f</i> corresponds to resting platelets in flow, <i>SRP_b</i> corresponds to bound resting platelets <i>SAP_f</i> represents the concentration of activated platelets in flow and <i>SAP_b</i> the concentration of bound activated platelets.....	90
Table 3-9: Reported wall shear rate values and corresponding mass flow rate at inlet for platelet deposition cases.....	95
Table 3-10: Initial reaction rate constants for platelet deposition sub-model	95
Table 3-11: The species included in the final formulation of the model, initial concentrations and diffusion coefficients.	104
Table 3-12: Source terms for the species of the model for the bulk reactions (reactions occurring in flowing blood).....	105
Table 3-13: Additional source terms for the model's species for the computational cells that include reacting boundaries.	106
Table 3-14: Values of all the reaction rate constants used in the model.	107
Table 4-1: The exact locations, beginning, ending and centre of the stenotic lesion for each group of the simplified LAD models. The centre of the lesion is also the point of maximum stenosis. All dimensions	

are given in mm..... 116

Table 4-2: Mass flow rate fraction for each side branch and the outlet of the main branch with respect to the mass flow rate at inlet 124

Table 4-3: Average values of TAWSS for the whole geometry and surface of the geometry with TAWSS>3 and TAWSS<0.15 (area in mm²). Coloured figures indicate that the specific value is more than 25% (orange) or more than 50% (red) than the lowest (green) value among the models with same degree of stenosis 137

Table 4-4: Average values of OSI and RRT for the whole model and surface of the geometry with OSI>0.3 and RRT>5 (area in mm²). Coloured figures indicate that the specific value is more than 25% (orange) or more than 50% (red) than the lowest (green) value among the models with same degree of stenosis 142

Table 4-5: Flow-based risk indexes for models with stenosis up to 70%. Overall the MI2 appears to be of higher risk, followed by MI1. 146

Table 5-1: The time instances used for the inlet pulse for the application of thrombus formation. The flow rates and inlet masses correspond to the inlet of the healthy vessel. The values of mass flow correspond to the flow rate pulse used for the healthy model. 148

Acknowledgements

First of all I would like to thank my supervisor Professor Manolis Gavaises for trusting me in dealing with this over-complicated problem, and for having minimum interference and flexibility with deadlines while at the same time providing sufficient funding. I would also like to thank –same reasons- my second supervisor Professor Constantinos Arkoumanis. Working with these people except of completing my PhD helped me understand certain aspects on how research works.

Besides my supervisors, certain people from the City University group that works on cavitation and ICR have contributed to the completion of this work. Dr Nicholas Mitroglou provided valuable help on the construction of the geometrical models, the computational grid and the post processing of the flow results, and he was always available for tips on the use of BETA software while his help on subject outside the field of science was also invaluable. Dr Phoevos Koukouvinis, whose knowledge on CFD issues seems to have no limits, also provided valuable help and advice on several technical issues and on the identification of certain mistakes that had troubled me for a significant period of time. Mr (soon to be dr.) Ilias Malgarinos provided significant help on the use of FLUENT, especially on how user defined functions are programmed. Dr Dimitris Papoulias, Dr Andreas Theodorakakos, Dr Giorgos Strotos and Dr Nikos Nikolopoulos also helped me on technical issues, while Professor George Bergeles gave me valuable advice on why and how to avoid getting mad. During the last year of my work I had also some useful discussions with Dr Konstantina Vogiatzaki.

From City University I would also like to thank Professor Panos Liatsis for some very helpful – for me- discussions on the application of boundary conditions for coronary flow simulations, Professor Chris Atkin for his contribution in publishing the first part of the work in a scientific journal, Mr (soon to be Dr) Anish Gami for several tips on Matlab and helpful discussions in general, and finally, Dr Youyou Yan and Mr Nikolaos Chatziarsenis for helping me out with any administrative issues that came up during these four years.

From the world of academia outside City University I would like to thank Mr Ioannis Pantos and Dr Demosthenis Katriasis from Euroclinic Hospital, Athens, for providing and explaining the statistical model for the culprit stenosed LAD arteries and the data for the reconstruction of the geometrical models. The role of Dr Manos Giannadakis and Dr Andreas Papoutsakis was also important, as they introduced me into the world of CFD, when I first started my training in Fluid-Research back in 2007-2008. I would also like to help Professor Sotiris Pratsinis from ETH for giving me some useful tips (and some of his papers) on zero dimensional models. I would

also like to thank Dr Prakash P. Punjabi, Dr Jim Crawley and Dr Nicholas Cooper from Imperial College (Hammersmith Hospital) for their valuable help for helping me see things from a different perspective and especially on their contribution to the development the thrombin sub-model by clarifying certain issues on the TGA process and results. Finally I would like to thank Professor Charalambos Lontos from NKUA (Physics department), for all these helpful advice he provided during these pleasant walks around Athens acropolis and Professor Aristides Baltas from NTUA who was my supervisor at my undergraduate dissertation.

Additionally I would like to thank BETA support team for their advice on the use of ANSA and μ ETA software and especially Mr Polykarpos Athanasiadis and Mr George Panagos for their contribution on the easier reconstruction of the stenosed geometrical model with the provision of a script particularly developed for this purpose.

I also recognize the contribution of Greek Ministry of Education that allowed me two years of paid and three years of unpaid leave for completing this work, and especially Mr Ioannis Simantirakis, (now former) director of secondary schools in Kos and Mr Antonios Ioannou, the headmaster of the school I was working, who both gave their permission for my leave.

I am also obliged to thank a number of people outside the world of academia and technology, which supported me in a more personal and non-scientific manner, but it is certain that without their contribution the completion of this work would be impossible. First of all I would like to thank my family and especially my parents Niki and Panayiotis Papadopoulos –their idea that I could do better than ‘that’, no clear definition on what exactly ‘that’ was a constant motivation for me to go a little further on the road of knowledge and science-, my sister Maria Papadopoulou and my companion in life Katerina Halkiadaki for their support and tolerance during this weird (regarding my behaviour) period. I would also like to thank all my good friends who, during all this period did not even complained for listening to boring stories about my work that they probably did not even understand while having dinner or drinks with me. Especially I would like to thank for their overall support Sotiris Vasilopoulos, Spiros Mitas and Korina Palikaraki who were a constant reference point during my breaks, Dimitris Kirikos for some helpful conversations on programming issues and for some relaxing drinks in Athens and in Anafi along with Lenos Christidis and Dimitris Posantzis, my very good friend Lazaros Fegaridis in Kos who also provided some tips on programming and for his hospitality during the last days of the writing-up process. I will stop bringing up names at this point, as this part could become disproportionately large. Finally, I would like to thank all my friends in Athens, London, Kos, Kalymnos and Anafi, as well as certain nightlife institutions, especially ‘Batman’ (Yiorgos Nasios) in Athens and ‘Sfougaras’ (Lefteris and Thoris) in Kalymnos that worked both as shelter

for some off-steam drinks when I needed it, and also as motivation (when I finish this...).

Hoping that I have not forgotten someone extremely important, while knowing that the last part could easily include another hundred names, thank you all!!

Abstract

Thrombotic complications often occur in stenosed coronary artery, causing permanent damage and even death. Although the exact factors and events leading to thrombus formation are not entirely known, the local rheological conditions as well as the different tendency for clotting of the blood of each individual are considered to have an important role both in progress of the disease and the relevant complications. Recently a statistical correlation between the exact location of the stenosis and the evolution of the disease has been reported [1]. In this work we investigated whether this connection can be predicted by computational simulations.

For this purpose, a simplified model for blood coagulation, focusing mainly on thrombin activation, has been formulated in three steps. A phenomenological sub-model for thrombin generation was developed and calibrated, based on clinical tests (not laboratory experiments). The model was proved capable of reproducing with acceptable accuracy the rate of thrombin generation for blood samples from individuals with different thrombogenic potential, including haemophilia cases. A second sub-model for platelet aggregation on reacting surface was developed and calibrated in order to reproduce experimental data [2]. Finally, the whole coagulation model was adapted for application under flow conditions, based on the threshold behaviour of blood coagulation under flow in respect to wall shear rate and reacting surface stream-wise length [3].

In order to test the developed models, 3 groups of left anterior descending (LAD) geometry models have been constructed based on the location of the stenotic lesion. Each group consisted by geometries with different degrees of stenosis. Two of these groups (named MI1 and MI2) were statistically assessed as of higher risk for complications with the third one (STA) considered safer. Transient flow simulations were performed for these three groups, with representative coronary flow conditions. Flow was resolved by employing the incompressible Navier-Stokes equations for Newtonian fluid, which are considered to describe with acceptable accuracy the blood motion in arteries. Processing of the results have shown that appropriate surface quantities can distinct between high and low complication risk cases. Finally, based on the results of the healthy model and on previous works, a set of flow-based risk indices was proposed in order to distinguish among arbitrary geometries the ones that are more likely to lead to coronary artery disease complications.

Finally the developed model for coagulation was applied in selected (based on the flow simulation results) geometries for the three groups, under the previously calculated pulsating blood flow conditions. The simulation results have indicated that in geometries with higher degree of stenosis and higher wall shear values (regardless of the geometric group considered) the propagation of thrombin is slower. All MI2 models had similar behaviour: low average thrombin concentration and production rate with high thrombin concentration restricted in specific sites. On the contrary, in STA and MI1 models we could not identify a uniform pattern. In most cases high risk sites (elevated concentration and production rate of thrombin) were found near the wall at the areas of recirculation vortices formed after the stenotic lesion. Although this study showed that computational simulations can be used for the assessment of stenosed LAD and probably coronary arteries in general, it also showed that in order to obtain results that can be safely trusted for diagnosis the method should be applied on a large number of real geometries from patients with known disease outcome.

Abbreviations

ACS: Acute Coronary Syndrome

APC: Activated Protein C, inhibitor of coagulation

ATIII: Antithrombin III, inhibitor of coagulation, most important inhibitor of thrombin.

CAD: Coronary Artery Disease

CAI: Coagulation Activation Index

Cmax: Maximum concentration of thrombin in TGA assay.

CFD: Computational Fluid Dynamics

CHD: Coronary Heart Disease

ETP: (Estimated thrombin potential) The integral of thrombin concentration in respect to time in TGA or in other words the area underneath the curve representing thrombin concentration vs time

fII,... fXIII: Coagulation factors in non-activated form (zymogenes)

fIIa,... fXIIIa: Coagulation factors in activated form (enzymes)

Ht: Haematocrit, volume fraction of red blood cells in blood.

LAD: Left Anterior Descending (artery)

M11, M12: Groups of stenosed LAD geometrical models with higher complication risk

OSI: Oscillatory Shear Index.

RBC: Red Blood Cells

RRT: Relative Residence Time.

STABLE: Group of stenosed LAD geometrical models with lower complication risk

TAWSS: Time Averaged Wall Shear Stress

TFPI: Tissue Factor Pathway Inhibitor, inhibitor of the coagulation process.

TGA: Thrombin Generation Assay

T_{lag}: Time until thrombin production reaches amplification phase in TGA

T_{max}: Time until thrombin reaches maximum concentration in TGA

T_p: Propagation time, the time interval between the triggering and downstream propagation of thrombin.

WBC: White Blood Cells

WSS: Wall Shear Stress

Chapter 1 Introduction

1.1 Coronary artery disease: impact and complications

Coronary Artery Disease (CAD) or Coronary Heart Disease (CHD) is the formation of plaques on the interior walls of human coronary artery. The development and growth of these plaques, known as atheromatous plaques, initially results in the reduction of the lumen of coronary vessels. The progression of CAD however, is often followed by sudden complications known as acute coronary syndromes (ACS), when blood clots (or thrombi) are formed in the area of the plaque after erosion or rupture. The thrombus occludes the supply of blood and oxygen to the heart muscle. When coronary artery or one of its branches is permanently blocked the part of the myocardium that depended on the specific branch for blood and oxygen supply is at the risk of dying due to lack of oxygen, a situation known as myocardial infarction (MI).

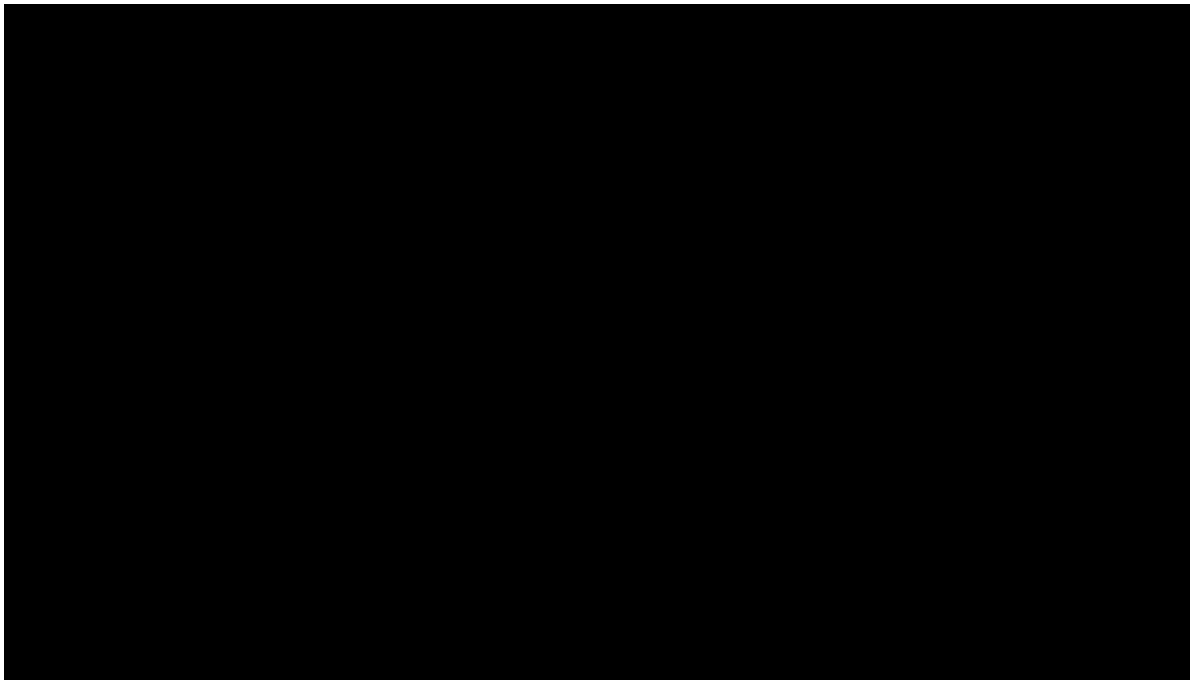


Figure 1-1: The different cases of ACS. (Image taken from <http://www.nottingham.ac.uk/nursing/practice/resources/cardiology/acs/arteries.php>)

There are several different conditions classified under the term MI. They are divided in two main categories based on the results of the electrocardiogram (ECG), STEMI and NSTEMI. STEMI cases usually correspond to total blockage of a part of the coronary network and the ST part of the ECG curve of the patient presents an elevation (STE) compared to the ECG curve of a healthy person. Non-STEMI or NSTEMI usually corresponds to partial blockage and no elevation of the ST part of the ECG is observed (NSTE) compared to the ECG curve of a healthy person. In

the cases where the occlusion is transient or of smaller degree (unstable angina) the part of the muscle depending on the specific vessel does not infarct (die) due to lack of oxygen supply but may malfunction (Figure 1-1). On the other hand, in a large number of cases the progress of the disease is mild or slow, and the symptoms are limited to chest pain or discomfort and breathe shortening (stable angina) occurring only when the patient is under physical or psychological stress conditions.

The complications of CAD are the leading cause of death worldwide, as they are responsible for one out of six deaths in the USA [4], 13% of men and 6.5% of women under 65 years old and about 21% of total deaths [5]. They are also responsible for the 10% of lost life years due to disability in Europe [6]. **The consequences of CAD complications show how important is to distinct the cases that are more likely to lead to ACS and decide on the optimum treatment.** Currently, the routine non-invasive medical tests performed for CHD (physical condition, blood pressure and haematological tests) do not lead to accurate diagnosis of the disease. At the same time, the available imaging techniques used for coronary network are either invasive and therefore cannot be used as a routine check-up (Coronary Angiography), or do not achieve the desired accuracy and are quite expensive (Computed Tomography and Intravascular Ultrasound). Even when the imaging techniques are used, they provide only geometric information of the stenosed area; they cannot give predictions on the possible evolution of CAD, therefore the decision on the optimum treatment is left to the doctor's judgment by experience.

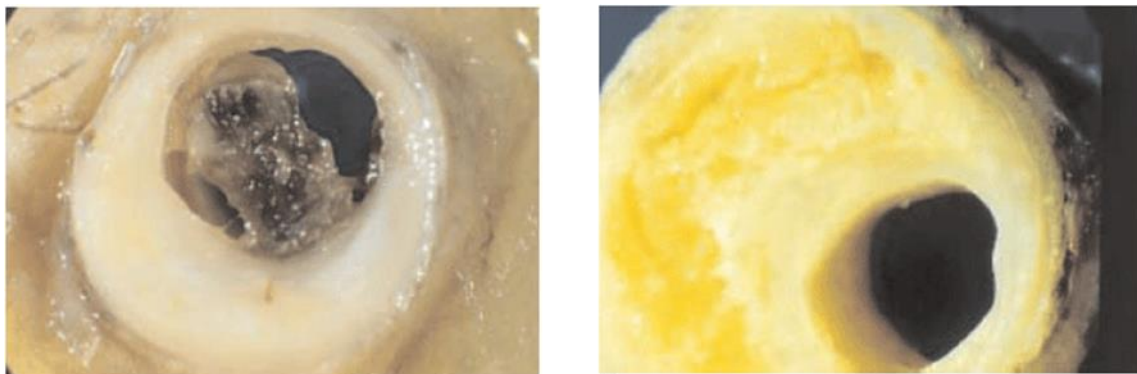


Figure 1-2: Thrombus formation in occluded coronary after rupture of the plaque (left) and stable stenosis without thrombotic complications (right).(images: M.H. Davidson, American Journal of Managed care)

1.2 Risk factors, symptoms and treatment

Specific behaviours and health characteristics have been identified as major or contributing risk factors for CAD, mainly via statistical correlations, with some of them probably being interrelated. Some of these factors can be controlled up to a point without the involvement of medical procedures. The non-physiological concentration of cholesterol and other lipids in blood, high blood pressure, diabetes, inactivity and obesity, and of course smoking, considered as major risk factors, and psychological stress, not-healthy diet and alcohol, considered as contributing factors [7] are probably subject to adjustment by modifying the diet and the habits of the patient. On the other hand, a number of major risk factors are not subject to change via modification of the behaviour of the patient; these are the gender -after 40 years of age the risk for developing CAD is 49% for men and 32% for women-age for both genders and inheritance [4]. As part of the causes of CAD cannot be controlled so no matter how good work is done regarding the prevention of the disease and more importantly, as lots of cases of CAD by the time they are first diagnosed they already require intervention, **a number of patients will at some point of their life be in the need of medical treatment for CAD**, especially in the developed world where the average age is higher.



Figure 1-3: Revascularization with the use of catheter and stent (PCI). Image taken from: http://www.birlaheart.org/Research/clinical_research.html

Figure 1-4: Coronary bypass. Vessel grafts connect the aorta with a point distal the stenosis. Image taken from: <http://uvahealth.com/services/heart/treatment/14782>

While 64% of lethal cases in USA have no previous reported symptoms [4], in a lot of patients

the reduction of blood supply to the myocardium (also called ischemia), especially during hyperaemia [8], gives some initial symptoms; pain in the chest related with physical activity or psychological stress, shortening of breath, and feeling of fatigue can function as a warning signs and lead a patient to seek for the appropriate medical examinations. Once a patient is diagnosed with CAD, the doctors have to choose between two options. The moderate one is to prescribe medical treatment (MT), usually drugs that prevent blood clotting and improve blood composition and reduce the heart load in order to relief the symptoms. At the same time they will advice the patient to adopt a number of life changes in order to reduce the risk of deterioration and perform regular medical check-ups.

In other cases the doctors judge that a more drastic approach is required. Then the patient undergoes either non-surgical angioplasty or a surgery, both combined with anti-thrombotic medication. In the first case (Figure 1-3) reopening of the blocked artery is performed with the insertion of a flexible tube with an attached balloon; this method is known as 'percutaneous coronary intervention' (PCI). When the balloon reaches the blocked location it is inflated and presses the plaque against the coronary walls. In some cases it is possible that a small mesh called stent is inserted in the previously stenosed location in order to hold the vessel walls in place. In the second case referred to as 'coronary artery bypass grafting' (CABG) (Figure 1-4), a part of vessel from another part of the patient's body is used for the construction of an alternative route for the blood around the stenosed location. The vessel graft –as it is called- connects the aorta with a site of the coronary distal the stenosis. The choice of the treatment method (PCI, CABG or MT) is based on the severity of the stenosis -in what percentage is the lumen reduced and on how many sites- the classification based on the ECG and the general clinical image of the patient (symptoms, risk factors). The effectiveness of a treatment method is judged by the rate of survival and the following clinical events. The choice of the optimum treatment in respect to survival and complications expectancy is still under discussion [9].

Up to 2010, approximately 30 randomized controlled trials comparing the progress of patients undergoing either revascularization or MT for different follow up times were published [10]. Analysis of the first 7 studies comparing CABG with medical treatment showed that patients that had undergone CAGB exhibited reduced mortality for a period 5 to 10 years [11]. A systematic review of the trials comparing PCI to medical treatment using 17 published randomized studies showed reduced mortality for patients that were subscribed to PCI [12] over an average period of 51 months compared to those who underwent MT. However, network analysis of the same studies showed no effect of PCI on the occurrence of severe complications compared to medical treatment [13] in accordance with the results of COURAGE trial which

included 2287 patients with an average 4.6 years follow up [14] [15]. A most recent meta-analysis including 28 randomized trials performed between 1977 and 2007 showed that revascularization in general improves the survival rate of patients compared to medical therapy but not the rate of non-fatal myocardial infarction [16]. At the same time MASS II trial, after following 603 patients treated at a single institution for 5 years, observed no significant difference among the results of the three methods [17]. For the patients where revascularization is prescribed, the choice between PCI and CABG is mainly based on the complexity of the case. According to three [18] and five [19] year follow-up results of the SYNTAX study, CAGB seems to work better in cases with multiple occlusion sites with PCI being a better alternative for cases with single branch stenosis.

To see the overall effectiveness of the treatment from a different perspective, in USA the statistical predicted number of recurrent events is approximately 36% of the number of the new events [4]. The same percentage of recurrent events was reported in a more detailed clinical study in Germany [20] performed using a smaller number of patients. In other words, approximately **one out of three people who undergo treatment of any kind for CHD have a follow-up incident**. Although the stenosed lesions are often characterized as culprit (the ones that require intervention) and non-culprit, the recurring events (total 20% in 697 monitored patients) in a period of three years were equally distributed among these categories [21]. The reported statistics on recurrent events include all ages including patients over 75 years and in general the total elimination of relapse seems utopic. However, the **statistics show that there is room for further improvement of the decision making process regarding the choice of the treatment that will lead to better results**, especially when keeping in mind that the two revascularization procedures have inherent complications; the graft sometimes is occluded, while thrombus is also formed on the stent after the procedure in some cases. Additionally, CAGB has also a small but considerable (about 1-3% in USA and UK) percentage of operating mortality, varying according to the special conditions of each case. It is of high importance the fact that **both ACS and after-treatment complications are related to thrombus formation**.

As the appropriateness of revascularization in a large number of clinical scenarios, especially with low and intermediate risk findings is uncertain [22, 23], it is almost certain that some patients take the risk of an unnecessary procedure or surgery, while others are unintentionally deprived from a necessary for their condition revascularization. It is possible that statistical analysis alone is not sufficient to indicate the optimum treatment in a patient specific manner. It may be more fruitful instead **to find and determine some additional case specific criteria**. **These criteria should be able to be measured or calculated and expressed in numbers**, in

the form of arithmetic risk indices, in a similar manner as the non-physiological concentrations of blood components or the results of haematological tests are expressed. The quantities chosen for monitoring and the resulting complication risk indices will be based on the underlying physical mechanism that leads to deterioration and complications while the final derivation of the physiological limits for each proposed quantity will be supported via statistical validation over a large number of patients.

1.3 The role of geometry

Besides the risk factors that have already been mentioned, there is at least another known parameter that seems to be related with the emergence and evolution of CAD, the geometrical shape of the coronary artery. The shape of the coronary is not an independent factor as it can be mainly attributed to heredity which has been included in the major risk factors, but it has some interesting characteristics that make it appealing in the pursuit of more specific risk factors and corresponding arithmetic risk indexes. Firstly, it is absolutely case specific and it seems there are significant differences between the shape of the coronary trees of different individuals (Figure 1-5), not just small details. Secondly, the coronary geometry is related to a number of parameters (some obvious and some more concealed) that are measurable and therefore suitable for defining arithmetic indexes. The apparent parameters that can be measured is the specific characteristics of the coronary vessels, such as curvature, length of specific segments,



Figure 1-5: Left coronary trees of different patients (same view). Note the significant variation of the shape of the coronary arterial tree between different individuals

diameter and tapering, bifurcations' location and bifurcation angles, provided that an accurate image of the patient's coronary artery is available.

The not-so-obvious parameter that is decisively influenced (but not fully determined) by the geometry of the artery is the local flow field in stenosed coronary vessels near the area of the stenosis. While the exact flow conditions are also influenced by other factors such as the blood pressure, the exact viscosity of a person's blood (which can even vary for the same person during rest and hyperaemia), the shape of the coronary imposes a general pattern for the flow conditions that will prevail in a vessel. As it will be shown as part of the present Thesis, **there is both experimental evidence and identified underlying mechanisms that relate the flow and the geometry of the vessels with the emergence and the progress of CAD and the formation of thrombus.**

The connection between the location of the plaque and the geometric characteristics of the vessel has long been indicated [24, 25]. Besides the surface effects of flow that depend on the exact location, the thickness of the vessel wall, which is not uniform, also depends on the coronary geometry; specific sites of the coronary wall (opposite bifurcations or at the external side of curvature) which are characterized by low values of wall shear are usually thicker (intima-media thickening) [26, 27] and this extra thickness is considered to predispose the specific locations to atherogenesis [28]. The general idea of using quantitative characterization of the coronary geometry as a dynamic risk factor for coronary disease [29] is under discussion for decades. Recently, statistical correlation between the location of the stenotic lesion and the incidence of acute coronary syndrome ACS [1, 30] has been reported. Events believed to occur previously of the final stages of the disease, such as rupture, erosion and thinning of the cap of the plaque [31], can also be related to mechanical factors (friction, residence time and stretching of vessel wall). But so far, it is has not been possible to quantitatively correlate the progression of CAD and the emergence of ACS with the shape of the coronary, while the available clinical information that leads to treatment decisions is often misleading or insufficient [22, 23]. An alternative new approach that to the best of my knowledge has not been suggested so far **is the correlation of the geometry of the coronary of a patient to the overall risk of severe deterioration**, using a number of blood flow-based indices.

1.4 The influence of flow

As plaque development and thrombus formation are processes that mainly occur on the vessel wall, the basic flow-related quantities that are considered more important influence are wall shear stress τ and wall shear rate γ . These two quantities at a specific location of the flow are proportional ($\tau_w = \mu \cdot \gamma_w$ where μ is the viscosity of the fluid a quantity with significant variations for blood depending on the conditions). Shear rate expresses the change of the velocity in a direction normal to the vessel wall (Figure 1-6) and therefore it is an indication of the

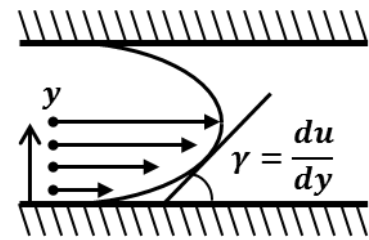


Figure 1-6: Schematic representation of shear rate

velocity magnitude near the surface. As convection is the basic transfer mechanism of blood flowing substances, wall shear rate has long been correlated with the presence of atheroma in specific locations of human arteries [32]. Besides the supply of reactants, shear rate determines the velocity of the biomolecules and particles in the flowing blood as they pass near the vessel's wall. The magnitude of this velocity enables, facilitates or makes impossible certain interactions between the blood flowing substances and cells and the cells of the vessel wall, purely by affecting the residence time and the friction between flowing blood and endothelium cells. Different mechanical stimulation alters the behaviour the same holds for the cells of endothelium [33-36]. Recent insights on the properties of vessel walls showed that while under physiological conditions they are not thrombogenic, pathological flow conditions can alter this behaviour.

Finally, another local factor considered of high importance for ACS is the nature of the atheromatous plaque, in terms of morphological characteristics and specific composition [31]. The assessment of the characteristics of the plaque up to a point is possible using advanced medical imaging techniques (multi-slice computed tomography or intravascular ultrasound), and there is a number of studies that have reported such results in the last decade (indicatively [37-42]). However, as this technique is invasive and of high cost it is not included in the routine clinical practice. The morphological characteristics of the plaque though, as vulnerability [43], and even the composition [44] are also related to flow and the same holds for the progress of CAD [45]. So **while imaging techniques provide information for a specific time instance and at a high cost, a quantitative correlation between flow and the evolution of CAD can serve both as diagnostic and predictive tool.**

1.5 Blood flow and thrombus formation

Formation of blood clot or thrombus occurs after the initiation of the haemostatic process within the circulatory system. This happens due to an initial stimulation, usually an injury on the wall of a vessel. In the case of CAD the stimulus is believed to be the rupture or erosion of the atheromatous plaque. The final outcome of the process of thrombus formation is a jelly-like mass composed mainly by platelets and a cross-linked protein called fibrin, also known as activated factor I of coagulation. Fibrin forms a mesh (Figure 1-7a), and in this mesh are also trapped other blood flowing particles as red blood cells and white blood cells (Figure 1-7b). Typically in arteries, thrombi consist mainly by platelets (white thrombi), while in veins the dominant component is red blood cells (red thrombi). Between the initial stimulation and the formation of thrombus take place a large number of biochemical reactions and cell responses. The process of thrombus formation will be described in more detail in the next chapter.

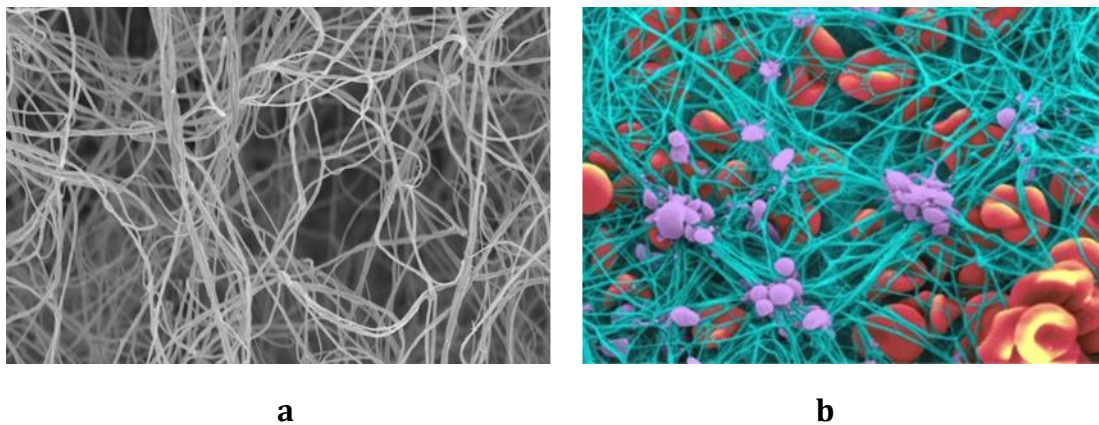


Figure 1-7: (a) Fibrin mesh as depicted by scanning electron microscopy Image: http://www.leeds.ac.uk/light/research/cdr/mechanisms_of_thrombosis.html (left) (b) Scanning electron microscopy image of fibrin mesh (blue) with trapped platelets (purple) and red blood cells (red) Image: *Yuri Veklich and John W. Weisel, University of Pennsylvania School of Medicine (right)*

Most of the cells and reacting substances participating in the coagulation are transported in the flowing blood. Therefore, flow determines the supply, residence time and abduction over the reacting site and subsequently the concentrations for these species. This is done via the balance of convection and diffusion mechanisms and via the flow dominated collisions of circulating cells and particles [46, 47]. So, at first sight stagnation points and areas with reduced flow look suspicious for thrombus formation as these conditions allow more time for interaction between blood-transported substances and the wall of the vessel or the surface of the plaque.

Nevertheless, studies on the effect of flow on coagulation mechanism revealed that increased flow can also contribute to the initiation of thrombus formation. Flow induced mechanical stress alters the behaviour of blood flowing particles and substances related to thrombus formation, as von Willebrand factor [48] and platelets [49]. High values and extreme variations of shear stress can cause activation of platelets [50-52], increase of Ca levels of blood (indicative of platelet activation and required mineral in different stage of coagulation) [53], aggregation of platelets to each other and to vessel wall [54] and generally initiation of the coagulation mechanism [46]. So especially for the cases of arterial stenosis where shear rates in the stenotic lesion is increased upstream the peak of the stenosis, triggering due to high values of shear stress may be equally important factor to the effect of transport on the concentration of the reactants.

Therefore, **knowledge of the flow field in a stenosed, stented or grafted coronary artery and generally in any susceptible vessel can provide information on whether it is more or less possible for a thrombosis to occur.** The tools that can classify different cases as of different risk for thrombosis it is not necessary (and probably it is infeasible as well) to model the whole process of thrombus formation from the initiation to the total occlusion. It is enough to provide some well-defined flow related information that will be based on the process of coagulation, provided that this information will be expressed in a manner that will allow statistical validation and correction.

1.6 Basis and aims of this work

From the data presented so far it is clear that **the choice of optimum treatment for CAD is a problem of high importance and at the same time far from understood.** While the diagnostic methods and applied treatments are constantly improving and this leads to a reduction of annual death rate due to CHD both in USA[4] and Europe [5], it seems that there is still need and space for improvement. More specifically, it seems that **the assessment of each specific case is based mainly on the current clinical image/condition of the patient, and there is no tool able to perform even a rough estimation of the possible evolution.** While this looks perfectly fine for patients with acute symptoms or patients with severe and multiple stenosis that obviously require immediate intervention of some kind, in patients with low but not negligible degree of stenosis though and chronic CAD this static perception of the case does not help in making a decision on whether the patient requires some kind of intervention or medical treatment is preferable. Trying to base such decision only on the statistics of random controlled trials and meta-analysis underestimates the importance of specific conditions prevailing for each patient.

The shape of the coronary artery plays decisive role on the evolution of CAD. However, to our knowledge there are very few studies that attempt to achieve a quantification of the effect of this risk factor. To be more accurate, there have only been some efforts for statistical classifications, i.e. to average the characteristics of stable and dangerous cases and to divide the stenosed coronaries in groups, depending on the position of the stenosis [1]. But **there is no advance in studies trying to extract case specific indexes that could be calculated for each case and afterwards be statistically calibrated and evaluated.** Such a case specific assessment that would actually provide some kind of prediction based on the geometry could also help on the choice of the optimum therapeutic procedure applied to each patient.

As the role of geometry seems to influence the progress of CAD via the imposition of different flow conditions at different sites of the artery, **flow simulations appear to be a very promising and novel way to assess different geometries in respect to the risk of ACS emergence.** Note that, in order such an assessment to be performed, it is not necessary for the simulation method to reproduce every detail of the flow field and take into account all the complex physical parameters involved in this problem, such as vessel wall elasticity, vessel wall movement and exact rheological behaviour of blood. It will be more than enough if, **by using a simplified method for the simulations we can extract a set of numerical indices that afterwards will be validated and calibrated by applying the method on a large number of real cases.**

As explained earlier, flow also effects the formation of thrombus, which is the underlying mechanism behind ACS and post-treatment coronary complications. Flow simulation techniques can be coupled with a model that describes thrombus formation, and indeed in a patient specific manner. Such a tool will be able to classify different patients according to their specific thrombogenic potential, as it is determined by the coronary geometry and haematological characteristics. The results will be expressed as a group of arithmetic indices. In order to perform such simulations the simplifications are inevitable due to the complexity of the processes, the large number and inaccessible nature of influencing factors, the different temporal and spatial scales that are involved. To give an indicative example, platelets have a typical dimension of $2\mu\text{m}$, coronary artery has a typical diameter of 4mm . Glycoproteins are expressed at non-determinable locations on the surface of platelets after activation and interact with circulating proteins with typical dimension of 10nm with the orientation of these biomolecules affecting the interaction. In terms of time, the cardiac pulse is of the order of 1sec . The time scale of coagulation in vitro is of the order of 10 min , while the onset of CAD symptoms and the variations of the heart activity of a human follow a circadian circle (24h). In order to

confront this difficulty most contemporary studies move towards the application of biological models of increasing complexity on two dimensional and relatively small computational domains. The route followed in this study is somehow different. The models were developed in a way that the complexity is determined by the amount of the available clinical data instead of trying to exploit the available laboratory data. This approach leads directly to patient specific simulations with relatively simple models. As throughout this work the details of the models including simplifications are thoroughly explained, the application of the method in cases other than the ones used in this study is straightforward. This is important as **in order for any simulation results in these subjects to have comparative value and be suitable for statistical validation, they should have been obtained using the exact same methods.**

Throughout the chapters of this Thesis, the following tasks will be performed. In Chapter 2, a relatively brief literature review on the state-of-the-art knowledge on blood coagulation and formation of thrombus is given, (as a search for articles related only to tissue factor, a substance that triggers the coagulation cascade will result to over 10,000 publications, a detailed review of all available literature on thrombus formation is infeasible). In the same chapter a review of the rheological properties of blood and the difficulties and techniques related to simulations of blood flow will be given. Following that, a simplified model for thrombin generation and thrombus formation is presented in Chapter 3, based on clinical results and previous studies. Then transient simulations of blood flow are reported on a number of different geometries in Chapter 4, statistically assessed as of different CAD risk, while some risk indexes are defined and compared for the different cases. Finally, the simplified thrombus model is coupled with the results of the flow simulations in Chapter 5. I believe that **this work is a first step towards a case specific prediction for patients with CAD using computational techniques.** At the moment, the only similar method proposed is the computational calculation of the fractional flow reserve (FFR) [55, 56], which is basically an index for ischaemic consequences of the stenosis on the myocardium [57]. Additionally, as the accuracy of the non-invasive imaging techniques such as multi-slice computed tomography for coronary improves, such a test **could be in the future applied as a diagnostic tool for prediction of the disease at its early stage, and could evolve to a routine clinical test** as electrocardiogram or stress test.

Chapter 2 Literature review

2.1 Blood flow and blood flow simulations

2.1.1 Blood rheology

A general problem when performing blood flow simulations is the complex rheological behaviour of blood. The main reason for these complex properties is that blood is a multiphase fluid and its macroscopic viscosity in low shear stress is strongly affected by the interactions among its components. In more detail, blood consists of plasma, red blood cells, white blood cells (RBCs and WBCs respectively) and platelets (1/600 and 1/800 of total volume) and

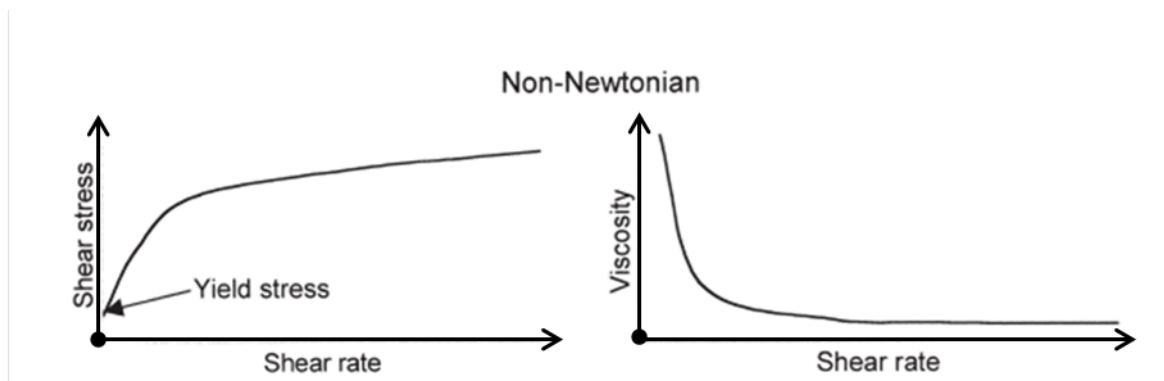


Figure 2-1: Characteristics of blood: Non-Newtonian (Baskut et al 2003). Bloods rheological behaviour becomes Newtonian above a level of shear stress. The exact value of the threshold is under discussion but in arterial flow condition the average shear is definitely above the threshold.

various proteins and minerals. Plasma and RBCs consist more than 98% of volume fraction of blood and under physiological conditions determine blood's rheological behavior. Plasma is an incompressible Newtonian fluid with density 1060-1080kg/m³ and constant viscosity about 1.2·10⁻³ Pa·s (1.1-1.35·10⁻³ Pa·s [58] under physiological conditions) at 37^o C. RBCs (35-45% volume fraction) are deformable cells with biconcave disc shape, diameter about 8µm, thickness about 2µm, neck 0.8µm, density very close to plasma (1080-1089 kg/m³) and viscosity about

$6 \cdot 10^{-3} \text{ Pa} \cdot \text{s}$ [59]. As shown in Figure 2-1, for a range of shear rate values blood is very well approximated as a Newtonian fluid with constant viscosity. This does not hold for blood flow in vessels with diameter comparable to blood cell size [60] where the deformation of RBCs plays major role, but this is not the case of this study as the typical diameter of the examined vessels is about three orders of magnitude bigger than the red blood cell dimensions. For small values of shear rate though, blood generally demonstrates shear thinning behavior regardless of the size of the vessel. The basic mechanism behind this non-Newtonian behavior of blood is the interactions between red blood cells. RBCs tend to aggregate to each other and in the presence of blood proteins and other macromolecules under specific conditions even form linear stacks (rouleaux). These linear aggregates when formed may also connect to each other creating three dimensional structures. So while for increased blood flow (when shear forces are sufficiently high) the links between RBCs break, the contribution of the particulate phase of blood to viscosity is stabilized and viscosity settles at a constant value, in low shear rates the effect of these forces is flow dependent. The exact value of blood viscosity varies for different individuals, as it is influenced by the specific properties of RBCs as the volume fraction (hematocrit Ht) [61] and deformability [62]. The pre-measurement treatment and storage of blood could affect the properties of RBCs and subsequently alter blood viscosity[63]. The measured blood viscosity in tube flow depends also on the diameter of the used tube [64]. All these factors cause some variations in the values reported in the existing literature. However for wall shear rate values above $\sim 100/\text{s}$ blood can be very well approximated as a Newtonian fluid, with generally accepted constant viscosity $\sim 3.5 \cdot 10^{-3} \text{ Pa} \cdot \text{s}$ [59].

In large vessels like the coronary artery, the average values of shear rate are relatively high ($\approx 1000/\text{s}$). Under pulsating flow conditions though, there are time intervals during the cardiac cycle where shear is low (in coronary there is even inversion of flow direction) and blood exhibits its non-Newtonian character. It is also possible that when shear rate drops there is a delay in RBCs re-aggregation, giving blood thixotropic properties. This gel formed by RBCs and plasma proteins can slip in respect to the walls depending of wall roughness, making even the 'no slip condition' that is usually used as boundary condition between fluid and walls inaccurate for the case of blood [65]. However for most part of the heart cycle the Newtonian fluid is a valid approximation [59].

Blood flow modeling exhibits some additional difficulties when it is intended to be combined with thrombus formation modeling. Concentration of RBCs is higher near the center of large arteries and the concentration profile is influenced by the values of shear rate; the axial distribution of platelet concentration is also non uniform and influenced by the value of shear

rate [67] and platelets are particles of high interest regarding thrombus formation as it is explained in the next section. The platelet-platelet and platelet-vessel wall interactions are influenced by the presence and elastic properties of RBCs [68, 69] and they are also influenced by the local value of shear rate [70]. The rotational motion of RBCs increases the diffusivity of platelets by two orders of magnitude [70, 71] and probably increases also the diffusivity of the other coagulation factors. Additionally as RBCs occupy the center of the vessel, platelet near wall concentration is increased

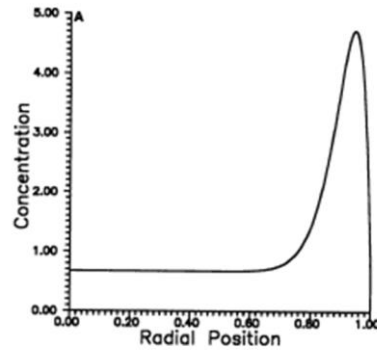


Figure 2-2: Axial distribution of platelet concentration. Values are normalized using the bulk platelet concentration (E.C. Eckstein 1991 [66]).

both in steady and pulsatile flow [72] (Figure 2-2). The same probably holds for the concentration of all the constituents of blood with relatively small dimensions. As they are pushed towards the wall by the RBCs the near wall concentration is higher than the reported bulk concentration values. The exact formula that gives the distribution of platelet concentration in respect to the distance from the center (or the wall) for flow in a tube is not determined but it has been shown that it is influenced by both hematocrit and shear rate [73, 74]. Finally after the initiation of blood coagulation, the viscosity of blood near the reacting site of the wall will be increased locally by the changes in the constitution of blood [75], more specifically by the activation and polymerization of fibrin strands and the adhesive properties of activated platelets.

A number of Newtonian models have been proposed for blood viscosity $\mu = \mu(Ht)$, being function of RBC volume fraction. Based on experiments and observations a number of non-Newtonian models have also been developed that express the viscosity as a function of haematocrit and shear rate in a time independent $\mu = \mu(Ht, \gamma)$ or in a time dependent $\mu = \mu(Ht, \gamma, t)$ manner-reviewed in [59]. As blood is a mixture of plasma and cells that for most cases behave as fluid drops, a number of multiphase or particle models have also been proposed that could be more appropriate for modeling of blood flow (shortly described and reviewed in [76]) as they can reproduce the distribution of different components of blood [77-79] and include the interaction between RBCs. To the best of my knowledge, **there is not a generally accepted model used in CFD simulation and the choice of the mathematical expression**

for blood viscosity depends on the specific simulation requirements.

Steady-state simulations and simulations of flow in large vessels are usually performed with constant viscosity, while the non-Newtonian models seem to be more appropriate for simulations of pulsating flow in microcirculation. Some studies comparing different models for blood viscosity show that for the same geometry and boundary condition the resulting axial velocity and wall shear stress distribution have significant

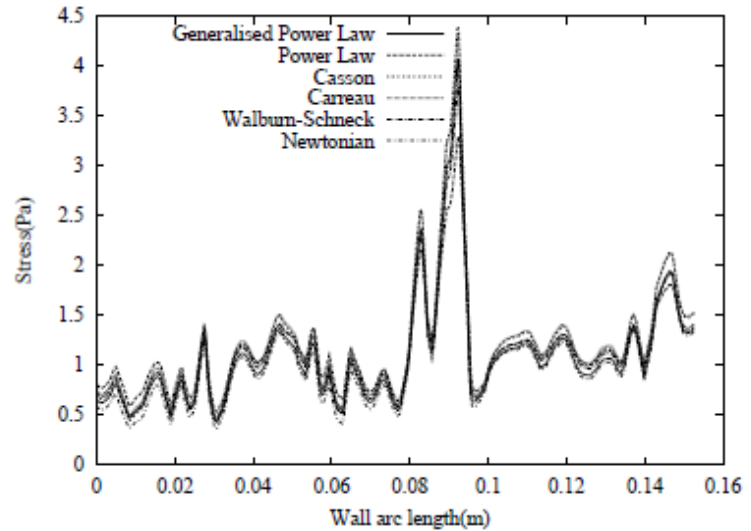


Figure 2-3: WSS along a stream-wise line in a right coronary geometry with the use of different models for blood viscosity for steady state simulation [80]. There are differences in the exact values but the distribution is very similar

differences both for steady [81] and pulsatile flow [82]. On the contrary, other studies report that for transient simulations [56, 83, 84] the Newtonian approach is an adequate approximation as it results in similar WSS distributions and the differences in results between the two approaches is limited both in terms of location and part of the heart cycle. Several models have been used for coronary flow simulations (e.g. the generalized power law model with haematocrit dependent constants[83, 85, 86], the Casson model [87, 88] or the Carreau model [89]). However, in the large majority of the reviewed CFD studies of coronary flow blood is modelled as an incompressible Newtonian fluid and the flow is considered laminar [86, 90-97] as the calculated Reynolds numbers are small (of the order of 100).

At first sight, the most appropriate choice for blood flow simulations related to thrombus formation seems to be a two-phase model (plasma and RBC), that could describe the non-uniform concentrations of the platelets and the substances that are involved in thrombus formation. Such a model would be even more realistic if it included an expression for the viscosity of plasma dependent on the local chemical composition of blood instead of using a constant value. Similar approaches are used in the work of Anand et al [98] where the viscosity depends on the clot formation, or the work of Bondar and Sequeira [99] where viscosity is a function of fibrin concentration. In reality though, this approach would increase significantly the computational cost of the simulations and probably affect the stability of the models as well, as it would require the solution of the flow equations at every time step coupled to the system of

the equations used for the biochemical reactions that describe thrombus formation. Additionally, as detailed information of the specific properties of blood for each patient is not available, the increase of the complexity of the method would not necessary lead to increased accuracy and would also reduce the patient specific character of the simulations. On the other hand, **the Newtonian approximation for blood's viscosity** –constant value for $\mu \approx 3.5 \text{ Pa} \cdot \text{s}$, not depending on shear stress and time- **is generally considered satisfactory for arterial flow conditions** [100] (Figure 2-3), it has been used in a great number of blood flow simulations, and it allows the application of the thrombus model on flow fields as obtained from CFD simulation, without requiring to solve the flow field again at every time step of the thrombus model. Finally, as the interactions between platelets and vessel wall will be modeled as surface biochemical processes, **at least part of the effect of shear rate can be included in the method with the use of shear dependent reaction rate constants and locally increased concentrations for the reactants near the wall**, that will be calibrated after applying the model on experimental results.

2.1.2 Geometry reconstruction

The first step for performing coronary blood flow simulation is the reconstruction of the appropriate geometry. The geometrical models that are used in coronary flow simulations vary, depending on the scope of each study. The reconstructed geometry also depends on the method used in order to obtain its shape. In studies that focus on a specific and small part of the coronary vessel network e.g. a segment of a stenosed branch, and aim to obtain the resulting

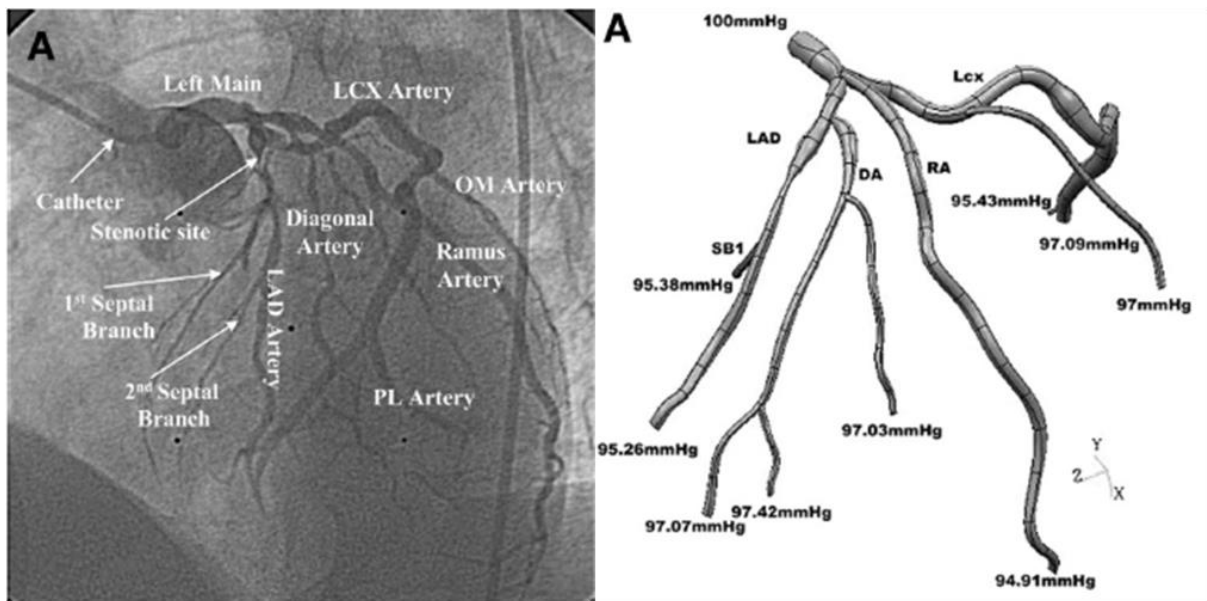


Figure 2-4: Image from conventional coronary angiography and the resulting reconstructed geometry (images from Chen et al 2005 [91]). Note the very small pressure drop values among the inlet and the outlets of the branches.

flow related quantities, simplified geometrical models have been used. Two dimensional stenosed tube based on images from stented coronary branches [89], idealized three dimensional models of bifurcation with different types of stents [97], in-plane and out-of plane coronary-like S-shaped geometries without side branches [95] and simplified in-plane geometries with aneurysm in different positions [94] are examples of geometries of reduced complexity that have been used in previous CFD studies. Single branch models have also been used [56, 78-80, 83, 84, 101, 102] for larger scale simulations as up-to a point it was believed that the properties of the flow field depend mainly on the curvature of the main branch with the existence of the bifurcations having minor influence [101]. However in more recent CFD studies it has been demonstrated that the existence of bifurcation has significant and non-linear

influence on the flow related quantities [85] and it is also related to the appearance of recirculation zones [88].

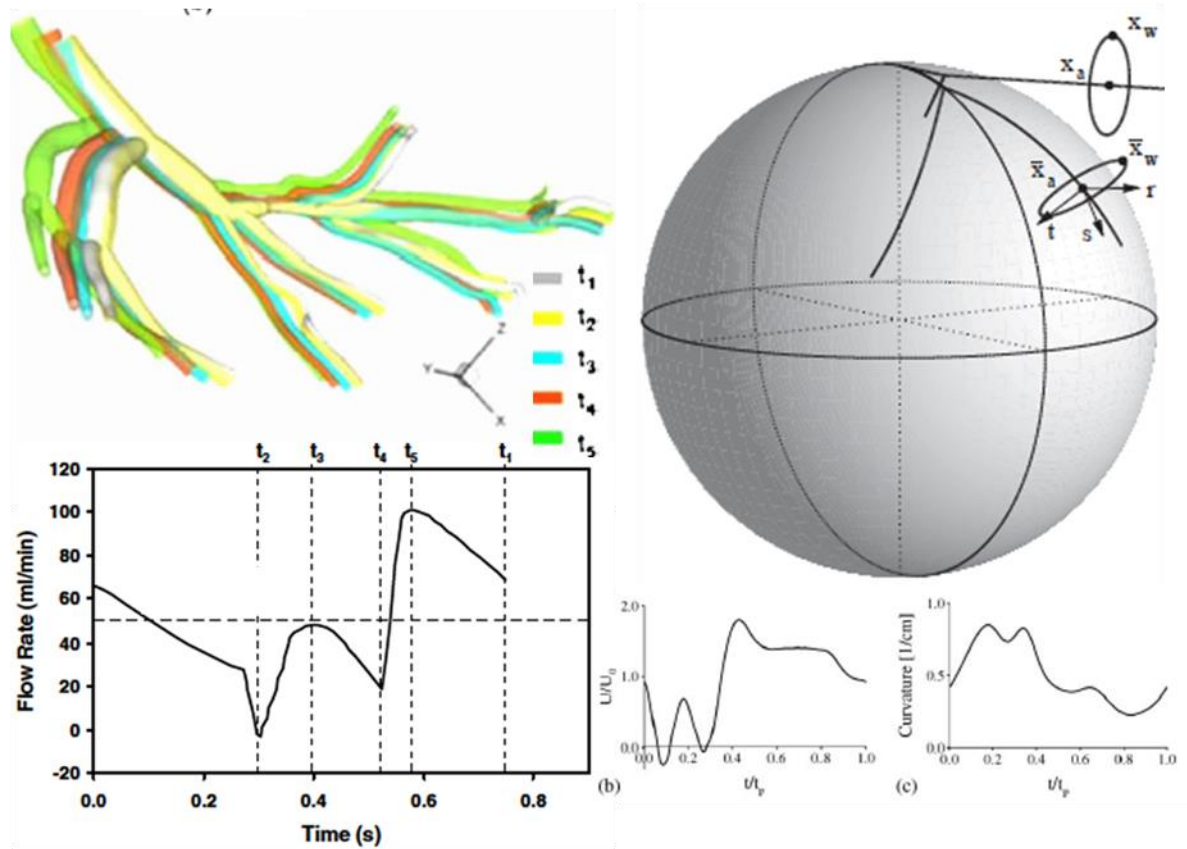


Figure 2-5: Methods for modelling the motion of the vessel network. Left: use of 5 different images from angiography corresponding to five different instances of the inlet waveform. The method uses the exact position of each point of the network (Theodorakakos et al 2008). Right: Use of a curvature-versus-time function for the modelling of the motion of coronary vessels (Prosi et al 2004).

In the cases where a more accurate model of human coronary is used, either single branch or with side branches, the reconstruction is usually based on data from medical images (CT or conventional coronary X-ray angiography) either for a single branch or a model with bifurcations [56, 78-80, 83, 86-88, 91, 92, 101, 103] and the three dimensional model is extracted with the use of image processing software (indicatively [104, 105]). There are also some studies where the model is extracted post mortem from the vascular system of a laboratory animal [90] or a deceased human [106].

In most studies the walls of the vessel are considered rigid and not moving. The actual case

though is somehow different as the coronary network is located on the heart muscle and as a result of that, the shape and the diameter of the vessels change within each heart cycle due to the muscle contractions. The real vessels exhibit also some elasticity, and the diameter is also affected by the pressure changes. While in most of the studies these facts are neglected, there are available techniques for incorporating such factors. The elasticity of the vessels can be taken into account with the use of fluid-structure interaction approach [96] or with a more phenomenological approach that uses data for the diameter for different instances of the pulse obtained from medical imaging [102]. The motion of the vessel has also been included in some works. This has been performed with the use of different methods. One way is to start from different images that correspond to different time instances of the pulse (five different images in the specific example) and use linear interpolation of the intermediate geometries for all the vessels of coronary network with diameters bigger than approximately 1mm [87]. This method takes into account the specific time dependent position of each branch during the heart cycle. Another way to model the movement of the coronary vessels is to use the curvature of the whole system. In the cited example this was done with the use of approximately 14 time instances per pulse, and the geometry was modified according to the resulting function of curvature versus time [93]. This method uses a single factor for the deformation (or rather bending) of the whole vessel network mode. (Figure 2-5).

Overall, the results reported these studies indicate that **the motion of the geometry has a small influence on the results** and therefore it can be justified to neglect it when it comes to studies that aim to compare different geometries. **The case is not the same with the bifurcations. The inclusion of bifurcations in sites of the geometrical model changes the flow field quantities** both in terms of velocity distribution and wall shear stress in a non-linear manner and therefore bifurcations cannot be neglected.

2.1.3 Inlet and outlet boundary conditions

Due to the nature of coronary circulation, obtaining proper boundary conditions for the inlet and more importantly the outlets of a geometrical coronary model that is used for flow simulation is not an easy task; the optimum way of imposing accurate boundary conditions in coronary flow simulations is still under discussion in the relevant literature. The actual factors that determine the pressure and the mass flow rates at the inlet and the outlets of each branch of the coronary network are (or considered to be) known in a qualitative manner. Coronary arteries originate from the aorta, near the aortic root (aortic valve) on the left side of the heart and the inlet pressure is equal to the aortic pressure with very good

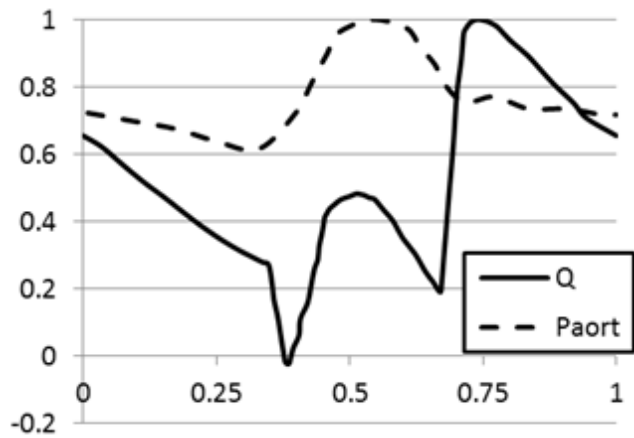


Figure 2-6: Non dimensional (maximum values set to 1) wave forms for the inlet pressure (Westerhoff et al 2006) on the coronary network (aortic pressure) and the inlet mass flow rate Q (Levi 2001) for non stenosed vessel. The two quantities are obviously out of phase as the inlet is severely influenced by the motion of the heart muscle.

approximation. Blood entering the CA is distributed through a network of arterioles, capillaries and venules that go deep into the myocardium, to end up finally in the right atrium of the heart. **So for the whole coronary network the driving pressure is the aortic pressure minus the pressure of the right atrium.** But as the location of the coronary network is on the heart muscle, coronary flow cannot be fully determined by the inlet and the outlet pressure of the system, because as the heart moves part of this network is blocked and there is also pressure exerted by this motion. As a result, coronary flow is mainly determined by the contraction of the heart muscle rather than by the inlet pressure and outlet pressure (Figure 2-6).

While the physical mechanism that determines coronary flow is known and well described, most of the information required for quantitative computations is not accessible. The currently available medical tools cannot provide individual-specific measurements or even safe estimations for the mass flow rate and the pressure at the inlet and mainly at outflows of a part of the coronary vessel network that can function as computational domain. Additionally, the factors that determine coronary flow have large variations among humans due to anatomic differences and even change for the same patients during different levels of physical activity or

psychological stress. Several approaches have been used in order to confront this difficulty. In almost all cases where pressure is used as inlet boundary condition, the aortic pressure wave forms available in the open literature are utilized. Similarly, anatomically correct generic waveforms available in the literature [78, 79, 84-90, 97, 101] are used when mass flow rate is used as an inlet boundary condition, while in a few cases simplified inlet pulses have been used [101]. An example of inlet pressure (aortic) and mass flow rate for left coronary artery are shown in Figure 2-6. Nevertheless, the use of a generic waveform is not the only used approach. Inlet boundary condition can also be obtained by in vitro experimental measurements in coronary models [106] or utilizing data obtained from laboratory animal models [102].

The second (and more difficult part) is to obtain conditions at the outflow boundaries of the coronary geometrical model. As the shape of the coronary network varies significantly for different individuals, there are no 'generic waveforms' for the outflows or standardized distribution of the inlet flow among the different branches. Excluding the cases of single-branch geometries where mass conservation and wall elasticity are enough to determine the mass flow rate at the outlet, the applied boundary conditions at the outlets always include some assumptions and approximations. One simple option is to assume a reference pressure value for the outlets (usually zero) [79, 80, 83, 88, 90, 92, 102]. This method results in the same pressure drop between the inlet and all the outlets (regardless the distance between them) so this approximation leads to bigger errors for larger geometries where the pressure drop is noticeably bigger as we move downstream (Figure 2-4). The method is also not applicable in the case of stenosed branches as the use of the same pressure value for the outlet distal the stenosis will lead to non-realistic reduction of the flow rate in the specific branch.

Another simple approach suitable for geometries with branches that correspond to healthy vessels is the use of predefined outflows. In case specific simulations (both for geometries with and without stenotic branches) it is possible to obtain the flow rate or even the velocity profiles at the outlets from experiments on vessel models [85, 90]. If experimental data is not available, a relatively simple and general way to determine the distribution of mass flow between the mother branch and the bifurcations is according to the radii fraction, under the assumption of poiseuille flow and constant wall shear stress [87, 91, 92, 103]. In the case of poiseuille flow there is a relationship between the wall shear stress the radius and the mass flow rate in a branch. The elasticity of the vessel wall are not expected to exhibit significant variations in a small area in healthy vessel. Therefore large variations of wall shear stress would be compensated via deformation and remodeling. So for the two branches at a bifurcation the distribution of the flow under the assumption of poiseuille flow is determined by the radii of the

two branches.

$$\tau_w = \frac{4\mu Q}{\pi r^3} \Rightarrow \dots \Rightarrow \frac{Q_{i,0}}{r_i^3} = \frac{Q_{m,i}}{r_{m,i}^3} \quad \text{Equation 2.1}$$

While this approach has also been used for branches with stenosis [97], the assumption of constant properties at the parts of the vessel where atheromatous plaque has developed does not seem valid. For these cases, the outflow boundary conditions should be based on assumptions describing the behaviour vessel network downstream of the CFD exit boundary, which are not included in the simulation. In general, it is reasonable to be assumed that the network properties downstream of the CFD exit boundary are not affected by the existence of the stenosis. Therefore its behaviour must be the same regardless the existence of stenotic lesions in the computational domain. The simplest way to take advantage of this assumption is to assume a constant pressure drop between the inlet and a point far downstream of the outlets of the computational domain; the pressure drop of the non-simulated the downstream part can be simply estimated by subtracting from the assumed total pressure drop the one calculated from the CFD model of the ‘healthy’ geometry (i.e. the one without the stenosis) [87, 91].

A more sophisticated method used to simulate the behavior of a part of the vessel network (or more generally a part of the circulatory system) is the use of ‘lumped models’. The computational domain is considered as a part of a much larger system for which some inlet and outlet conditions (pressure or flow rate or both) are known. The part of the system between the inlet or outlet of the geometry and a point with for which pressure and/or flow rate are prescribed is modeled as a dimensionless system with known properties.

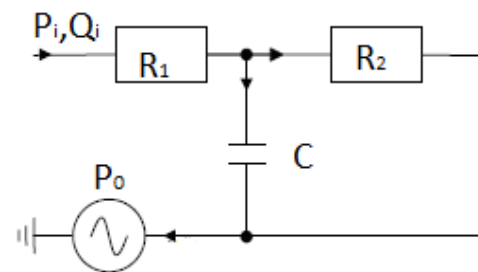


Figure 2-7: Schematic representation of the three element Windkessel model.

These lumped models actually impose a predetermined relationship between pressure and/or flow rate at the boundaries of the geometry and the pressure/flow rate at the input and output of the system. Depending on the specific type of the model used, this relationship may also include the time derivatives and the integrals of the flow rate and the pressure. These relations are similar to the equations that describe the relationships between the current and the potential in RLC electrical circuits (Figure 2-7). The simplest case of lumped model considers

only a plain resistance [87, 91] that results in a simple linear relationship between the mass flow Q_i at the outlet i , the pressure at the outlet P_i the reference pressure P_0 and the resistance of the downstream vessel network:

$$P_i - Q_i \cdot R_i - P_0 = 0 \quad \text{Equation 2.2}$$

As real vessels are elastic, a more accurate description of the downstream vessel network should include its compliance C ($C = dV/dP$) as for increased values of pressure the volume of the blood in the vessel would be also increased and the input-output mass balance is not zero at a given time instant. For this purpose, more complicated models have been suggested, that include also the capacitance of the vessel network after the outlet of the computational region, known as Windkessel models; these may consist of two (R-C) or three (R-C-R) elements [107-110]. Indicatively, the pressure-mass flow relationship at the outlet of the computational domain with the use of a three element model with resistance and capacitance is:

$$P_i(t) - [P_i(0) - RQ_i(0) - P_0(0)]e^{-t/R_2C} - P_0(t) - RQ_i(t) - \int_0^t \frac{e^{-(t-y)/R_2C}}{C} Q_i(y) dy = 0$$

$$\text{Equation 2.3}$$

In an attempt of obtaining patient -specific boundary conditions lumped models with more elements for both inlet and outlet have been introduced. These models include resistance, capacitance, inductance and pressure sources so that they are capable of using as inputs quantities related to the activity of the heart (atrial and ventricular pressures etc) and have been used as boundary conditions for both one [111] and three dimensional flow simulations [96, 112]. However when it comes to assigning specific values for the properties of each part of the flow circuit, the approximations and assumptions for the unknown model coefficients become inevitable.

Concluding, existing methods for obtaining boundary conditions for the coronary network include some assumptions and the accordance of the prescribed conditions with those actually prevailing on a real human coronary network is still under discussion; larger uncertainties exist for the flow outlets. In transient flow simulations of the cardiac cycle the time dependent behaviour of the vessels downstream the computational domain cannot be neglected. Use of complicated lumped models, while at first sight may seem to improve accuracy, introduces also additional uncertainties, as in all the reviewed studies there are assumptions and approximations regarding both the inlet and the outlets. Therefore, especially **in the current Thesis, a simple representation of the time-dependent pressure drop of the vessels**

network downstream of the exit boundaries has been adopted. The pressure drop was introduced via a time dependent resistance term. This method is based on generic data of the total pressure drop during the cardiac cycle and the geometrical characteristics of the coronary models and can provide consistent comparative results between the investigated cases.

The feasible anatomical hypothesis behind the used method is that for each outlet the downstream network is structured in a way that the average wall shear stress is 1-2Pa; this value is more or less the same for all branches of a healthy coronary artery. It is based on the elasticity of the vessel, assuming that large variations of the wall shear stress would lead to remodelling (change of shape) of the arteries. Additionally it is assumed that the possible existence of stenosis does not affect the structure of the downstream vessels. Validation of the anatomical hypothesis is almost impossible as it would require the knowledge of the shape of the entire coronary arterial and vessel network for a specific person (at least) before and after the emergence of the stenosis. However, provided that the anatomical hypothesis holds, the effect of the stenosis on the flowrate at the inlet and the outlets can be validated using a relatively simple experimental setup. Transparent geometrical models of arteries with and without stenosis will be mounted in a test rig. At the inlet a pressure pulse will be applied. The outlets of the geometries will be connected to a time varying resistance (e.g an elastic tube that goes through a compliance tube). The flow rate at the inlet and the outlets will be measured both for stenosed and non-stenosed geometries and they will be compared to the flow-rates calculated via simulations.

2.1.4 Indicative results

The results reported in published works on coronary flow simulations depend strongly on the scope of each study. Some works focus mainly on the dependence of the obtained CFD results on the relevant techniques used. Simulations on simplified one branch geometries that used a physiological and a simplified sinusoidal pressure pulse with the same time averaged flow at the inlet resulted in similar stream-wise distributions of WSS (Figure 2-8) on the walls of the model; this showed that the average WSS is mainly determined by the geometry rather than the exact inlet waveform [95, 101]. The application of different velocity profiles at the inlets has also been shown to have minor influence on the result and causing only small differences that are restricted near the inlet [101].

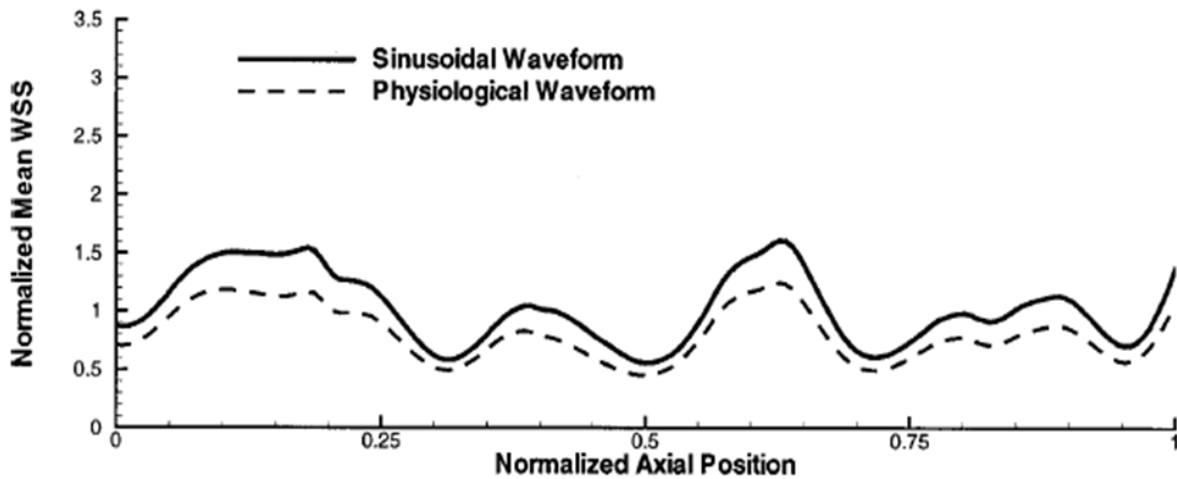


Figure 2-8: WSS distribution along a line in a single branch coronary model for two different types of inlet waveforms. The distribution is almost identical and there is an almost constant difference between them (Myers et al 2001 [101])

On the contrary, there is an approximate 20% difference between the values of WSS for steady flow simulations and the averaged WSS for transient simulations with the same time average flow rate. The same holds for pressure drop [89], a fact that indicates that **the relationship between the WSS and the mass flow rate is not linear and that the transient nature of flow has to be taken into account**. The application of both the Newtonian and non-Newtonian models (power law, generalized power law, Carreau, Casson, Wallburn-Schneck) did not produce significantly different WSS distributions and the influence of the non-Newtonian model was restricted in small specific areas [56, 83, 87]. The changes in the WSS distribution is also small when multiphase models were used [79] but a differentiation in the WSS gradient was observed [84]. Comparison of simulation results on the same geometry for moving and stationary walls, (with constant diameters) did not show significant variation in the results except for a small local differentiation at the area of the stenosis [87].

On the contrary -as expected- it has been shown that geometrical features of the model have major influence on the results. Recirculation zones appear downstream the stenotic lesions, both on the main branch and side branches even for moderate stenosis (50%)[87, 88] and downstream the LAD-LCX bifurcation in the branch with the bigger diameter [90]. Recirculation zones were also observed in simplified models of coronary arteries with the location of the

vortex depending on the location of the aneurysm [94], another indication of the strong influence of geometry modifications on the flow field. The curvature and the vessel tapering also influences the velocity profiles and WSS distribution [95, 101]. The factor that seems to have the strongest influence on the simulation results though is the existence and the position of side branches compared both to curvature and tapering, and this seems to hold for both steady and transient simulations[85, 86, 93]. Geometries with side branches have lower values of WSS, something that was expected as the same quantity of fluid is distributed in more branches, but also the distribution of WSS along the main branch is significantly different.

In most of the published studies, the reported values of time averaged WSS are in the range of 1.5-2 Pa, with the minimum value 0.25-0.4 Pa and local peak maximum values especially at the stenotic lesions that reach up to 20Pa [85, 86, 90, 92]. Low WSS is a subject of high interest, as reduced WSS at an area of the vessel wall is related to CAD progression and thrombotic complications. The reported minimum values of WSS in all reviewed studies lie within the range of 0.2-0.5Pa. **Despite the previously described important role of WSS in the evolution and complications of CAD there is not a generally accepted range for non-pathological WSS values in the literature in order to assess the CFD findings.** The local value of WSS, as it is estimated by CFD simulations, seems very sensitive to geometric changes. The existence of stenosis in the artery has also strong effects on WSS values (Figure 2-9). The existence of a stent, an obstacle with 100 μ m intrusion in the flow region, has a strong effect on WSS distribution. This finding is repeated for different geometries and flow rates [102]. In another computational work in a more complex geometry, the placement of the stent in the location of a stenosis, while restores pressure and flow-rate, it does not seem to revert the local WSS gradient to a non-pathological distribution [91].

At the branches without stenosis, the maximum calculated pressure drop between the inlet and the outlets of vessels with diameters up to 1mm is less than 2% of the average inlet (aortic) pressure; although the calculated value of absolute pressure value the outlets is depends strongly on the choice of boundary conditions, the pressure drop within the computational domain does not exceed 200Pa [90-92] and, as shown in Figure 2-4, in some cases it is negligible compared to the operating pressure of the system. However when a stenosis is involved the pressure downstream the stenotic lesion can be significantly reduced and in an unpredictable manner [55, 56, 91]. This pressure drop determines the flow rate in the stenosed branch, influences the flow rate at the inlet and therefore affects all the calculated quantities. So in cases with stenosis this pressure value cannot be estimated or measured in a non-invasive way and the same holds for the flow rate in the stenosed branches. This is the fact that makes

necessary the use of models for the behaviour of the network downstream the outlets of the computational domain.

Finally, there are several studies aiming to explore specific scenarios, evaluate the effect of specific factors or compare the impact of performed procedures. Coronary CFD simulations have been used to examine the effect of stent placement [91], the persistent stenosis after stenting [89], the effect of different types of stent [97] or the impact of the existence of stenosis at different location [88]. However, in most studies, the reported results seem to be detached or at least not directly connected to the main problem of CAD which is the possibility of complications. To the best of knowledge, only in three studies where there is an attempt to use CFD as a tool of assessment of the severity of the case with definition of appropriate indices and even these studies deal more with ischemia than the possibility of complications : (i)Chen et al [91] defined the computational flow stenosis index, a non-dimensional quantity calculated from the CFD results in order to express the reduction of the blood supply due to the presence of stenosis; (ii) Wellnhoffer et al [86] defined a set of non-dimensional indices based on a the geometrical features of coronary and shear stress distribution to be used for coronary

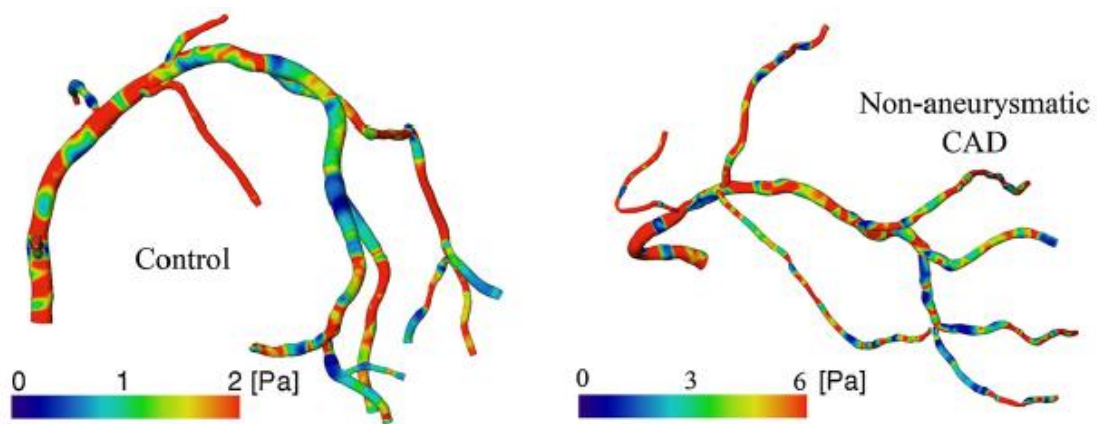


Figure 2-9: WSS distribution in different coronary models with bifurcations for a normal (left) and a stenosed (right) case [86]. The differences in geometry lead to much higher values of WSS for the vessel with CAD. Although the view angle is different it is clear that the values of WSS are approximately three times higher in the right image.

assessment [86] (iii) Finally Morris et al [56] developed and validated an integrated method for virtual calculation of the fractional flow reserve (FFR) based on CT coronary images, the first to our knowledge actual connection of CFD with medical diagnosis. It can be said that although the CFD studies provide a detailed description of the flow field and calculate the flow quantities that

are related to pathological situations in more detail than the medical examinations, **there is no use of CFD as a diagnostic tool**. The difficulty of the validation of the CFD under in-vivo conditions leads inevitably to mistrust towards these results in clinical practice. However **the author of this Thesis is motivated from the potential of developing future diagnostic tools that may include validated CFD tools**. Specific flow characteristics can be directly related to CAD deterioration and complications and also flow patterns that favour the formation of thrombus can be identified, as it is attempted in the current Thesis. Simulation of flow for a small number of cases with known outcome (stable CAD or ACS) and detailed processing of the results can lead to an arithmetic expression of these culprit flow patterns and produce quantitative criteria for the complication risk. These criteria can thereafter be tested and validated with application on a large number of patients.

2.2 Coagulation and thrombus formation

2.3 Thrombus formation- The process

The formation of blood clot is, in most occurrences, a physiological response of human body to vessel injury, necessary for the stop of bleeding. It is initiated when blood contacts certain substances like those exposed after the rupture of endothelium and also when pathological flow conditions prevail in a region [46]. At the same time, thrombus formation is involved in a number of life threatening situations like venous and venous thromboembolism, ischemic episodes at different sites of the vascular system and ACS (after rupture of atheromatous plaques in stenosed vessels [113]); it is often a result of the contact of blood with artificial materials and implants as mechanical heart valves. The occurrence of pathological clotting in the circulation is believed to be the result of the co-existence of three conditions, traditionally referred to as Virchow's triad. Virchow's triad was initially proposed in order to describe venous thrombosis, but it can be applied also in the cases of arterial thrombosis and coronary complications [114]. The first prerequisite for pathological clotting is the prevalence of abnormal flow condition in the area [115]. The second prerequisite is a pathological condition on the vessel wall, as in the presence of an injury or inflammation site certain substances (like TF and collagen) are exposed and make contact with the blood components initiating the coagulation process [116]. The presence of foreign materials from implants, as stents or artificial heart valves, can also possibly be considered as pathological condition on the vessel wall. The third prerequisite is the increased coagulability of blood, locally or globally. The exact chemical composition of blood of an individual favours or makes more difficult the clotting, as differentiation of the concentration or behaviour of several blood components has a decisive effect on the process [117]. The occurrence of thrombosis requires the synergy of all three conditions. However it has been shown that there is interaction among these factors, and that when one of these conditions exists can lead to the appearance of the others. Pathological flow conditions can influence the endothelium cell responses and create an abnormal condition on the vessel wall [118]; pathological values of shear stress can also stimulate platelets and lead to the initiation of coagulation [49]. However the use of Virchow's triad as an interpreting tool is still useful when approaching the problem of blood thrombus formation in vivo. As described in the following section, thrombus formation is a multi-scale phenomenon both with respect to time and space, involving a number of biochemical substances, blood circulating minerals and cellular responses.

Between the initiation and the formation of a thrombus, a series of enzymatic reactions takes

place; this is traditionally referred to as coagulation cascade [119]. Some of the substances taking part in these reactions are known in the literature as coagulation factors, and they are named with Roman numerals. As a big part of the reactions involved in the coagulation are enzymatic activations, most of the coagulation factors while inactive in their blood circulating state (except from FVIIa) take part in the process after obtaining their activated form. For example, fibrin is the result of the fibrinogen activation by thrombin. Fibrinogen is also known as factor I of coagulation and fibrin as activated factor I.

Coagulation cascade is classically divided in three parts: (1) the extrinsic or Tissue Factor (TF) pathway, (2) the intrinsic or contact pathway and (3) the common pathway. In the extrinsic pathway the process is initiated when factor VII of coagulation is bound on TF and activated, forming the complex TF:VIIa. In the intrinsic pathway the triggering is the activation of fXII after contact with specific substances. The two separate paths, identified on the basis of the different events that cause the initiation, have been studied and reproduced in in-vitro experiments [120, 121]. However, this distinction is not actually representative for the in-vivo process as the TF factor pathway activates part of the intrinsic pathway with the activation of factors XI and VIII by thrombin. Both pathways finally result to the activation of factor X, which is the first step of the common pathway. The final outcome of the process is the activation of fibrin and the formation of the fibrin mesh.

The main concept of the cascade description is that in every step of the coagulation process a circulating zymogen is activated and the activation reaction is being catalysed by the products of the reactions of previous steps. Coagulation is a dynamic process that includes a number of feedback loops which may have amplifying, inhibiting or regulative role. The inhibition processes are partially due to substances that already exist in plasma, like tissue factor pathway inhibitor (TFPI) and antithrombin III (ATIII) and partially due to substances that are activated during the process, for example activated protein C (APC) is possible after the activation of protein C by thrombin. Also there is a process that breaks up fibrin network aka as fibrinolysis. While for physiological haemostasis the TF pathway is considered more important [122] as patients with deficiencies of the intrinsic pathway do not suffer from bleeding disorders, it is possible that the intrinsic pathway has significant involvement in the thromboembolic complications [123], as in some cases the inhibition of fXII can protect from pathological thrombosis without bleeding complications [124].

The initiation of the coagulation cascade occurs mainly on the TF-bearing cells on the vessel wall [125, 126]. During the following steps of the process though, two of the involved substances, platelets and thrombin, have particularly important contribution. Thrombin

catalyses the final step of clotting converting fibrinogen to fibrin, activates factor XIII that forms bonds that crosslink the fibrin strands [127], causes the activation of platelets [128] and activates factors V, VIII, XI and the inhibitor protein C. Platelets (also thrombocytes) are blood circulating cell fragments that have the ability to adhere to the materials exposed after arterial damage [2] or plaque rupture such as collagen [129-131] and play a major role in thrombin formation [132, 133]. Platelets become activated when they contact thrombin and other chemical agonists or when they are subjected to mechanical stimulation [49, 134]. After activation, platelets are modified in order to support biochemical reactions on their membrane and release chemical substances and micro-particles [135] that in turn activate other platelets and promote blood clotting [126]. Finally after activation platelets obtain the ability to adhere to each other and form aggregates on surfaces or in flowing blood. Due to their important role, platelets and thrombin are the subject of most coagulation tests and the target of most anti-platelet drugs and require special attention in the process of modelling thrombus formation.

The scheme presented above has been used widely for the study and the interpretation of coagulation process in vivo. The cascade model has also inspired and guided a large number of laboratory experiments on coagulation. During these experiments the impact of different coagulation factor was studied, by adding all or some of the coagulation factors and plasma in a test tube and monitoring the change in the concentration of the different substances. A number of studies were performed in this manner have managed to identify the mechanism and to measure the reaction rate constants of each of the involved reactions [120, 136].

Table 2-1: Localization of some of the enzymatic activations of the coagulation process [126, 132]

Vessel wall surface	Plasma	Platelet surface
VII binding with TF VIIa binding with TF Xa activation of TF:VII TF:VIIa activation of X TF:VIIa activation of IX	Xa activation of VII IIa activation of VII IIa activation of V IIa activation of VIII Xa activation of II	Xa activation of V IIa activation of V Xa activation of VIII IIa activation of VIII VIIIa binding with IXa Va binding with Xa VIIIa:IXa activation of X Va:Xa activation of II

However, while the cascade model deals with all the processes as they were sequential bulk reactions, a large part of the enzymatic reactions involved in the coagulation process occur either exclusively or significantly faster when the enzymes are bound on cell membranes or on phospholipids [137, 138]. Additionally, a number of the activated factors (fXa, fIXa, fVIIa...) of the coagulation cascade can bind on TF-bearing cells or platelets even before the activation of platelets [132, 139] and avoid the action of the inhibitors in plasma. In more detail, the formation of the complex TF-VIIa with the activating ion Ca^{+2} (extrinsic tenase) that causes the activation of fIX and fX occurs on the surface of TF bearing cells and TF-rich sites of the vessel wall. At the same time the complex IXa-VIIIa (intrinsic tenase) which also causes activation of fX acts on the membrane of activated platelets, so this step is cross-linking the two classical paths of coagulation. Finally, while the circulating activated fXa causes activation of small amounts (pM) of thrombin, the complex Xa-Va (prothrombinase) which also acts on the activated platelets' membrane, causes a burst of thrombin generation as it has much higher activity than circulating fXa and also is less prompt to inhibition. Also the activation of protein C is faster on the cells of endothelium by the thrombomodulin-thrombin complex than in plasma [140]. The acknowledgement of the crucial role that cell membranes play on the coagulation process has led to a new perception of coagulation and the development of cell based models describing the process, without cancelling of course the importance of the previous works.

According to the cell based approaches and models for blood coagulation [125, 126], the process is divided in three discrete but overlapping phases, initiation, amplification and propagation (see Figure 2-10). The initiation phase takes mainly place on the endothelium or generally the vessel wall, after the exposure of tissue factor. TF binds fVIIa and causes the activation of fVII. The formed extrinsic tenase complex activates fIX and fX. As mentioned before, these activated enzymes can bind on TF bearing cells and avoid inhibition by TFPI or other inhibitors in plasma. So their action is initially limited near the surface of the vessel wall. During the amplification phase small amounts of thrombin are formed on the surface or near the surface of TF-bearing cells by circulating fXa. This amount is not enough to trigger directly the formation of clot, but it is capable of activating platelets and other co-factors. At the same time, platelets adhere and tether at the reaction site by binding on von Willebrand factor [141]. At the final stage of the amplification phase, activated platelets bearing activated coagulation factors enter the circulation. During the propagation phase, the complex of fIXa:fVIIIa is formed on the activated platelets' surface. This complex activates fX to fXa which forms complex with fV, fXa:fVa aka as prothrombinase. This complex converts prothrombin to thrombin in a rapid way

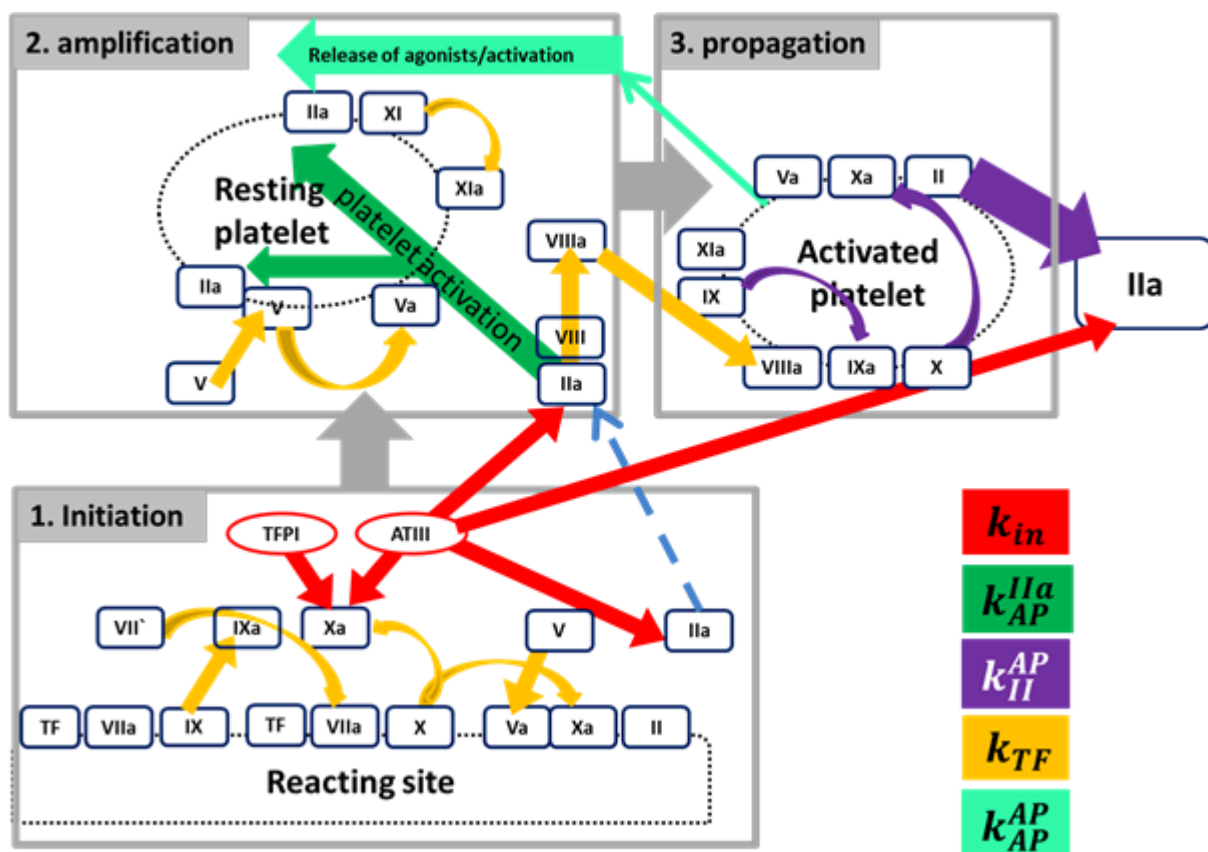


Figure 2-10: The cell based model for blood coagulation, image from K.P. Papadopoulos et al 2014 [142] inspired from the work of Smith 2009 [126]. The different steps of the process (initiation, amplification and propagation) occur at different sites. The arrows show how the processes are lumped in a smaller number of reactions in the developed phenomenological model (Chapter 3)

(>100,000 faster than the conversion in plasma [137]) that finally leads to activation of fibrin and formation of blood clots. The cell based models of coagulation can provide explanation for some specific clinical conditions like bleeding complications due to fXI, fIX, and fVIII deficiencies, where the cascade description fails. Additionally, the binding of activated co-factors of coagulation on cells explains two other parts of the coagulation process in vivo: (i) the small amounts of activated enzymes initially produced remain active for a time period disproportionally long compared to their half-life in plasma. This is because they escape the inhibition due to the protected environment that this binding provides for the enzymes. (ii) Localization of coagulation process as it is observed in in arterial flow conditions would not be possible without enzymes binding on the reacting site. Arterial wall shear rate values are high and flow would cause the abduction of the reacting substances, even if they were produced with

rates much faster than the ones that have been reported for the coagulation reactions. Therefore the role of cells and the localization of the reactions have to be taken into account for the modelling of the coagulation in-vivo.

2.4 Simulations of thrombus formation

This section is divided in three parts: the first one reviews only the coagulation reaction models, the second reviews models used for simulating platelet aggregation and finally the third one reviews integrated models that attempt to reproduce coagulation in the maximum possible detail.

2.4.1 Models for the coagulation process

The basic idea of a model for blood coagulation is a set of differential equations that represent the temporal evolution of each of the involved substances. These equations are derived from the biochemical reactions that describe the generation or consumption of each substance. Modelling of enzymatic reactions leads finally to an expression of a source/sink term (S_i) for all enzymes and chemical substances involved in the coagulation process. If a substance is produced or consumed through more than one reaction, the source/sink term is the sum of the quantity of this substance produced or consumed per unit time in each reaction. In the general case the reactions may also include binding and unbinding between substances or between substances and cells. For example in Equation 2.4a (hypothetical) source term for plasma circulating thrombin for a model that simulates thrombin generation as a bulk reaction is presented as:

$$\begin{aligned}
 S_{IIa} = & -k_2^{on}[IIa]([p] - [IIa^b] - [II^b]) && \text{binding of thrombin molecules on the available} \\
 & && \text{binding sites (p) of platelet membrane} \\
 & +k_2^{off}[IIa^b] && \text{unbinding of thrombin molecules from the surface} \\
 & && \text{of platelets} \\
 & -k_2^{in}[IIa][ATIII] && \text{inhibition of thrombin by anti-thrombin III} \\
 & +k_2^{prod1}[II][Xa:Va] && \text{activation of thrombin by the complex Xa:Va} \\
 & +k_2^{prod2}[II][Xa] && \text{activation of thrombin by fXa in plasma}
 \end{aligned}$$

Equation 2.4

In the case a model includes the spatial evolution of coagulation reactions the source terms

would take different forms for the different domains of the computational area. The previous term at a site of the computational domain without platelets would be reduced to the simpler form of Equation 2.5:

$$S_{IIa} = -k_2^{in}[IIa][ATIII] + k_2^{prod2}[II][Xa]$$

Equation 2.5

The reaction speed can be modelled as first order or second order reaction or with the use of the Michaelis-Menten approach [143] as shown in Table 2-2. Note that most of the reactions are enzymatic activations of the form described in Equation 2.6:



Equation 2.6

The enzyme E (activator) binds onto the substrate B in order to produce A (activated form of enzyme B). The Michaelis-Menten expression actually includes under some assumptions the binding and unbinding of the enzyme and the substrate into the empirically derived constant k_m . The choice of the appropriate way of modelling each reaction of the system depends on the specific purpose the system is developed for, and the available computational resources.

Table 2-2: Different ways for simplified modelling of enzymatic biochemical reactions. The specific way used in every case depends on the type of the reaction, the desired accuracy and the available data.

Reaction kinetics	Process	Conversion rate
First order	$B \rightarrow A$	$v = k[B]$
Second order	$B + C \rightarrow A$	$v = k[B][C]$
Michaelis-Menten	$B + E \leftrightarrow BE \rightarrow E + A$	$v = k[E][B]/(k_m + [B])$

The purpose of a coagulation model is to reproduce the concentration of the different substances versus time in accordance with experimental measurements. As the usual target is

to predict the evolution of thrombin (and sometimes also fibrin) concentration, a general problem is that the mathematical models of coagulation have disproportional ratio of input and output parameters. While the mathematical model includes a large number of substances and respective reactions, only a small part of the calculated data is reported in the results and used for evaluation of the model, usually the temporal evolution of the concentration of thrombin, fibrin and sometimes factor Xa [144, 145]. Therefore if a mathematical model for coagulation aims to reproduce the production of thrombin while including a detailed description of the involved reactions it is very possible that it gives correct final outputs for a number of different simulation setups.

An ideal model for thrombus formation in flowing blood should incorporate a large number of parameters. The starting point is the system of biochemical reactions for both intrinsic and extrinsic path of blood coagulation up to the formation and lysis of fibrin, including the amplifying and inhibiting feedback loops that were mentioned earlier. If the model is to be used under flow conditions, or just in simulations where the substances that participate in the process are not homogeneously distributed in space the model should additionally include the localization of reaction on different sites (endothelium cells, platelets or plasma), the formation of enzyme complexes and the binding and unbinding of certain zymogenes and enzymes on the cell membranes. In the case the model intends to describe the formation of thrombus in flowing blood, it should also include the motion of the blood circulating cells RBC and WBC as these cells can also be trapped in the fibrin mesh [146]. In reality though, we have not found any of the published models that include all these factors in full detail.

The actual evolution of the existing models was from very simple zero dimensional to complex three dimensional ones and it was boosted by two factors. First, since the initial mathematical models for thrombin and fibrin generation were introduced around 1990, our understanding of the coagulation processes has improved dramatically. There have also been published a number of experimental works on coagulation that provided detailed quantitative information on the involved reactions. All this new information was gradually incorporated in the proposed models. Second, the increase of the computational power and the emergence of new computational techniques have made possible the conduction of much more demanding computational studies that include more parts of or the whole process and in greater detail. More or less, the trend in mathematical models of coagulation and thrombus formation is to move towards higher complexity and computational cost.

The first mathematical simulation of thrombin and fibrin generation in plasma consisted of 14 reactions describing the activation and inhibition of four coagulation factors (fI, fII, fV and fX)

and the action of two inhibitors (AT-III and APC); exponential time functions have been used as fixed inputs for the concentration of fX [147]. The model actually reproduced the common pathway and the threshold for the explosive increase in thrombin generation was a critical value of fXa while most of the reactions were modelled using the Michaelis-Menten approach.

The next model was based on an in-vitro study of TF-induced thrombin generation [120]. The reaction rate constants measured in this study were used for the development of a system of 20 reactions describing the activation and inhibition of six coagulation factors, fII, fV, fVII, fVIII, fIX and fX. The reactions were modelled as second order, accounting separately for the formation and breakage of complexes, while there were no inhibition reaction and the activation of the factors was restricted by a 'maximum velocity of production'. That study mainly focused on the effect of variation of the concentration of different factors [148].

A similar model was proposed for the intrinsic pathway including fibrin production (in total factors fI, fII, fV, fVIII, fIX, fX and fXI) and AT-III and APC inhibition mechanism, and was used to investigate threshold values for some enzymes and the spatial propagation of coagulation from the reacting site due to diffusion [121, 145]. Subsequent work on extrinsic path included more chemical substances and biochemical processes [144] up to thrombin production, resulting in an improved version of the model of Jones et al [148]. The system consisted of 27 reactions and 42 reaction rate constants, included all factors involved in the TF-pathway (fII, fV, fVII, fVIII, fIX and fX) inhibiting action by TFPI and AT-III and the concentration of TF as triggering substance. The model was mainly used to investigate the effect of different concentrations for the involved substances.

This model was also combined with a Monte Carlo simulation method, in order to detect changes to the coagulation initiation behaviour, due to small variation of the concentration of enzymes induced by the stochastic approach [149]. In a similar model but more detailed with respect to the number of substances (22 fluid phase, 19 lipid bound and 6 complexes) and reactions Bungay et al [150] included for the first time the effect of lipids (phospholipids) on thrombin generation. The presence of lipids in the model actually reduced the rate of the inhibition reactions (by TFPI and AT-III) while the increase of some activation reactions due to the presence of lipids was not considered. This model also included the action of APC as an inhibiting loop due to thrombin production

At the same time some studies used simulations to investigate a specific part of the coagulation process, as the function of positive feedback loops and threshold concentrations for the initiation of the process [151], the triggering threshold with respect to Tissue Factor Pathway

Inhibitor (TFPI) concentration [152] or the inhibition mechanism of APC [153]. Closing this brief reviews of the coagulation models we must emphasize on three things: (1) Generally, the described models are sensitive to the concentration of the inputs and while they produce reasonable results for near-to-physiological concentrations when used for unusually high or low input (mainly high) concentrations can give controversial results as oscillating solutions [153]. (2) At the same time, the mismatch between the number of inputs and outputs makes possible the reproduction of the coagulation by a much simpler system of six reactions [154] and indeed in different ways, as much of the information included in the inputs is not reflected in the outputs -or rather there is overlapping in this reflection so small changes in one reaction can be compensated by small changes in others. (3) Last but not least, **these models describe thrombin generation in a closed and actually non-dimensional system**. The result is a number of curves describing the temporal evolution of the involved factors, assuming that the whole process occurs in a closed homogenous system. The used reaction rate constants and the experimental validation of the results are also based in closed reaction systems. In such a system, a factor that plays crucial role is the depletion of the initial reactants (fII for example). The reduction of the initial substances will control the curve of thrombin generation. On the **contrary, when studying thrombin generation in flowing blood, there is a constant supply of the initial reactants due to convection**, and there is also rapid removal of the produced substances due to flow motion.

2.4.2 Models for platelet aggregation and deposition

The major role of platelets in blood clotting is well established and thus, there is also a number of computational studies that focuses on platelet behaviour and responses (adhesion, aggregation and activation). These studies usually ignore or oversimplify the biochemical reactions of coagulation and deal with the behaviour of platelets in a mechanistic manner.

Some of these studies examine only the formation of platelet aggregates in flow, using collision efficiency, disaggregation models and population balance equations [155-157] while others include the changes to the tendency of platelets to form aggregates due to the presence of biochemical stimulators [158]. From the last study, which were the first attempt to model platelet deposition on a surface an important conclusion was drawn regarding platelet disaggregation. It was demonstrated that the disaggregation process could be relatively easily modelled with success. At the same time it was shown that under flow conditions, disaggregation has an important role and cannot be neglected.

Similar mechanistic studies –in the sense that the process is attributed to convection and

diffusion of platelets- have been published also for platelet deposition on surfaces in the case of stagnation flow [159] and stenotic vessels [160]; the effect of shear rate on the rate of the deposition of platelets was modelled as an increase to diffusivity due to shear rate. The enhanced platelet deposition on an adhesive surface due to increased shear rate can also be attributed to the presence of RBCs and was initially suggested by Brash et al [161]. This specific effect has also been reproduced in a simulation of primary haemostasis for arterial values of shear rate (1000 s^{-1}), where Stokesian dynamics were used to describe platelet-platelet and platelet-wall interactions under flow [162].

The same approach for the influence of shear on deposition rate was used in a different model that was applied on predefined parabolic flow profiles, in order to examine platelet deposition on stenotic surfaces [163, 164]. This model used a constant reaction rate, took into account platelet chemical activation by agonists and considered the effect of thrombin generation, inhibition and heparin related reactions. The model was applied to simulate deposition assuming Poiseuille flow over collagen coated surface. In this model, a function for chemical activation of platelets was proposed, based on a threshold concentration for the agonists. This approach for chemical activation was used later in several models. Another interesting finding in this work was that the differentiation of the deposition rate between resting and activated platelets did not change significantly the results, probably due to the small number of activated platelets in flowing blood.

David et al [165] in a study aiming to assess downstream activation and adhesion due to transport and diffusion of activators generated by adherent platelets have confirmed that the performance of platelet deposition models depends on flow conditions. Longest et al [166] applied different models for platelet deposition in pulsating flow conditions with streamlines deviating from the parabolic profile. Compared to experimental data, the better results were achieved with a deposition model including the residence time of platelets near the reacting surface. The inclusion of residence time in the platelet deposition time is actually the same as taking into account (but not explicitly modelling) the biochemical

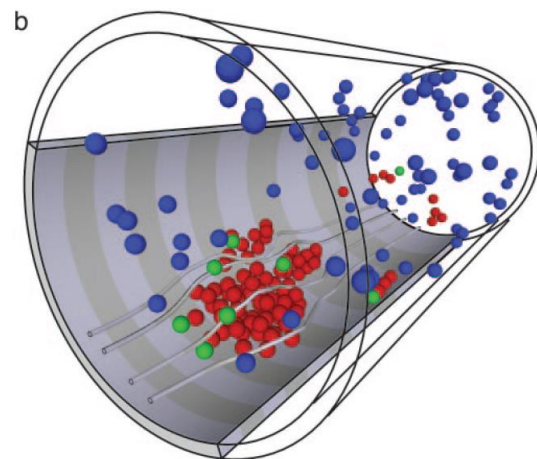


Figure 2-11: Lagrangian simulation of platelet aggregation in a tube of $50\mu\text{m}$ diameter and $500\mu\text{m}$ length (Pivkin et al 2006)

reactions that lead to the binding of platelets on reacting surfaces and other platelets. The shear dependent diffusivity gave satisfactory results in these studies. It is important to keep in mind though, that shear dependent diffusivity has a direct impact on the aggregation rate. However, the experimentally observed dependence of the platelet aggregation rate on shear rate values could be attributed to a number of mechanisms: Shear rate influences the diffusivity of both platelets and activating factors; it causes increased platelet concentration values near the wall, especially in the presence of RBCs, and this increase depends on the volume fraction of RBCs; it regulates the supply of new platelets over the reacting site of the vessel wall; in a bio-chemical level, it changes the prevailing mechanism of platelet adhesion [167]. Therefore the shear dependent diffusivity or aggregation rate used in modelling may be lumping a number of different physical processes.

Pivkin et al [168] performed 3D simulation of platelet aggregation inside a tube (Figure 2-11). The computational model included also the effect of the growth of thrombus on the flow field. In this study the platelets were allowed to be in one of three states: resting activated and triggered. It turned out that the transition time from triggering to activation was important for the growth of the aggregate, or in other words, that the fraction of activated platelets and their residence time near the reacting site was important for the growth rate. The same research group in a later study also reproduced again (numerically) the combined influence shear and the presence of RBCs on platelet distribution and deposition [169].

In almost all models described above the effect of shear rate on platelet binding was taken into account either using the enhanced diffusivity or by straightforward modelling of the collisions between platelets and RBCs. It has been shown though that, even when compared to in-vitro experiments, the success of the model depends on the flow conditions. **It seems that there is no unique and generally accepted way to model the effect of shear on platelet aggregation that works equally well for any possible flow conditions** Additionally, **the way the platelet state (i.e. if they are activated or not) should be included in the modelling of these interactions is not clarified yet** and it also seems **that the simple distinction of platelets into resting and activated may be oversimplified**. It is also still unclear how the demonstrated alteration of the behaviour of platelets due to shear is to be included. Therefore, **a phenomenological model for thrombus formation that adopts a simplified way for modelling platelet aggregation on vessel wall and other platelets may overcome the lack of models required for simulating in detail the complex biochemical mechanisms.**

2.4.3 Integrated models of thrombus formation

When thrombus formation is modelled under flowing blood conditions, the source terms S_i that come from the assumed biochemical reactions must be coupled with the equations describing the effect of blood flow on the concentration of blood transferred substances; the same also holds for the source terms referring to platelets. The equation that is usually used to describe the combined effects of production (or consumption) and flow on the spatial and temporal evolution of the concentration C_i of a substance i in a flow field is the convection diffusion equation with source term (Equation 2.7):

$$\frac{\partial C_i}{\partial t} + \nabla(C_i \cdot \vec{u}) = D\nabla^2 C_i + S_i$$

Equation 2.7

In a more realistic approach, the growth of thrombus at a site of the vessel will affect the flow field, as the formed thrombus will restrict the flow. In the case that this effect is also considered, the equations that describe the formation of thrombus are coupled with flow (as the concentration of the substances will alter the local properties of blood); otherwise the equations for the evolution of concentrations are solved independently from the already developed flow field.

Despite that the integrated models of thrombus formation are rather demanding in respect of computational power, the first studies of this kind were performed more than 25 years ago, with the production rates of substances mainly modelled as fluxes or with the use of few reactions [170, 171]. The model of Sorensen could also fit into this category [163, 164] although it mainly focused on platelet aggregation. There are also some more recent attempts to approach the effect of flow on thrombus formation in a phenomenological way, using a set of (only) three equations describing fibrin production and showing different patterns of fibrin formation for different flow conditions [172].

The increase of computational power has allowed more complicated multi-scale and multi-phase models to be developed. These models include an integrated coagulation sub-model, a set of chemical reactions similar to the one proposed by Hockin et al [144] and additionally may incorporate the movement of the cells, the localization of equations and the change of blood properties due to blood clotting. Kuharsky and Fogelson [173] proposed an integrated model of thrombus formation under flow conditions, taking into account the localization of reactions on surfaces. The localization of reactions on endothelium and platelets was achieved with the inclusion in the model of binding sites on cell membranes for enzymes and zymogens. The

alterations in blood flow due to the presence of aggregated platelets [178]. The macro-scale model was tested in simulations with pulsating flow in an idealized two dimensional vessel bifurcation [179]. The continuous model, with coupling of flow with thrombus growth and including flow and transport within the thrombus, was used to demonstrate the effects of flow conditions and the quantity of TF exposed in thrombus growth [180]. As these models actually calculate the position of individual platelets, produce very realistic images of thrombus formation (Figure 2-12).

Another multi-scale model was proposed by Xu et al [181], that included a cellular pot model [182] for discrete cells; cell movement was simulated through an energy-based stochastic process. The simulation involved differentiation of cell movements depending on fibrin levels and cell-cell or cell-surface interaction and bonds. The model was used to evaluate the role of fVII in venous thrombus formation due to vessel injury [183] and to examine the impact of pulsating flow and the non-Newtonian characteristics of blood on thrombus growth [184].

Anand et al [98, 185] presented another multi-process model that used a viscoelastic model to simulate flow for both free vessel lumen and clot. This model also incorporated the activation of platelets due to excessive shear stress and fibrin production and lysis. In a similar work, a model for the viscosity of blood depending on fibrin concentration was proposed and used in a three-dimensional simulation of blood coagulation in a tube with a reacting site; in this study the area where fibrin concentration exceeded a specific value interpreted as the area occupied by the clot [99]. This model was applied in three dimensional geometries, on the contrary with most models of this category where the applications were restricted in small two dimensional domains (Figure 2-12).

While **the detailed description of coagulation included in these works makes them appropriate for studying the influence of different factors, at the same time it increases dramatically the computational cost**; thus published applications mainly refer to small two dimensional regions ($\sim 100\mu\text{m}$) while the dimensions of computational regions for studying thrombus formation in a coronary artery or in mechanical heart valves are much larger (typically, the diameter of the coronary artery at the inlet is about 4mm while the diameter of the aortic root is of some cm) with the flow distribution being three-dimensional and strongly time dependent preventing use of simplified flow models.. Finally **the models reviewed here do not have and probably cannot obtain patient-specific characteristics**, as the use of reaction rate constants derived from experiments do not allow the significant variability of thrombin generation observed for different individuals [186]. Also it is difficult in practice to have detailed blood analysis for each individual in order to perform patient specific simulations.

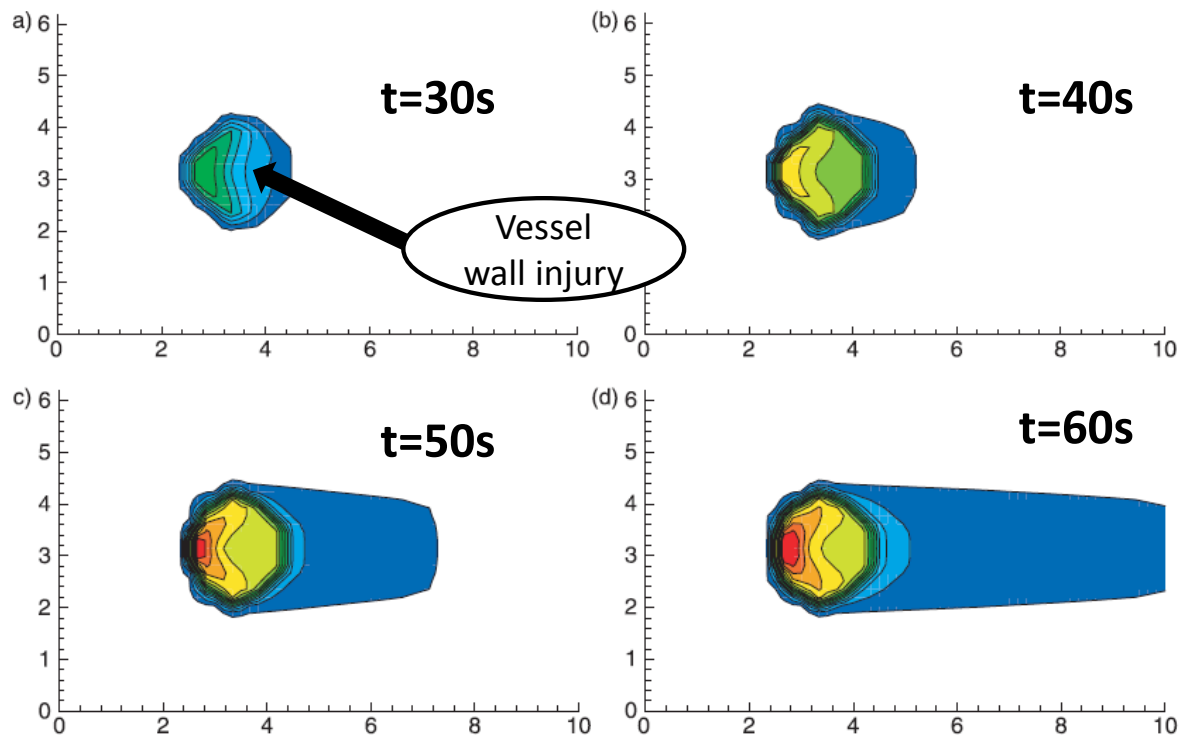


Figure 2-13: Three dimensional simulation of fibrin concentration on vessel wall. Simulation of coagulation in rigid wall tube ($D=6.2\text{mm}$, $L=31\text{mm}$) using a fully developed velocity profile (Bondar and Sequeira 2007)

As the process between the initial stimulation and the formation of thrombin consist the main part of the coagulation reactions, our motivation is to develop a phenomenological model for thrombin formation that would be 'light' enough to be used with three dimensional Computational Fluid Dynamic (CFD) simulations while also being adjustable in order to reflect measured differences existing in data of different individuals. As the intention here is to combine the model with CFD simulations, it should also account for a rough localization of the different processes. A case-specific simplified model like this, though not including the full biochemical details of the process, could be used for comparison of different cases of clinical interest. The thrombin sub-model will be combined with a simple sub-model for platelet aggregation on the vessel wall and can be evolved in a useful comparative tool for thrombus formation in different cases.

Chapter 3 The simplified thrombus model

3.1 Introduction

As mentioned earlier, blood coagulation is a process that involves a great number of substances and biochemical reactions, with some parts still being under investigation. In this chapter the development of a simplified-phenomenological model of coagulation is described. The model is light enough to be coupled with transient flow simulations in relatively large computational domains utilised in CFD. The development of the model can be separated into three distinct steps. The first step is a simplified sub-model for platelet aggregation on the reacting site. The initial calibration of the platelet sub-model is based on the experimental data reported from Badimon et al [2], and does not distinguish between activated and resting platelets. The second step is the development of a system of equations describing thrombin generation [142]. The validation of these equations is based on the thrombin generation assay results, an in-vitro test measuring the generation of thrombin in samples, under well determined conditions. The third part is the validation of the combination of the two sub-models under flow conditions. The initial thrombin model consisted by equations representing bulk reactions even for the processes that under flow conditions occur only on a part of the vessel wall. In order to convert these bulk reaction rate constants to surface reaction constants (actually surface flux terms similar to the ones used in Sorensen et al [163]) we used the threshold values for the initiation of coagulation under flow reported in Shen et al [3], modifying the surface reaction rate constants until the computational results agree with the experimental ones, i.e. until the threshold values for the flow and geometrical parameters of the problem in the simulations coincided with the ones reported in the experiments. As some of the experimental results used refer to the TGA and some others to the 'perfusion or flow chamber', this chapter provides also some information on these processes and then moves to the detailed description of the three steps and finally provides some details on the programming technics used.

3.2 Perfusion chamber

Perfusion or flow chamber is a device mainly used for the in vitro study of biological phenomena that require flow of blood, plasma or other liquids over a biological substrate. It is generally accepted that the effect of shear stress on cells is not limited to

the obvious mechanical consequences [35] (cell membrane deformation etc) but can also trigger biochemical responses like the expression of certain glycoproteins on cell surfaces and even alter gene expression [187]. Specialized types of perfusion chambers have long been designed to investigate the subjects under discussion in this study [188]. The device is able to produce controlled values of wall shear stress values within a range and create the appropriate flow conditions in order for the cell response to be studied. There are two main types: the parallel plate chamber and the tube chamber. In all types, the relationship between the applied mass (or volumetric) flow at the inlet of the chamber and the resulting shear rate or shear stress is obtained under the assumption of Poiseuille flow. The flow field is assumed to have a parabolic velocity profile similar to the one depicted in Figure 1-6. For the parallel plate chamber, the dynamic viscosity of the fluid μ , the volumetric flow rate Q at the inlet of the chamber along with the geometric characteristics (height h and width w) determine the value of wall shear stress and wall shear rate (Equation 3.1):

$$\tau = 6 \cdot \frac{Q \cdot \mu}{w \cdot h^2}$$

Equation 3.1

In the case of cylindrical flow chamber with internal radius R , the wall shear stress and wall shear rate are given by Equation 3.2

$$\tau = \frac{4\mu Q}{\pi R^3} \text{ or } \gamma = \frac{4Q}{\pi R^3}$$

Equation 3.2

In all flow simulations performed in this chapter, when shear rate or shear stress is reported, the corresponding mass flow at the inlet of the chamber was calculated using the formulas above, and the resulting shear rate in the calculated flow field was compared to the reported one. In the cases of the platelet sub-model where a difference greater than 2% was observed, the boundary layer of the computational grid was refined in order to get more accurate results (less than 2% difference).

3.3 Exploiting the results of thrombin generation assay

Because of the large number of enzymes involved in the process, the detailed modelling of the coagulation process (using values for the concentration of all involved substances and all the biochemical reactions) as exhaustively explained in the introduction is computationally extremely expensive. It also includes the risk of highly unstable models when applied to relatively large geometries. Additionally, the scope of this study is that the coagulation model should address patient specific data without demanding a great series of laboratory results regarding the possibly different species concentrations and reaction rates for each individual that lead to different rate of thrombin production (Figure 3-1).

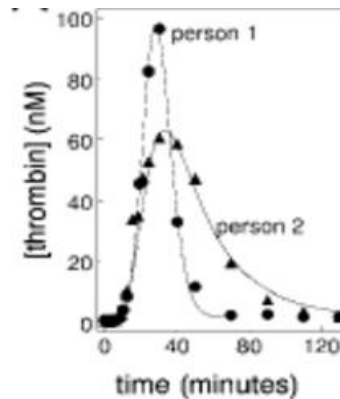


Figure 3-1: Variation of the temporal evolution of thrombin generation for different individuals [132]

Instead, for a patient specific approach, it is preferable for the model calibration to be based on data obtained via clinical procedures that assess the differentiation of the coagulation process for each patient. For those reasons, the thrombin generation sub-model calibration was based on the results of thrombin generation assays (TGA). The typical outcome of a TGA test is a curve of thrombin concentration versus time that is supposed to be indicative of the temporal evolution of thrombin generation in vivo. The results of such a test vary depending on the laboratory and the method used, but efforts are made for a standardization of both methods and results. In

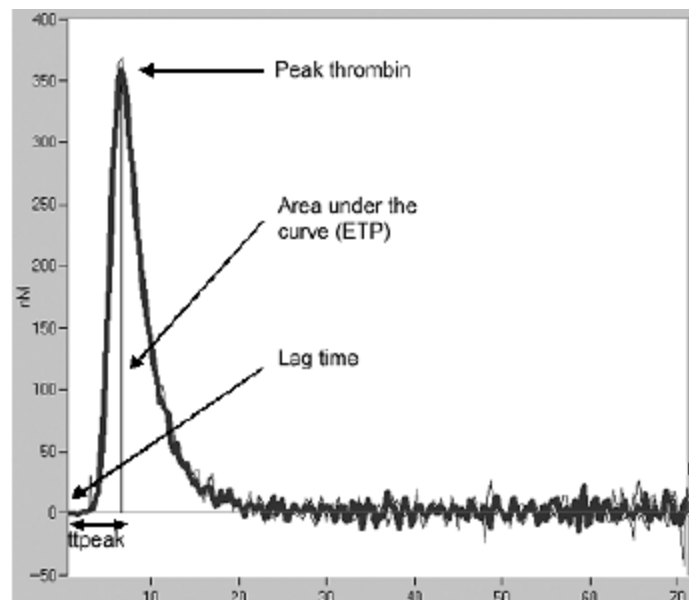


Figure 3-2: Typical thrombogram curve and the main parameters of the test (image from J.J. van Veen et al [189])

general, the test provides five main parameters [189, 190] as shown in Figure 3-2

- 1 The lag time (T_{lag}), i.e. the time until thrombin generation reaches the amplification phase, usually expressed in minutes.
- 2 The time when thrombin concentration reaches its maximum value (T_{max} or $ttPeak$), usually expressed in minutes.
- 3 The maximum concentration of thrombin (C_{max} or Peak), usually given in nM.
- 4 The endogenous thrombin potential (ETP) represented by the area under the curve of thrombin concentration over time, usually given in $nM \cdot min$.
- 5 The thrombin production rate is also considered an important parameter. However it is not an independent parameter as it can be calculated from the lag time, the peak and the time to peak ($C_{max}/(T_{max} - T_{lag})$).

As it has been shown in previous studies, lag-time depends strongly on the concentration of the stimulator used for the initiation of coagulation (in most cases recombinant TF), while for concentrations above a certain value lag time is totally eliminated and the production of thrombin starts immediately. The concentration of the triggering substance affects also T_{max} and C_{max} , while the concentration of platelets affects all the parameters of the test [120, 191, 192]. Typical values of the parameters of a TGA test [191] using fresh PRP are shown in Table 3-1 **Error! Reference source not found.**

Table 3-1: Typical values for the 5 main parameters of TGA test

parameter	Typical value
Tlag	$3.6 \pm 0.8min$
Tmax	$7.4 \pm 1.8min$
Cmax	$164 \pm 50nM$
ETP	$1321 \pm 100nM \cdot min$
Production rate	60nM/min

As it will be shown in the next paragraphs, the thrombin generation sub-model was structured in such a way that its parameters can be modified appropriately using a method based on the four parameters of TGAs. The final result of this modification process is that the results of the model reproduce a wide range of curves of different TGAs while at the same time the reactions and substances used in the (phenomenological) model retain the connection with the physical properties of the process.

3.4 Structure of thrombin generation sub-model

The aims when developing the thrombin generation sub-model was to propose a set of equations that describe the thrombin generation in blood using the minimum possible

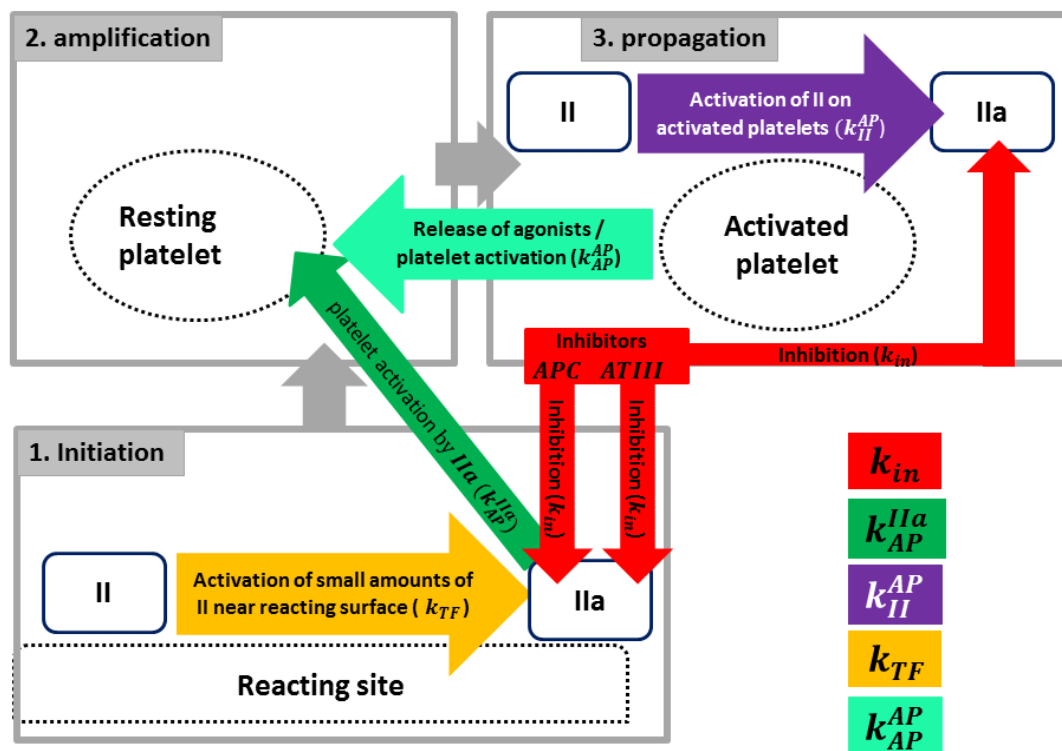


Figure 3-3: Schematic of the reduced version of the cell based model of coagulation I shown in Figure 2-10 that was used for the development of the thrombin sub-model.

number of parameters but which are able to describe with acceptable accuracy the whole process. The proposed model for thrombin production is based on the cell-based models of coagulation [126]; the full description of the biochemical processes are mainly

based on [125]. For a detailed modelling of coagulation, the localization of the different reactions makes the task more complicated, as it requires taking into account additional parameters such as the binding rate of the substances on cell membranes and the expression, concentration and availability of appropriate binding sites on the cell surfaces.

For the development of a simplified model however, the fact that the different stages of the coagulation occur in different sites can function as an advantage, as the processes can be grouped in respect to the location they occur (on platelet surface, on the vessel wall or in plasma). This approach is rigorous in cases where the transport of reactants is mainly due to convection (such as arterial flow conditions), or in cases where the different species are well mixed.

Table 3-2: The source terms for each substance of the thrombin sub-model, for zero dimensional simulations.

Substance	Source term
Thrombin [IIa]	$\frac{\partial[IIa]}{\partial t} = -(k_{in,0} + k_{in,add})[IIa] + (k_{surf} + k_{II}^{AP} \cdot [AP]) \cdot [II]$
Prothrombin [II]	$\frac{\partial[II]}{\partial t} = -(k_{surf} + k_{II}^{AP} \cdot [AP]) \cdot [II]$
Activated Platelets [AP]	$\frac{\partial[AP]}{\partial t} = k_{AP}^{AP} \cdot [AP] \cdot [RP] + k_{AP}^{IIa} \cdot [RP]$
Resting Platelets [RP]	$\frac{\partial[RP]}{\partial t} = -k_{AP}^{AP} \cdot [AP] \cdot [RP] - k_{AP}^{IIa} \cdot [RP]$

As the proposed model used a reduced number of four species (thrombin, prothrombin, resting and activated platelets) and four reactions (see table), each reaction rate represents the integral effect of more than one actual process. Also, ‘activated platelets’ actually represent platelet activity, in the sense that 100% activated platelets implies

Table 3-3: The values of the model's constants and parameters that were used as a starting point for the calibration and the fine tuning of the model.

Process	Constant symbol	Initial value (S.I.)	Reference
Thrombin generation by activated platelets	k_{II}^{AP}	$0.0856 - 1.81s^{-1}$	[133, 163]
Thrombin generation on reacting surface	$k_{TF,surf}$	$10^{-5}s^{-1}$	n/a
Platelet activation by thrombin	k_{AP}^{IIa}	$0, if [IIa] < [IIa]_{thr}$ $0.5, if [IIa] \geq [IIa]_{thr}$	[173]
Platelet activation by activated platelets	k_{AP}^{AP}	$5.24 \cdot 10^{-2}s^{-1}$	[173]
Thrombin inhibition*	k_{in}	$1.71 \cdot 10^{-2} - 0.2s^{-1}$	[144, 180]
Thrombin concentration threshold for platelet activation	$[IIa]_{thr}$	$1.75 - 4.18 \cdot 10^{-8}kg/kg$ (0.5-1.2nM or 0.05-0.12U/ml)	[133]

maximum platelet activity rather than the fact that all platelets are activated. Figure 2-10 illustrates the actual biochemical reactions that influence each constant of the model, while Figure 3-3 shows the reduced model. The model is structured as follows: During the initiation phase thrombin generation is described by a slow first order reaction. This reaction, which is localized on the TF-bearing cells (when modifying the model for applying to 3D simulations), is used to describe the whole pro-coagulant activity that

occurs on the TF-bearing cells – formation of the TF-VIIa complex, activation of factors IX, X and V. In this reaction the inhibition of the amounts of IXa, Xa that leave the cell surfaces by TFPI in plasma are also included. The initial value for the reaction rate constant was estimated using the lag times reported in [120, 192]. Inhibition of thrombin during this phase is also modelled as a first-order reaction, with the value of the reaction rate constant for thrombin inhibition calculated from the Ila · ATIII inhibition reaction, using the initial bulk concentration of ATIII ($k_{in,0} = k_{in,ATIII} \cdot \varphi_{ATIII,0} = 1.71 \cdot 10^{-2} s^{-1}$); this reaction is the major process of thrombin inhibition. Thrombin inactivation is 77% by anti-thrombin, 14% a₂ macroglobulin and 9% by minor inhibitors [193].

With this setup for the initiation phase, the model describes the threshold behaviour of the initiation of blood coagulation in respect to TF concentration [3, 194], as there is a minimum value of activation constant capable of causing thrombin burst and, as this constant is related to the TF concentration, a threshold value for TF concentration. The threshold values used are within the range of thrombin concentration values that have been reported in Rosing et al [133] as being capable of causing platelet activation: 0.5 to 1.2nM of thrombin (0.05 to 0.12U/ml). The equations (source terms) of the thrombin sub-model are shown in Table 3-2. The initial values for the reaction rate constants, shown in **Error! Reference source not found.** are taken either from already existing models or from experimental studies.

Beyond the point that thrombin concentration has reached the threshold value, the conversion of prothrombin to thrombin is mainly attributed to platelets after their activation. This process is modelled as a second-order reaction, with the initial values for the reaction rate constant used from [133, 163]. Platelets can be activated either by thrombin, if its concentration is greater than the threshold value, or directly by other activated platelets. Thrombin in concentration about 1nM can initiate the activation of platelets [195], from 0.5nM for minimum activity to 1.2nM for maximal [133]. Platelet activation by thrombin is modelled as a first-order reaction that is initiated when thrombin concentration reaches the threshold value. The activation of platelets by activated platelets represents the activation by platelet-released substances and it is modelled as a second order reaction. The reaction rate constants for the activation of platelets used were found in [173]. In the case of TF induced coagulation, the contribution of the later reaction is negligible, but it can make the model capable of being used to describe shear induced coagulation.

Inhibition of thrombin during the propagation phase is again modelled as a first-order reaction. The reaction rate constant for the inhibition of thrombin in plasma is not the same as for the initiation phase; here it must be noted that this constant is significantly smaller than the one used by Leiderman et al [180] for modelling this reaction in the same manner, which was based on thrombin half-life in plasma. However, as the activation of protein C that acts as an inhibitor to the coagulation process mainly occurs on the endothelium cells, for the areas near the endothelium cells the value used for thrombin inhibition is larger. The exact value of the inhibition constants for the computational cells that are near the wall is derived from the adjustment of the model with the use of TGA results.

3.5 Calibration based on TGA parameters

By adjusting the values of the constants and parameters within 'physiological' limits, based on the four main parameters of a thrombin generation assay (Tlag, Cmax, Tmax and ETP), the model can reproduce, to a good level of accuracy, actual thrombin production as it is depicted by the TGA for different patients. The initial attempts of adjustments were performed manually (on a Microsoft Excel sheet), but in general the adjustment can be done using the following procedure and assumptions.

Platelet response is very fast compared to the other processes included in the model [196]. With the approximation that all platelets are activated as soon as thrombin concentration reaches the threshold value an approximate solution can be found for the system of differential equations, giving the equation that describes thrombin concentration through time. To get this approximate solution, we make the assumption that all platelets are instantly activated when thrombin reaches its threshold value. Under this assumption, concentration of activated platelets is zero when thrombin concentration is below the threshold value. When thrombin exceeds the threshold values, the concentration of activated platelets becomes instantly equal to the initial resting platelet concentration. In the general case thrombin concentration is given by Equation 3.3 while prothrombin concentration is given by Equation 3.4:

$$\frac{\partial[IIa]}{\partial t} = -k_{in}[IIa] + k_{tot} \cdot [II]$$

Equation 3.3

$$\frac{\partial[II]}{\partial t} = -k_{tot} \cdot [II]$$

Equation 3.4

Here k_{tot} represent the total rate of prothrombin conversion to thrombin and includes both the production on the reacting site and on the platelet surfaces:

$$k_{tot} = k_{TF,surf} + k_{II}^{AP} \cdot [PL], \text{ if } [IIa] > [IIa]_{th}$$

Equation 3.5

$$k_{tot} = k_{TF,surf} \quad , \text{ if } [IIa] \leq [IIa]_{th}$$

Equation 3.6

The approximate differential equation (Equation 3.4) that describes prothrombin concentration can be solved analytically and provide an expression for the prothrombin concentration vs time (Equation 3.7):

$$[II](t) = [II](t = 0) \cdot e^{-k_{tot}t}$$

Equation 3.7

The PDE describing thrombin concentration becomes:

$$\frac{\partial[IIa]}{\partial t} = -k_{in}[IIa] + k_{tot} \cdot [II]_o \cdot e^{-k_{tot}t},$$

Equation 3.8

$$\text{or } \frac{dx}{dt} = Ax - CB e^{Ct}$$

$$\text{where } A = -k_{in}, B = [II]_o \text{ and } C = -k_{tot}$$

Equation 3.9

The equation can be rewritten as follows,

$$\frac{dy}{dt} = (A - C) \cdot y - CB, \text{ where } y = x \cdot e^{-Ct}$$

Equation 3.10

The last expression, after manipulation leads to an (approximate because of the assumption of instant platelet activation) analytic solution for the temporal evolution of thrombin concentration (X):

$$X(t) = \frac{e^{Ct}}{A - C} [(A - C)X_0 e^{-Ct_0} - CB] e^{(A-C)t} + CB \text{ or}$$

Equation 3.11

$$[IIa](t) = \frac{e^{-k_{tot}t}}{k_{tot} - k_{in}} [(k_{tot} - k_{in})[IIa]_0 e^{k_{tot}t_0} + k_{tot} \cdot [II]_0] e^{(k_{tot}-k_{in})t} - k_{tot} \cdot [II]_0$$

Equation 3.12

For $[IIa](t = 0) = 0$ the equation acquires the simplified form:

$$[IIa](t) = \frac{k_{tot} \cdot [II]_0}{k_{in} - k_{tot}} (e^{-k_{tot}t} - e^{-k_{in}t})$$

Equation 3.13

This equation has the general form:

$$[IIa](t) = \frac{B_i}{A_i - C_i} (e^{A_i t} - e^{C_i t}) = F_{IIa}(t, \vec{k})$$

Equation 3.14

The term $F_{IIa}(t, \vec{k})$ represents the approximate analytical expression for the temporal evolution of thrombin concentration for a given set of reaction rate constants \vec{C} . The equation is similar to the equation proposed by Wagenvoord et al [154] when applied to zero dimensional modelling of thrombin generation, but it can also be applied in cases where platelets and TF are not uniformly distributed in a sample and the results will vary in space. Here the constants A, B and C depend both on the model parameters and TGA results and they have different values for the initial phase and the propagation phase.

In the case where only the four characteristic parameters of TGA are available the physical meaning of each parameter poses a mathematical condition that the function $F_{IIa}(t, \vec{k})$ must fulfil. Tlag is the moment thrombin reaches the threshold concentration; Tmax is the time when thrombin reaches maximum concentration therefore the time

derivative of thrombin concentration for $t=T_{max}$ must equal zero; C_{max} is the maximum concentration of thrombin, and it occurs when $t=T_{max}$; ETP is the area under the thrombin concentration curve therefore it is equal to the integral of thrombin concentration over time. According to these, for the function F we obtain the equations shown in Table 3-4. From this set of equations, the reaction rate constants can be approximated numerically, making the resulting system of equations capable of reproducing the curve of the TGA with the given parameters.

Table 3-4: Set of equations for tuning thrombin sub-model to reproduce the results of a specific TGA with the use of the four main parameters of TGA

$F_{IIa}(T_{lag}, \vec{k}) = [IIa]_{thr}$
$F_{IIa}(T_{max}, \vec{k}) = C_{max}$
$\frac{dF_{IIa}}{dt}(T_{max}, \vec{k}) = 0$
$\int_0^{\infty} F_{IIa}(t, \vec{k}) dt \cong \int_{T_{lag}}^{t_{\infty}} F_{IIa}(t, \vec{k}) dt = ETP$

In the cases where the data from the whole curve are available, there is another –and more accurate– way for obtaining the model constants. The surface reaction rate is obtained by solving (numerically) Equation 3.15, which describes thrombin concentration during the initiation phase:

$$[IIa]_{th} - \frac{k_{surf} \cdot [II]_o}{k_{in} - k_{surf}} (e^{-k_{surf} T_{lag}} - e^{-k_{in} T_{lag}}) = 0$$

Equation 3.15

The activated platelet concentration is approximately,

$$[AP] = [RP](0) \left(1 - e^{-(t-T_{lag})k_{AP}^{IIa}} \right), t > T_{lag}$$

Equation 3.16

Analytical expression can be obtained for prothrombin concentration versus time:

$$[II](t) = [II](t = 0) \cdot e^{-k_{tot}(t) \cdot t}$$

Equation 3.17

Therefore, for the differential equation describing thrombin evolution for $t > Tlag$

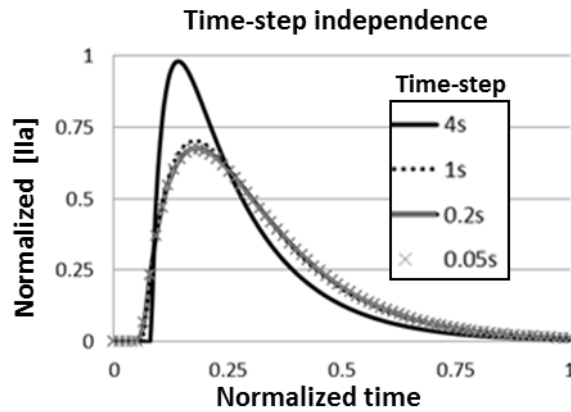
$$\frac{d}{dt}[IIa] = -k'_{in} \cdot [IIa] + k_{tot}(t) \cdot [II](t)$$

Equation 3.18

In that case, the constants can be obtained numerically using an iterative process for the differential equation. In most of the results that will follow, only the constants related to thrombin production k_{II}^{AP} , k_{surf} , k_{in} (Table 3-7) were adjusted.

3.6 Results of thrombin sub-model

We first applied the model using the initial values for the constants; while the resulting curve has the shape of a typical thrombin generation curve, the actual values of the TGA parameters were significantly higher than the typical experimental results for fresh platelet rich plasma as reported in [191]. Performing simulations for different time steps, it



was found that the results of the model are identical for time steps below 0.5s (Figure 3-4: Time step

Figure 3-4: Time step independence test for the thrombin sub-model. For time-step values below 0.5s the results coincide.

independence test for the thrombin sub-model. For time-step values below 0.5s the results coincide.. As a whole heart cycle at rest conditions is about 0.8s (for 75 bpm), the maximum magnitude of the time steps for simulating pulsating flow is much smaller (about one order of magnitude smaller), thus in terms of temporal discretization, the coupling of the reaction system model with CFD simulations can be straightforward.

Table 3-5 : Brief description of the different cases simulated with appropriate modification of the model constants.

Case number	Description
1	Reproduction of a TGA curve that corresponds to typical parameter values [191].
2,3	Simulation of thrombin generation without inhibitors, in plasma with the addition of phospholipids [120]. The initiation was triggered using 5pM and 100pM fVIIa and 5 pM TF for 1nM TF, 200µM phospholipids and the rest of the zymogens at the normal plasma concentrations.
4	Reproducing an arbitrary TGA curve with different parameters compared to case 1 [197]. Platelet poor plasma with the addition of 1pM of TF.
5-7	Simulations for different platelet concentration (100, 150 and 400 x 10 ⁹ pl/L) using the same setup for the model [191]. The reported TF concentration was approximately 3pF.
8	TGA curve corresponding to very low platelet concentration (75 x 10 ⁹ pl/L) [198]. Clotting factors were close to the normal level, initiation was triggered by adding 0.2nM fVIIa and TF bearing monocytes at approximately 0.17pM.

Subsequently, the model was applied in 8 different cases, denoted as Case1-8. In the corresponding plots, when both model and experimental results are represented, model results are named 'C# model' and the experimental results 'C# exp'.

Table 3-6: The experimental TGA parameters for all the cases used for the model testing and calibration and the resulting numerical ones

		<i>Tlag (min)</i>	<i>Tmax (min)</i>	<i>Cmax (nM)</i>	<i>ETP (nM·min)</i>
Case 1	experiment	3.6 ± 0.8	7.4±1.8	164±50	1321±330
	model	3.7	6.8	165	1364
Case 2	experiment	1.5	3.5	(1.5·10 ³)	n/a
	model	1.5	4	(1.5·10 ³)	n/a
Case 3	experiment	0.67	2.25	(1.5·10 ³)	n/a
	model	0.65	2.38	(1.5·10 ³)	n/a
Case 4	experiment	3.5	4.8	199	735
	model	3.7	4.6	196	710
Case 5	experiment	5±0.5	11±2.7	161±38	1633±81
	model	5.8	9	190	1718
Case 6	experiment	5.5±0.5	11±0.2	98±40	1316±255
	model	6	9.4	91	1370
Case 7	experiment	5.8±0.7	13±0.9	72±38	1135±300
	model	6	9.6	62	1118
Case 8	experiment	15	27	101	2012
	model	13.3	25.3	102	1934

The equations for the adjustment of the constants were solved in MATLAB, while the

adjustment of the platelet related constants was done manually using Excel and Systems Biology Toolbox 2 [199]. Case 1 represents the tuning of the constants in order for the model to give a thrombin generation curve that will match the typical values of the four TGA parameters as reported in [191] the resulting curve (C1 model) is shown in Figure 3-5. Figure 3-8 compares curves representing cases with lower rate of thrombin generation. In the absence of inhibition (case 2 and case 3), the time interval between the end of the initiation phase and the moment that thrombin concentration reaches its maximum value, is 2-4 min depending on the constant for thrombin activation by activated platelets; the results match approximately the experimental thrombin production curves found in [120] (Figure 3-6).

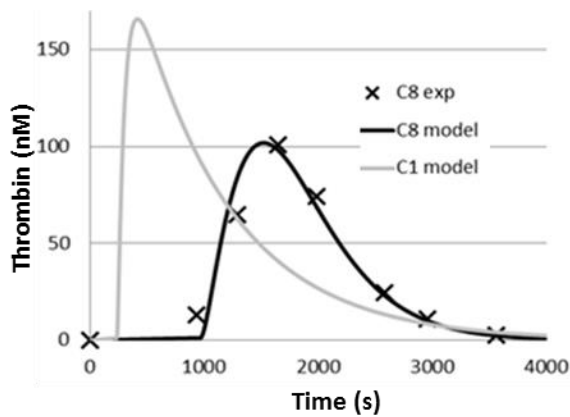


Figure 3-5: Curve matching the typical TGA parameters C1 and the curve that matches thrombin generation for low platelet concentration C8.

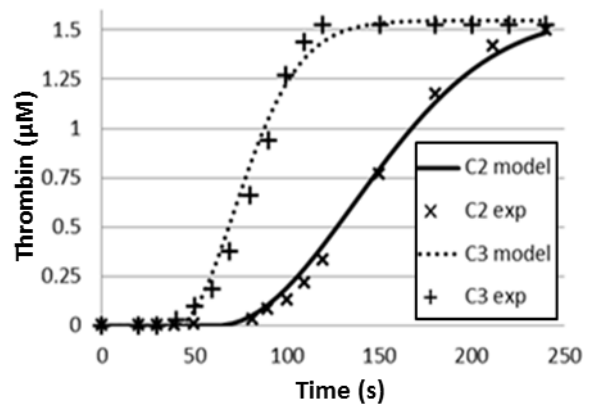


Figure 3-6: Fitting of cases with added phospholipids in the absence of inhibitors. Triggering substance is r-TF:VIIa

The next test (Case 4) involved adjusting the model constants in order to fit an arbitrary thrombin generation curve. The experimental curve was found in [197]. Figure 3-7 shows that the model predicts the experimental curve with good accuracy. For future application of the model under flow conditions characterised by non-uniform concentrations of platelets, it has been considered important to test its behaviour with given constants for varying concentration of platelets near to the physiological values. The constants were adjusted so that the model approximated the TGA results for platelet concentration 150×10^9 pl/L (physiological values are $200-400 \times 10^9$ pl/L). Then the model was applied with the same setup for two other values of platelet concentrations; Cases 5-7 use the same values for reaction rate constants with platelet concentration 400, 150 and 100×10^9 pl/L, respectively. The results shown on Table 3-6 are within the

range of values reported in [191] although the dependence of maximum concentration of thrombin on platelet concentration seems a little stronger than for the in vitro experiments. The resulting curves are shown in Figure 3-8. Further increase of platelet concentration resulted in higher values for maximum thrombin concentration and small decrease of T_{max} , without significant effect on ETP. If the constants describing platelet activation are also suitably modified, the equations can match curves that depict slower thrombin formation like the ones reported in [198] for lower platelet concentrations (75×10^9 pl/L) as shown in C8.

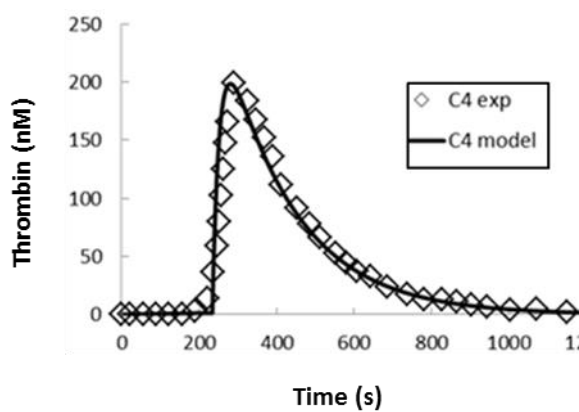


Figure 3-7: Adjustment of the model in order to reproduce a specific TGA curve. Experimental results from Hemker et al [197]

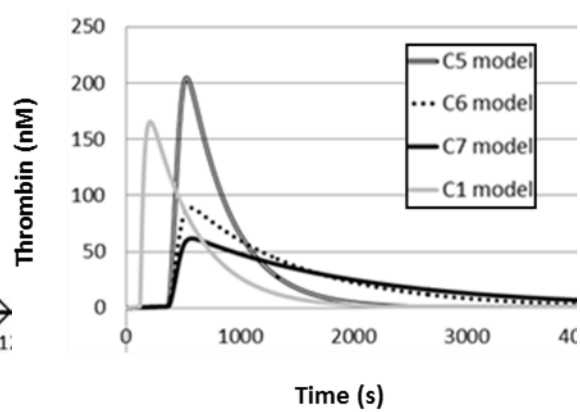


Figure 3-8: Simulated thrombin generation curves for different platelet concentrations, C5-C7 and the typical curve C1. Values of the reaction rate constants are identical for cases C5 to C7

The values of the model constants after modification, in order to fit different cases are shown in Table 3-6; it can be seen that for all cases the values are within a reasonable range and close to the initial estimations. The reactions related to platelet activation actually represent the transition from the initiation to the propagation phase. Although, as mentioned earlier, activated platelets in that model actually represent platelet activity compared to a maximum value rather than actual activated platelet count, it is interesting that the calculated time until platelets reach half of the maximum activity for Case 8 is 5-10 min, is in agreement with the findings of Allen et al [198]. As the curves used to reproduce a wide range of TGA results correspond to different experiments, these constants vary significantly between two groups of cases. In the experiments

corresponding to cases 1-4, where phospholipids have been used as a substrate for enzymatic reactions, this transition is much faster than for cases 5-8 where human platelets have been used. For cases 5-8, the values of these constants have been adjusted manually. However, as shown in recent experiments [200], TGA results in whole blood resemble more the curves of case 1 and 4, (possibly because red blood cells that are not included in most TGA also contribute to thrombin generation [200, 201]), so this modification of the parameters related to platelet activation is not necessary for modelling thrombin generation in healthy whole blood; for these cases the model can be adjusted to reproduce thrombin generation without modifying the reaction rate constants related to platelet activation by thrombin.

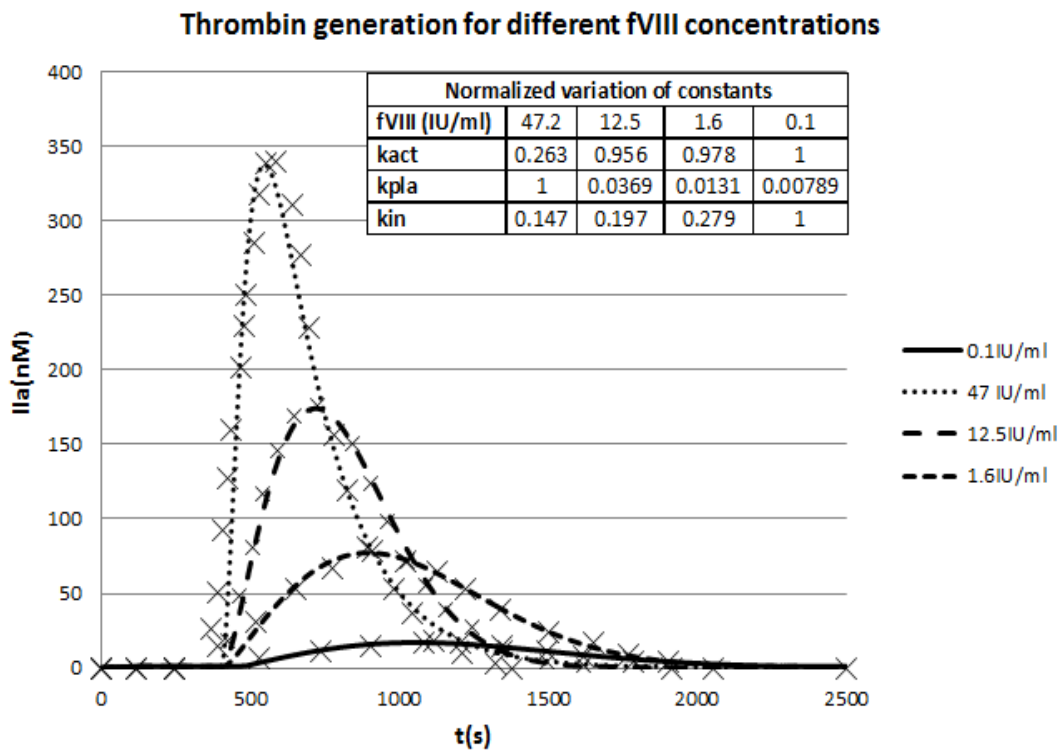


Figure 3-9: Simulation of thrombin generation for cases of haemophilia. In order for the equations to reproduce pathological cases the reaction rate constants have been significantly modified compared to their values with the use of the equations of Table 3-4.

On the other hand, by modifying also the rate of platelet activation by thrombin, the model could also approximate pathological cases as haemophilia or results of patients' blood analysis after anticoagulation treatment. Curves corresponding to pathological

situations as severe haemophilia A [154] can be very well approximated as shown in (Figure 3-9). Haemophilia is fVIII deficiency. Thrombin generation curves shown in the Figure 3-9 were obtained by adding fVIII in the blood of haemophilic patient and performing measurements after specific time intervals. The concentrations of VIII reported have been calculated using 12.8 hours as half-life of fVIII [202]. In order to describe pathological TGA results, the same adjustment techniques described earlier were used. The parameters of the model obtained values that are significantly modified compared to the initial ones. However, that was expected as the pathological results correspond to different function of the coagulation system for the patient. In the specific case, factor VIII is mainly involved in the amplification and propagation of coagulation, as it is the co-factor of fIXa for thrombin activation on the membrane of activated platelets. In order to reproduce curves for different fVIII concentrations the constants related with the specific phases (k_{in} , k_{AP}^{IIa} and k_{IIa}^{AP}) required modification while the constant related only to the initiation phase remained unchanged.

In contrast to the methods described and reviewed in [203] where the effect of the variation of each factor concentration and activity have been investigated, this model uses only the information included in the TGA curve; thus, it has some limitations. If the production rate of thrombin at the moment of the transition from the initiation to the amplification phase is close to the rate of inhibition ($k_{in,0}[IIa]_{th} \geq k_{surf}[II]$) there is a possibility of oscillating solutions. This can be avoided either with the use of small time step or with a slight rearrangement of the involved parameters.

The most significant inaccuracy of the model is recorded when the initial values of the parameters are used and refers to the time interval between the initiation of thrombin burst and the maximum concentration of thrombin. The time interval $T_{lmax}-T_{lag}$ is smaller than the one reported in TGAs (2.8min compared to 2min predicted by the model) when adjusting only the three previously mentioned parameters. The increase of thrombin concentration

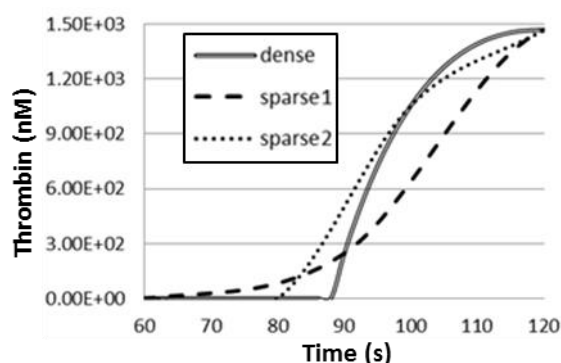


Figure 3-10: Effect of the sampling frequency to the resulting curve after automated curve fitting on the results.

predicted by the model is sharper compared to the experimental data while the shapes of the two curves are different for this time interval. That can be fixed by adjusting manually the constants related to platelet activation as it was the case for cases 4-8. However, the experimental data, while in all studies are presented in the form of a continuous curve, usually correspond to measurements in discrete time intervals; the resulting curves are obtained through data fitting.

In Figure 3-10 three curves are plotted for the time interval of thrombin concentration increase. The data points were using the same setup for the thrombin generation model so the data points for the three cases actually belong to the same continuous curve. The only difference among the three cases is the time interval between two consequent points. In one case labelled as 'dense', the time interval between two data points is 2s, while for the other two cases (labelled as sparse1 and sparse2), it is 30s and 20s, respectively. The time intervals between two consecutive data points for this test were chosen so as to be comparable to the time interval that intervenes between the extraction of two consequent samples from the investigated reacting solution; for example in the results presented by Lawson et al [120] the time interval between two samples is 7.5 to 30s. It can be seen that curve fitting on experimental values, that was used in studies prior to the introduction of continuous monitoring of thrombin generation, while making the results more presentable can also give incorrect information on the actual evolution of the process between two measurements. So differences between modelled and experimental curves do not necessary indicate inadequacy of the model.

The constant that represents the initial thrombin production rate $k_{TF,surf}$ (for a given value of the inhibition rate) is mainly calculated from lag time. While the reported experimental results seem to depend on the exact composition of the samples and the triggering substance used, (e.g. for the cases described in [191, 192]) in the results reported by Gerotziafas et al [191] there seems to be a clear relationship ($R^2=0.989$) between TF concentration and lag time, and therefore $k_{TF,surf}$, for the same experimental conditions and for TF concentrations varying between 1 and 30pM:

$$k_{TF,surf} = k_{TF,surf,max} \left(A + \text{Bln} \left(\frac{[TF]}{[TF_{max}]} \right) \right)$$

Equation 3.19

The constant values are $A = 0.996 \approx 1$, $B = 0.0372$ while for the aforementioned study the maximum calculated value for the rate of thrombin generation during the initiation phase is $k_{surf,max} = 7.91 \cdot 10^{-6} s^{-1}$ and the relationship can approximately be written as:

$$k_{surf} = k_{surf,max} \left(1 + 0.0372 \cdot \ln \left(\frac{[TF]}{[TF_{max}]} \right) \right)$$

Equation 3.20

Equation 3-18 gives good results when used for the estimation of $k_{TF,surf}$ for other experimental studies where TF has been used for the initiation of the process. For experiments where recombinant TF:VIIa has been used as triggering substance for the coagulation process, again a good correlation between $k_{TF,surf}$ and trigger concentration can be established, ($R^2 > 0.98$) but the resulting formulas are different, so equation 3-18 is valid only for cases where a quantity of TF is added to the reacting solution in order to trigger the initiation of coagulation process. Equation 3-18 can be used when there is a reference value for the initiation rate constant $k_{surf,max}$ for a known TF concentration, in order to estimate the value of the initiation rate reaction k_{surf} for lower TF concentrations. It is mainly presented because it is possible that the TF concentration in atheromatous plaques is different than the TF concentration used in the TGA experiments, so the calculated value from TGA will require modification for applying under flow.

As this thrombin sub-model was developed in order to be coupled with flow simulation techniques in three dimensional geometries, the initial and slow phase of thrombin generation that occurs on the TF bearing endothelium cells should finally be expressed as a surface reaction term. The reaction rate for the surface reaction can be calculated with the use of the reported surface TF concentration in atheromatous plaques (33 pg/cm^2) [204] and the molecular weight of (46,000Da approximately [205]). For a computational cubic cell of e.g. $100 \mu\text{m}$ this numbers would lead to a TF concentration of about 70 pm resulting in $k_{surf} = 9.75 \cdot 10^{-6} s^{-1}$. It must be noted that any value for the initiation constant obtained via TGA corresponds to bulk reaction in a stationary solution. Experimental validation for the value of the surface reaction rate constant k_{surf} and the relation to the bulk reaction rate constant requires experiments on coagulation under flow. Perfusion of blood samples for different wall shear rate values over a surface with immobilized TF can lead to an independent derivation of the value

of k_{surf} , by measuring the lagtime. At the same time, if the TGA results for the examined sample are known, a more solid relationship between the bulk and the surface reaction rate constant can be established. It is preferable that the adjustment of the thrombus model for specific patients is based on TGA results rather than perfusion experiments. Perfusion experiments, while providing more accurate and direct information, require significantly larger blood samples and are harder to be repeated in an identical manner.

Sub-threshold concentrations of thrombin actually represent also all the products of the previous steps of coagulation. At the same time, this approach allows a slow rate of fibrin production before the burst of thrombin and a realistic prediction of clotting time. As TGA results demonstrate inter-laboratory variation [189], this model, based on TGA results and with its simplified character, does not claim to reproduce with precise accuracy thrombin generation. But it can offer a way to model thrombin generation that has some specific advantages: (1) can be adjusted to describe different rates of thrombin generation, and (2) can be easily coupled with CFD simulations as it will be demonstrated in the following sections. Finally, as the model describes the production of thrombin in blood in a phenomenological way, it does not require detailed information on the composition of blood for each patient. Instead of using detailed systems of biochemical reactions that require as input the concentration of all the involved coagulation factors, this model can be calibrated and applied directly for different patients using only the parameters or the curve of the TGA.

3.7 Variation of the model parameters

The proposed thrombin sub-model, although simplified compared to the actual process that is due to describe, still has an imbalance between the used parameters and the outputs. There are five independent reaction rate constants and three input concentrations that produce one output for which data for validation are available: thrombin concentration curve. Therefore, while the reaction rate constants could almost certainly be fitted directly without the use of a starting point for their initial values, it is possible that there is a large number of sets with different values for the fitted parameters that can satisfy the equations and reproduce a given thrombin concentration curve or the results of a given TGA; obviously most of this sets of values, while giving an output that fits the experimental TGA curves, have no connection to the actual processes at all and as a result of this would give big errors for different input parameters (platelet, prothrombin and triggering substance concentration).

Table 3-7: The variation of the reaction rate constants during the process of fitting the model to the different cases. In cases 2 and 3 there is no inhibitors in the experimental procedures and in cases 5-7, used to test the function of the model for different platelet concentrations the reaction rate constants were fixed.

Const. (s^{-1})	Initial estimations	Case 1	Case 2	Case 3	Case 4	Cases 5-7	Case 8
$k_{TF,surf}$	10^{-5}	$7.3 \cdot 10^{-6}$	$9.1 \cdot 10^{-6}$	$1.5 \cdot 10^{-5}$	$7.4 \cdot 10^{-6}$	$7.2 \cdot 10^{-6}$	$4.06 \cdot 10^{-7}$
k_{II}^{AP}	0.085 – 1.8	0.73	2.8	4	1.55	0.53	3.6
k_{in}	$1.7 \cdot 10^{-2} - 0.2$	0.032	0	0	0.052	0.026	0.024
k_{AP}^{IIa}	0.2 – 0.5	0.5	-		0.5	0.002	0.0018

There were two ways to overcome this problem. The first one was to simultaneously fit the model in a number of cases with different inputs, and modify the parameters until optimum results are obtained. Unfortunately we could not find either a large number of cases or an appropriate method for this kind of fitting. The second way which has been used in this Thesis, was to look through the existing literature and establish an initial set of values for the parameters based on experimental results or previous computational models of coagulation. In this way the resulting ‘lumped’ reactions are linked to the actual corresponding biochemical processes; at the same time, a range of accepted values for the parameters was obtained and used during the process of fitting. Additionally, it was checked whether the variation of the parameters was in agreement with the different conditions of each case. The results presented on Table 3-7 demonstrate that at least quantitatively, the change of the parameters is the expected according to the different conditions. Cases 2 and 3 required modification of the initiation constant as different amount of the triggering substance was used while in cases 5-7 the results of TAGs that corresponded to different platelet concentrations were reproduced without modifying the parameters of the model. The initiation constant $k_{TF,surf}$ is directly related to the amount of the triggering substance. It seems that the dependence of the initiation constant to the amount of the triggering substance can be

described by a logarithmic relation. Note that the relationship between this constant and the lag time is approximately linear, as the reduction of prothrombin concentration during the lag time is very small and the amount of thrombin up to the threshold concentration increases linear with time. The variations of this constant were in agreement with the different concentrations of the triggering substance used in each case. At the same time, the case of haemophilia was successfully modelled without modification of the specific constant, in agreement with the alterations to the process caused by the disease. The only case where this constant was significantly lowered was the case with low (less than 20% of the normal) concentration of platelets. This indicates that in total absence of lipid surfaces, the initiation phase or at least the transition from the initiation to the amplification is also affected. This fact also supported by the small increase of the (experimentally derived) lag time for smaller platelet concentrations as reported in cases 5-7. So it is possible that the addition of a platelet concentration dependent term on the initiation would benefit the accuracy of the model. An overall comparison of the values of this constant has no meaning as different substances were used as triggering (human TF, r-TF and rTF:VIIa).

Larger variations were observed in the fitted values of the reaction rate constant of prothrombin conversion to thrombin by activated platelets, k_{II}^{AP} . The initial range of values for this process were extracted from the computational work of Sorensen et al [163] and an the experimental work of Rosing et al [133] that gives a large range of prothrombin activation rate by platelets for different experimental conditions. In the 'construction' of the reaction, the results for not stimulated platelets and platelets stimulated by thrombin were taken into account, but the rate of activation was kept constant. The results for cases 2 and 3 (although close to the predicted value) have no comparative value as in the specific experiments phospholipids were used instead of platelets. This variation for different cases was not surprising. This pseudo-reaction incorporates a large number of actual reactions therefore its variation may express altered function of several different parts of the coagulation process. Additionally, a small part of these reactions do not actually occur on activated platelets. Therefore the relationship between the platelet concentration and the activation rate of prothrombin by activated platelets was not expected to be accurately linear in the first place. The changes of the value of k_{II}^{AP} may reflect change of the non-used in the model real inputs of coagulation as fX, fV concentrations, different rate for one of the lumped reactions, but also big change in the platelet concentration.

The inhibition process was the most accurate part of the model. The minimum value was estimated using the ATIII inhibition at its maximum rate. All values used were within the predefined range with small variations; they were greater than the minimum value as they include inhibition of thrombin by other factors as well as all the other inhibiting reactions of the process that reduce the intermediate products of coagulation. The inhibition constant has almost the same value with the exception of the case where platelet poor plasma was used. That is feasible as thrombin that is bound on platelets is protected from inhibitors. Actually this would also justify allowing a small variation of the inhibition constant in cases 5-7 where platelet concentration varied, and possibly this would lead to better agreement of the simulation results with the experiments. The changes of the inhibition rate constant were applied only to the phase after the initiation in order to include the inhibiting feedback loops of the process.

Finally the rate constant for the platelet activation by thrombin k_{AP}^{IIa} had also large variations among the different cases. As mentioned earlier, this term in most cases was modified manually. In the resulting thrombin generation curve this term is the main factor that determines the difference between lag time and the time of maximum thrombin concentration when the values of the parameters are within the accepted range. When the initial reaction rate was used for the process this difference, $(T_{max} - T_{lag})$, was too small. This happened because the value for the constant, while taken from works where it represented only platelet activation, in this work is representing the whole process of transition from the initiation to the amplification phase of thrombin generation. This involves more processes and it is obviously slower. So for cases 5-8 the value of k_{AP}^{IIa} was lowered significantly until the desired result was achieved.

The presented model was developed in order to represent the temporal evolution of thrombin generation in a simplified manner while at the same time allowing the spatial distribution of the processes when applied to three dimensional cases. Each of the lumped reactions corresponds to a number of actual processes that occur in different sites and, with the exception of the inhibition, to a different phase of the coagulation process. Changes in one parameter of the physical system might require the modification of more than one constant of the equations. These modifications can be justified by the actual processes; the increase of the inhibition rate for lower platelet concentration is due to the reduction of the amount of the platelet-bound thrombin and the reduced platelet activity for lower fVIII concentrations can be attributed to the smaller amounts

of intrinsic tenase produced. However, the idea was to propose **a system of equation that it would be able to reproduce the process as a whole** rather than equations that independently describe different parts of the coagulation; therefore the variation of the reaction rate constants within a reasonable range was expected and does not require quantitative correlation with the experimental conditions of each case.

3.8 Platelet adhesion sub-model

The responses of platelets are modelled using a system of equations that is independent from the coagulation reactions. The platelet sub-model takes into account three different actions for platelets: binding on surface, binding on already bound platelets and unbinding from the surface. It has been assumed that the corresponding three reaction rates for activated platelets are different, as one would expect them having more tendency to bind on the reacting surface or to each other and less tendency to disaggregate and return to the blood circulation. Therefore four different platelet-related states are required: resting platelets in flow $RP^{(f)}$, activated platelets in flow $AP^{(f)}$, bound resting platelets $RP^{(b)}$ and bound activated platelets $AP^{(b)}$; for each one of the possible platelet states corresponding source term for each state should be introduced. The model makes no distinction between platelets bound directly on the vessel wall and platelets binding on other platelets. The binding of platelets was introduced as a surface reaction term, similar to the one describing surface thrombin generation.

In the equations of Table 3-8, the subscripts 'bi' and 'diss' refer to binding and unbinding respectively. The activation of platelets is not included in these terms. The binding of the platelets occurs only on the free part of the surface (the part not covered with platelets). The maximum platelets per surface was calculated based on the close packing ratio $p_{Smax} = 7.4 \cdot 10^{-4} kg/m^2$, a value close to the one used by Sorensen [163] $7 \cdot 10^6 pl/cm^2$ or $7.05 \cdot 10^{-4} kg/m^2$ after the unit conversion. Based on this value, the fraction of the surface that is available for platelet binding is calculated as:

$$A_f = 1 - \frac{[RP^{(b)}] + [AP^{(b)}]}{p_{Smax}}$$

Equation 3.21

Table 3-8: Source terms for the four different states considered in the platelet aggregation sub-model: $S_{RP(f)}$ corresponds to resting platelets in flow, $S_{RP(b)}$ corresponds to bound resting platelets $S_{AP(f)}$ represents the concentration of activated platelets in flow and $S_{AP(b)}$ the concentration of bound activated platelets.

$S_{RP(f)} = -((k_{bi,surf}^{RP} \cdot A_f + k_{bi,RP}^{RP} \cdot [RP^{(b)}] + k_{bi,AP}^{RP} \cdot [AP^{(b)}]) \cdot [RP^{(f)}] + k_{diss}^{RP} \cdot [RP^{(b)}]^2) \cdot A_{SV}$
$S_{RP(b)} = (k_{bi,surf}^{RP} \cdot A_f + k_{bi,RP}^{RP} \cdot [RP^{(b)}] + k_{bi,AP}^{RP} \cdot [AP^{(b)}]) \cdot [RP^{(f)}] - k_{diss}^{RP} \cdot [RP^{(b)}]^2$
$S_{AP(f)} = -((k_{bi,surf}^{AP} \cdot A_f + k_{bi,RP}^{AP} \cdot [RP^{(b)}] + k_{bi,AP}^{AP} \cdot [AP^{(b)}]) \cdot [AP^{(f)}] + k_{diss}^{AP} \cdot [AP^{(b)}]^2) \cdot A_{SV}$
$S_{AP(b)} = (k_{bi,surf}^{AP} \cdot A_f + k_{bi,RP}^{AP} \cdot [RP^{(b)}] + k_{bi,AP}^{AP} \cdot [AP^{(b)}]) \cdot [AP^{(f)}] - k_{diss}^{AP} \cdot [AP^{(b)}]^2$

The reaction rate constants are adjusted in order to function properly with the species in the units used in the model. The units for the bound resting and activated platelets are kg/m^2 and for the corresponding source terms are $kg/m^2 \cdot s$ while for during the implementation of the model the source terms for circulating platelets must be multiplied by a constant to convert their units to kg/kg .

$$A_{SV} = \frac{S_C}{\rho \cdot V_C}$$

Equation 3.22

Here S_C , V_C and ρ are respectively the reacting surface of the boundary cell, the volume of the cell and the fluid density. The reaction rate constants were adjusted in order for the model to be able to reproduce the results of platelet binding on sub-endothelium [2].

It was not possible to figure out a way to derive different reaction rate constants for resting and activated platelets for the specific experiment used for the calibration of the platelet sub-model. Therefore, the following approach was used: the constants of the model were adjusted to a single value, both for resting and activated platelets, using a system of only two species, circulating $PLA^{(f)}$ and bound $PLA^{(b)}$ platelets. So, for the development of the platelet aggregation sub-model only, the source terms that describe the change of the population of flowing and bound platelets presented in Table 3-8 are reduced to the ones described by Equation 3.23 and Equation 3.24, while the used species are also reduced to flowing and bound platelets.

$$S_{PLA^{(f)}} = -(k_{bi,surf}^{PLA} \cdot A_f + k_{bi,PLA}^{PLA} \cdot [PLA^{(b)}]) \cdot [PLA^{(f)}] \cdot A_{SV}$$

Equation 3.23

$$S_{PLA^{(b)}} = (k_{bi,surf}^{PLA} \cdot A_f + k_{bi,PLA}^{PLA} \cdot [PLA^{(b)}]) \cdot [PLA^{(f)}] - k_{diss}^{PLA} \cdot [PLA^{(b)}]^2$$

Equation 3.24

In this set of equations, platelets that disaggregate from the reacting site are not considered able to aggregate again or contribute in any way to the whole process. As described in the following sections, the different behaviour of platelet was included with the use of an additional constant, k_{diff} , in a manner similar to the work of Sorensen [163]. The reaction rate constants for the transitions of activated platelets were set to be proportional to the reaction rates of resting platelets. For example the reaction rates for binding of resting and activated platelets on the surface of the vessel wall were related through the equation $k_{bi,surf}^{AP} = k_{diff} \cdot k_{bi,surf}^{RP}$.

3.9 Initial estimation of reaction rate constants

An mentioned earlier, the verification-calibration of the platelet aggregation sub-model was based on the rate of platelet deposition on de-endothelized vessel segments [2]. The initial values of the reaction rate constants were based on some rational assumptions while fine tuning was performed after coupling the model with flow simulations, using the test cases described in the aforementioned study.

An initial estimation of the reaction rate constant of platelets binding on the vessel surface can be obtained by using the conservation of mass for the platelets above the reaction rate, assuming that for the initial stages of the process the concentration of the platelets in that area will have a time-independent value $[PLA^{(f)}]^*$. So the rate of platelet supply due to convection must be equal to the rate of binding. If a rectangular volume with dimensions Δx , Δy and h (x is the direction of the flow) is considered, then the previous assumption will lead to Equation 3.25:

$$\frac{\delta[PLA^{(f)}]}{\delta t} = -k_{bi,surf}^{PLA} \cdot [PLA^{(f)}]^* \cdot \Delta x \Delta y + \rho h \Delta y u ([PLA^{(f)}]^{(0)} - [PLA^{(f)}]^*) = 0$$

Equation 3.25

Here the height h is actually the depth of the reacting area. Platelets located outside this reaction zone, in a distance above h from the wall are considered unlikely to bind on the surface. The initial deposition rate can be approximated by:

$$\lambda = k_{bi,surf}^{PLA} \cdot [PLA^{(f)}]^*$$

Equation 3.26

By combining Equation 3.25 and Equation 3.26 and substituting the velocity from Equation 3.27:

$$u = \frac{\gamma h}{2}$$

Equation 3.27

the approximation for the reaction rate constant shown in Equation 3.28 is derived:

$$k_{bi,surf}^{PLA} = \frac{\lambda \rho \gamma h^2}{\rho \gamma h^2 [PLA^{(f)}]^{(0)} - 2\lambda \Delta x}$$

Equation 3.28

The value that this relationship gives, using as reaction zone depth $h = 6 - 10 \cdot 10^{-6} m$ or in other words 3-5 times the diameter of a platelet, is of the order of $10^{-5} kg/s \cdot m^2$

As in all cases the quantity of bound platelets per surface reaches more or less a steady-state value, it is reasonable to assume that at this point the aggregation and disaggregation rates are equal.

$$(k_{bi,surf}^{PLA} \cdot A_f + k_{bi,PLA}^{PLA} \cdot [PLA^{(b)}]) \cdot [PLA^{(f)}] = k_{diss}^{PLA} \cdot [PLA^{(b)}]^2$$

Equation 3.29

As these values are well above the value where the surface is fully covered with platelets ($A_f = 0$), Equation 3.29 gets the simpler form:

$$k_{bi,PLA}^{PLA} \cdot [PLA^{(b)}] \cdot [PLA^{(f)}] = k_{diss}^{PLA} \cdot [PLA^{(b)}]^2$$

Equation 3.30

From that form one can get an initial estimation for the relationship between the disaggregation rate and the rate of platelets binding on other platelets, using the maximum value for bound platelets as shown in the graphs $[PLA^{(b)}] \approx 8 \cdot 10^{-4} kg/m^2$ and the initial concentration of circulating platelets. $[PLA^{(f)}] = 0.0285 kg/kg$

$$k_{bi,PLA}^{PLA} \cdot [PLA^{(f)}] = k_{diss}^{PLA} \cdot [PLA^{(b)}]_{max} \rightarrow \frac{k_{diss}^{PLA}}{k_{bi,PLA}^{PLA}} \approx 35 \cdot \frac{kg}{m^2}$$

Equation 3.31

Additionally, as the difference in the initial rate is more obvious when the mass of aggregated platelets is less than 10% of the maximum, it was assumed that at this point the two processes must have comparable contribution to the increase of the quantity of aggregated platelets. This assumption provided a rough estimation for the ratio of the two reaction rate constants of these processes:

$$k_{bi,PLA}^{PLA} \cdot [PLA^{(f)}] = 0.1 \cdot k_{bi,surf}^{PLA} \cdot [PLA^{(b)}]_{max} \rightarrow k_{bi,PLA}^{PLA} \approx 10^5 \cdot k_{bi,surf}^{PLA}$$

Equation 3.32

The initial values used as a starting point for the fine tuning of the model for the three constants were: $k_{bi,PLA}^{PLA} = 0.2s^{-1}$, $k_{diss}^{PLA} = 7(\frac{kg}{m^2} \cdot s)^{-1}$ and $k_{bi,surf}^{PLA} = 4 \cdot 10^{-5} kg/m^2 \cdot s$. Time-step independence test showed that the results of the model when programmed in FLUENT were identical, even for large time-step values $\Delta t = 2s$. Also, while the boundary cells of the test geometry had low height to length ratio (0.1), the maximum value of bound platelets corresponded to a low volume (and mass) fraction of platelets in the cell (<0.07) one order of magnitude lower than the close pack ratio.

3.10 The fine tuning of the platelet sub-model

As mentioned earlier the calibration of the model was based on the result reported by Badimon et. al [163]. A tube shaped geometry was constructed, with dimensions 0.04m × 0.002m (length × diameter). A computational grid of 172,800 cells was constructed, with layers of denser grid near the walls. The reacting surface was defined as the part of the wall 0.025m stream-wise and 0.001 width, starting 0.01m downstream the entrance of the computational domain; this was similar to the dimensions of the de-endothelized stripes described in the reference experiments. Flow simulations were performed for three different flow rates shown in Table 3-9. The actual values of wall shear rate were close to the reported ones, (<2% difference). The inlet length was enough to allow the development of a velocity profile identical to that of the outlet proximal to the reacting area (Figure 3-11). The flow conditions for these three cases are also reported in Table 3-9. The bulk platelet distribution was set to 0.0042kg/kg, or $4.4 \cdot 10^8 pl/L$ according to the value reported in the experiment. Initially, only the flow field was solved as a steady state case and following that, the platelet deposition sub-model was applied as a transient simulation. Wall shear rate values that were calculated

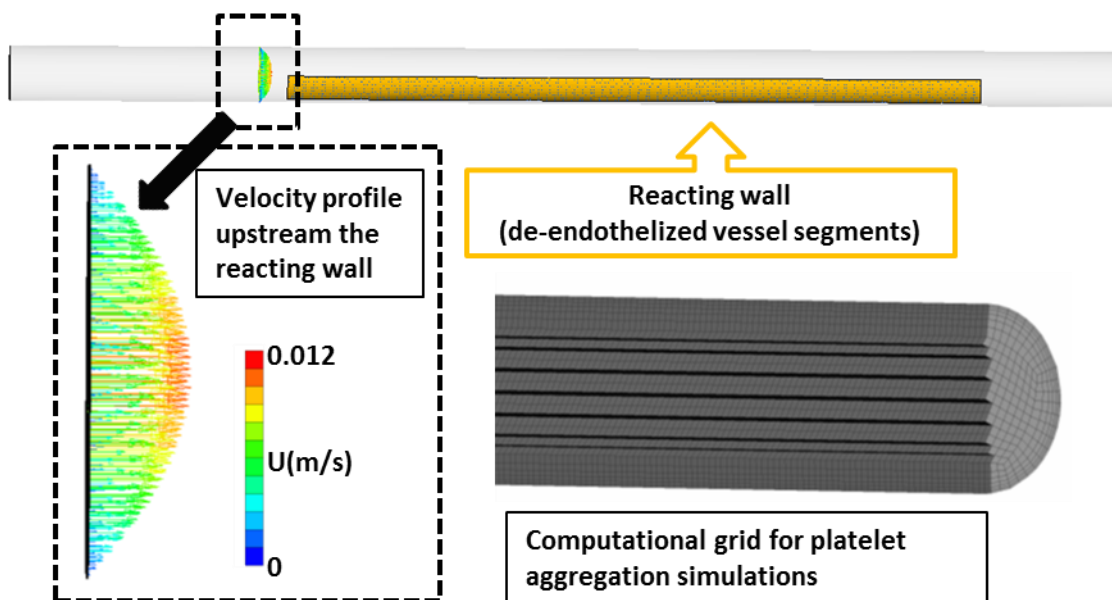


Figure 3-11: The geometry used for adjusting the platelet deposition sub-model and a cut of the computational grid showing the dense cells of the boundary layer. The contour of the velocity profile corresponds to the case PLA1; the other cases had identical velocity profiles but the values of the velocity magnitudes were scaled according to the flow rate at the inlet.

from the simulation results were very close (less than 1% variation) to the reported ones.

Table 3-9: Reported wall shear rate values and corresponding mass flow rate at inlet for platelet deposition cases.

Case	Shear rate(s^{-1})	Inlet mass flow (kg/s)
PLA1	106	$8.8247 \cdot 10^{-5}$
PLA2	212	$1.7649 \cdot 10^{-4}$
PLA3	1690	$1.4069 \cdot 10^{-3}$

The fine tuning of the model was mainly based on case PLA1 while the values of the constants used as a starting point for the fine tuning are shown in Table 3-10: Initial reaction rate constants for platelet deposition sub-model

Table 3-10: Initial reaction rate constants for platelet deposition sub-model

Process	Reaction rate constant
Platelets binding on surface	$k_{bi,surf}^{PLA} = 10^{-5} kg/m^2 \cdot s.$
Platelets binding on platelets	$k_{bi,PLA}^{PLA} = 0.28s^{-1}$
Platelets unbinding	$k_{diss}^{PLA} = 10.5(\frac{kg}{m^2} \cdot s)^{-1}$

As shown in Figure 3-12 this setup of the model performed very well against the experimental values for the case with minimum shear.

As the shear value affects the platelet binding rate [206], probably by changing the diffusivity of platelets and the frequency of collisions between the platelets and the reacting site, the constants of the model regarding the aggregation should be somehow increased to reproduce the experimental results of cases with higher shear rates. The constants were multiplied by a shear dependent factor $A_\gamma = (\frac{\gamma}{\gamma_0})^{1/3}$.

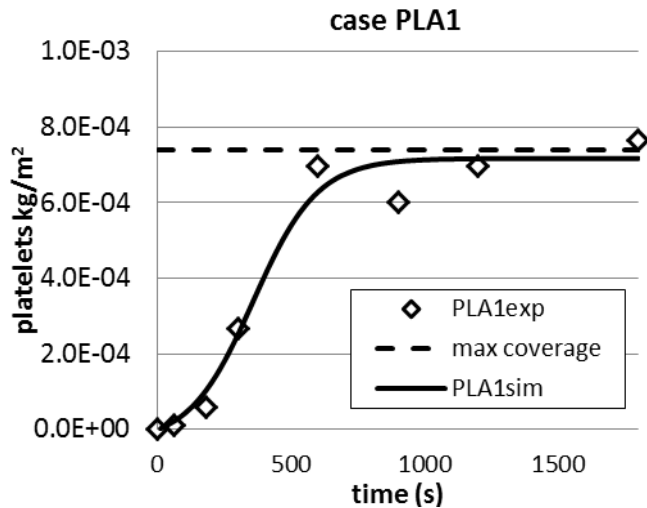


Figure 3-12: Platelet deposition on de-endothelized vessel segments. Computational results against experimental for the PLA1 case.

As shown in the related plots

Figure 3-13 this modification gives good results for $\gamma = 2\gamma_0$, (case PLA2) while the results for $\gamma = 16\gamma_0$ (case PLA3) show some deviation; in this case the model overestimates the maximum value of bound platelets, and it fails to predict the decrease of the quantity of bound platelets.

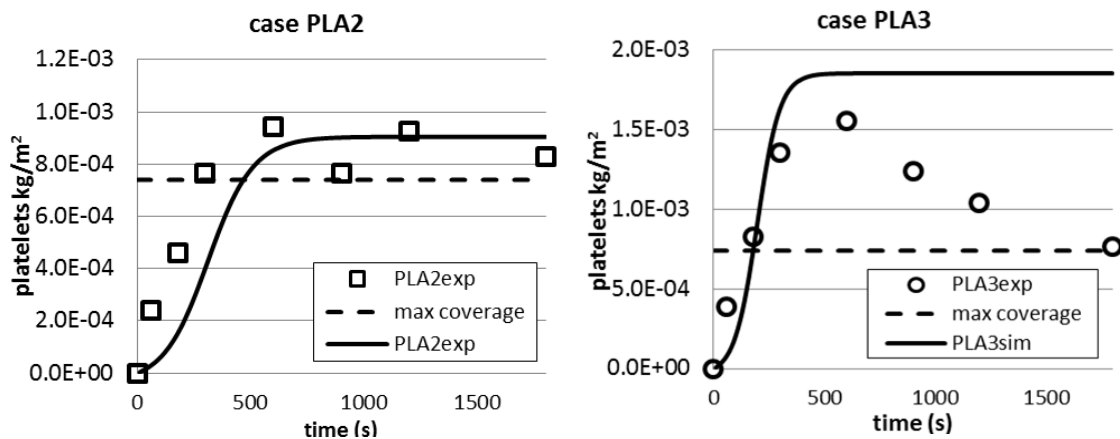


Figure 3-13: Platelet deposition for cases PLA2 and PLA3. The introduction of shear dependent platelet aggregation rate captures the aggregation rate, but the model fails to reproduce the reduction of the quantity of aggregated platelets. However this occurs approximately 600sec after initiation, while the maximum simulation time for the realistic models was 480s.

The first insufficiency of the model is probably due to the influence of shear on platelet unbinding process. Thus, it was reasonable to assume that increased shear rate (and subsequently shear stress) will cause more platelets to disaggregate. The experimental values in Figure 3-13 indicate that high shear stress could cause large amounts of aggregated platelets to dis-aggregate after some time, perhaps due to stress accumulation. Such a prediction, platelet disaggregation after reaching the maximum value (and without any alteration in the flow conditions or concentrations) is not in the capabilities of the model, as under steady-state flow conditions the final stage of the process is achieved at an equilibrium state, where aggregation and disaggregation balance each other. It has also been reported that the dominant mechanism for platelet aggregation on a surface is not the same for all the range of wall shear rate (and wall shear stress) values [207].

3.11 Introducing the coagulation activation index (CAI)

It has been reported [3] that the initiation of the coagulation process has a threshold behaviour with respect to the value of the wall shear rate and the size of the reacting surface. More specifically, for a given geometry and stream-wise length of the reacting surface, there seems to be a maximum value for the wall shear rate ($\dot{\gamma}$), while for a determined value of wall shear stress there is a minimum threshold size of the stream-wise length of the reacting area (L). This can be attributed to the lag-time of the thrombin generation that is shown in the TGA curve when the quantity of the triggering substance (usually TF) is below a threshold. In other words, it is possible that the substances that are involved in the initiation phase of coagulation are required to stay near the reacting surface for a minimum time interval in order to actually trigger the initiation. As the reactions occur due to the existence of substances on the surface (and not the whole mass of the flowing blood), these reactions must take place within a relatively small zone near the reacting boundary. For such a reaction zone with a given depth h , these two threshold quantities actually define a threshold for the actual residence time of chemical substances above the reacting zone:

$$t_{res} = \frac{L}{u} = \frac{2L}{\dot{\gamma}h}$$

Equation 3.33

Under the reasonable approximation that the reaction zone depth does not change, a

threshold value for the quantity $CAI = L/\gamma$ can be defined, describing the activation of the coagulation process. Actually, as diffusivity of platelets and other substances involved in the coagulation process is enhanced by the red blood cell motion, it will be increased for higher values of shear, possibly causing also a slight increase of the reaction zone depth. From the threshold values reported in the aforementioned study, the CAI threshold value was calculated $0.8 - 1 \cdot 10^{-5} m \cdot s$. Though it is highly unlikely that the threshold cases reported in the study to be able to represent the exact threshold conditions, the threshold value proposed is the minimum calculated ($0.8 \cdot 10^{-5} m \cdot s$) provided that the geometry and the reacting surface is well defined. On the other hand, in a realistic geometry it will be impossible to calculate the 'stream-wise length of the reacting surface' with accuracy. Probably the value of shear has variations, so the maximum seems like a better choice. It is interesting that the in the following simulations for the calibration of the coagulation model under flow conditions, the maximum thrombin concentration in cases with sub-threshold conditions was exactly proportional to CAI.

3.12 Coupling of the coagulation model with flow simulations

In order to test the coagulation model (especially the thrombin generation sub-model) under flow conditions and to obtain a justifiable value for the surface reaction rate constant of initiation ($k_{TF,surf}$), the experimental data concerning the threshold behaviour of the coagulation initiation with respect to the value of the wall shear rate and the stream-wise length of the reacting surface reported by Shen et al [3] were used. The geometries that correspond to the described experimental setups were reconstructed, the flow conditions were simulated via CFD and finally the coagulation model was applied.

Two different geometries used for the adjustment of $k_{TF,surf}$ were chosen from the ones described in the experiment of Shen et al [3] and they are shown in Figure 3-14; these will be referred to as SA and SB, respectively. The only geometrical difference between SA and SB is the length of the reacting wall (RWL). The reported wall shear rate and corresponding mass flow rate at the inlet are also different between the two geometries. The choice of the specific geometries was based on the values of CAI. The simulations should include mainly the two borderline cases: the case with minimum value of CAI where initiation of coagulation was observed and the case with maximum value of CAI where the initiation of coagulation did not occur. A computational grid (the same for

both geometries) with 227,200 cells with 10 layers of thin boundary cells was constructed. As CAI is lower for case SA, it can be expected that if the value of the $k_{TF,surf}$ is set high enough to initiate the coagulation in case SA, there would be also initiation of the coagulation process in case SB. As the model's behaviour was in accordance to that expectation, the calibration of $k_{TF,surf}$ was actually the task of finding the minimum value of the constant capable of initiating the coagulation in case SA. This was done via a trial-and-error process. The range of the values tested were of the same order of magnitude as the predicted value reported in the thrombin generation sub-model [142].

The initial idea for an initiation criterion was to check whether the average surface concentration of thrombin in a cross section of the tube near the exit, exceeded the threshold value of the thrombin sub-model. After performing the initial simulations though, it was found out that the model under flow conditions had a very clear threshold response. The surface average of thrombin concentration in three cross-sections downstream the reacting boundary was calculated. It was interesting to discover that for sub-threshold setup of the model the concentration decreased as we moved downstream, while for above threshold setup the concentration increased. Therefore this was set as a criterion to decide on which cases initiation of the coagulation process took place. The result of the process gave a value of $k_{TF,surf} = 1.785 \cdot 10^{-6} kg/m \cdot s^{-1}$; this is somehow lower than the value estimated earlier based on the cell size, but this was not a surprise, as this value was calculated using approximations from the constant of the bulk reaction, and was only used as a starting point; more importantly, there was no way to compare the TF concentration of the vesicles used in the experimental study for the surface activation to the bulk recombinant TF concentration.

Although a large number of test simulations were performed until this result was achieved, in **Error! Reference source not found.** only 5 characteristic cases are presented. Cases SA and SB were the original cases, shown in Figure 3-14. Case SB was simulated just to show that the chosen value for the constant, based on case SA was also capable to initiate the coagulation in case SB, as expected. In the third case, SA_LC (lower reaction rate constant) the value of the reaction rate constant was a little lower, $k_{TF,surf} = 1.775 \cdot 10^{-6} kg/m \cdot s^{-1}$. However this small change (less than 1%) was enough to prevent the initiation of coagulation. For application of the model in real geometries, a slightly higher value was used $k_{TF,surf} = 2 \cdot 10^{-6} kg/m \cdot s^{-1}$, as it seems very unlikely that the case SA is exactly the threshold case. The next cases, SA_HS (High

Shear) and SB_HS are presented to show that increased values of shear (that cause the CAI value to drop) prevent the initiation of coagulation.

Table 3-11: Test cases simulated in order to adjust the rate constant for the surface initiation reaction.

Case	WSR (s^{-1})	Q(kg/s)	RL (m)	$k_{TF,surf}$	CAI ($(10^{-5}m \times s)$)	initiation
SA	25	$2.37 \cdot 10^{-7}$	$2 \cdot 10^{-4}$	$1.785 \cdot 10^{-6}$	0.8	YES
SB	40	$3.79 \cdot 10^{-7}$	$4 \cdot 10^{-4}$	$1.785 \cdot 10^{-6}$	1	YES
SA_LC	25	$2.37 \cdot 10^{-7}$	$2 \cdot 10^{-4}$	$1.775 \cdot 10^{-6}$	0.8	NO
SA_HS	30	$3.03 \cdot 10^{-7}$	$2 \cdot 10^{-4}$	$1.785 \cdot 10^{-6}$	0.625	NO
SB_HS	60	$5.69 \cdot 10^{-7}$	$4 \cdot 10^{-4}$	$1.785 \cdot 10^{-6}$	0.667	NO

The simulations for determining the reaction rate constant for surface thrombin generation were performed without taking into account the platelet activation due to contact with the reacting surface. In the final formulation of the model, a simple source term for contact platelet activation was added, applying only to bound resting platelets.

$$S_{AP(b)}^{surf} = k_{AP}^{surf} \cdot [RP^{(b)}]$$

Equation 3.34

This term was added to the source term of bound activated platelets and subtracted from the source term of bound resting platelets. The reaction rate constant was estimated from the findings of Allen et al [198] for the time interval up to 50% platelet activation. The time interval reported for this process was about 7min, leading to an estimation of the reaction rate constant:

$$\frac{1}{2} \cong e^{-420 \cdot k_{AP}^{surf}} \rightarrow k_{AP}^{surf} \cong 1.6 \cdot 10^{-3} s^{-1} \quad \text{Equation 3.35}$$

This constant actually includes the activation of platelets due to all possible mechanisms, as thrombin, agonists released from other activated platelets and direct surface activation; it is obtained under the assumption that the rate of activation is constant, something that contradicts with the behaviour of the thrombin generation sub-model. On the other hand, the presence of aggregated platelets on the vessel surface will probably cause locally increased residence time and augmented concentration of

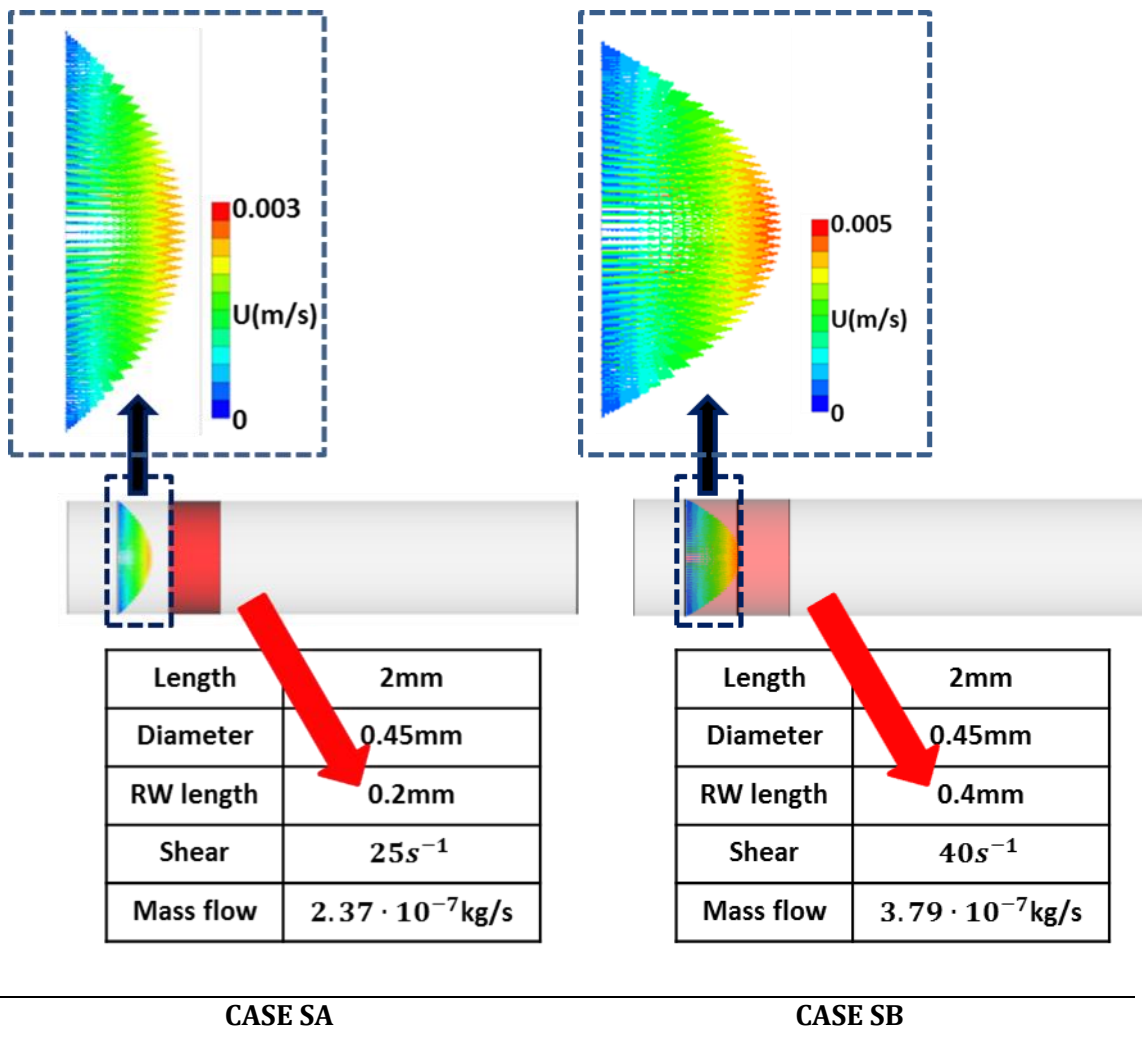


Figure 3-14: Geometric and flow characteristics for cases SA and SB. Note that in both cases the entrance length (upstream the reacting area) is sufficiently long for the development of velocity profile, which was identical with the velocity profile at the outlet.

substances, as they will induce a type of local surface roughness at sub-grid level.

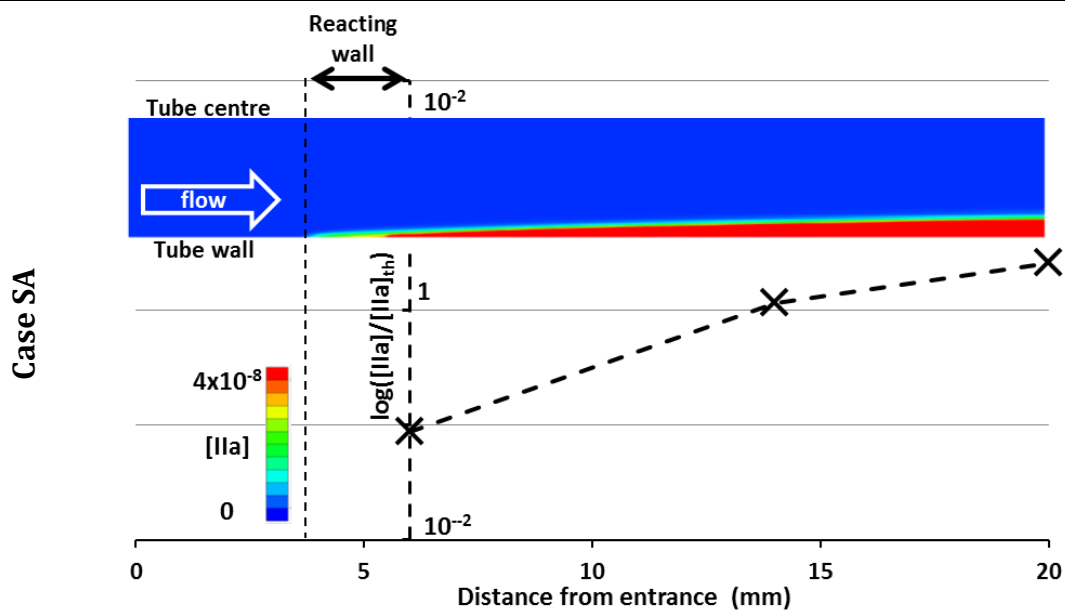
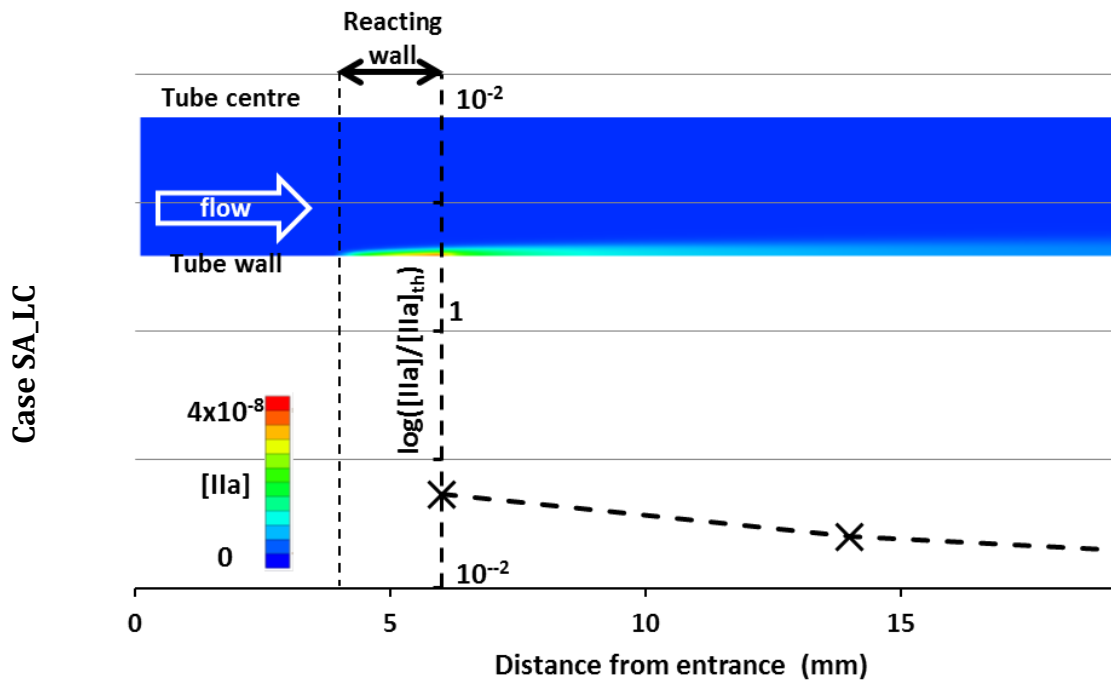


Figure 3-15: Comparison between the sub-threshold and the above-threshold cases. The X sign indicate the logarithm (base 10) of average thrombin concentration in the specific points, divided by the threshold thrombin concentration, while in the contours it is depicting the distribution of actual thrombin concentration in kg/kg. This distribution of thrombin concentration is after 300s of perfusion.

Therefore the value used in the final formulation of the model was a little bit augmented ($2 \times 10^{-3} \text{s}^{-1}$), but still has a significant role only in the coagulation pre-activation phase in

realistic models and flow conditions, when thrombin concentration levels are below the threshold value; at the same time, it is not causing significant changes in the simple test cases in tube geometries.

In the following figure we compare the concentration and distribution of thrombin concentration for cases SA and SA_LC; these two cases have identical geometrical and flow characteristics, with only differentiation being in the value of the surface thrombin generation rate constant, $k_{TF,surf}$. It is obvious that for the cases with sub-threshold setup, the inhibition process reduces the concentration of thrombin downstream the reacting surfaces, while for the above-threshold cases, the concentration of thrombin continues to increase downstream the reacting surface. Thrombin concentration increases in areas away from the wall due to diffusion. It is interesting that, while at the point right after the reacting boundary, the difference in the average thrombin concentration is not very high, the above-threshold case presents one order of magnitude higher values downstream.

3.13 Overview of the model

The final formulation of the model includes 6 different species as shown in Table 3-12. Prothrombin, thrombin and four different states for platelets.

Table 3-12: The species included in the final formulation of the model, initial concentrations and diffusion coefficients.

Name	Symbol (Units)	Initial concentration	Diffusivity ($kg/m \cdot s$)
Thrombin	[IIa] (kg/kg)	0	$3.52 \cdot 10^{-8}$
Prothrombin	[II] (kg/kg)	$9.509 \cdot 10^{-5}$	$4.41 \cdot 10^{-8}$
Circulating resting platelets	$[RP^{(f)}]$ (kg/kg)	0.004	$1.06 \cdot 10^{-8}$
Circulating activated platelets	$[AP^{(f)}]$ (kg/kg)	0	$1.06 \cdot 10^{-8}$
Bound resting platelets	$[RP^{(b)}] \left(\frac{kg}{m^2}\right)$	0	0 (surface bound)
Bound activated platelets	$[AP^{(b)}] \left(\frac{kg}{m^2}\right)$	0	0 (surface bound)

There are additional processes occurring in the area and consequently the computational cells that lay near the wall of the vessel and this results in different forms for the source terms. Therefore, for circulating species there one part of the source term represents the bulk reaction (Table 3-13). These terms are similar to the ones used in

the thrombin sub-model but they are presented again here because there are two important modifications: (i) the initiation term is not included, as it is presumed that TF is only present on the vessel wall and therefore the initiation takes place only at these sites; (ii) the added inhibition term is not included either, as the increased rate of inhibition is attributed to the APC and activated protein C is mainly found on the endothelium.

Table 3-13: Source terms for the species of the model for the bulk reactions (reactions occurring in flowing blood and not at the cells near the vessel wall).

$[IIa]$	$-k_{in,0}[IIa] + (k_{II}^{AP} \cdot [AP^{(f)}]) \cdot [II]$
$[II]$	$-(k_{II}^{AP} \cdot [AP^{(f)}]) \cdot [II]$
$[RP^{(f)}]$	$-(k_{AP}^{IIa} + k_{AP}^{AP} \cdot [AP^{(f)}]) \cdot [RP^{(f)}]$
$[AP^{(f)}]$	$+(k_{AP}^{IIa} + k_{AP}^{AP} \cdot [AP^{(f)}]) \cdot [RP^{(f)}]$

For the cells that included reacting boundary faces there are two additional species, resting and activated bound platelets and additional processes attributed both to the surface properties and to these species. Therefore there have been included extra terms that describe the binding and unbinding of both resting and activated platelets on the surface, the contribution of the reacting surface and activated bound platelets on thrombin activation and the activation of platelets due to contact with the reacting surface. For the resting and activated platelets source terms, part of the term in the first line ('Bind') refers to the binding and unbinding while the second line ('act') contains the part of the source term related to the activation of platelets. The parts of the source terms referring to the activation of platelets by thrombin are active only when thrombin concentration is above the threshold value in the specific cell. In other cases the corresponding reaction rate is zero. Finally, the additional term for inhibition that refers to the thrombomodulin-APC inhibition loop is also active when thrombin is above threshold as protein C is activated by thrombin. As thrombomodulin is expressed on

endothelial cells without requiring any special pathological conditions, this term (the increase of inhibition rate) is also applied to all the computational cells that are attached to the vessel wall, provided the concentration of thrombin is above the threshold. **The additional parts** of the source terms for the reacting boundary cells are presented in Table 3-14.

Table 3-14: Additional source terms for the model's species for the computational cells that include reacting boundaries.

[IIa]		$-k_{in,add}[IIa] + (k_{TF,surf} + k_{II}^{AP}[AP^{(b)}])[II]$
[II]		$-(k_{TF,surf} + k_{II}^{AP}[AP^{(b)}])[II]$
[RP^(f)]	bind	$-\left((k_{bi,surf}^{RP} \cdot A_f + k_{bi,RP}^{RP} \cdot [RP^{(b)}] + k_{bi,AP}^{RP} \cdot [AP^{(b)}]) \cdot [RP^{(f)}]\right)$
	act	$-k_{AP}^{AP} \cdot [AP^{(b)}] \cdot [RP^{(f)}]$
[AP^(f)]	bind	$-\left((k_{bi,surf}^{AP} \cdot A_f + k_{bi,RP}^{AP} \cdot [RP^{(b)}] + k_{bi,AP}^{AP} \cdot [AP^{(b)}]) \cdot [AP^{(f)}]\right)$
	act	$+k_{AP}^{AP} \cdot [AP^{(b)}] \cdot [RP^{(f)}]$
[RP^(b)]	bind	$+\left((k_{bi,surf}^{RP} \cdot A_f + k_{bi,RP}^{RP} \cdot [RP^{(b)}] + k_{bi,AP}^{RP} \cdot [AP^{(b)}]) \cdot [RP^{(f)}]\right) - k_{diss}^{RP}[RP^{(b)}]^2$
	act	$-k_{AP}^{IIa}[RP^{(b)}] - k_{AP}^{AP}([AP^{(b)}] + [AP^{(f)}]) \cdot [RP^{(f)}] - k_{AP}^{surf}[RP^{(b)}]$
[AP^(b)]	bind	$+\left((k_{bi,surf}^{AP} \cdot A_f + k_{bi,RP}^{AP} \cdot [RP^{(b)}] + k_{bi,AP}^{AP} \cdot [AP^{(b)}]) \cdot [RP^{(f)}]\right) - k_{diss}^{AP}[AP^{(b)}]^2$
	act	$+k_{AP}^{IIa}[RP^{(b)}] - k_{AP}^{AP} \cdot ([AP^{(b)}] + [AP^{(f)}]) \cdot [RP^{(f)}] + k_{AP}^{surf}[RP^{(b)}]$

The values used for all the constants used in the model are summarized in the Table 3-15. As there are no available data for the different behaviour of resting and activated platelets in respect to binding and unbinding, a standard ratio between the constants referring to resting and those referring to activated platelets was used and denoted as k_{diff} . For computational times up to 10 minutes, the addition of this term did not have any significant effects on the results of the model, as the activated platelets that were not bound on the vessel wall were washed down by flow.

Table 3-15: Values of all the reaction rate constants used in the model.

	Symbol	Order	Value	Process description
Thrombin generation	$k_{TF,surf}$	1	$2 \cdot 10^{-6} kg \cdot m^{-2} \cdot s^{-1}$	Thrombin generation on the reacting boundary surfaces
	k_{II}^{AP}	2	$0.5s^{-1}$	Thrombin generation by activated platelets
	$k_{in,0}$	1	$1.7 \cdot 10^{-2}s^{-1}$	Inhibition of thrombin in interior cells
	$k_{in,add}$	1	$3 \cdot 10^{-3}s^{-1}$	Enhanced inhibition of thrombin due to the presence of ATH III in boundary cells
Platelet activation	k_{AP}^{IIa}	1	$\begin{cases} 0 \text{ if } [IIa] < [IIa]_{thres} \\ 0.5 \text{ if } [IIa] > [IIa]_{thres} \end{cases}$	Platelet activation by thrombin
	k_{AP}^{AP}	2	$5 \cdot 10^{-2}s^{-1}$	Platelet activation by other activated platelets
	k_{AP}^{surf}	1	$1 \cdot 10^{-4}s^{-1}$	Platelets activated due to contact with reacting boundary surface
Binding of resting	$k_{bi,surf}^{RP}$	1	$1 \cdot 10^{-5}s^{-1}$	Binding of resting platelets on reacting surface
	$k_{bi,RP}^{RP}$	2	$0.28s^{-1}$	Binding of resting platelets on

				bound resting platelets
	$k_{bi,AP}^{RP}$	2	$0.28s^{-1}$	Binding of resting platelets on bound activated platelets
	k_{diss}^{AP}	2	$10.5s^{-1}$	Disaggregation of resting platelets
Binding of activated platelets	k_{diff}	0	1.0	Differentiation of the activated platelets in respect to binding
	$k_{bi,surf}^{AP}$	1	$k_{bi,surf}^{RP} \cdot k_{diff}$	Binding of activated platelets on reacting surface
	$k_{bi,RP}^{AP}$	2	$k_{bi,RP}^{RP} \cdot k_{diff}$	Binding of activated platelets on bound resting platelets
	$k_{bi,AP}^{AP}$	2	$k_{bi,AP}^{RP} \cdot k_{diff}^2$	Binding of activated platelets on bound activated platelets
	k_{diss}^{AP}	2	k_{diss}^{AP}/k_{diff}	Disaggregation of activated platelets

In the function of the model there were also two very important parameters, the maximum amount of platelets per surface and the thrombin concentration threshold for platelet activation, with the last one also signalling the transition of the coagulation process from the initiation to the propagation phase and giving a boost to thrombin generation rate. The amount of platelets for full coverage of the surface was $p_{surf,max} = 7 \cdot 10^{-4} \text{ kg/m}^2$ for all the simulations. The thrombin concentration threshold used in the thrombin generation sub-model was $[IIa]_{th} = 4 \cdot 10^{-8} \cdot \text{kg/kg}$ and the same value was used during the calibration of the model under flow when a fixed grid was used. But as explained before, in order to apply the model on geometries with different grid cell sizes a different approach was used as explained below.

3.14 Some details on simulations and programming

The initial testing of the model was performed in Microsoft Excel and Matlab for the zero-D cases. For the coupling of the model with simple flow fields a simple explicit code was developed that applied the model in very simple geometries with already dependent laminar flow field. For the coupling of the model with complex flow fields the commercial CFD software ANSYS FLUENT was used. The results of FLUENT with the results of the custom code for the simple cases were identical. All the species of the model were introduced in FLUENT as user defined scalars (UDSs). While FLUENT provides the option of species with reaction terms, this was not applicable in that case as in the case of the species setup FLUENT calculates the concentration of the last species based on mass conservation. This would lead to added complexity and a number of possible errors for two reasons. Firstly, the circulating species concentrations were expressed in mass per fluid mass (kg/kg), while the surface bound species were in mass per surface (kg/m²); unfortunately there is no way to use two different concentration units for the same species in FLUENT. So all the bound species should be measured in kg/kg and converted to the correct units kg/m² at the end of the calculations. However using this approach, the concentration of the surface bound species involved in the reaction rates would depend on the dimensions of each cell. Second, in the conversion of prothrombin to thrombin the resulting molecule has almost half the size of the original one, the molecular weights are 72kDa and 37kDa respectively, as during the activation a part of the prothrombin molecule is cut-off. Thus in order to achieve mass conservation in the system of the reactions an additional species would be required, only to represent the cut-off part of prothrombin.

According to FLUENT user manual (9.1.3), for each UDS named φ_i , FLUENT solves the convection diffusion equation with source terms, S_{φ_i} :

$$\frac{\partial \rho \varphi_i}{\partial t} + \nabla(\rho \varphi_i \vec{u}) - \Gamma_i \nabla^2 \varphi_i = S_{\varphi_i}$$

Equation 3.36

In all cases, the flow was initially solved (either as steady-state or time-dependent during the cardiac cycle) and the UDSs were applied afterwards. In the simple geometries, regarding the temporal discretization, all the terms of the reactions were treated implicitly; for example, the source term for thrombin for the t_n -th time step was:

$$S_{[IIa]}^{(tn)} = -k_{in,add}[IIa]^{(tn)} + (k_{TF,surf} + k_{II}^{AP}[AP^{(b)}]^{(tn)})[II]^{(tn)}$$

Equation 3.37

This approach gave correct results for the simple cases and made the model practically time-step independent (identical results for time-step values larger than 2.5 seconds or 3 heart-cycles). But when it was used in the cases of complex geometries, it resulted in numerical generation and diffusion of substances in small quantities (of the order of 10^{-25} or ten orders of magnitude smaller than the lower produced amount by the reactions), a fact that for a simulation of a long time period (more than 500 heart cycles) had an effect on the results. In order to avoid this, terms of the reactions were treated as explicit. With this approach the source term for thrombin was changed to:

$$S_{[IIa]}^{(tn)} = -k_{in,add}[IIa]^{(tn-1)} + (k_{TF,surf} + k_{II}^{AP}[AP^{(b)}]^{(tn-1)})[II]^{(tn-1)}$$

Equation 3.38

This approach gave identical results with the fully implicit approach for the simpler cases, when relatively small (but still large enough) time steps up to 0.5s were used. Additionally, the explicit formulation of the source terms eliminated the numerical generation and propagation of substances in the more complex geometries.

The surface reaction terms were actually programmed as surface fluxes and, as shown in Table 3-14 they were expressed as mass production per surface unit. So for the complete expression of a source term that included surface contribution, the surface-produced quantity of the substance had to be converted to match the units of the bulk production terms (kg/kg). So for the cells attached to the reacting boundary the source terms consisted of two parts the surface and the bulk reaction term:

$$S_{[X]}^{(tot)} = S_{[X]}^{(bulk)} + S_{[X]}^{(surf)} \cdot \frac{A_{rf}}{\rho V_c} = S_{[X]}^{(bulk)} + S_{[X]}^{(surf)} \cdot \frac{A_{rf}}{\rho A_{rf} \cdot h_c}$$

Equation 3.39

Here A_{rf} is the surface of the reacting boundary face, V_c and h_c the volume and the height of an approximately rectangular cell. It is obvious that it is impossible for the results to be completely mesh independent, as by increasing the height of the cells, the resulting concentration is inherently reduced. On the other hand, if for the surface

reaction terms is chosen another formulation that would express the products directly to bulk concentrations we would have the total amount of the produced (or consumed) substance depending on the grid. So using the first formulation there would be production of the correct amount of substance but the value of the concentration would be grid dependent while with the second formulation we would have correct bulk concentration values but the total amount of the produced substance would be time dependent. As the total amount of produced substances is generally considered more important than the local concentration values, the total amount of the species produced by surface reactions were calculated and the dependence on the cell dimensions was reduced with the use of refined mesh for the boundary layers. There was only one exception to that approach: the threshold value of thrombin concentration for the initiation of coagulation. In the calibration cases, the threshold value for bulk thrombin concentration was used was $4 \cdot 10^{-8} \text{ kg/kg}$. However, as the initial rate of thrombin mass generation is due to surface reactions, the sub-threshold concentration of thrombin in the cells near the reacting boundary, as explained earlier, depends very strongly on the height of the computational cells. For the total amount of thrombin produced, this discretization error is corrected by diffusion and the choice of sufficiently small time-step, as the gradient of thrombin concentration in the direction perpendicular to the wall is very high. The threshold value though requires more attention, as if for one time-step the thrombin amount exceeds this value, the source terms are different for the next time step. This could lead to serious error, as the transition of the coagulation process from the initiation to propagation phase which is an essential part of the model, would depend strongly on the grid. To prevent this, the threshold value for the computational cells that are attached to the wall was based on the amount of thrombin above the reacting surface. The boundary cells in the grid used for the calibration of the model under flow were purposely identical and had a cell volume $V_c = 7.09 \cdot 10^{-16} \text{ m}^3$. The surface of the reacting face was $S_f = 2.38 \cdot 10^{-10} \text{ m}^2$. So the 'surface threshold' of thrombin amount for platelet activation in the boundary cells used for the model in the realistic model simulations was:

$$[IIa]_{th}^{(s)} = [IIa]_{th} \frac{\rho V}{S} = 1.272 \cdot 10^{-10} \cdot \text{kg/m}^2$$

Equation 3.40

So after this modification, the triggering of the coagulation progress for the reacting boundary cells depended on the actual amount of thrombin above the reacting area. This

is equivalent to the physical assumption that the initiation reactions occur within a boundary layer of $3\mu\text{m}$.

Finally in the simulations where the model of coagulation was applied to realistic geometries, the value of the wall shear rate (required for the shear-dependent adhesion rate) was calculated using the simplified formula of dividing the magnitude of the velocity at the centre of the boundary computational cell by the distance between the centre of the cell and the 'centre' of the boundary face. In order to make sure that this method for the calculation of shear rate does not introduce significant error, we calculated the shear rate in one case in a more detailed way; we calculated the component of the velocity vector that was parallel to the boundary face and divided by the distance of the centre of the computational cell from the boundary face. As in all the geometrical models refined boundary layers were used for the grid, the two methods for the calculation of shear rate gave the same results and therefore the simpler and less time consuming method was used.

Chapter 4 Flow simulations

4.1 Introduction

In this chapter it is examined whether computational simulations of flow field can indicate differences between geometrical models of LAD that are already statistically assessed as of different risk for CAD complications. Initially, it is described how the models of LADs corresponding to healthy individuals and stenosed LAD arteries were obtained. The data on which these arterial tree reconstructions were based are reported, while a short description of the techniques used for the reconstruction and the creation of the computational mesh are also given. Following, the formulation of a method for obtaining boundary conditions for coronary and LAD arteries based on the geometrical characteristics is described. The quantities used to characterize the disturbance of the flow field due to the stenosis are defined and finally the results are presented and discussed.

4.2 Construction of the geometrical models

As mentioned earlier, the comparison of a number of X-ray coronary angiographies of patients showed that the possibility of acute coronary syndrome can be related to the location of the stenosis [1, 30]. Based on that clinical finding, a total of 16 LAD geometries were constructed. The first one is a model without stenosis and corresponds to a healthy individual while all other 15 geometrical models had different degrees and

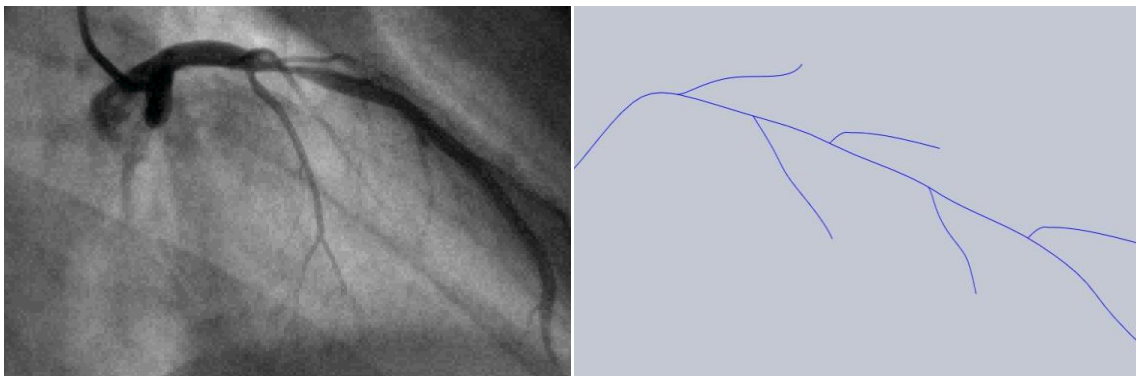
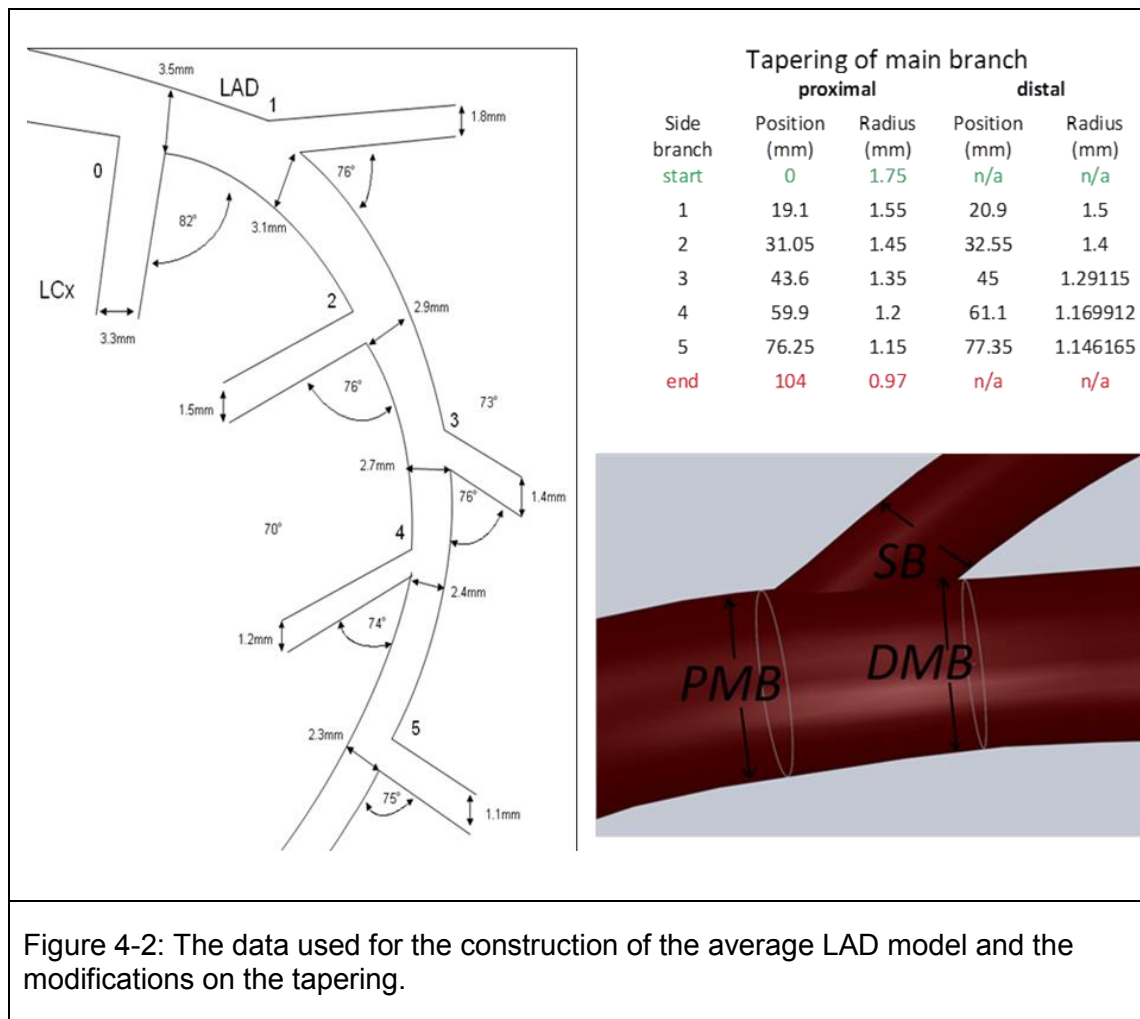


Figure 4-1: (left) Typical image from X-ray angiography and (right) the centrelines of the main branch and the side branches used for the averaged LAD model.

location of stenosis.

Initially the healthy model was developed, using the centrelines of the main branch and the major bifurcations and the diameter of the vessels at each point as these were extracted from X-ray angiograms of patients using the methods developed by Andriotis et al [105]. The three dimensional models for the main branch and the five side branches were constructed in Solidworks. These vessel shapes were used for the assembly of an ‘average’ LAD model. The information regarding the location of the bifurcations on the main branch and the angle between the main branch and the bifurcations were extracted from the statistical processing of the LAD geometries of 85 patients performed by Katritsis et al [1]. The models of the side branches were attached on the main branch and appropriately rotated in order to approximate the description of the average LAD (Figure 4-2).

Instead of using a constant value of about 0.024mm/mm for the tapering of the main branch that resulted from the proximal distal and intermediated values of diameter of

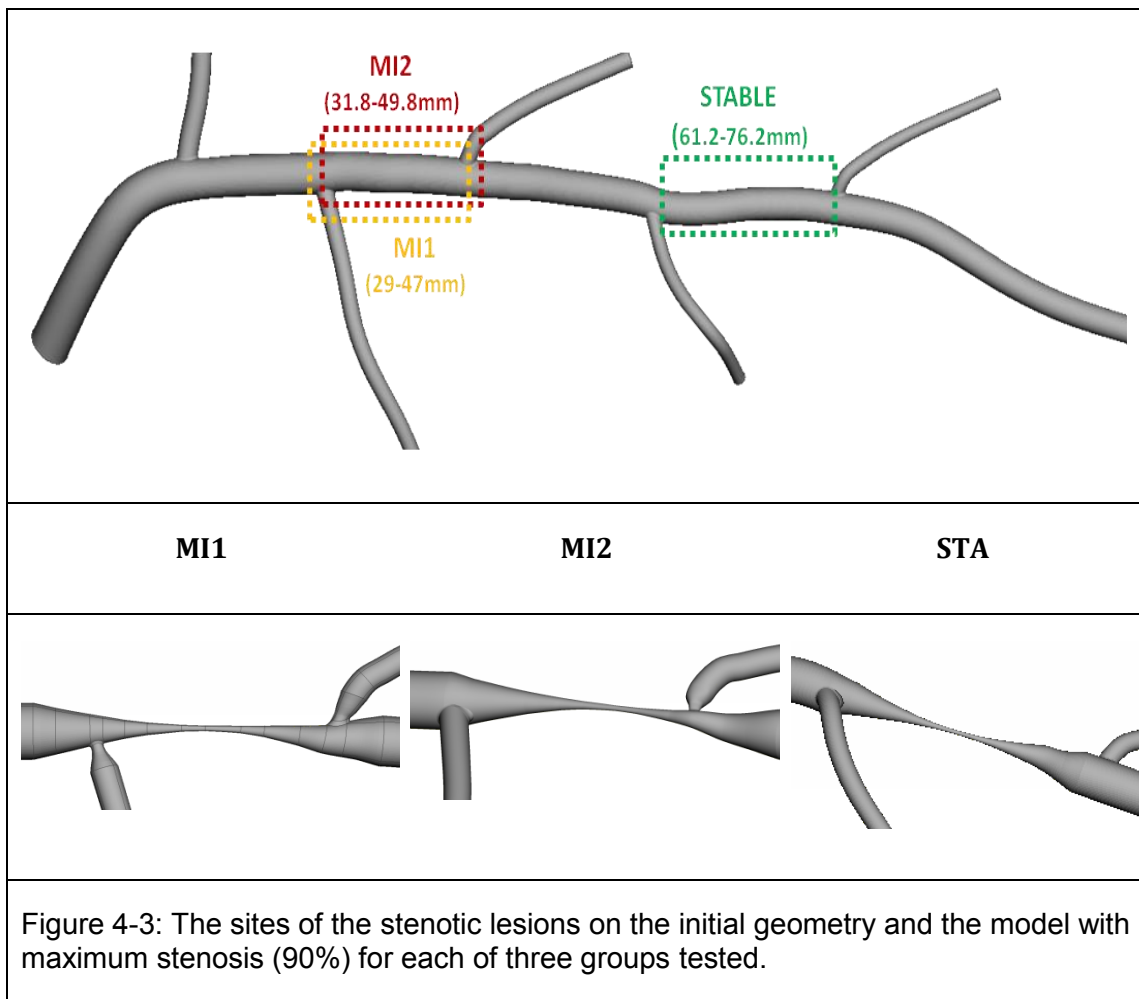


LAD (3.5mm-1mm/104mm), tapering was introduced only in the area of the bifurcations. For the calculation of the diameter of the main branch after a bifurcation Equation 4.1 was used [208, 209].

$$PMB = (DMB + SB) \times 0.678$$

Equation 4.1

Here PMB, DMB and SB are the diameters of the proximal main branch, the distal main branch and the side branch, respectively (see Figure 4-2). For the side branches, a constant tapering of 2mm/100mm was used. The resulting geometry had a total volume of $6.922 \cdot 10^{-7} m^3$ and the total wall surface was $0.0012 m^2$. Finally, a small fillet of radius 0.02mm, of the same order of magnitude with the X-ray pixel dimensions, was added at the point where each side branch meets the main branch.



The stenosed models were constructed by ‘adding’ stenotic lesions at the healthy LAD

model on specific points (Figure 4-3). The position of the stenotic lesion for each case and the total length are shown in Table 4-1. The centre of each stenotic lesion is also the point with the maximum degree of stenosis. Based on the location of the stenotic lesion the stenosed models were divided in 3 groups, MI1, MI2 and STABLE. Each group included geometries with the centre of the stenotic lesion on a specific location and different degrees of stenosis 20%, 35%, 50%, 70% and 90%.

Two of these groups are considered more likely to cause myocardial infarction (MI1 and MI2) while the third one is considered by far less dangerous (STABLE). More specifically, in MI1 and MI2 models at least one bifurcation was involved in the stenotic region. In MI1 the stenosis affected the second bifurcation of the model. The affected bifurcation was upstream the peak of the stenosis. In the MI2 models the stenosis mainly affected the third bifurcation, distal the peak of the stenosis, but there was a small change also at the second bifurcation, upstream the peak of the stenosis. In both of these groups the peak of the stenosis was located between the second and third bifurcation. In the models of the group STABLE, the stenotic region did not involve bifurcations and the peak of the stenosis was between the fourth and the fifth bifurcation. As seen in Table 4-1 the stenotic lesions in MI1 and MI2 groups were of greater length and the original diameter of the LAD in the stenotic lesion was greater than in the STABLE one.

Table 4-1: The exact locations, beginning, ending and centre of the stenotic lesion for each group of the simplified LAD models. The centre of the lesion is also the point of maximum stenosis. All dimensions are given in mm

group	MI1		MI2		stable	
	position	LAD diameter	position	LAD diameter	position	LAD diameter
beginning	29	1.47	31.8	1.45	61.2	1.12
center	38	1.38	40.8	1.375	68.7	1.1
end	47	1.29	49.8	1.27	76.2	1.12
length	18		18		15	

By modifying the normal LAD model, the geometry with the maximum degree of stenosis (90%) was constructed for each group. The degree of stenosis is defined based on the relation between the diameter of the stenosed vessel at the point of maximum stenosis and the diameter of the healthy vessel (Equation 4.2):

$$(\textit{stenosis degree}) = \frac{R_0 - R_{min}}{R_0} \times 100$$

The reduction of the radius along the centreline of the vessel follows a sinusoidal law, a method that has also been used in previous studies [210, 211]. As the minimum radius is at the centre of the stenotic lesion, the radius of the stenotic vessel at the distance x from the beginning of the vessel was calculated using Equation 4.3:

$$R_s(x) = R_0(x) \left(1 - \frac{(st)}{100} \cdot \sin \left(\frac{x - (c - a)}{2a} \cdot \pi \right) \right)$$

Here c is the centre and $2a$ the length of the stenotic lesion respectively, while R_0 and R_s are the radii of the healthy and the stenotic vessel, respectively. The position x of each

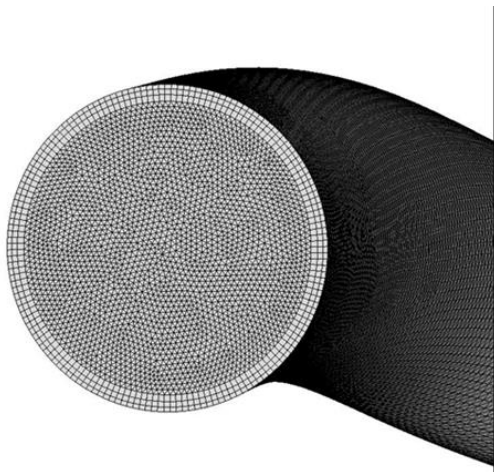


Figure 4-4: Boundary layers near the wall surface as seen at the inlet of the computational domain.

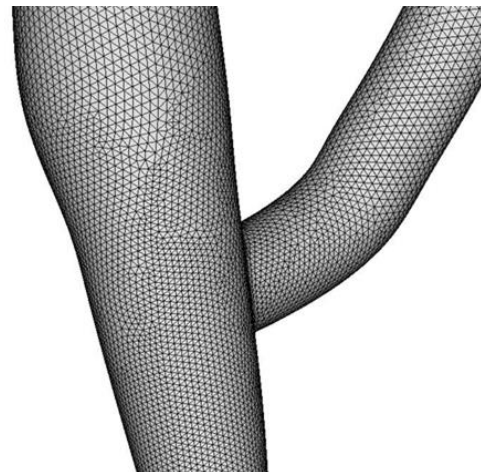


Figure 4-5: The denser grid at the areas of main interest (bifurcations and stenotic lesions) is shown

point of the main branch is defined using the length of the centreline from the inlet to the point. The final geometry was created by determining the value of the radius in some points of the centreline using Solidworks, while the exact formula used for the calculation of the radius did not have serious influence on the shape of the resulting geometry. In cases MI1 and MI2, the diameter of the second and third side branches from which they originate, are within the stenotic lesion; these, are lessened so that they can fit on the main branch. As a result of this, in these cases the second side branch is also

stenosed by approximately 20% (for MI1) and the third side branch is stenosed approximately 50% (for MI2).

A computational grid with denser boundary layers (Figure 4-4) of about 1.5 million hexahedral cells was initially created for the non-stenosed geometry. Preliminary mesh independence tests with number of cells varying from 600 thousand to 2 million indicated that for grids with more than 1 million cells the simulation results were almost identical regarding wall shear stress, pressure drop, velocity profiles and streamlines in indicative locations of the geometry. The grid was constructed using the Hexa-Block tool of ANSA. With the use of this specific tool, the geometry was split to 'boxes' that were accurately fitted on the geometry's surfaces and created the grid and the boundary layers for each box. Special attention was paid in order to have denser grid in the areas of higher interest, near the bifurcations and the fillets at the inlets of side branches as well as the main branch at the stenotic lesions (Figure 4-5).

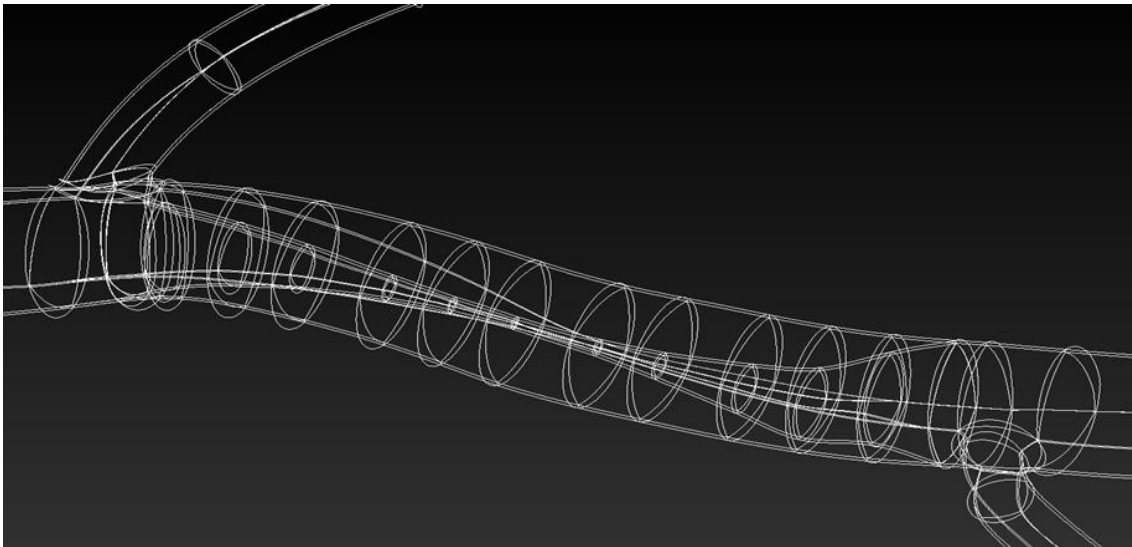


Figure 4-6: Curves for the model without stenosis and the model with maximum stenosis (90%). The grid points for the intermediate models were obtained directly (without constructing new mesh) by interpolating the coordinates of the two extreme states.

The topology of the grid boxes of the normal model was exported, along with their grid nodes. Following, three sets of curves were constructed (Figure 4-6), for the three models with 90% stenosis (one for each group). The curves defined both the boundary surfaces of each model and the boundary layer (Figure 4-6). The next step was to fit the hexa-boxes on the curves. For the parts of the geometry that not affected by the stenosis,

the hexa-boxes were obviously left as they were initially constructed. For the affected part, each edge of the hexa-boxes was fitted on the corresponding curve of the geometry. This process produced four identical computational grids with respect to the grid point number; one for the non stenosed model and three models with stenosis 90%, each one corresponding to the geometry with maximum degree of stenosis for each group. With the use of a script that was programmed within ANSA, it was possible to obtain directly the mesh for any intermediate geometry with stenosis between 0 and 90% by interpolating the grid point coordinates, without constructing the geometry for each model from the beginning. Giving as input a user defined parameter between 0 and 1, 0 for normal model and 1 for 90% stenosed model, the script obtained the coordinates of the mesh nodes for any intermediate geometry as a linear interpolation of the coordinates of the nodes of the normal (x_N) and the stenosed (x_S) vessel.

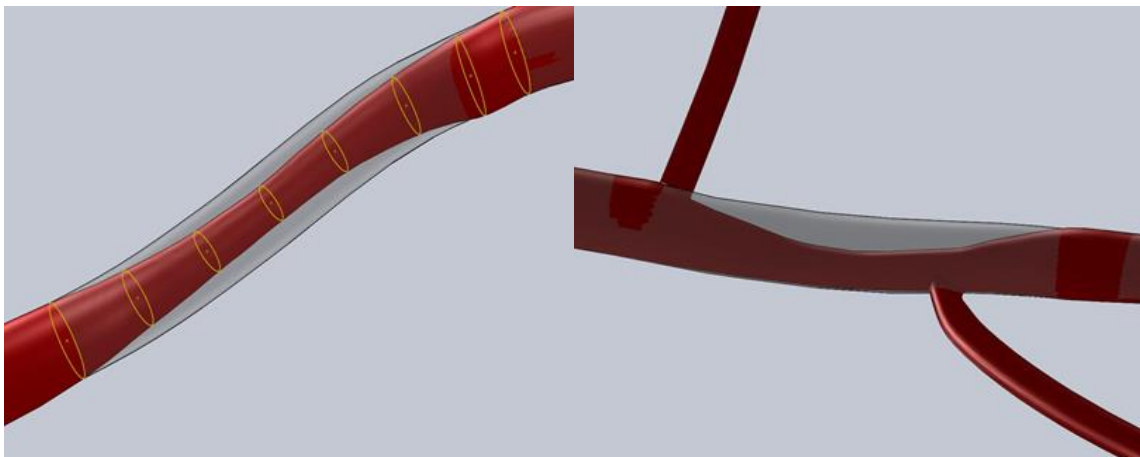


Figure 4-7: Symmetric stenosis (Case STABLE with 50% of stenosis)

Figure 4-8: Eccentric stenosis (Case MI2 with 50% stenosis)

For example for the geometry with 35% stenosis, the user defined parameter was $\lambda=0.3889$ and the coordinates x_A of a node of the geometry was given by the formula:

$$x_A = \lambda \cdot x_S + (1 - \lambda) \cdot x_N$$

Equation 4.4

However, a number of the intermediate geometries were also constructed in Solidworks independently, in order to place eccentric stenosis instead of symmetric (see Figure 4-7

and Figure 4-8). Finally all the models of the STABLE group had symmetric (to the centreline) stenosis, while the geometries of stenosis 20%-50% of the groups MI1 and MI2 were constructed in two versions, both with symmetric and eccentric stenotic lesions.

Here it must be noted that as the side branches are attached on the main branch based on averaged numbers (and not on the shape of a specific geometry) and the stenosis is artificially introduced onto the averaged LAD model, the resulting geometries might not correspond 100% to existing ones.

4.3 Governing Equations

Blood was modelled as a Newtonian fluid, using the incompressible Navier-Stokes equations (Equation 4.5); this was justified as for typical LAD dimensions the shear rate is well above the limit where blood exhibits shear-thinning behaviour for almost the whole of the cardiac cycle [58].

$$\rho \frac{\partial u}{\partial t} = -\nabla p + \mu \nabla^2 u + F,$$

$$\nabla u = 0$$

Equation 4.5

The viscosity was constant, $\mu = 3.5 \cdot 10^{-3} Pa$ [88, 212, 213] and density $\rho = 1.06 \cdot 10^3 kg/m^3$. The calculated Reynolds numbers were below 100 even when the maximum calculated velocity and the minimum diameter of the models with 90% stenosis were used. Therefore the flow was modelled as laminar and no turbulence model was used. In all simulations the vessel walls were considered rigid and stationary as it has been shown that at least for the flow rate and pressure distributions, wall deformability and movement have small influence [105, 112].

4.4 Boundary conditions

As already described, inflow and outflow boundary conditions for the coronary arteries exhibit some additional difficulties compared to other human vessels. While in literature

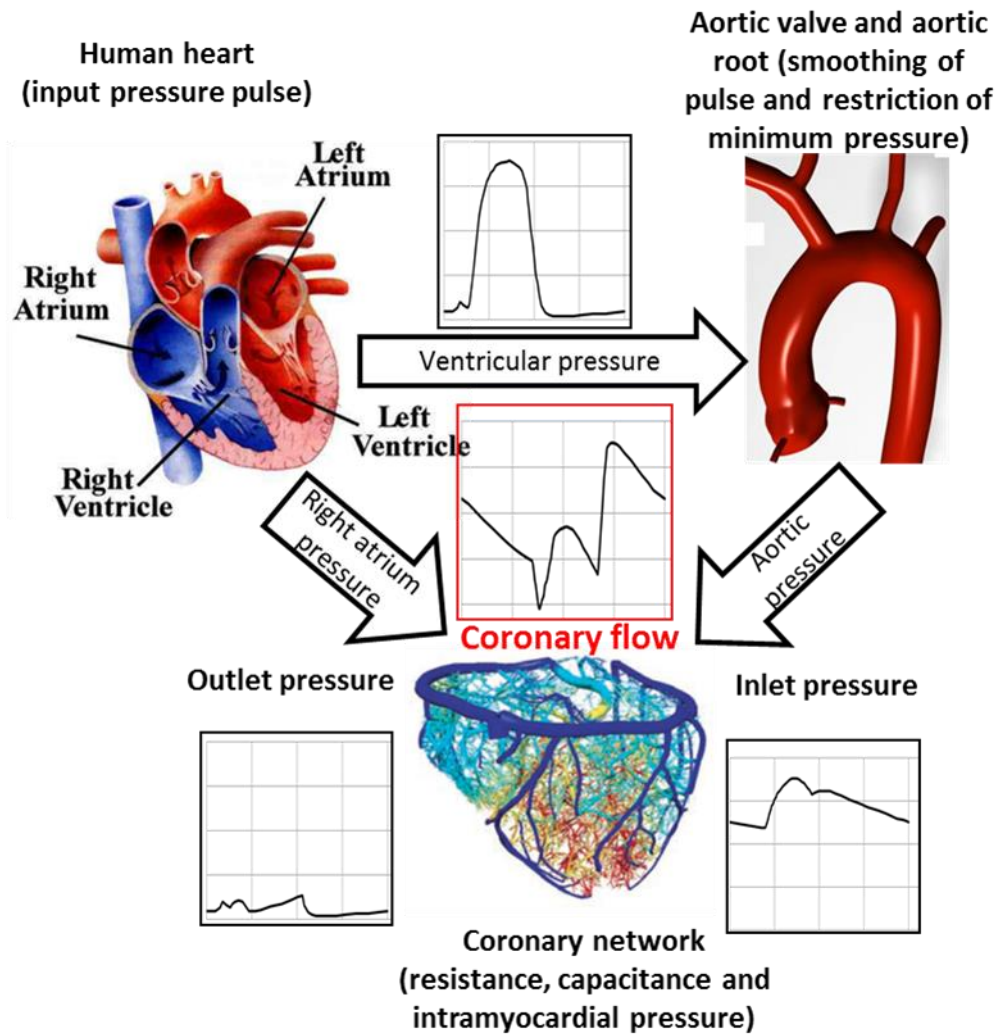


Figure 4-9: Factors determining the coronary flow. As it can be seen, the 'operating' pressure and the resulting flow rate are out of phase. The flow is mainly determined by the intramyocardial pressure, exerted on the coronary vessel network due to contraction. The vessels are coloured according to the intra-myocardial pressure [214] (blue is 0 red is 8kPa) at a random instance of the cardiac cycle.

there are available at least indicative waveforms for the aortic pressure, there is very little information for the pressure or the mass flow rate at intermediate points of the coronary vessel system. The difficulty lies in the fact that there is no obvious way to know with acceptable accuracy the pressure or the flow rate at the flow outlets of the part of the coronary network that is used as computational domain for these simulations. As the coronary vessel system is located on the myocardium, there is pressure due to the heart contractions (intramyocardial pressure), which is also not

uniformly distributed [214] on the vessel network; thus the final outlet pressure alone P_{RA} (atrial pressure) is not of much use. Mass flow rate and coronary ‘operating’ pressure defined as the difference $\Delta P = P_{aort} - P_{RA}$, between the aortic minus the atrial pressure are out of phase; the mass flow rate waveform is mainly determined by the behaviour of the coronary vessel system and the intramyocardial pressure (Figure 2-6 and Figure 4-9). The determination of the required for the simulations waveforms for the inlet and outlets of the computational domain is not straightforward and for the requirements of this Thesis it was achieved in two steps. The first step was the application of a method in order to obtain boundary conditions for the healthy vessel while the second step was to develop a method capable of providing boundary conditions for the stenosed vessels with an acceptable accuracy.

4.5 Inlet and outlet for the normal LAD model

The inlet and outlets for the physiological models were calculated with a simplified method that has already been used in previous studies [87, 213, 215]. For the left coronary inlet, the mass flow rate waveform available in the literature considered previously in other studies [90, 215, 216] has been utilised. For a healthy vessel it can be assumed that the value of wall shear stress is more or less constant, or to be more precise, it does not vary significantly in a small area, as the vessel walls are elastic and a sharp gradient of WSS would have as a result the change of the shape of the vessel up to the point where this gradient is somehow compensated. A typical value for the WSS in vessels is 1.5 Pa [34]. The distribution of the mass flow between the main branch and the side branches was determined under this assumption by employing the formulas that describe Poiseuille flow in a cylindrical tube of constant diameter (Equation 4.6). With the use of the equation that describes the WSS for a cylindrical tube, the wall shear stress is related to the mass flow rate in a branch, and this leads to a relationship between the mass flow and the radius of the two

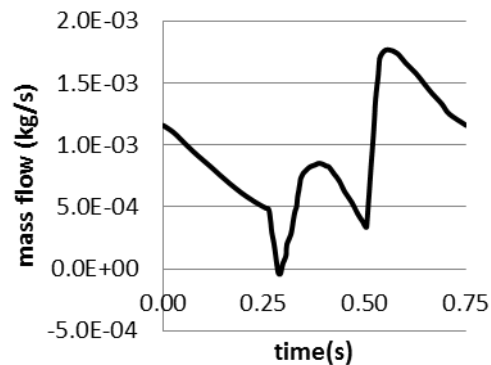


Figure 4-10: Mass flow rate inlet waveform for the healthy LAD model inlet. Waveforms for the six outlets are identically shaped but scaled according to the f_i fraction factors.

branches:

$$\tau_w = \frac{4\mu Q}{\pi r^3} \Rightarrow \dots \Rightarrow \frac{Q_{i,0}}{r_i^3} = \frac{Q_{m,i}}{r_{m,i}^3}$$

Equation 4.6

The last form of this equation has also been extracted from experiments of animal models [217]. Here $Q_{i,0}$ and Q_m represent the mass flow in the i-side branch and the main branch past the i-th bifurcation, while r_i and $r_{m,i}$ represent the radius of the i-th side

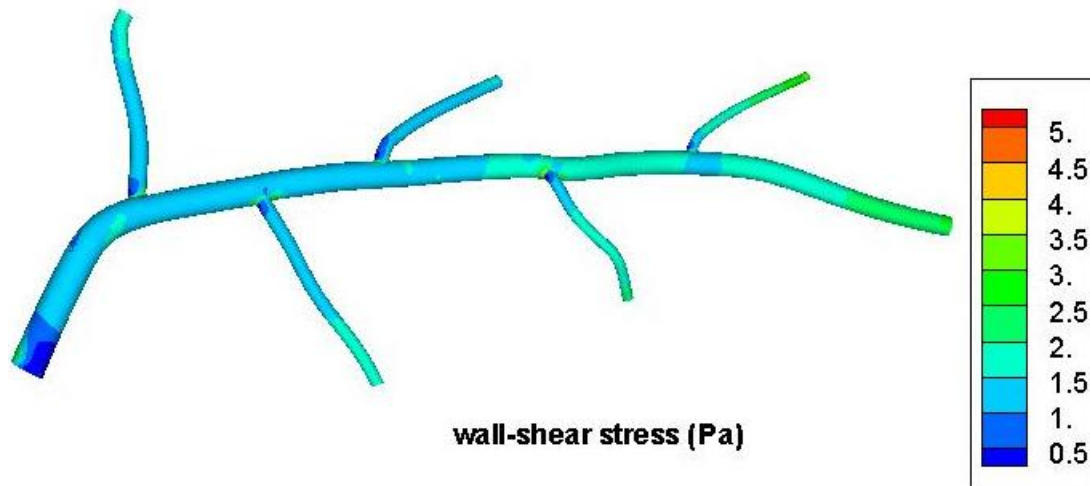


Figure 4-11: The distribution of the WSS on the walls of the healthy LAD model. For most part of the geometry, the WSS is between 1.5 and 2 Pa, confirming the assumption used for determining mass flow rates at the outlets.

branch at the bifurcation and the radius of the main branch after the i-th bifurcation. Using this formula and the diameters of LAD and Left Circumflexing Artery (LCX), the mass flow at the inlet of the non-stenosed geometry of the LAD was calculated as constant fraction (0.52935) of the total mass flow rate at the inlet of the coronary artery. The resulting curve for the inlet of the computational domain is shown in Figure 4-10.

The mass flow rate for each side branch was calculated using the same assumption, as a fraction of the total inflow. After calculating the mass fraction going into the first side branch, the same formula for the remaining mass flow of the main branch and the second side branch were used. Finally, the mass flow rate at the i-th outlet of the

geometry was a fixed fraction f_i of the mass flow rate at the inlet, with the factors f_i fully determined by the geometrical characteristics of the vessel:

$$Q_i = Q_{tot} \cdot f(r_1, \dots, r_i) = Q_{tot} \cdot f_i$$

Equation 4.7

The fraction of the total mass flow rate for each side branch (SB) and each part of the main branch of the non-stenosed LAD geometry along with the radii used for the calculation are shown in Table 4-2

The simulation of flow in the non-stenosed model actually showed small variation of WSS, with more than 99% of the vessel wall surface having TAWSS values 1-3Pa (Figure 4-11), within the reported non-pathological arterial range [34]

Table 4-2: Mass flow rate fraction for each side branch and the outlet of the main branch with respect to the mass flow rate at inlet

Branch	Branch diameter (mm)	LAD diameter (mm)		flow rate fraction	
		proximal	distal	main	outlet
main	3.5	3.5	n/a	1	n/a
SB 1	1.8	3.1	2.9	0.807	0.193
SB 2	1.5	2.9	2.8	0.699	0.108
SB 3	1.4	2.7	2.6	0.605	0.0945
SB 4	1.2	2.4	2.34	0.533	0.0719
SB 5	1.1	2.3	2.3	0.480	0.0526
outflow	n/a	n/a	n/a	n/a	0.480

A full validation of the flow distribution among the branches requires the knowledge of the structure or at least the overall behaviour of the vessel network that lies downstream the outflows of the computational domain and therefore it is very difficult to obtain. However an experimental setup where realistic pressure pulses are used as an input at the inlet while the outlets are connected to tubes with time varying resistance can be used to investigate the outcome of the method in in-vitro experiments. As the constant wall shear stress assumption is based on the deformability of the vessel the coronary or LAD geometry used should also have some elastic properties similar to the

vessels. By measuring the flow rates for different geometries it is possible to check how close the flow distribution described in Equation 4.7 is to the experimental results and probably add a correction due to the compliance of the elastic tubes.

4.6 Inlet and outlet for stenosed LAD models

In the case of a stenosed vessel, the mechanical properties of the unaffected vessel wall are different from the properties of the wall at the sites where the atheroma has developed. Probably the mechanical properties of the plaque itself would depend on its thickness and composition, so the assumption of constant or almost constant wall shear stress is no longer justified. Therefore, the previous method cannot be applied. On the other hand, there is no obvious reason to assume that the behaviour of the downstream vessel network will be seriously altered by the presence of the stenosis. The boundary conditions for the stenosed vessels were obtained under the assumption that both the cardiac output and the behaviour of the downstream vessel remain unaffected by the presence of the stenosis. As operating pressure for the coronary network the pressure drop between the aorta and the atrium (Figure 4-12) was used in most of the simulations. Some test simulations were also performed using only the aortic pressure as total pressure drop, while aortic pressure is actually the inlet pressure for the coronary network. The obtained resulting flow rates with the use of the two different pressure pulses, although not identical, had less than 1% difference. As aortic pressure is available on an individual-specific manner in the case a patient undergoes conventional coronary angiography the use of aortic pressure as operating pressure can lead to more consistent results. In a number of already published simulations of coronary flow, as well as for the calculation of the fractional flow reserve (FFR) for stenosed coronary vessels, the aortic pressure alone is also used as operating pressure [218], a simplification that introduces an average underestimation error of 8% of the operating pressure, with the maximum error being 18% (1.9kPa); this difference can be significant but probably of minor importance when compared to all other uncertainties involved in the problem. Additionally, as in our method the pressure drop is used to calculate the downstream resistance, this error is not transferred to the calculated flow rates for the stenosed vessels where the difference is much smaller (~1%).

The behaviour of the downstream network was described by a time dependent resistance (Figure 4-13). The value for this resistance is different at every instance of the cardiac pulse. It depends on the inlet (aortic) pressure and the flow rate of the healthy vessel and **expresses, at each time instance, the total influence of the downstream network vessel to the flow rate in a linear manner.** This means that at a

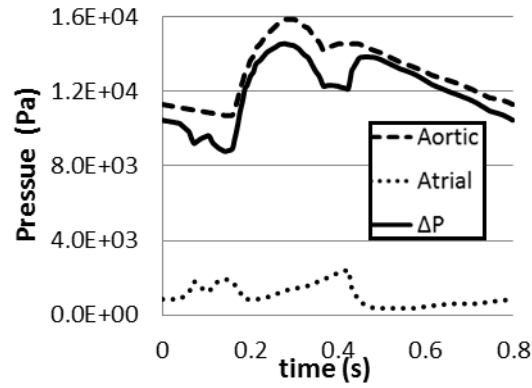


Figure 4-12: The pressure waveforms used as inlet and outlet pressure for the whole coronary network.

given instance of the cardiac cycle t_k , the pressure drop $\Delta P_i(t_k)$ between the i -th outlet and the right atrium and the corresponding mass flow at the specific outlet $Q_i(t_k)$ must fulfil Equation 4.8

$$\Delta P_i(t_k) = P_{out,i} - P_{RA} = R_i(t_k) \cdot Q_i(t_k)$$

Equation 4.8

In this equation, **the value of $R_i(t_k)$ is the same for all the models for the specific outlet and time instance (but not the same for all time instances).** In order to

calculate the transient values of the resistance $R_i(t_k)$ the results of the simulation of the non-stenosed coronary model were used. The value of the aforementioned variables (resistance of the downstream network for each outlet, mass flow rate and pressure at each outlet) and the total pressure drop at each moment must fulfil Equation 4.9. Using the outlet pressures obtained from the healthy model and the flow rate for each outlet, the time dependent outflow resistance for each outlet using as a total pressure drop the difference between aortic and right atrium pressure is calculated.

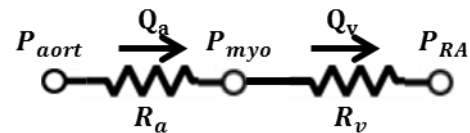


Figure 4-13: Simplified representation of the electrical circuit equivalent of the system considered for the extraction of the boundary conditions.

$$P_{out,i} + Q_{out,i} \cdot R_i = \Delta P_{tot}$$

Equation 4.9

Here it must be noted that the time dependent resistance term that is imposed to each outlet of the coronary geometry, simulates the behaviour of the whole system downstream the outlet, both vessels and arteries, up to the right atrium; the main in this approach is that the vessels and arteries of the system are considered to have constant volume. As shown in Figure 4-13, the electrical equivalent to system assumed in order to obtain the boundary conditions neglects the changes in the total blood volume that is in the vessels (capacitance of the vessels) and the inertia of blood. If we denote Q_a and Q_v the mass flow rate through the arteries and veins of the coronary vessel network, as there is no change in the total volume of blood, the flow rate must be the same for all the length of the one dimensional model, or $Q_a - Q_v = 0$. Then, the equations relating the resistance with the pressure drop and the flow rate become:

$$P_{aort} - Q_a R_a - P_{myo} = 0$$

$$P_{myo} - Q_v R_v - P_{RA} = 0$$

Equation 4.10

And as the flow rate is constant, the relationship between the pressure drop and the flow rate for a given time instance is indeed linear:

$$P_{aort} - P_{RA} = Q(R_a + R_v)$$

Equation 4.11

The main disadvantage of this method is that it is not able to reproduce the inversed coronary flow that occurs for a small time interval during the cardiac cycle, at the point of maximum pressure.

During the application of this method it was found that, at least for this size of geometries tested here that do not include small vessels, the downstream resistance could be estimated without using the outlet pressures from the non-stenosed geometry, as follows:

$$R_i = \frac{\Delta P_i}{Q_i} = \frac{\Delta P_{tot} - P_{out,i}}{Q_i} = \frac{\Delta P_{tot} - P_{out,i}}{Q_{tot} \cdot f_i} \approx \frac{\Delta P_{tot}}{Q_{tot} \cdot f_i} = \frac{R_{tot}}{f_i}$$

Equation 4.12

This approach obviously gives somehow greater values for the outflow resistances as it

does not take into account the pressure drop within the computational domain (during the estimation of the resistance from the healthy case); however the resulting outflows (and inflow) of the two methods have less than 2% difference, as the pressure drop between the inlet and the outlets of the computational domain is very small (>4% maximum difference) compared to the total pressure drop (see also Figure 2-4).

The described boundary conditions, together with the values of the outflow resistance estimated using the geometrical features of the geometry were also tested in the healthy LAD geometry, both for steady and transient flow conditions. The shapes of the resulting mass flow rate curves for the outlets were very similar to the ones calculated under the assumption of constant WSS. The actual values of the mass flow rate were slightly reduced. This was due to the over-estimation (of about 2%) of the downstream resistance described in previous paragraph. In the steady-state simulations, the fractions of the mass flow rate were the same for the two methods. In the transient simulations, the waveform for the inlet mass flow rate was identical for the two methods, but there were some differences in the waveforms of the outlets. The distribution of mass flow rate under the assumption of constant wall shear stress leads to identical shapes for the waveforms of all outlets, with the only difference being the scaling, as each outlet has a different ratio of the total inlet mass flow. The method using the estimated resistance resulted in slightly different curves, as the side branches that were closer to the inlet had sharper changes and some 'spikes'; on the contrary, the outlet of the main branch and the outlets of the last two side branches were smoother than the inlet. The same differences between the outlet waveforms were observed when the method was applied to the stenosed models. It should be noted that this small differentiation of the mass flow rate waveforms at the outlet is similar to the experimental results for mass flow distribution in coronary tree reported by Boutsianis et al [90] after performing flow measurements in human coronary arteries.

The advantage of this final simplification is that while introducing a minor error in the calculation of the resistance, it makes the method applicable to any arbitrary coronary geometry, without having to 'reconstruct' the corresponding healthy model and perform additional simulations. It is easy to notice that the difference between the two methods will be larger for geometrical models that include a bigger part of the coronary vessel network. For significantly larger geometries, it is possible to reduce this error up to a point. This error is introduced because the resistance from the inlet to the outlet is partially ignored because it is considered very small compared to the resistance

downstream from the outlet. The result of this simplification is that the inside resistance is finally added in the downstream resistance. This added resistance though in cases of larger geometries, can be estimated based on the diameters of the main and the side branches and the analogy between electrical circuits and flow, and subtract it from the calculated value in order to correct it.

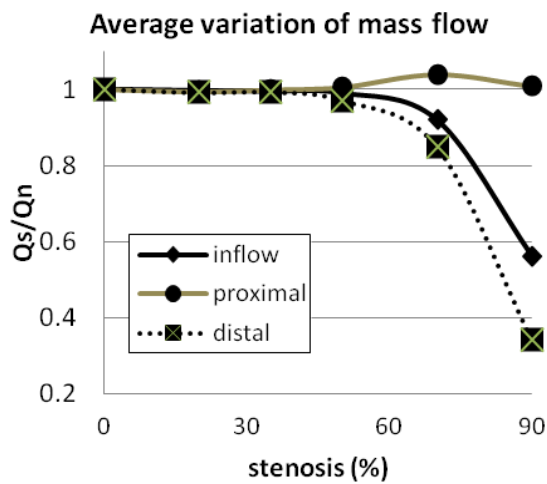


Figure 4-14: Normalized average mass flow for the inlet, the side branches distal and proximal to the peak of the stenosis. Results were similar for the three groups.

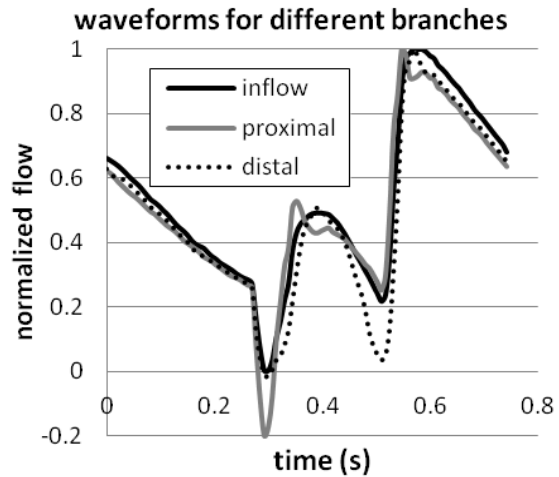


Figure 4-15: Normalized waveforms of mass flow for the inlet and the side branches distal and proximal to the stenosis. Side branches proximal to the stenosis exhibit sharper variations of flow rate.

All flow simulations were performed in FLUENT and the time-dependent-outflow-resistance boundary conditions were applied using User Defined Functions (UDFs). The resistance and the total pressure drop were given as input as function of time. During the solution and at every time step the mass flow rate at the outlets was modified in order to fulfil the mass-flow and pressure relationship; at the end of every iteration, the mass flow at the inlet was corrected to satisfy mass conservation. This process was repeated for every iteration until flow rates were stabilized and convergence was achieved.

The application of the previously described boundary conditions gave reasonable results for the flow rates in LAD main branch and side branches. The mass flow is reduced at the inlet and the side branches distal the peak of the stenosis. This effect is more intense for higher degrees of stenosis. For the side branches proximal to the stenosis, there is a small increase of the flow rate for small degree of stenosis while for severe stenosis (>70%) the flow rate is approximately the same as for the healthy LAD (Figure 4-14). Again, as in the healthy LAD model, the flow rate curve for the inlet is almost identically

shaped with the one of the non-stenotic LAD, but in these cases it is significantly scaled down for high degrees of stenosis. It is interesting that for low and intermediate degrees of stenosis (up to 50%) the total blood supply is practically not affected by the stenosis, as the difference is less than 2%, and there is only a small reduction of the blood flow after the stenosis up to 5% depending on the case. The flow rate waveforms for the side branches in the stenosed models are similar but with small differences as the proximal side branches and in general the side branches that are closer to the inlet have more sharp variations and higher values at inversed flow point (Figure 4-15) with these differences being more obvious than the ones observed in the healthy model. The flow-rate curves for the inlet and the outlets remained unchanged after simulating four cardiac cycles; the values from the last simulated cardiac cycle have been used for the specific plots.

4.7 Processing of simulations results

The results were processed using META post processor [219] and have included the time averaged wall shear stress vector and magnitude (defined as TAWSS (Equation 4.13) and TAWSS^(V) (Equation 4.14), respectively) the visualization of the flow field using streamlines and velocity profiles. In addition the oscillating shear index (OSI, Equation 4.15) and relative residence time (RRT, Equation 4.16) also introduced in previous works [97, 220], have been plotted:

$$TAWSS = \frac{1}{T} \int_0^T |\overline{WSS}| dt$$

Equation 4.13

$$TAWSS^{(V)} = \frac{1}{T} \left| \int_0^T \overline{WSS} dt \right|$$

Equation 4.14

$$OSI = 0.5 \times \left(1 - \frac{\left| \int_0^T \overline{WSS} dt \right|}{\int_0^T |\overline{WSS}| dt} \right)$$

Equation 4.15

$$RRT = [(1 - 2 \times OSI) \times TAWSS]^{-1}$$

Equation 4.16

The last two surface quantities, OSI and RRT defined in Equation 4.15 and Equation 4.16

respectively have the following interpretation. OSI takes dimensionless values from 0 to 0.5; it is an index of the variation of the direction of the velocity component parallel to the wall. OSI value equal to 0 denotes that the flow in that area is fully oriented in the direction of the average WSS vector for the whole time period, while OSI value equal to 0.5 means that in that area there is no dominant direction of the flow. So high OSI values are possibly, but not necessarily related with the walls around a recirculation zone. RRT (units Pa^{-1}) is an estimation of the residence time of the fluid components over the wall surface. As the actual residence time is not calculated, RRT can only be used as a means of comparison between two different cases. RRT is higher for larger values of OSI (so when the direction of the flow changes within one period) and when TAWSS (or the time averaged velocity magnitude) is small. So, increased values of RRT can be attributed either to great variation of the direction of the velocity vector, or to small velocity magnitude. Either way, **the result will be an increased residence time of the fluid in that area, especially in the case that OSI is low and RRT is high.**

In addition, in order to assess the thrombogenic potential of each model, the coagulation activation index (CAI) was calculated for each model. In order to calculate this quantity in the realistic models, as there is no 'stream-wise length of reacting area', CAI was approximated as \sqrt{S}/γ_{th} , where S is the area where average wall shear rate was below a certain value γ_{th} ; this was set as $\text{AWSS} < 0.15 \text{ Pa}$. Indicative threshold value for CAI used were $1.2 \times 10^{-5} \text{ m} \times \text{s}$, based on the results of the simulations for the normal model; the latter was approximately 10% higher than the value calculated for the normal case. It is interesting that this value is significantly closer to the one calculated from the experimental studies [3] in the previous chapter. In the case of realistic geometries a higher threshold value for CAI was used, based on two reasons. Firstly, the area with low WSS may be split in two or even more sites of the geometry. Secondly, the shape of this area is not rectangular; by elevating the threshold value the case of lower ratio of stream-wise length to surface was also represented. Note also that in these geometries there is no specific reacting surface, so the high values of CAI indicates just that there are areas in the model where, provided that the appropriate triggering or substrate exists, can occur initiation of coagulation. It is also important to note that the threshold value calculated in the previous chapter agrees with the values calculated for the different models with the use of a totally different method. This agreement of values indicates that perhaps the CAI can be used as a risk index.

4.8 Results

Besides the standard CFD plots which consist the usual detailed manner for the presentation of the results, quantities that can characterize each geometry with the use of one or a group of well-defined numbers have been also calculated. It seems that there are no generally accepted non-pathological values for the minimum and maximum TAWSS in coronary network. OSI and RRT indices are mainly used in computational studies the problem of non-pathological limits has not been addressed at all. Therefore the results of each model were compared mainly to the results of the non-stenosed model and the area of each model where the value of these quantities is well above the maximum value of the normal model have been plotted. This can be seen as an indication of the area most vulnerable to thrombus formation. Especially for TAWSS, as low values could increase the probability of causing the activation of blood coagulation, CAI was also used as an indication of the areas where flow conditions can allow the initiation of coagulation in flowing blood. It is interesting to note here that when the mathematical model for thrombin generation [142] was applied on the two cases extracted from the experimental work of Shen et al [3], the ratio of the calculated values of CAI for the two geometrical models (0.8) matched exactly the ratio of the maximum thrombin concentration (0.799) and was really close to the ratio of the average thrombin generation downstream the reacting area (0.759). This could indicate that CAI, a quantity that can be obtained via flow simulations and is directly related to flow conditions, although it does not take into account the shape or the exact location of the problematic surfaces, could be actually related to the thrombogenic potential of pathological flow. Obviously, in order for such a correlation to be fully established and ready to be used in clinical practice it is necessary to apply the method in a relatively large number of real patients' coronary geometries with known progress, to validate and possibly modify the range of non-pathological values of the quantities suggested here.

4.9 Velocity field

Regarding the velocity field, recirculation zones were observed distal the stenotic in all models with more than 20% stenosis, for some part of the cardiac pulse. The recirculation zones were not of the same size or duration for the models of all groups. In MI1 and MI2 these zones were longer in the stream-wise direction and lasted for a larger fraction of the cycle. Also, in the STABLE models, the recirculation zone was restricted to the main branch. On the contrary, in the models of the group MI1 mainly, but also in MI2,

part of the recirculating flow ended up in the side branch (magenta-coloured streamlines in Figure 4-16). In some cases a small recirculation zone in the side branch distal the stenosis is also observed.

The disturbed velocities in the areas downstream the stenosis for some parts of the cardiac pulse have also impact on the average velocity profiles. As shown in Figure 4-17, the average velocity is reduced near the wall vessel for the cases with stenosis of 35% and higher, only on one side of the vessel. The velocity profiles for the normal LAD model are almost symmetric to the centreline of the main branch. A slight asymmetry is expected and it is due to the curvature of the geometry and the presence of the bifurcations. In the presence of the stenosis this image is significantly altered, as the velocity profile is no longer symmetric with respect to the centreline.

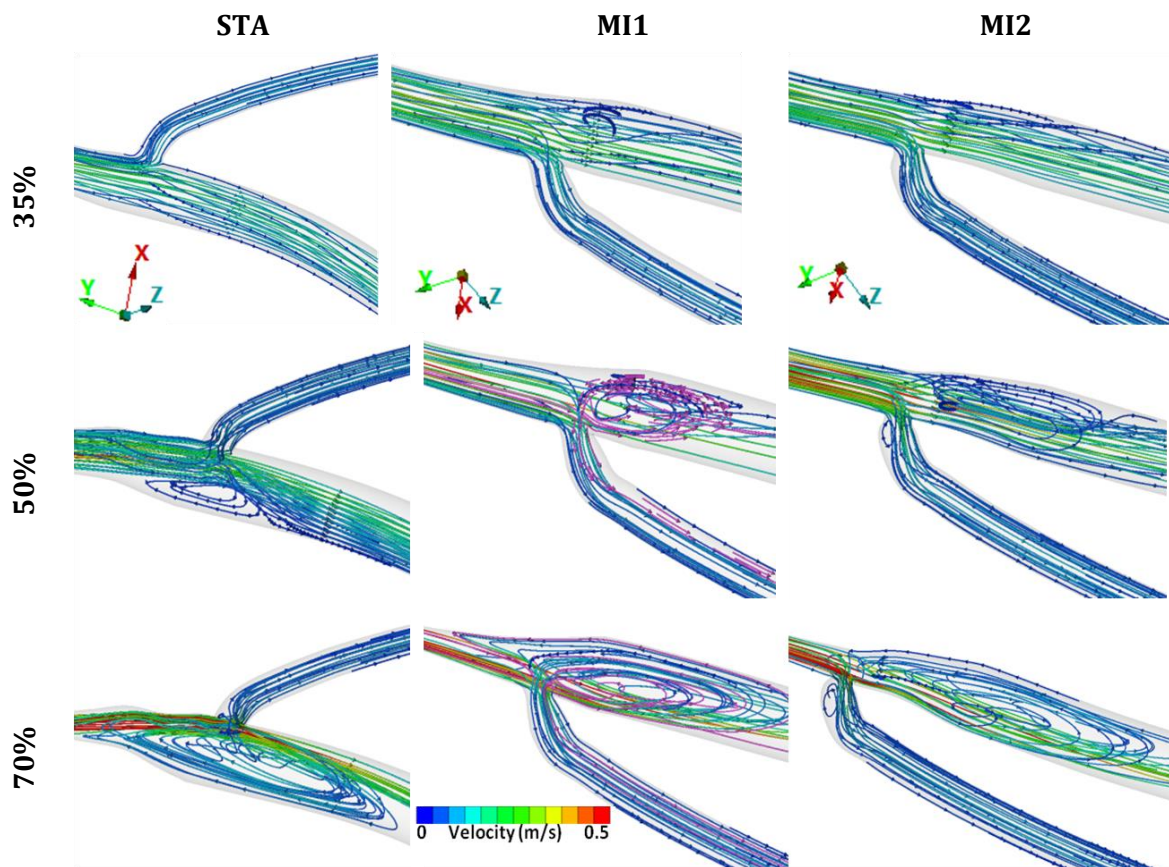


Figure 4-16: Recirculation zones downstream the stenotic lesion. Magenta-coloured streamlines indicate that part of the flow from the vortex area ends up in the side branch mainly in MI1 cases. Vortex stream-wise length is considerably larger for MI1 and MI2 models. All snapshots correspond to the same instance of the pulse.

The point with maximum velocity is moved towards one side of the vessel wall and the maximum of the velocity is significantly increased despite the reduction of the flow rate. Additionally, at the side of the vessel with the high velocities, there is an increase of the spatial gradient of the velocity in the direction of the flow. At the same time, at the opposite side of the vessel, the average velocities are reduced and the increase of the velocity in the direction from the wall to the centreline is diminished.

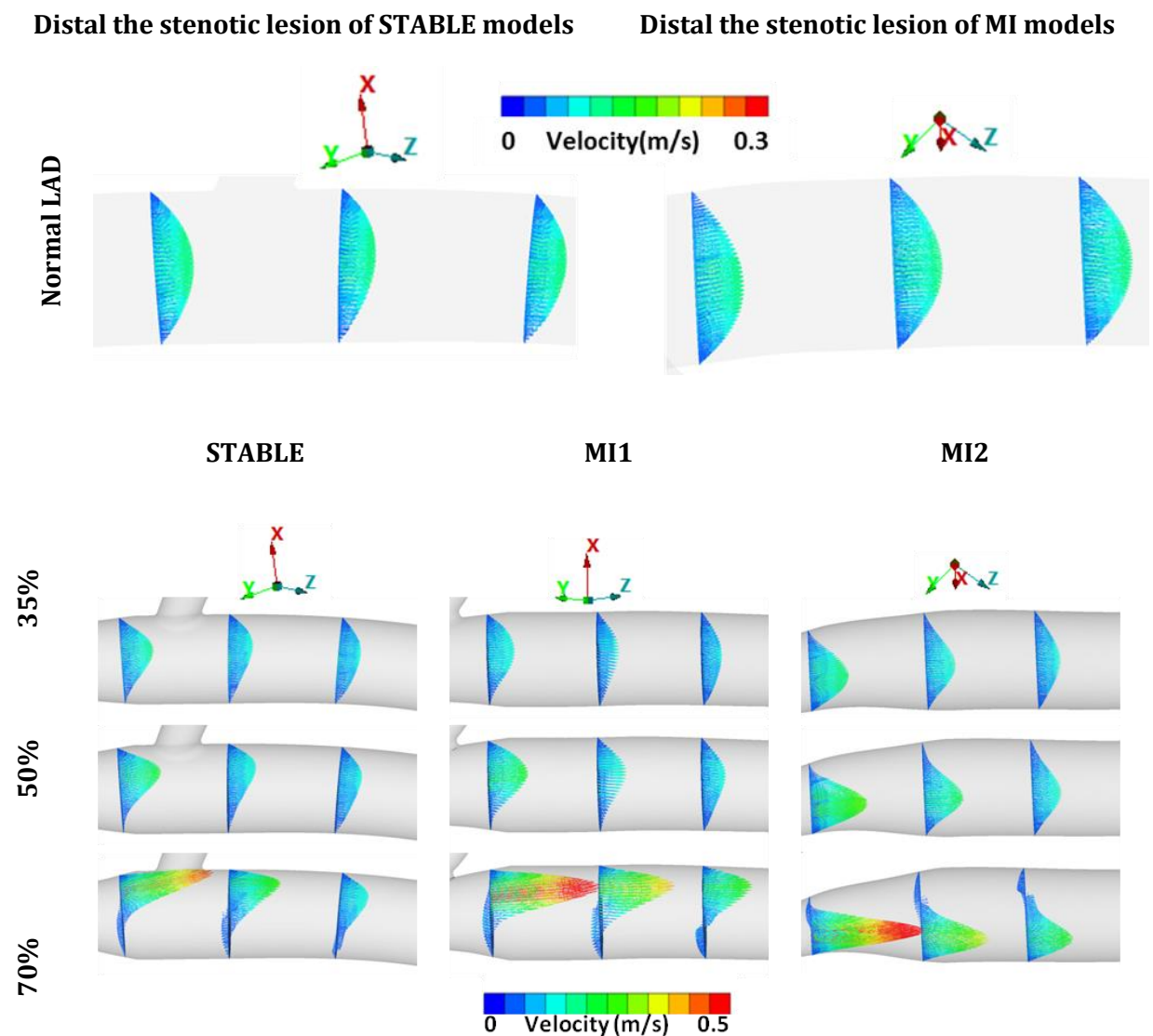


Figure 4-17: Time averaged velocity profiles downstream of the stenotic lesion. Note that a small difference in the location of the stenosis (<3mm, less than 20% of the total length of the whole lesion) as it is between MI1 and MI2, changes significantly the location of the areas with inversed average flow velocity.

This asymmetry might have two possible effects. At the side of the vessel with high velocities and sharp spatial velocity gradients, the values of shear stress might be sufficiently high to cause activation of platelets and the coagulation process in general, as shear gradients are thought of being capable to initiate the coagulation process [49] independently of biochemical triggering. At the other side of the vessel, the small averaged velocities result to a prolonged residence times in this zone for any substances produced upstream in the stenotic lesion or at the side of the vessel with the high velocities, transported by the recirculation vortex. The effect of the stenosis to the downstream average velocity profile is more intense as we move to higher degrees of stenosis and at 70% stenosis for a part of the cross section of the vessel the time averaged velocity is opposite to the main direction of flow.

4.10 TAWSS

In the normal model there is a small variation of WSS due to the curvature of the geometry and possible imperfections of the model. The values are between 0.13 and 2.9 Pa, but for the most part of the vessel wall (>99%) is between 0.5 and 2 Pa (Figure 4-11). The existence of stenosis had significant effect on the WSS distribution on the vessel walls (Figure 4-18). The stenotic lesion was characterized (as expected) by elevated values of wall shear stress that increase the surface average of TAWSS even for the cases with only 20% stenosis. This is more intense for all groups as we move to models with higher degrees of stenosis, with the TAWSS being higher than 3 Pa for the total of the stenotic lesion, while especially for the MI1 and MI2 cases there are zones of high TAWSS also distal the stenotic lesion. In the MI1 case there is also an area with high WSS at the entrance of the two side branches proximal and distal the stenosis and in MI2 case there is such an area only at the entrance of the side branch distal the peak of the stenosis, while in the STABLE models the WSS at the bifurcation is not significantly higher than the WSS in the normal case.

As blood was simulated as a Newtonian fluid, WSS is proportional to wall shear rate. Thus, high and low values of TAWSS correspond directly to low and high values of time averaged wall shear rate. As already mentioned, low WSS is associated with the progression of the CAD and the growth of atheroma and coagulation is more likely to be initiated in areas with low wall shear rates. It is also possible that the initial products of coagulation and the activated platelets, existing as a result of high and sharply changing TAWSS in the stenotic lesion, will have a relatively high residence time in those areas, as

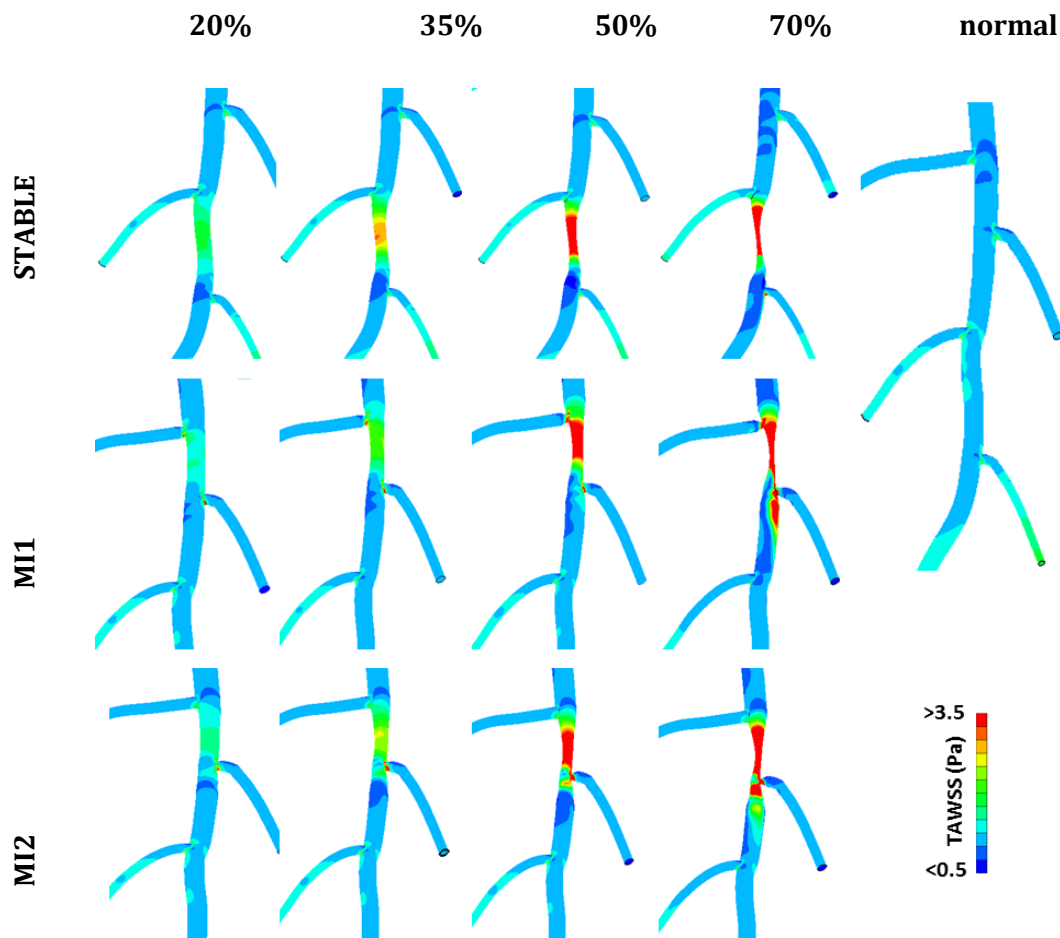


Figure 4-18: Distribution of time averaged wall shear stress for all geometry groups. Note that for groups MI1 and MI2 there are areas with high TAWSS after the stenotic lesion.

the lower values of wall shear indicate also smaller velocities near the wall. So, for all models, the area that seems of high risk (according to the TAWSS distribution) in terms of thrombus formation and progression of the disease is mainly the area distal the stenotic lesion. But as both areas of low and high TAWSS are larger in the MI1 and MI2 geometries, and in these models the same flow pattern (from high to low TAWSS) is repeated in a smaller scale in the side branches involved in the stenosis, it could be claimed that for MI1 and MI2 models there is increased risk for deterioration and complications are higher.

As wall shear rate values in the stenotic area are extremely high compared to the threshold values reported in by Shen et al [3], the results also show that in order to have initiation of the process inside the stenotic lesion, this can only happen due to surface reactions and surface bound substances and bound platelets, as any initial products of

the coagulation process generated in flowing blood will be rapidly transferred downstream due to the high velocities above the vessel wall. At the same time, while values of TAWSS sufficiently high (>30 Pa) to be considered capable of causing platelet activation at a very short exposure time [221] were observed only in the cases of severe stenosis 70%, in all cases with stenosis higher than 35% there were areas with shear stress above 3.5-4 Pa, which can be considered capable of increasing platelet activation rate [134].

Table 4-3: Average values of TAWSS for the whole geometry and surface of the geometry with $TAWSS > 3$ and $TAWSS < 0.15$ (area in mm^2). Coloured figures indicate that the specific value is more than 25% (orange) or more than 50% (red) than the lowest (green) value among the models with same degree of stenosis

		TAWSS								
		surface average			area with $TAWSS > 3Pa$			area with $TAWSS < 0.15Pa$		
group stenosis		STA	MI1	MI2	STA	MI1	MI2	STA	MI1	MI2
	0		0.697			0.000			0.222	
0.2		0.719	0.727	0.728	0.00	0.07	6.75	0.000	0.092	0.656
0.35		0.750	0.747	0.765	0.00	0.49	0.88	0.139	2.010	1.072
0.5		0.795	0.822	0.824	25.08	31.25	32.08	0.204	0.650	1.289
0.7		0.994	1.113	1.012	25.53	36.73	36.01	0.442	0.044	0.364

As shown in Table 4-3 and Table 4-4, the surface averaged values of the calculated quantities (TAWSS, OSI and RRT) for the whole wall surface of the models had small variations among the cases with different location or degree of stenosis, except from the OSI average value that was significantly higher for MI1 and MI2 geometries with stenosis more than 50%. Therefore, in order to examine whether there is a difference between the different groups that can be described by a set of numbers we calculated the area where each quantity (TAWSS, OSI and RRT) was above or below a selected value for each model. As mentioned earlier OSI and RRT have not been widely used so the only way to assess the resulting values is by comparing them with the results of the normal geometry. For TAWSS and wall shear stress in general, more literature data is available and it was co-estimated with the results of the healthy geometry, Special attention was paid to the plot in Gibson et al. [45] that correlates the WSS with the reduction of vessel radius, the results of Asakura et al [25], where WSS was measured experimentally in left and right coronary arterial trees obtained post-mortem where the minimum value reported was 0.12Pa. Here it must be noted again that although the correlation between

wall shear stress and deterioration of CAD and even thrombogenicity are considered established, it was not able to find specific threshold values or a generally accepted range of non-pathological values. However, the WSS values that were calculated in the non-stenosed model were in agreement with the values that were experimentally observed in previous studies [25, 45]. So, the results of the healthy LAD model that were used as a reference point for assessing the geometrical models based on the TAWSS distribution were in any case very similar to the previously published experimental data. Generally, the values in Table 1 and Table 2 indicate that there is a distinct difference between the models of different groups with the same degree of stenosis, but the only index that is of the same order of magnitude and therefore can be used for an overall comparison quantity is the area with low ($<0.15\text{Pa}$) TAWSS.

The area averaged TAWSS for the whole vessel wall was 0.7-1.1Pa for all the models, within the range reported for in vivo measurements [222]. For the healthy geometry TAWSS was below 2 Pa except for some small areas (less than 0.5% of total area) of the side branches right after the bifurcation where TAWSS was between 2 and 2.9. This could also be attributed to differences in details between the 'averaged' reconstructed model and a real LAD geometry at the specific points, as the averaging of the geometric parameters does not ensure that the final model will be 100% anatomically correct. The distribution of surface averaged TAWSS for cases with stenosis higher than 50% exhibited small differences between the three groups as in all cases there was a big area of high TAWSS ($> 3\text{Pa}$) in the stenotic region that caused an increase on the average TAWSS value. The surface average TAWSS for the whole geometry was more or less the same for the models of all three groups with the same degree of stenosis, (variation $<2\%$), while the surfaces with high ($> 3\text{Pa}$) and low (<0.15) values were significantly larger ($>50\%$) for the MI1 and MI2 groups. The results for the cases with small degree of stenosis though were more interesting, as only in cases MI1 and MI2 were observed areas with low AWSS ($<0.15\text{ Pa}$) and areas with high TAWSS ($>3\text{ Pa}$). Flow from areas with high shear stress, where platelet activation is more likely to occur, towards areas with low shear stress (Figure 4-18), where substances secreted by activated platelets, will have higher residence times and possibly boost the coagulation process.

4.11 OSI and RRT

OSI and RRT values are expressing similar things as they are both quantities related to low average wall shear stress values, either due to small magnitude or high variation of the direction of WSS vector. Therefore, the contour plots for these two quantities were almost identical. OSI (Figure 4-19) had

significant variation only in specific areas of the geometry, downstream the stenotic lesion and after the first bifurcation (Figure 4-19) at the area of the recirculation zones shown in Figure 4-16. For models with stenosis 20% and for MI2 and STABLE with 35% of stenosis the values of OSI was low for the whole of the vessel wall indicating the absence of recirculation zones, while there was a small area with

elevated values in MI1 model with 35% stenosis, in the recirculation zone near the bifurcation (Figure 4-16). In cases

with 50% stenosis there is an area with elevated values right after the stenotic lesion while for the rest of the geometry the value is zero, meaning that for the rest of the geometry flow is fully oriented. The models with 70% stenosis had different distribution in the area where variation on the direction of the flow was larger (as the recirculation vortices are larger and occupy larger part of the cycle). As shown in Figure 4-19, the areas with high OSI were larger for MI1 and MI2 models (the images are in the same scale) and they are more or less next to the recirculation zones shown in Figure 4-16.

For the RRT distribution again the results of the non-stenosed geometrical model were used as a reference point. The MI geometrical groups had elevated values of RRT starting from the geometries with 35% stenosis. Large areas with elevated RRT values were observed both in MI1 and MI2 models after the bifurcation. In MI2 model was also observed a zone with high RRT after the root of the side branch. The fact that OSI has values near zero in these areas implies that the flow is very slow. Increased values of RRT also appeared distal the stenosis in models of STABLE group with stenosis higher than 50% and for models of MI1 and MI2 groups with stenosis higher than 35%. In the

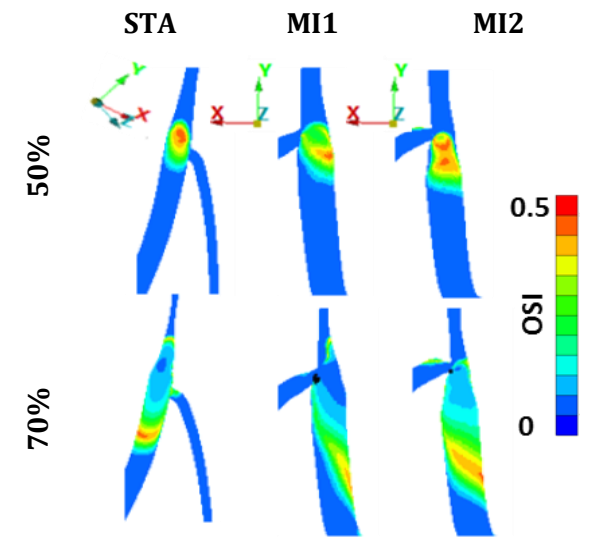


Figure 4-19: Spatial distribution of OSI for the models with 50% and 70% of stenosis.

models of group MI2 there is also an area with high RRT values at the wall of the bifurcation after the stenosis. As we move to higher degrees of stenosis, the areas with high RRT and OSI as shown in Table 4-4 were larger. At the same time, these areas were moved downstream the vessel, probably following the growth of the recirculation zones and spread in a larger area of the vessel wall instead of being concentrated in specific points (Figure 4-16).

Summarising, in order to compare the results among the different geometries, the same method as for TAWSS was utilised, but in this case the results have smaller absolute meaning as there are no known clinical or other threshold values regarding the non-pathological values of these quantities. For these quantities, comparisons have been performed relative to the value obtained for the healthy case. The magnitude of the surface where the value of OSI and RRT exceeded some specified values have been also calculated. For OSI a baseline value 0.25

was used, as the values of the OSI for the normal model were below this value for almost the whole of the wall surface (less than 0.01% of the vessel wall exceeded that value). The areas with OSI greater than 0.25, 0.3, 0.35, 0.4 and 0.45 have been also calculated. Following similar considerations for RRT, a baseline value 5 Pa⁻¹ corresponding to the healthy vessel was used. The areas with RRT greater than 5, 10, 17, 30, 50 and 100 have been calculated. The results, shown in Figure 4-21, indicate that the surface of the wall vessel with high values of OSI and RRT increases with the increase of the degree of

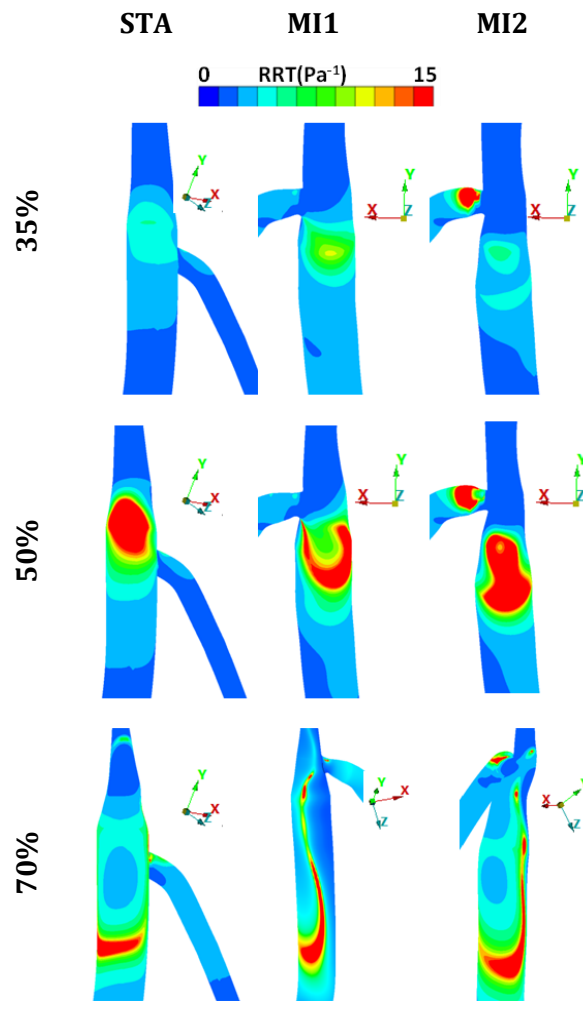


Figure 4-20: Contours of RRT. For great degrees of stenosis the areas with high RRT values are moved downstream. MI1 and MI2 have larger areas with high RRT, and in MI2 models there is also an area with high RRT in the side branch after the stenosis.

stenosis for all groups but not with the same degree. Areas with high OSI occupy a significantly part of the vessel wall for the models of MI1 and MI2 compared to STABLE models. The MI2 models have more elevated values for intermediate degrees of stenosis (35% and 50%) while for the maximum degree of stenosis these two groups have almost identical distribution of OSI. It should be noted that Table 4-4 the area with OSI higher than 0.3 is double for the MI1 and MI2 models relative to the STABLE model. The results are similar for RRT, with MI1 and mainly MI2 models having more elevated values than STABLE.

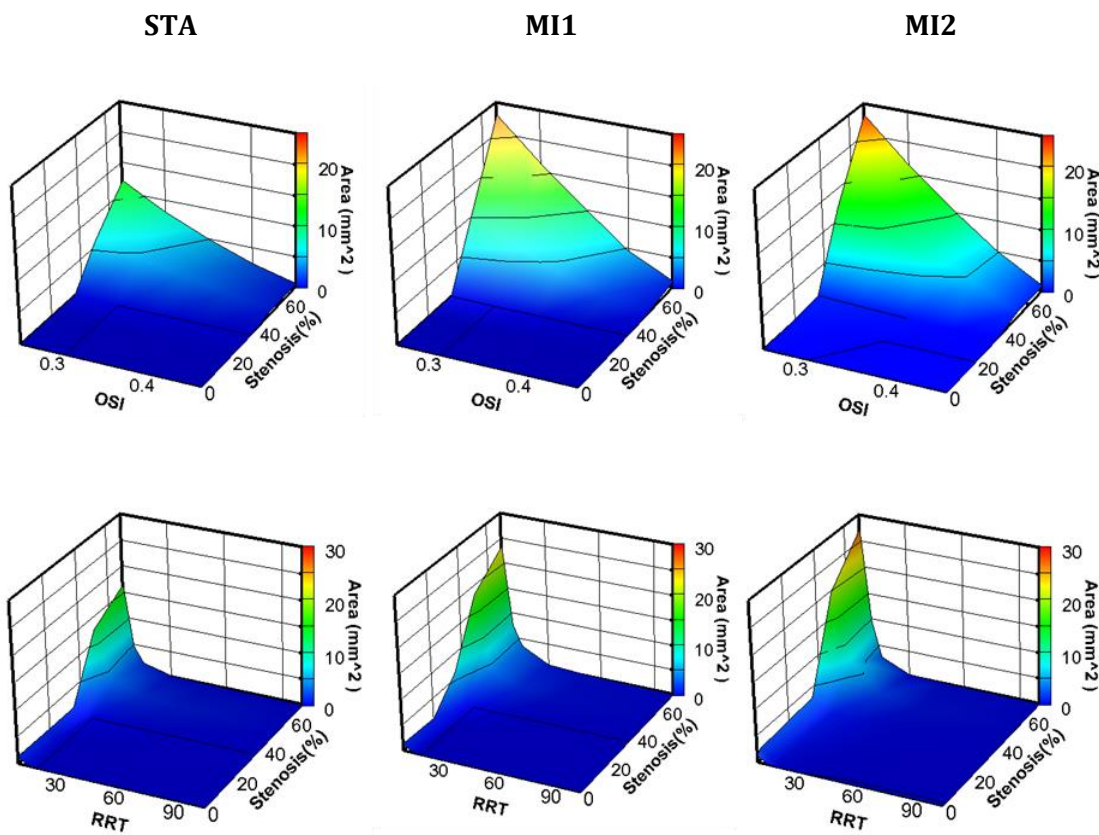


Figure 4-21: Surface of the vessel wall with OSI and RRT above certain values. The areas with high RRT and OSI are definitively higher for MI2 and MI1 geometries compared to STABLE for the same degree of stenosis, but the change of these values is mainly determined by the degree of stenosis rather than the exact location of the stenotic lesion.

The contours of OSI and RRT show that while in terms of WSS values (mainly low) the effect of the stenosis is more intense for the models of the group MI2, MI1 and MI2 models are characterized of equally disturbed flow. Again, the effect of stenosis on flow

was remarkably smaller for the models of STABLE group with stenosis less than 50%. In the models of the three groups with high degree of stenosis (>50%), there are distinct differences between them. The areas with elevated values of OSI and RRT are larger for MI1 and especially MI2 models and especially for OSI and even the surface averaged values are significantly higher. At the same time though, the results for all these models seem very close to each other when compared to the results of the healthy LAD or even to the results of the models with 35% of stenosis. So if these quantities are to characterize the risk of each case, it could be claimed that MI1 and MI2 are of higher risk compared to STABLE, while all of these cases are of very high risk compared to an LAD with low degree of stenosis. In any case, these quantities currently cannot be used as an absolute assessment of a stenosed LAD artery without further investigation in real geometries, but it is also possible that these quantities should be normalized according to the degree of the stenosis before used for assessment.

Table 4-4: Average values of OSI and RRT for the whole model and surface of the geometry with OSI>0.3 and RRT>5 (area in mm²). Coloured figures indicate that the specific value is more than 25% (orange) or more than 50% (red) than the lowest (green) value among the models with same degree of stenosis

group stenosis	OSI						RRT					
	surface average(x1000)			area with OSI>0.3			surface average			area with RRT>15		
	STA	MI1	MI2	STA	MI1	MI2	STA	MI1	MI2	STA	MI1	MI2
0	7.62			0.00			1.57			1.41		
0.2	5.49	5.41	5.63	0.00	0.00	0.05	1.54	1.51	1.52	1.26	1.06	2.15
0.35	5.58	6.42	5.91	0.00	0.00	0.55	1.55	1.55	1.54	1.33	6.35	3.10
0.5	8.23	10.39	11.02	4.59	6.77	9.78	1.72	1.70	1.78	12.58	18.30	19.88
0.7	13.67	20.32	18.81	8.09	16.36	16.40	1.86	1.89	1.82	16.42	23.36	27.29

4.12 Coagulation activation index (CAI)

Of very high interest were the results regarding CAI for the different models. As CAI was related to low TAWSS, some similarity was expected. But **the threshold values used for CAI, partially derived from the results of the healthy LAD were also close to the values suggested in the previous chapter, that were based on experiments investigating threshold conditions for the initiation of coagulation.** The geometries of the MI2 group with low or intermediate degree of stenosis had CAI values clearly above the healthy geometry ($1.1^{-5}m \cdot s$) and the threshold value defined in the previous

chapter ($1.0^{-5}m \cdot s$). The same holds for geometries with intermediate degree of stenosis for the MI1 group while all the STABLE cases and the MI1 and MI2 cases with 70% stenosis have CAI values lower or near the threshold as shown in Figure 4-22. This means that, even if further investigations are required for establishing a threshold value, stenosed LADs similar to MI1 and MI2 with intermediate degrees of stenosis (30%-50%) may be more likely to cause activation of the coagulation process, which could subsequently lead to thrombus formation. Additionally, as low values of TAWSS alone are also related to faster progression of atheroma [223] and high CAI values are related to areas with low TAWSS, high values of CAI may indicate that these cases may also deteriorate faster.

As it is reasonable to assume that the triggering for the initiation of coagulation will occur somewhere in the stenotic lesion, some estimations for the value of CAI in these areas has been performed, regardless of the fact that the shear in these areas is at least one order of magnitude larger than the threshold values reported. The stenotic lesions have maximum length of 16mm while wall shear rate in these areas varies depending on the case.

For the cases with 50% and 70% stenosis, the average values of wall shear rate in the stenotic lesion are around $2000s^{-1}$. So the value for CAI, even in the extreme estimation with the whole stenotic lesion considered as reacting surface, is below the suggested thresholds (less than $8.0^{-6}m \cdot s$), showing that initiation of coagulation in the specific area can occur only if surface processes and surface reactions occur.

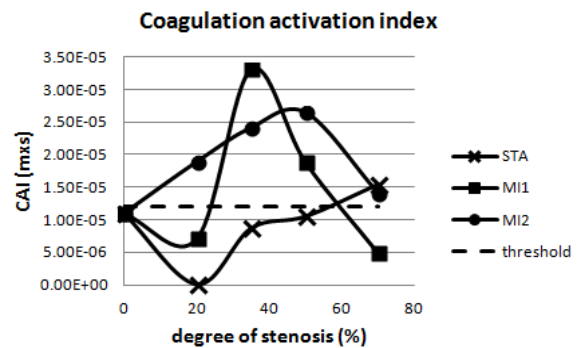


Figure 4-22: The variation of CAI for all groups and degrees of stenosis. .

4.13 Grouping of the results

If we conclusions of this study were to be limited to the models used in this study, this would be that the **group MI2, the one corresponding to geometries with a bifurcation involved in the stenotic area downstream the peak of the stenosis**, exhibits more disturbed flow and it is more likely to cause complications relevant to ACS. This statement is more intense for the intermediate degrees of stenosis between 20%-50% for MI2. Similar were the trends that have been observed in MI1 group for stenosis between 35-50%.

Low values of WSS have been related to the progress of CAD [25, 45] but there is no definite lower non-pathological value for WSS in the relevant literature. As WSS all varies along vessel walls, there should be a surface area with low shear stress in order to consider a specific case of high risk. At the same time, low values of wall shear rates have been shown to allow the initiation of coagulation over a surface with TF, but the WSS values reported are much lower compared to the arterial flow conditions. Combining the data found in the literature with the results of the healthy LAD model (which is considered of no risk) and keeping in mind that the initial assumption was that STABLE models were of lower risk, it can be concluded that a geometry where TAWSS is lower than 0.15 Pa for a surface bigger than 0.4 mm² could be considered of intermediate risk; when this surface becomes larger of 0.5mm² then it can be considered a case of higher risk.

Regarding the areas with high values of WSS, a value of 3Pa has been chosen as reference value. High values of shear stress are related to platelet activation. However it seems that it is stress accumulation that causes their activation rather than an instant or local high value of shear stress [134]; therefore, it is more important whether the platelets are exposed to high shear stress value for relatively long time interval. In terms of spatial distribution this is equivalent to having elevated shear stress values along the streamlines. So the effect of high stress on platelets is better expressed if the areas with high shear stress values are considered instead of the local values of shear stress.

High WSS may also trigger plaque rupture but the evidence on that is weak [224, 225]. In any case, at least for the examined model the index related to high TAWSS does not seem to give any useful information for comparison, as the value depends strongly on the degree of the stenosis and extremely high values of shear stress (>30 Pa), capable of causing platelet activation [221] were observed only in the cases of severe stenosis (>70%) and in a very small part of the vessel surface. In respect to platelet activation it is possibly of more interest to examine also whether there are values of high shear stress within the flow and not only on the surface.

The increased residence time and the recirculation in the post stenotic region is expressed via the RRT index. RRT is definitely related to the recirculation zones as it has clearly higher values (>3) in all cases where recirculation occurs (Table 4-5 and Figure 4-16). OSI has similar variation to RRT (Table 4-4 and Figure 4-21) and with the proposed threshold which is based on the results for the healthy model does not give any additional information. RRT and OSI indexes have distinctively higher values for the

cases where recirculation zones were observed and the variation of their values is in accordance to the different size and duration of the vortices.

Previous studies also showed that slowly recirculating flow due to core jet flow patterns through a stenosis promote aggregation of platelets and platelet-activating factors and that blood stagnation occurring at areas with disturbed flow may facilitate the accumulation of blood thrombogenic factors near the wall [226]. Since adhesion of platelets to a surface is greatly enhanced by prior activation [227], this mechanism offers an explanation for the increased platelet deposition at the recirculation zone: platelets that are already activated by the high shear stresses at the throat and along the shear layer between the jet and the slow vortices, are brought for a considerably large time interval close to the vessel wall at the slower side of this shear layer. In terms of the calculated quantities and indices, this condition can be expressed using the combination of TAWSS and RRT. This scenario is more likely to occur in the cases with high values of TAWSS and large areas with elevated RRT.

With the aforementioned criteria, the models are clearly divided in two categories: all models with stenosis above 50% and only the model MI2 with 20% exhibit high risk index. The difference in the extent of the surface with high TAWSS between the two groups is at least of one order of magnitude. This difference makes it possible to extract safely an exact threshold value as there is a big difference between the cases that are considered of high complicated risk and the cases that are considered safe. However, taking into account the results of all cases we used as a threshold condition for high WSS the existence of an area with 5mm² magnitude with TAWSS higher than 3Pa.

For OSI and RRT, non-pathological values or non-pathological distributions do not exist in literature; thus, absolute calibration of these indexes is not possible. The limits were set according to the results of the healthy model and the models that were considered of lower complication risk. For the OSI the limit was 5mm² total area with OSI above 0.25 and for RRT 2mm² area with RRT above 5 Pa⁻¹. The threshold values for CAI were explained in the previous section. In the following table the indices above the risk value for each case are summarised with + or - while in the parenthesis the ratio of the value of the index to the specific model is also given.

While the demonstrated indexes could obviously undergo further statistical manipulation and result to an overall index for each model, or for each group, or even for each degree of stenosis, as the examined cases were somehow limited, the extraction of

more general results may not correspond to real cases.

Table 4-5: Flow-based risk indexes for models with stenosis up to 70%. Overall the MI2 appears to be of higher risk, followed by MI1. Each risk index is based on the extent that the specified condition (stated in the first row) is present in each model.

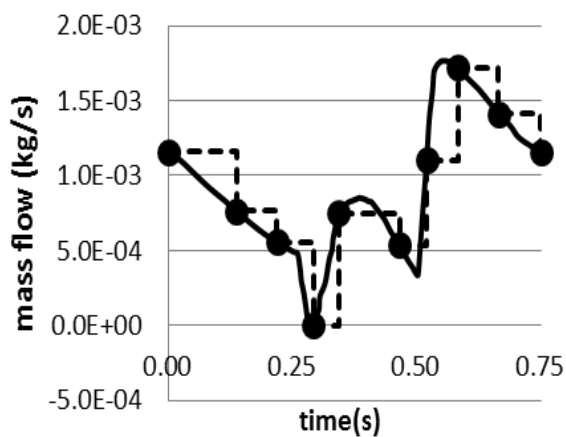
	group	Low TAWSS	High TAWSS	OSI	RRT	CAI
20%	STA	-(0.0)	-(0.0)	-(0.0)	-(0.63)	-(0)
	MI1	-(0.18)	-(0.014)	-(0.0)	-(0.53)	-(0.59)
	MI2	+(1.3)	+(1.4)	-(0.010)	+(1.1)	+(1.6)
35%	STA	-(0.28)	-(0.00011)	-(0.0)	(-0.66)	-(0.72)
	MI1	+(4.2)	-(0.098)	-(0.0)	+(3.2)	+(2.8)
	MI2	+(2.1)	-(0.18)	-(0.11)	+(1.55)	+(2.0)
50%	STA	-(0.41)	+(5.0)	-(0.91)	+(6.3)	-(0.88)
	MI1	+(1.3)	+(6.3)	+(1.36)	+(9.1)	+(1.6)
	MI2	+(2.6)	+(6.4)	+(3.0)	+(9.9)	+(2.2)
70%	STA	-(0.88)	+(5.11)	+(1.7)	+(8.2)	+(1.3)
	MI1	-(0.088)	+(7.2)	+(3.27)	+(12)	-(0.41)
	MI2	-(0.73)	+(7.2)	+(3.28)	+(14)	+(1.2)

In Table 4-5 it can be seen that in terms of disturbed flow there is a gap between the cases with 35% or less stenosis when compared to cases with 50% and above. The appearance of recirculation zones causes a sharp increase in the quantities related to the variation of the velocity vector above the walls of the vessel OSI and RRT. While in most indexes the difference between MI and STABLE cases is clear for the same degree of stenosis, it is possible that for geometries with high degrees of stenosis there should be defined different limits for the calculated quantities, especially for OSI and RRT. However, RRT seems capable of indicating the existence of recirculation zones without plotting more complex visualization requiring the velocity vector.

Chapter 5 Applying the thrombus model to realistic geometries

5.1 Method of application

The thrombus model developed in chapter 3 was applied to the realistic LAD models, using the time dependent flow fields that were calculated in chapter 4. More specifically, the geometries with 35%, 50% and 70% of each group were used, as the sharpest change of the characteristics of the flow field was observed between these cases. the geometries with stenosis of 20% were classified as of less interest because the alterations of flow compared to the healthy vessel was negligible. Additionally, the assessment of models with 20% stenosis was considered of no practical use, as the



t (s)	Δt (s)	Q_m (kg/s)	Δm (kg)
0.00	0.138	$1.16 \cdot 10^{-3}$	$1.60 \cdot 10^{-4}$
0.14	0.081	$7.62 \cdot 10^{-4}$	$6.20 \cdot 10^{-5}$
0.22	0.073	$5.55 \cdot 10^{-4}$	$4.06 \cdot 10^{-5}$
0.29	0.050	$1.72 \cdot 10^{-6}$	$8.71 \cdot 10^{-8}$
0.34	0.124	$7.50 \cdot 10^{-4}$	$9.27 \cdot 10^{-5}$
0.47	0.054	$5.35 \cdot 10^{-4}$	$2.87 \cdot 10^{-5}$
0.52	0.063	$1.10 \cdot 10^{-3}$	$7.00 \cdot 10^{-5}$
0.58	0.081	$1.72 \cdot 10^{-3}$	$1.40 \cdot 10^{-4}$
0.67	0.085	$1.41 \cdot 10^{-3}$	$1.20 \cdot 10^{-4}$
total	steps	0.75	$9.52 \cdot 10^{-4}$
	original	0.75	$9.44 \cdot 10^{-4}$

Figure 5-1: The discrete steps used for the application of the thrombus model, shown on the mass flow rate pulse corresponding to the healthy model. The resulting flow rate pulse that was used is described by the dashed lines.

Table 5-1: The time instances used for the inlet pulse for the application of thrombus formation. The flow rates and inlet masses correspond to the inlet of the healthy vessel. The values of mass flow correspond to the flow rate pulse used for the healthy model.

resulting geometries after the introduction of the stenosis would not be classified as stenosed vessel when seen in a coronary angiography. The initial intention was to show the results of the model under steady-state flow conditions, in order for the method to be easier to apply. Unfortunately, the steady-state state simulation results were found to depend strongly on the choice of the specific time instance of the flow or more accurately, on the pressure drop and the resistance values corresponding to the specific time instance, as the recirculation zones appear in a part of the time steps. An alternative could have been the use of the average flow field, but this totally eliminates the effects of recirculation for the cases with less than 70% stenosis and does not demonstrate areas

where the velocity vector is opposite to the dominant direction of the flow. For these reasons, the application of the coagulation model under flow was performed using a number of flow instances much smaller than the 100 timesteps that consisted each pulse during the flow simulations.

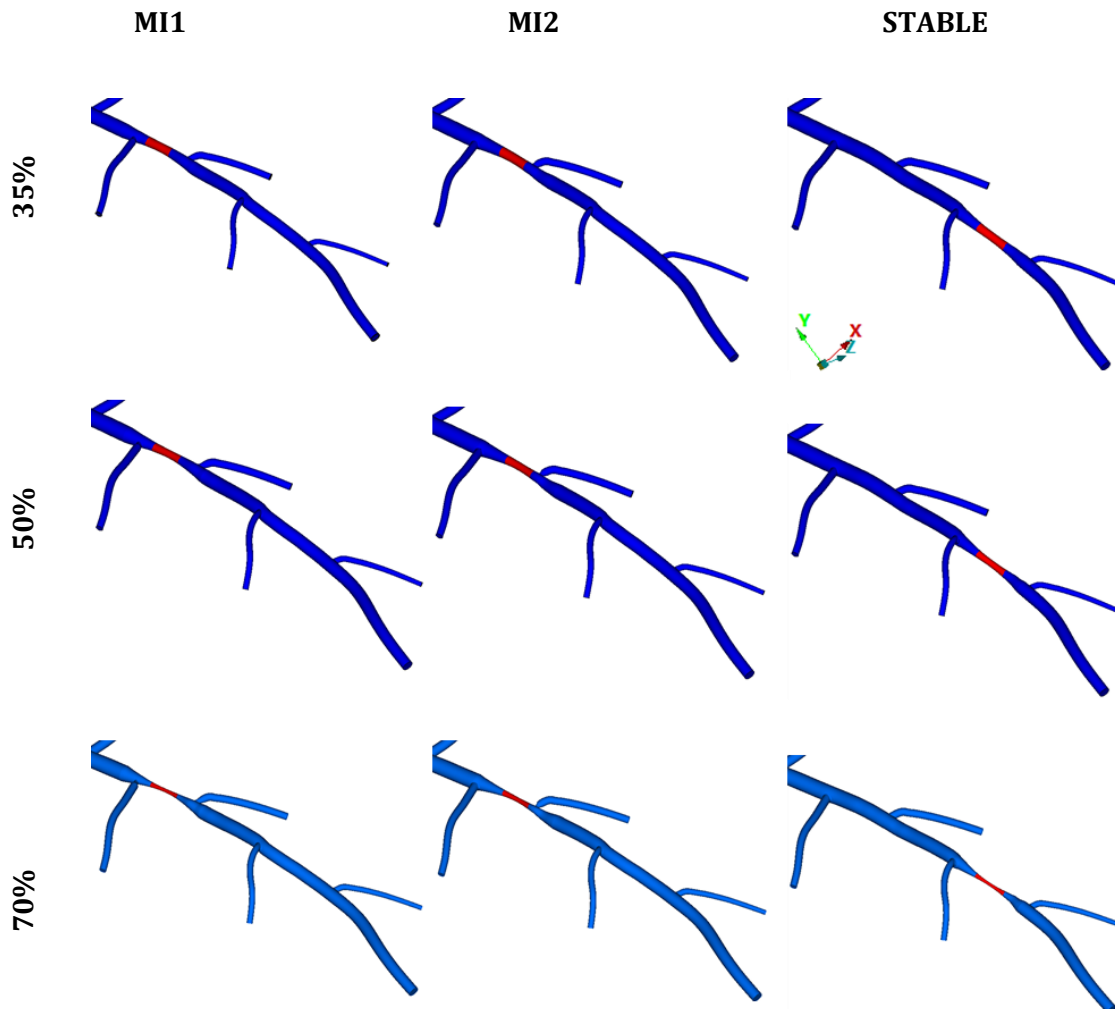


Figure 5-2: The defined reacting boundary (RED) for all the geometries on which the model was applied. The images are in the same scale. The reacting area has the same stream-wise length for all models, approximately 6mm while the middle is at the point of maximum stenosis.

In more detail, for each one of the tested geometries the flow field (velocity and pressure drop) was exported for 9 time instances of the heart pulse as shown in Table 5-1 and Figure 5-1. The flow fields used were the ones obtained via the transient flow simulations presented in chapter 4. The time instances were chosen in a way that they include moments where there is reversed flow in the areas of recirculation for all models that exhibited recirculation zones as well as instances where the flow rate value is close

to the maximum value of the cycle. As the time scale of thrombus models was in the magnitude order of minutes and the used heart pulse duration was 0.75s (80 bpm) the sufficient period of time for such a simulation is about 3-5 minutes or 350-400 heart pulses; this corresponds to about 4000 time steps for each case. As mentioned earlier, the use of more dense time steps made the process extremely time consuming, as at each time step the program loads the new flow field and applies the model again. Some preliminary tests for the model M11 with 35% degree of stenosis performed with more time steps (20) within a heartbeat for a small (>10) number of heart pulses did not show any significant differences in the monitored quantities (thrombin concentration, thrombin production rate, bound platelets and activated platelets). As shown in Table 5-1 the time instances used for the flow fields were chosen so as the resulting average mass flow rate and the total mass flow of the discretized pulse are close to those of the original pulse while the difference is approximately 0.8%.

In order to apply the thrombus generation model to the realistic geometries, a reacting area on the vessel wall had to be defined. No experimental data regarding the exact location where the initiation occurs is available. The size of the reacting area is also unknown. The reacting boundary for the scope of this Thesis was defined as the part of the stenotic lesion. The reacting boundary was symmetric to the peak of the stenosis with respect to the direction of flow and, as shown in Figure 6-2, it has had approximately the same 6mm stream-wise length for all the geometries.

5.2 Results

The behaviour of the coagulation numerical model on different geometries appears strongly related to the findings of chapter 4, as the results depend strongly on the degree of the stenosis while there are also differences among the different groups of geometries. The results showed that the evolution of the process, at least as it is described by our model, depends strongly on the distribution of wall shear rate, especially on the reacting part of the vessel wall. The wall shear rate distribution on the other hand depends mainly on the degree of the stenosis. As a result of these the process had similar –but not identical- temporal evolution on the geometries with the same degree of stenosis rather than the geometries of the same group.

The time interval between the beginning of the simulation and the moment when thrombin concentration exceeded the threshold value in sites downstream the reacting area varied significantly between the models (2s to approximately 5min) but in all cases

was small compared to the time scale of human life. The emergence of thrombin in above threshold concentration in the area distal the reacting boundary was utilised as the event that signals the initiation of the clotting process; from this point onwards these locations will be referred to as downstream propagation. The time interval between the initiation of the process and the initiation of downstream propagation, T_p , increases about one order of magnitude with higher degree of stenosis. At the same time, for models with higher degree of stenosis, downstream propagation requires a bigger amount of bound activated platelets in order to occur. Note that according to what has been described for the thrombus model in chapter 3, activation of platelets actually occurs during the transition from the initiation to the propagation phase of coagulation, so bound activated platelets represent also added surface bound activity.

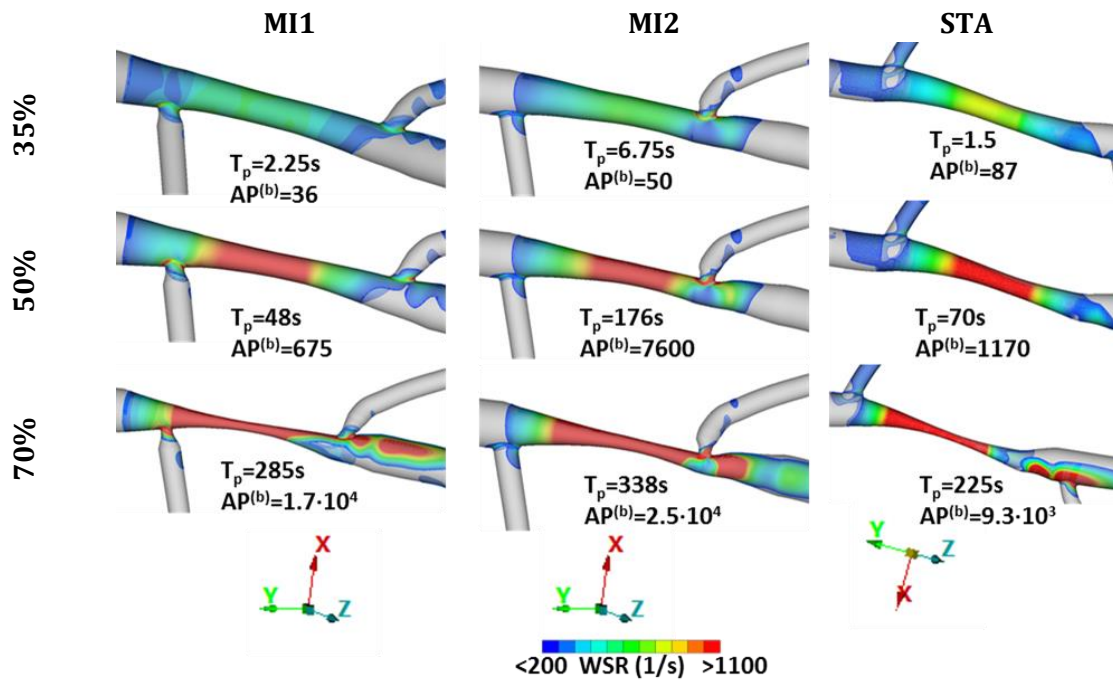


Figure 5-3: The different temporal evolution of the process for different distributions of wall shear rate (WSR) with the time (T_p) and the amount of bound activated platelets ($AP^{(b)}$) required for downstream propagation. It is clear that the cases with low values of WSR do not require the presence of bound activated platelets (additional surface bound activity) for downstream propagation.

In Figure 5-3 the distributions of time averaged WSR for each model along with the time between the initiation and the downstream propagation and the amount of bound activated platelets T_p and $AP^{(b)}$, respectively, are demonstrated. The minimum value of the contour is the average WSR of the normal geometry ($200s^{-1}$). The total mass of bound

activated platelets was normalized by dividing with the average platelet mass. As mean platelet volume is about 6.5fL [228] and platelets are considered non-buoyant particles (density $\rho=1060\text{kg/m}^3$), an approximate value for platelet mass is $7 \cdot 10^{-15}\text{kg}$, so $AP^{(b)}$ is approximately the number of bound activated platelets. Due to this differentiation of the behaviour of the model for different degree of stenosis the results are presented in three different groups, corresponding to different degrees of stenosis.

Indicative values for thrombin concentration of 1.15nM (or $4 \cdot 10^{-8}\text{kg/kg}$) in the thrombin production sub-model has been utilised as a threshold for the transition from the initiation to the propagation phase. This value of concentration of thrombin, besides being the threshold value in the thrombin production sub-model, is considered capable of igniting the fibrin activation and clotting [229]. From the typical result of TGA [191] one can obtain a reference value for the thrombin generation rate:

$$\frac{\partial [IIa]}{\partial t} = \frac{C_{max}}{T_{max} - T_{lag}} = 0.72\text{nM/s} \approx 2.5 \cdot 10^{-8}\text{kg/kg} \cdot \text{s}$$

Equation 5.1

As in most parts of the computational domain thrombin generation rate is negative, implying that inhibition process dominates, the legend for thrombin production rate includes also negative values. It must be noted that, as the typical thrombin generation curve is not symmetric with respect to the maximum of thrombin concentration, the rate of production (absolute value) is significantly greater than the rate of inhibition; this means that values for thrombin concentration change rate smaller than $-2.5 \cdot 10^{-8}\text{kg/kg} \cdot \text{s}$ should be considered as significantly high rates of inhibition. The average concentration and production/inhibition rate for IIa that are presented above have been calculated for the area near the vessel surface as the concentration away for the vessel walls was near zero for all the cases. As the area distal the reacting boundary (S_{DS}) is not the same for all models, the average concentrations ($\langle [IIa] \rangle_{TOT}$) that were calculated for the total surface of the geometry (S_{TOT}) were corrected to correspond to the average for the area downstream the reacting site ($\langle [IIa] \rangle_{DS}$). As the concentration upstream the reacting site is zero, the correction was performed using the following formula:

$$\langle [IIa] \rangle_{DS} = \langle [IIa] \rangle_{TOT} \cdot \frac{S_{TOT}}{S_{DS}}$$

Equation 5.2

Finally, in all the cases presented, the spatial distribution of thrombin concentration one minute after the downstream propagation (Figure 5-6, Figure 5-10 and Figure 5-14) and the temporal change of thrombin concentration ($\partial[I\text{Ia}]/\partial t$) one and two minutes after the downstream propagation (Figure 5-7, Figure 5-11 and Figure 5-15) are presented.

5.3 35% stenosis

In the geometries with stenosis of 35% the downstream propagation is almost immediate after the initiation of the triggering, as shown in Figure 5-3. Besides that common characteristic, the results of the coagulation model varied significantly among the three cases.

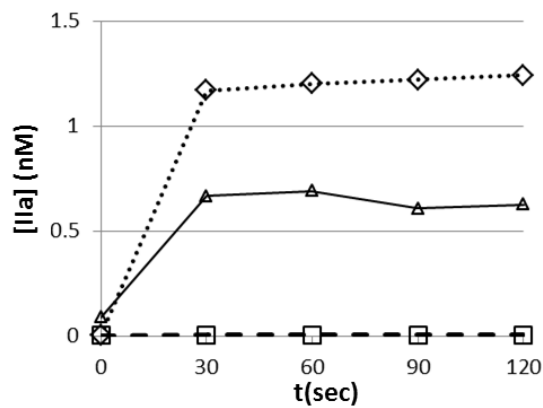


Figure 5-4: Temporal evolution of thrombin concentration near the vessel wall within two minute time interval after the downstream propagation.

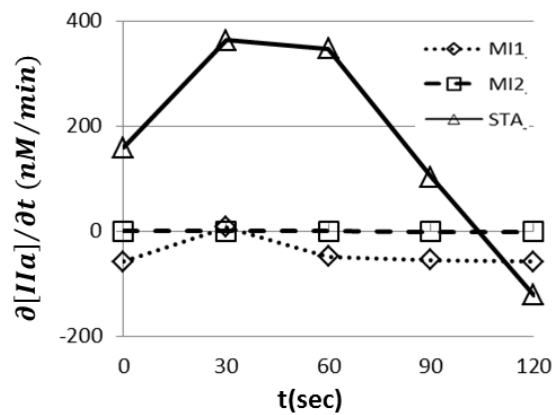


Figure 5-5: Temporal evolution of thrombin generation/inhibition rate near the vessel wall –excluding the surface production– within two minute time interval after the downstream propagation

As shown in Figure 5-4, a sudden burst of thrombin exists in the STABLE model followed by one also sudden fall. On the MI1 model, a relatively smaller production rate is observed, which is positive only for a small period of time; it is to be noted that there is also production of thrombin before the moment of downstream propagation so the fact that the rate of the [IIa] change is mostly negative is reasonable. Finally in the MI2 model both average concentration and production rate have very small values, negligible compared to the other two cases. However, the average values do not completely describe the situation as the quantities of thrombin are not uniformly distributed.

For the MI1 and the STABLE models, above-threshold values of thrombin concentration

are present in a large area of the downstream vessel wall, while in the MI2 model this phenomenon is localized in a specific site (Figure 5-6). The maximum calculated values of thrombin concentration downstream the reacting sites were similar for the three models and approximately 20 times higher than the threshold value ($\sim 1 \times 10^{-6} \text{ kg/kg}$ or 30nM); but at the same time, these values are more than five times lower than the typical maximum values of TGA (160nM) and remained almost unchanged during the last 30 seconds of the simulation as their increase was less than 1%.

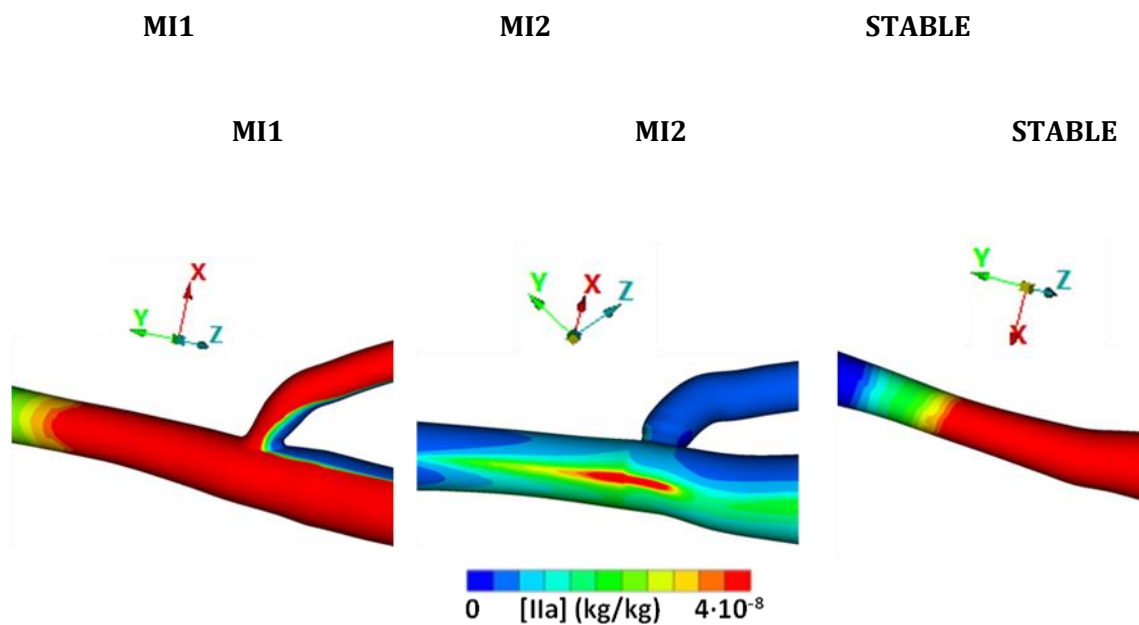


Figure 5-6: The distribution of thrombin concentration for the three models with 35% stenosis, 1 minute after the downstream propagation. While in MI1 and STABLE models there is a large area with above threshold values for thrombin concentration in the MI2 models high thrombin concentration is localized in a specific site.

Finally as shown in Figure 5-7, generally the rate of production of thrombin decreases at the area downstream the reacting site after the downstream propagation in all cases. In the MI1 geometry inhibition dominates 2min after the downstream propagation, with an exception at a small area at the root of the side branch. As it has been demonstrated in chapter 4 (Figure 4-16), a recirculation zone was observed in the MI1 model with 35% stenosis, located at the end of the reacting zone where thrombin is initially produced. The inhibition of thrombin is more rapid at the cells near the wall due to the action of protein C, which is included in the coagulation model with an increase of the inhibition rate constant. This spot of increased activity observed in MI1 model with 35% of stenosis is probably due to activated thrombin that is transferred at the root of the side branch via the recirculation vortex and escapes the action of APC.

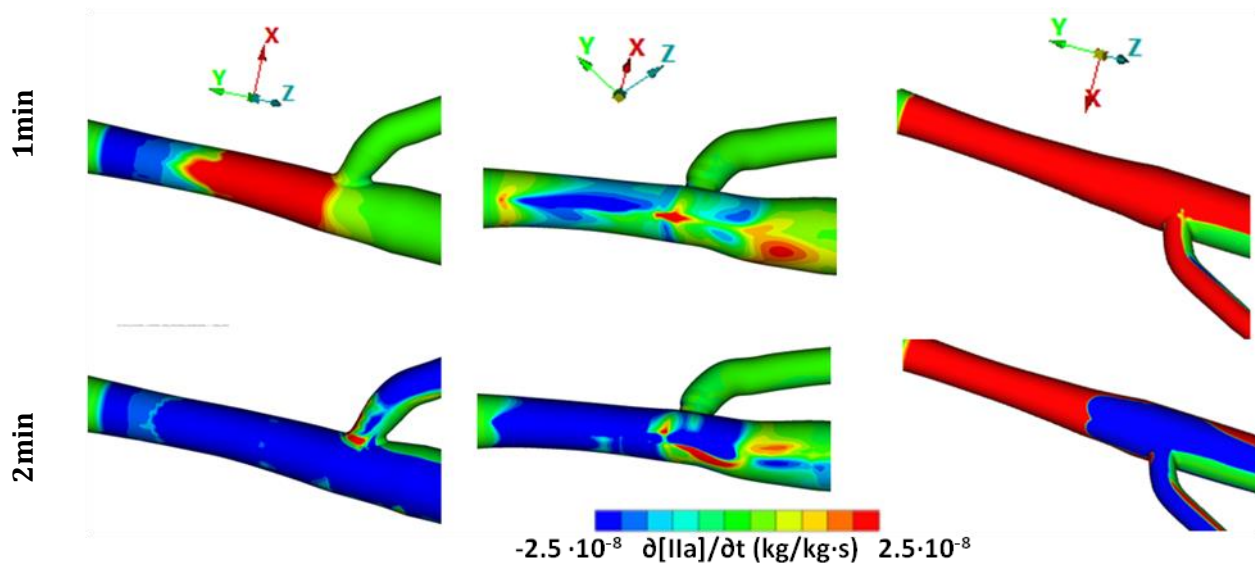


Figure 5-7: The spatial distribution of the rate of change of [IIa] one and two minutes after the downstream propagation for 35% stenosis. In all cases the rate of production decreases and it is interesting that for the MI2 geometry the areas with high production rate coincide with those of high concentration.

In the MI2 case the areas with high rate of IIa production are small and coincide with the areas with high [IIa]. As shown in chapter 4, this area has smaller flow velocities (Figure 4-17) but not significantly low WSS (between 0.5 and 1Pa) while the area with very low WSS (Figure 4-18) and high RRT at the root of the side branch does not exhibit any noticeable differentiation in terms of thrombin production. Finally, in the STABLE case, there is a dramatic drop at the rate of IIa production, with inhibition dominating at the most part of the vessel walls but with certain areas -root of the side branch and the wall of the main branch opposite to the main branch- where the rate of production of thrombin is positive and indeed above the maximum of the scale. These areas were also characterized by relatively low WSS (in most area below 0.5Pa) and high RRT. It must be noted that in the STABLE model, while of smaller risk regarding to thrombosis is expected (according to the initial hypothesis and the flow based assessment), there is a significantly large area where production of thrombin exists and takes values above threshold concentrations, even 2 minutes after the downstream propagation, making it of higher risk based on the evolution of the coagulation model.

Overall it can be said that the thrombin model indicates areas of elevated thrombin concentration and thrombin production is generally different from the ones indicated by the flow risk assessment indexes. If the different geometries with 35% stenosis were to

be classified based only on the behaviour of this model, probably the one of higher risk would have been the STABLE geometry, followed by the MI2 and the least dangerous would be the MI1 case. Additionally it is clear that after the downstream propagation the process in MI1 and STABLE geometries advances with similar pace while the evolution in MI2 geometry is quite slower and significantly different. However as it can be seen in Table 4-5, the flow conditions prevailing in the STABLE model with 35% of stenosis do not favour the progress of CAD or the initiation of thrombin as the calculated indices are below the suggested level for all the involved factors.

5.4 50% stenosis

Average thrombin concentration had similar temporal evolution for all three models of 50% stenosis as it can be seen in Figure 5-8. The maximum values of thrombin concentration were the same with the models of 35% ($\sim 1 \cdot 10^{-6} \text{ kg/kg}$ or 30 nM) and also obtained a constant value after 1.5 minutes after the downstream propagation. However, in terms of production/inhibition rate the findings for the MI2 model differ from the other two, as the average rate of production of thrombin for the whole area downstream is nearly 0 for the two minutes after the downstream propagation. Obviously, these two facts indicate that in MI2 geometry thrombin generation and high thrombin concentrations are restricted to a small part of the downstream area. The areas with elevated thrombin concentration in MI1 model are more or less the same with those of the MI1 geometry with 35% stenosis. High thrombin concentration values are observed at the part of the main branch starting opposite the side branch and at a part of the side branch starting from the root part closest to the stenosis (Figure 5-10). These areas are characterized by low WSS (below 0.5 Pa and one part below 0.15 Pa , Figure 4-18 and Figure 4-20, respectively) and high RRT (in some parts above 10 Pa^{-1} Figure 4-20) which, at the same time, is the area of a large recirculation vortex (Figure 4-16). Thrombin concentration above the threshold value was also observed at the bifurcation.

The areas with high thrombin concentration in the MI2 model were also restricted in specific areas, in a manner similar to the MI2 model with 35% stenosis, but these areas were in slightly different locations and were significantly larger. Elevated thrombin concentrations were observed in a small area at the root of the side branch, at two stripes of the reacting area and at the wall of the vessel downstream the reacting site and opposite to the side branch (Figure 5-10). In both the main and side branches the areas

of elevated thrombin concentration include the areas of recirculation and the areas with high RRT and low WSS, with an exception at the root of the side branch which is an area with high WSS.

In the STABLE model, the above-threshold values of thrombin concentration were observed in the same area of the main branch as for the model with 35% stenosis. This areas are also characterized by low WSS values (below 0.5Pa, figure) extremely high RRT compared to the values observed in the healthy vessel (in most parts above 15 Pa⁻¹, Figure 4-20) and also partly recirculating flow motion. On the contrary, the concentration in the side branch downstream the stenosis was nearly zero, unlike what was observed in the STABLE geometry with 35% stenosis.

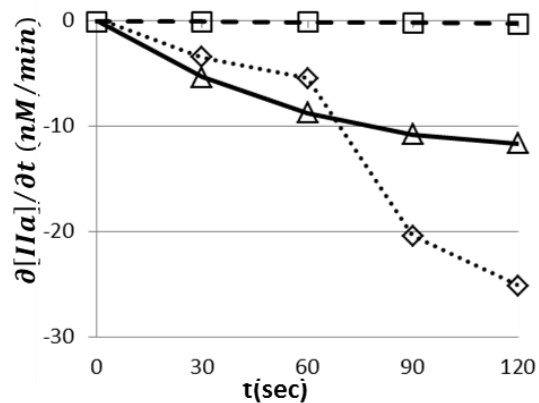
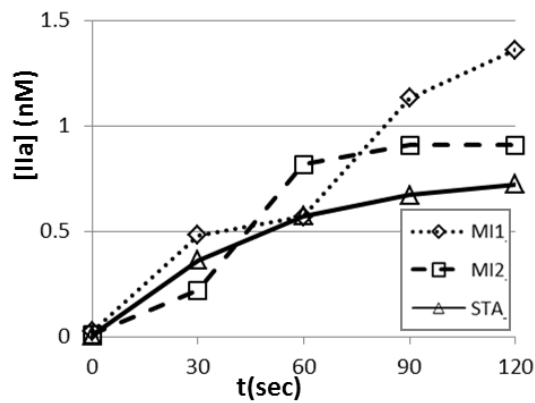


Figure 5-8: Temporal evolution of thrombin concentration near the vessel wall during two minutes after the downstream propagation for models with 50% stenosis. The three geometries have similar images.

Figure 5-9: Temporal evolution of thrombin generation/ inhibition rate near the vessel wall –excluding the surface production- during two minutes after the downstream propagation. There is an increase of the inhibition rate for MI1 and STABLE while MI2 exhibits very small values.

The MI1 model has an area with high thrombin concentration opposite the side branch. The size of this area is slightly reduced and displaced downstream after 2 minutes but it remains considerably large. This area is a part of the area with thrombin concentration above threshold value and therefore it has the same flow characteristics, low WSS, high RRT and recirculation. In the MI2 model the area with elevated thrombin production rate increases its size with time, and after two minutes it includes most part of the area

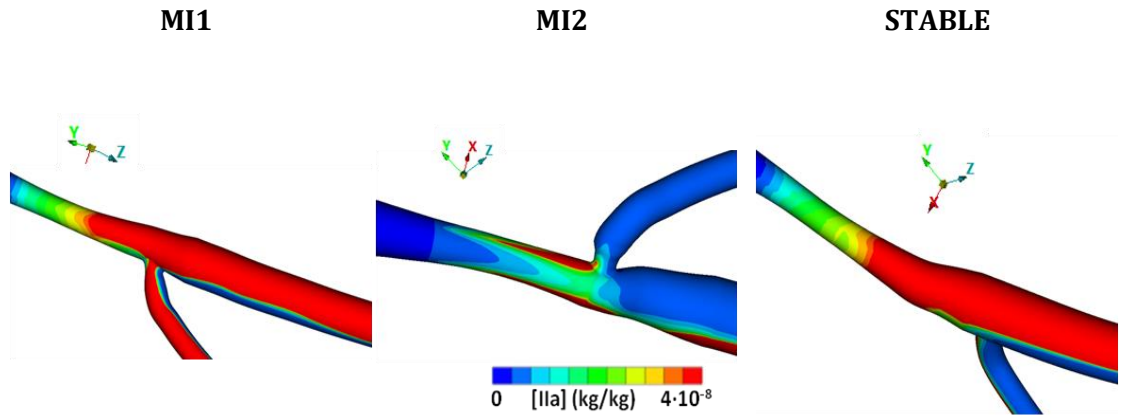


Figure 5-10: The distribution of thrombin concentration for the three models with 50% stenosis, 1 minute after the downstream propagation. While in MI1 and STABLE models there is a large area with above threshold values for thrombin concentration in the MI2 models high thrombin concentration is localized in a specific site.

with elevated thrombin concentration, while after two minutes an area of thrombin production has also appeared at the root of the bifurcation. It is also important that for the rest of the geometry the rate of production after two minutes is approximately zero, meaning that while we have production at specific site this is not balanced by the domination of inhibition at the rest of the vessel. Finally, in the STA geometry while the

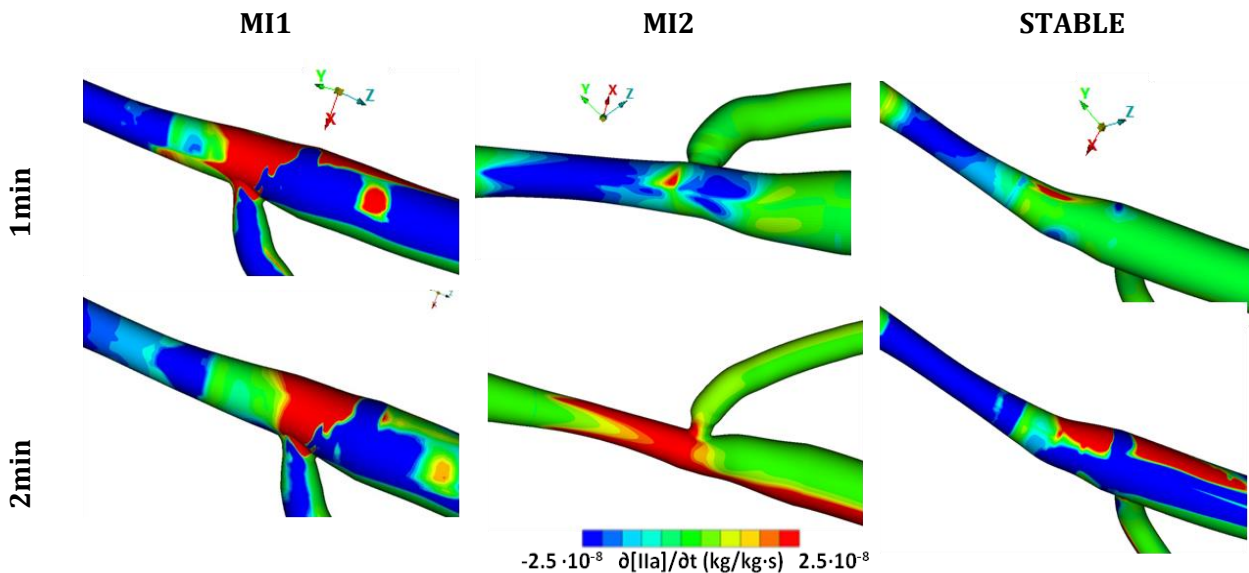


Figure 5-11: Thrombin production rate for 50% stenosis. The rate of production for the MI2 model is significantly increased near the reacting site while there is not increased inhibition rate downstream.

average production rate is reduced with time, or rather the inhibition rate is increased, the situation moves from a state with zero production/inhibition almost for the whole downstream area to a state where there are areas of rapid production and rapid inhibition. The areas of high production in this case are also part of the area with elevated thrombin concentration; they are also inside the recirculation zone and have high values of RRT and low values of WSS.

Summarizing, for all the geometries with 50% of stenosis, the areas of high susceptibility (elevated concentration and production rate) almost always coincide with the recirculation zones. In the MI2 model seems to be an increase of production rate with time in areas with already high thrombin concentration, while in MI1 and STABLE there are also susceptible areas.

5.5 70% stenosis

In the MI1 and MI2 models, the average thrombin concentration is changing slowly, and it has in general a low value of approximately two orders of magnitude lower than the threshold value of thrombin concentration for the transition from the initiation to the propagation phase. The maximum values are approximately 10^{-7} kg/kg ($\sim 3\text{nM}$) and they are also lower than the ones observed in the models with lower degrees of stenosis, but well above the threshold value. This fact indicates again that the elevated thrombin concentration areas are restricted in specific locations. In the STABLE model with 70% of stenosis. The temporal evolution of the average thrombin concentration has similarities to the model of 50%. There is an increase up to approximately $3 \times 10^{-8} \text{ kg/kg}$ (sub-threshold value) but this increase is sharper, starting approximately one minute after the downstream propagation (Figure 5-12Figure 5-15). The maximum value is higher than the ones at MI1 and MI2, $9 \cdot 10^{-7} \text{ kg/kg}$ ($\sim 27\text{nM}$), close to the maximum values of the models with lower degree of stenosis.

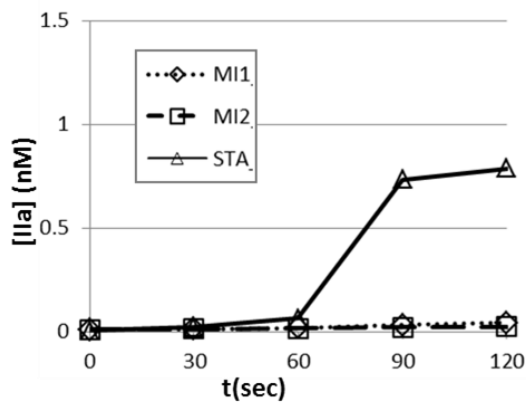


Figure 5-12: Temporal evolution of thrombin concentration near the vessel wall during two minutes after the downstream propagation.

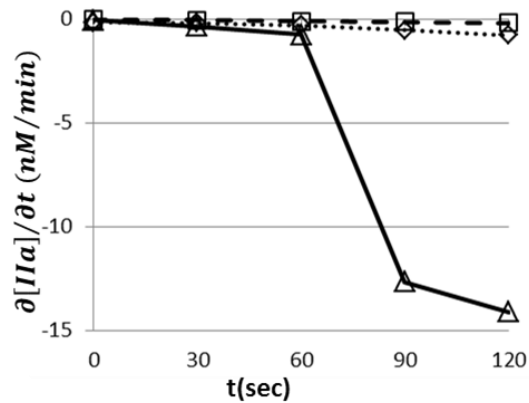


Figure 5-13: Temporal evolution of thrombin generation/ inhibition rate near the vessel wall –excluding the surface production- during two minutes after the downstream propagation

The rate of production has also similar temporal evolution for the MI1 and MI2 models, with a slow increase of the inhibition rate, while for the STABLE model there is a fast increase of inhibition rate one minute after the downstream propagation (Figure 5-13).

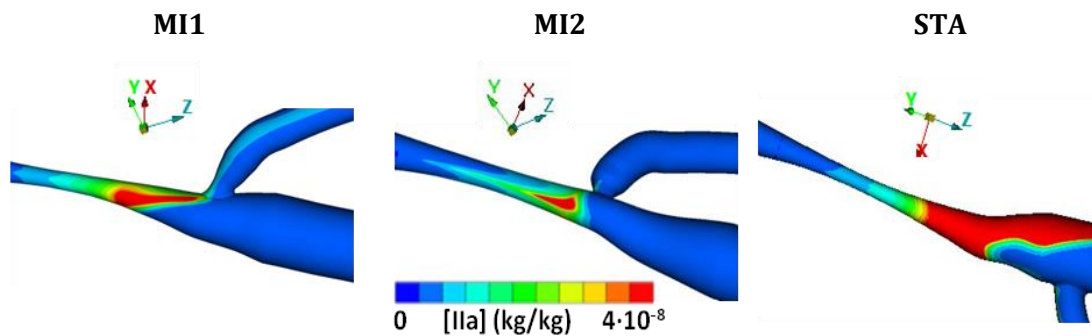


Figure 5-14: The distribution of thrombin concentration for the three models with 70% stenosis, 1 minute after the downstream propagation. While in STABLE model there is a large area with above threshold values for thrombin concentration in the MI1 and MI2 models high thrombin concentration is localized in a specific sites.

The average inhibition rate in all cases is much slower than the typical inhibition rate of the TGA ($2.5 \cdot 10^{-8} \text{ kg/kg} \cdot \text{s}$ ($\sim 0.7 \text{ nM/s}$)). In the STABLE model, initially the inhibition rate has similar evolution to the MI1 and MI2 models. One minute after the downstream propagation the inhibition rate increases; still it remains much lower than the values

observed with the 35% and 50% stenosis and the average rate of TGA.

In MI1 and MI2 models the distribution of the areas with elevated thrombin concentration and increased production rate resembles the image from the MI2 models with lower degree of stenosis (Figure 5-15, Figure 5-11 and Figure 5-7).

In both models, the areas with high production rate are within the area of high thrombin concentration, and do not change with time (Figure 5-15) while inhibition dominates in the rest of the geometry. On the contrary, in the STABLE model there is a definitively larger area with high thrombin concentration. This area includes the area of the geometry where we have production of thrombin (figure); however this area changes with time.

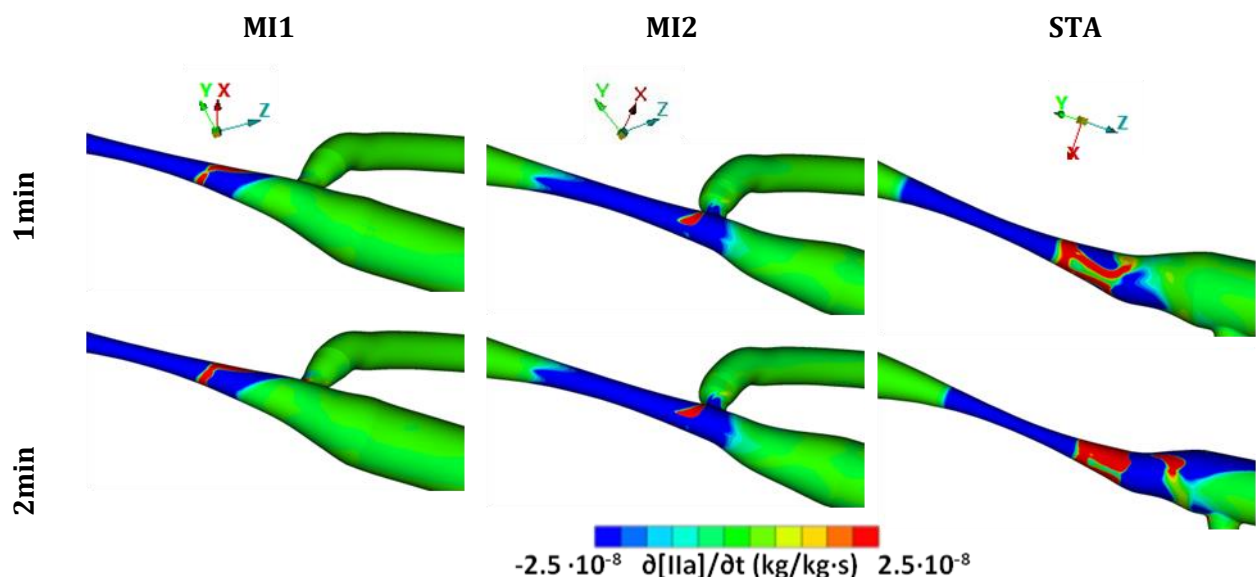


Figure 5-15: Thrombin production rate distribution for the models with 70% stenosis. In MI1 and MI2 models thrombin production is localised in specific sites that do not change with time. In STABLE model the area with high thrombin production rate is larger and changes with time.

In general, the three models have lower values of thrombin inhibition rate and average thrombin concentration than the ones with lower degrees of stenosis. However, in terms of spatial distribution, the three models have similar images, with localization of thrombin in specific spots. It has been mentioned that in models with higher degree of stenosis the downstream propagation requires a greater amount of bound activated platelets (or additional surface activity). In the models with 70% stenosis, the areas where we have thrombin production (and not inhibition) are restricted within the area

of the reacting boundary, while it seems that outside the reacting boundary zone inhibition takes over. It is possible that if simulations with longer time interval had been performed, one could get a different image, but this time interval is impossible to be determined and additionally, as the amount of bound platelets increases with time, that in fact would also cause alterations in the geometry of the models.

5.6 Comments

As the thrombus model focuses mainly on thrombin production, it was decided to identify the susceptible areas based on the thrombin concentration and thrombin concentration rate, claiming that when elevated thrombin concentration is calculated while at the same time there is increased rate of production at the same area, then this area can be considered as of high risk for thrombus formation. Maximum thrombin concentration was used only as an index of stabilization of the phenomenon, as at the end of the two minutes after the downstream propagation, in all geometries it showed in the worst case a very slow increase. Maximum physical time for the simulations was 8 minutes and it was necessary only for the MI2 geometry with 70% of stenosis. Nevertheless, the possibility that if simulations had been performed for longer time interval, the behaviour might be different cannot be excluded, as the average surface concentration of bound platelets was below 5% of the maximum. Unfortunately, there was no method to estimate the 'proper' maximum time interval for the simulations. It was necessary though to set an end point, since the method was extremely time consuming (each case was running for more than one week). More importantly, while coagulation is progressing, certain occurring processes as local alteration of viscosity due to fibrin polymerization, change of the vessel wall properties and shape due to bound platelets and fibrinolysis become too important. As these processes have not been yet incorporated in the used coagulation model, it was chosen to stop the simulations at a point that they seemed to reach to a steady state solution. Continuing beyond that point has extremely high computational cost while at the same, with the current setup for the coagulation model neglects important parts of the process.

In general, the model of coagulation has different behaviour in each geometry and there seems to be no general rule capable of describing all cases. In the STABLE cases, downstream propagation occurs faster compared to the MI cases with the same degree of stenosis. Again the degree of stenosis is a very important factor regarding how fast the process progress but the models of MI2 group seem to follow a similar pattern, with

localization of thrombin generation in small areas. The whole process seems to reach a steady state after 2.5 minutes in the cases of 35% stenosis for all geometries. For higher degrees of stenosis this time interval increases and varies among the different groups. The cases can be divided into two clearly distinct groups. In some of the geometries (all the groups of MI2 and MI1 model with 70% of stenosis) the areas with high concentration and high production rate are restricted in specific sites in a small distance downstream the reacting area and the average thrombin concentration was low and below the threshold value and at the same time the production rate had small absolute values ($|\partial [IIa]/\partial t| < 2 \cdot 10^{-9} \text{ kg/kg} \cdot \text{s}$). In the rest of the geometries (all the STABLE cases and the MI1 cases with 35% and 50% of stenosis) there are areas with high thrombin concentration and production rate in great distance downstream the reacting site and the inhibition has larger variations ($|\partial [IIa]/\partial t| > 6 \cdot 10^{-9} \text{ kg/kg} \cdot \text{s}$).

There is also differentiation regarding the side branch downstream the reacting site. In some cases (MI1 and STABLE with 35% and MI1 with 50% stenosis) we have thrombin transportation via the side branch, while for the rest of the cases (all MI2 cases, STABLE with 50% stenosis and STABLE and MI1 with 70%) the side branch has almost zero thrombin concentration (and zero rate production). Among the cases with high thrombin concentration in the side branch only in the case STABLE with 35% stenosis there is positive production rate in the side branch and therefore only in that case we can identify a high risk area in the side branch downstream the bifurcation and additionally a possibility of propagation of the coagulation process towards smaller vessels downstream.

Another interesting general conclusion is the relationship between the shear rate and the surface activity required in order for the downstream propagation to occur. While there is not accurate one-to-one pairing of wall shear rate values and the amount of bound activated platelets, it is clear that geometries with higher degree of stenosis and therefore areas with higher shear rate require much larger amount of bound platelets or in other words increased surface activity. This means that **the flow field prevailing in the reacting area might change the significance of the different processes involved in the coagulation process**. In more detail, as some of the reactions occur both in plasma and on surface bound cells, it is possible that while in areas with low wall shear rate the reactions occurring in plasma are capable of initiating the coagulation process, in areas with high wall shear rate the processes occurring on surface cells have a more essential role.

The big difference between the time intervals required for the transition from the initiation to the propagation phase has an additional interpretation. The results show that, at least for the tested flow conditions, the surface processes have major importance all the active components that are not surface-bound are washed away by flow. Provided that in an area there is a triggering for the initiation of coagulation the effects, during the time interval between the initiation and the propagation the quantity platelets in the reacting site increases, and the majority of them are not yet activated. The burst of thrombin concentration during the propagation phase will cause the activation this large amount of platelets that will remain immobilized near the reacting site. **Therefore a big time interval between triggering and propagation may enhance locally the coagulation process.**

The connection between the downstream propagation time and the amount of bound platelets at the beginning of the propagation phase can lead to another conclusion. The propagation time, except from the geometric characteristics of each case, is also related to the TGA results of a patient. The rate constant for the surface related initiation in the used coagulation model is mainly determined by the lag time of thrombin generation curve. This means that increased lag time in the TGA results will lead to increased downstream propagation times for coagulation under flow conditions and larger amount of bound platelets at the beginning of the propagation phase. **So, it is very possible that this large amount of bound platelets at the beginning of the propagation phase enhances the coagulation locally in patients with increased lag time in the TGA and therefore these patients have increased risk for thrombotic complications compared with patients with smaller thrombin lag time.**

Compared to the flow-based assessment presented in the previous chapter, the application of the coagulation model on the same flow fields indicated different areas as of high risk with more characteristic the case STABLE with 35% degree of stenosis, in which almost all flow related risk indexes were lower than the suggested threshold while the application of the model showed revealed a large area of high risk, where both thrombin concentration and production rate had high values. This was somehow expected, as the two methods actually focus on different things. The flow-based assessment criteria, mainly WSS related, **indicate areas that are prompt to cause the initiation of the coagulation process** either due to extremely low values of WSS and alteration of the endothelium properties, either due to high or oscillating values of WSS that could lead to a rupture of the atheromatous plaque. On the contrary, the coagulation

model is supposed to **describe the progress of the phenomenon once the triggering is present**. Therefore the two methods are meant to complete each other rather than contradict. It is important though that **the thrombus model indicated as high risk areas the part of the wall that was near the recirculation vortex and specifically near the site of the vortex where the flow was inversed** compared to the dominant direction of the flow.

The average values of thrombin concentration and production rate, although corrected in order to take into account the different downstream length from the reacting site to the outlets which is significantly smaller for STABLE geometries still contain an error that cannot be corrected. The time interval between the moment blood passes the reacting site and the moment it reaches the exit of the computational domain is different, smaller for the STABLE geometry. So the production and inhibition reaction (except for the surface production terms) occur in different extend within the different geometries. Unfortunately, although this error was identified, it was not possible to find a way to correct it, so the only correction performed was based on the downstream surface magnitude. Therefore, the comparison of the average values (and possibly maximum value as well) between the MI models and the STABLE models is somehow risky. However it is believed that a minor commentary is allowed. The average value of thrombin concentration was for all degrees of stenosis higher for the model which had the minimum amount of bound activated platelets at the moment of downstream propagation. This indicates that when the initial surface activity is more or less enough to cause downstream propagation, larger quantities of thrombin are transported downstream the reacting area, while the surface activity due to bound activated platelets has more local effects. The average production rate was negative for the whole time interval after the downstream propagation with only exception of MI1 and STABLE cases with 35% degree of stenosis where it also had positive values for a time interval. As in this number are summed up both production and inhibition, so actually a small value can be either due to very small or due to very high production and inhibition rate, in theory the interpretation is controversial. In the studied cases though, small absolute values of average production rate were always combined with restriction of high concentration of thrombin to small regions of the vessel wall.

Chapter 6 Overview, conclusions and future work

The main idea behind this work was to investigate whether it is possible to perform an assessment of the thrombogenic risk of different LAD geometries and more generally coronary artery geometries with the use of computational methods. For that purpose were constructed a number of geometries that were previously assessed as of different risk for CAD complications in other works with the use of statistical methods. So, one **main hypothesis behind this work was that the geometries of the group named STABLE were less prone to lead to complications compared to the geometries of the MI1 and MI2 groups.** Consequently, one of the main questions this work had to answer was whether this different risk was mirrored somehow in the results of the simulations and if it was possible for the risk to be expressed in a quantitative arithmetic manner.

The work in its final form consisted from two almost independent parts. Initially, a phenomenological thrombus model was developed. Then a method for simulating the flow in LAD arteries was developed and some complication risk indices were proposed, based on identified physical mechanisms that are related to the progression of CAD and thrombus formation. Finally, these two independent tasks were combined in the last chapter where the coagulation model was applied under transient flow conditions. As a general conclusion, CFD results had significant differentiation between the different groups; the flow related complication indices were in agreement with the initial hypothesis. This result indicated that the use of CFD for the assessment is feasible. The coagulation model had also different behaviour for the different geometrical models but in a manner that made it hard to extract general conclusions.

6.1 Thrombus modelling

6.1.1 Overview of model development

In Chapter 3 a simplified model was proposed that simulates the coagulation process up to the activation of thrombin. The development of the model was performed in three steps. As most part of the biochemical reactions involved in the coagulation process occurs between the initial triggering and thrombin formation, the first step was to propose a set of equations describing that part of the process. As the final purpose of the model was to be appropriate for coupling with CFD simulations of relatively large scale,

the minimum number of substances (prothrombin, thrombin, resting and activated platelets) and equations (one differential equation for each substance) was used. At the same time the model was built in such a way that would enable the differentiation of the processes with respect to the location they occur (plasma, activated platelets or vessel surface) according to the cell-based models of coagulation rather than following the cascade models. The cell based models divide the processes of coagulation to three distinct parts: initiation, amplification and propagation. In this work each part is actually related to the different parts of thrombin generation curve in TAGs. Each of the model's reactions represented a number of actual processes. Therefore, there were no available constants for the reaction rates of each source term from previous experimental works. To obtain values for the reaction rate constants initially a rough estimation was performed using calculations and values from previous computational works (which alone gave reasonable results). The estimated initial set of values for the reaction rate constants of the model was necessary as a starting point for the fitting of the model as it provided a reasonable range for the value of each constant. Following that, the initial values of the reaction rates were corrected and fine-tuned using the results of thrombin generation assays (TGA), by modifying each one of the constants within the range that the initial estimations determined. TGAs provide a curve that represents thrombin concentration versus time in vitro, after stimulation with tissue factor, a substance that is also exposed when there is endothelium or plaque rupture.

The second step was the development of a model for the aggregation of platelets on a reacting surface. This was done by using experimental data for the aggregation of platelets on a reacting part of a tube shaped flow chambers for different values of (wall) shear rate. In the initial form the platelet aggregation sub-model did not distinct between resting and activated platelets, so it was formulated using two species (circulating and bound platelets) and three different processes, platelets binding on surface, platelets binding on bound platelets and unbinding of bound platelets. The reaction rate for the binding of platelets was shear-dependent. Initial values for the reaction rate constants of the processes were again obtained using previous works and rough estimations. The model was applied to three different cases (for different values of shear rate) and the reaction rate constants were corrected using the trial and error method, until the results of the simulations matched with acceptable accuracy the available experimental results. The method gave good results for the three different cases with the use of a shear dependent reaction rate constant for the aggregation with the main insufficiency being that due to its structure it was unable to reproduce the

reduction of the amount of bound platelets.

The third step during the development of the coagulation model was the calibration under flow conditions. The constants of the thrombin sub-model were obtained using data from TGA which is steady state (in terms of flow) experiment where also the reacting substances including the triggering one (TF) are well mixed and the reaction rate constant for the initiation reaction was calculated for this conditions. However, when the process is initiated in a vessel under flow conditions, the triggering substance is expressed only on the reacting site of the vessel wall, so the source term describing the initiation of coagulation needed to be converted from a bulk to a surface one. The correction was based on experiments describing the threshold behaviour of the coagulation process in respect to the stream-wise length of the reacting area (a TF bearing patch) and the shear rate. The reaction rate constant for the surface source term of the initiation (which replaced the bulk term) was changed using again a trial and error method until we had agreement with the results reported (initiation or no-initiation) for all the cases. As 'initiation' we identified the appearance of high thrombin (above threshold) concentration downstream the reacting site. This process was performed without the terms describing the aggregation of platelets as the substances involved on platelet aggregation were not present or active in the experiment. It was interesting that the resulting value for the reaction rate of the surface initiation obtained with the use of this method was close to the one estimated by the size of the computational cell and the surface density of TF in atheromatous plaques. The main conclusions drawn from the process of thrombus modelling are the following:

- The simplified thrombin sub-model was proved capable of reproducing TGA results for different cases (including haemophilia) while at the same time the results of the model with a fixed setup of the constants followed the changes in initial conditions (mainly platelet concentration) with acceptable accuracy. Therefore **it was showed that it is possible to reproduce the part of the coagulation reactions up to thrombin generation using only 4 substances and 4 equations.** Additionally, although the development of the thrombin sub-model was zero dimensional, **it is structured in such a way that it can account for processes occurring at different locations.**

- The proposed set of equations has a case specific character as with appropriate modification of the constants it is able to reproduce different TGA results that may correspond to different patients.
- Platelet aggregation can be modelled with the use of shear dependent aggregation rate constants and reproduce the initial aggregation rate and maximum concentration of bound platelets.
- The disaggregation of platelets that is observed for high values of wall shear rate (after ~10 minutes) of perfusion is not captured. As this disaggregation is possibly due to stress accumulation, requires a different approach that would model the temporal evolution for the whole aggregate in order to be captured.
- **The exact concentration of TF on the reacting surface might not change significantly the constant of the initiation for the phenomenological model** a reasonable result as TF acts as a catalyst for the initiation .
- The experimental data on the threshold behaviour of coagulation reported a minimum size for the stream-wise length of the reacting surface for a given value of the wall shear rate and a maximum value for wall shear rate for a given size of the reacting area. Exploiting these findings, **we introduced coagulation activation index (CAI), a number that indicates whether coagulation is initiated under specified flow conditions for a given reacting area**, and using the available data we proposed a threshold value for the initiation. In test simulations with steady flow the process was indeed initiated when CAI exceeded the threshold value, while for sub-threshold setup maximum concentration of thrombin was proportional to the value of CAI.
- The initiation and also the amplification of the coagulation was limited in a small depth near the reacting wall. This finding was confirmed also by the application of the model on the realistic geometries.
- It was observed that the model's results under flow were sensitive to small changes of the reaction rate constants, especially with respect to the initiation and the inhibition. This finding demonstrates that patient specific conclusions require taking into account the different coagulability of each individual.

The model in its final form had some additional species (compared to the sub-models) in order to make the distinction between bound and circulating platelets that can be either in resting or activated state. In a last step two more aspects were incorporated into the model. The first one was the addition of a term that altered the behaviour of the activated platelets compared to the resting platelets. With this modification activated

platelets were more prone to bind and more unlikely to unbind. Although based on a reasonable assumption and estimations from experimental data, this change had minor effect on the model behaviour under flow for the time interval of the simulations. The second one was the addition of a very slow term of platelet activation due to contact with the reacting site. The overall of the binding-unbinding in at different rates depending on whether the platelets are activated or resting and activation due to contact are used to mimic the transition of platelet behaviour from tethering to forming permanent bonds.

6.1.2 Discussion and suggestions for future work on coagulation model

The proposed phenomenological model for blood coagulation focuses mainly on thrombin generation, as in this work we did not want to include processes that alter the flow conditions. However it is possible and probably useful **as a next step to make additions to the model in order to include the processes that describe the final step of coagulation, fibrin activation and cross-linking and fibrinolysis.**

Additionally, in order to capture the effect of thrombus formation on the local flow conditions, the spatial development of the clot, the entrapment of circulating platelets and in the fibrin mesh should be included. As the most part of coagulation reactions are already included in the model the next step could be added independently, with the only interaction with the existing model being the binding of thrombin on fibrin strands which has effect on the inhibition rate of thrombin. Finally the platelet aggregation model could possibly be improved (if appropriate experimental data exist) as the distinction made for the behaviour of resting and activated platelets is somehow oversimplified.

Thrombin sub-model was based on clinical rather than laboratory information. It is intended to maintain this characteristic for the further additions to the model. So the platelet aggregation equations should be re-calibrated according to the results of clinical platelet function assays. This modification will provide to the function of platelets a patient specific character. The same concept will be used for fibrin polymerization and lysis. The results of the thromboelastography can be used to model the last steps of

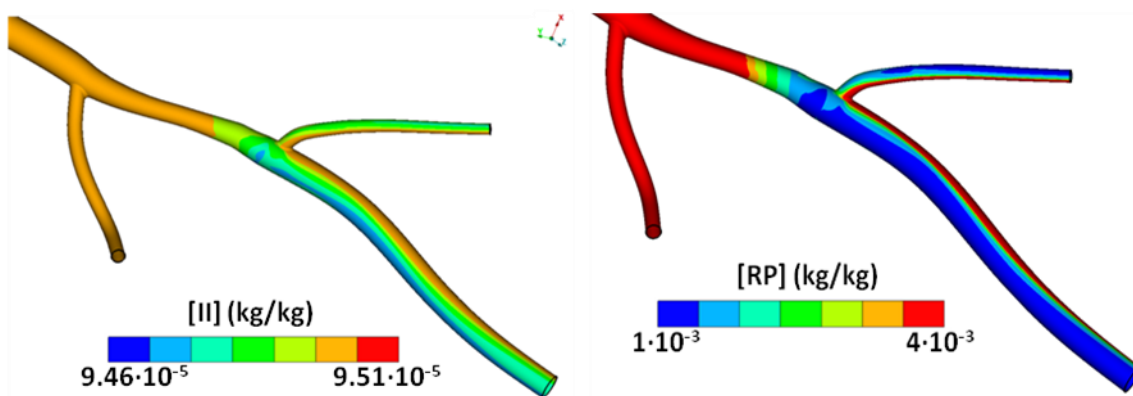


Figure 6-1: (left) The variation of prothrombin concentration. The snapshot is from STABLE model with 35% stenosis, and one of the moments with lowest [II] concentration yet the maximum variation is approximately 0.5%. (right) The variation of resting platelet concentration. The case is different compared to prothrombin as in some areas the concentration falls to the 25% of its initial value.

thrombus formation in a phenomenological and patient specific manner, similar to the methods used for thrombin in this Thesis.

The application of the model under transient flow conditions revealed that there was room for some simplifications and probably some improvements as well. First of all, the concentration of prothrombin seems to have very small variations when the model is applied under flow. While during the calibration of the thrombin sub-model the initial concentration of prothrombin had crucial role as it influenced all the parameters of TGA, under flow conditions the case is different. The maximum variation is 0.5% (figure) which respectively causes a 0.5% reduction of the thrombin production source terms, where prothrombin concentration is involved. As this change is small compared both to the approximations of the model but also the accuracy of the experimental techniques measuring thrombin concentration and the inter-laboratory variation of TGA tests, **the species corresponding to prothrombin may be omitted on the model and the initial prothrombin concentration value can be merged into the reaction rate constants.** Unfortunately the case is not the same for resting platelets, as there is significant variation of the concentration.

Another interesting conclusion when applying the model under flow conditions was the crucial role of shear. Under conditions of increased shear similar to what prevails in coronary artery ($\sim 1000s^{-1}$) any quantities of thrombin produced due to surface activity are abducted by flow. In the proposed model this is compensated by the binding and activation of platelets, which increase the activity of the reacting surface and probably also by the extremely large size of the reacting area. As several coagulation factors actually bind on endothelium cells and on platelets **it is possible that the model would become more realistic if it included a term for bound thrombin, similar to the term for bound platelets.** Unfortunately we have not come across any experimental data that would allow us to include such a term in the model in a reliable way. This could be possibly achieved by performing coagulation experiments under flow conditions, using a solution of coagulation factors over immobilized activated platelets and measuring the amount of the coagulation factors in the area of the activated platelets. Repeating the same process without the presence of activated platelets and possibly correcting for any extra amount of coagulation factors produced, the amount of coagulation factors that are bound on the reacting substrate can be estimated.

6.2 Flow simulations and risk factors

6.2.1 Overview of simulation results

In chapter 4 a flow based assessment of LAD geometries in respect to complications or rapid deterioration of coronary artery disease was introduced. The first step was the construction of 16 different LAD geometrical models, one healthy and three groups with induced stenosis (MI1, MI2 and STABLE). Each group consisted of 5 geometries with different degree of stenosis (20%, 35%, 50%, 70% and 90%) with the stenotic lesion located at a different site in each model. According to previous works these geometries were considered of different risk. After performing indicative mesh independence tests a computational mesh of approximately 1.5 million cells with refined boundary layer was constructed for each model.

Following that, we developed a simplified method in order to obtain boundary conditions for the inlet and the outlets of each model. The method uses as inputs the geometric features of the model (diameters of main branch and bifurcations) and the pressure (aortic pressure) and the mass flow rate at the inlet of healthy coronary. For the inlet we used average waveforms for mass flow rate and aortic pressure throughout one cardiac cycle under resting conditions. The method can be easily applied on any arbitrary coronary artery geometry.

Transient numerical simulations of the flow were performed for each case. Blood was modelled as Newtonian fluid and the flow was considered laminar. The results were periodic after the first cardiac cycle of simulations and the resulting waveforms for mass flow rates resembled waveforms obtained by in-vitro and ex-vitro experiments. The resulting flow field was processed for the geometries with stenosis up to 70% and average wall shear stress, oscillating shear index and relative residence time were calculated over the time of one heart circle as well as coagulation activation index with the use of average wall shear rate value and an estimation for the reacting area. We identified the sites of the models where wall shear stress had very high or low values and where oscillating shear index and relative residence time had very high values. The range of 'normal' values for these quantities was basically based on the results obtained for the healthy geometry while especially for the wall shear stress we also took under consideration the values reported in previous studies. The findings of this part can be summarized as follows:

- The culprit flow patterns as recirculation zones and areas with low and high TAWSS were present to a greater extent in geometries of higher complication risk when comparing models with the same degree of stenosis.
- The complication related flow patterns were expressed via arithmetic indices and non-pathological limits were proposed for each index. This makes possible the assessment of an arbitrary coronary geometry.
- Most indices showed that in general, the properties of the flow field are strongly influenced by the degree of the stenosis but the location of the stenosis has also a very important impact.
- **The geometries of the group MI2 (two bifurcations involved in the stenosis) had higher values of the risk indices followed by the models of MI1 group (one bifurcation in the stenosed lesion), with STABLE group (no side branches affected) having lower values for stenosis up to 50%.** For the models with 70% stenosis the indices had similar values for all groups.
- **CAI had exceeded the suggested safe value only for the cases MI1 and MI2 with stenosis 35% and 50% while the rest of the models had clearly lower values.** This shows that only in the models of high risk the areas where local flow conditions favour the initiation of coagulation were sufficiently large.

6.2.2 Suggestion for improvement of flow based assessment method

A simple method for simulating blood flow, both in respect to viscosity model and boundary conditions was chosen. This approach, except for the fact that it reduces the computational cost, it makes the method repeatable in an identical manner on any coronary geometries.

Boundary conditions are obtained with a method that can be further evolved in order to include more of the actual factors that determine the flow field in coronary artery (counter pressure from myocardial contractions, changes of the volume of the downstream vessel network etc) while still applied in the same manner. However, while such additions in boundary conditions might change the mass flow rate distribution among the vessel branches, there is no reassurance that they would also lead to improved accuracy of the method or to a more patient specific character. The use of more complicated methods for the application of boundary conditions leads inevitable to a large number of assumptions, regarding mainly the downstream vessel network and introduces an additional number of parameters that are not accessible in a patient specific manner. Therefore, I considered more important to propose a method that can

be directly applied on any coronary geometry. This approach makes any obtained results consistent and directly comparable. The proposed method also allows the modification of the pressure and flow waveforms used for the inlet according to the size of the vessel, the patient weight or in order to simulate hyperaemic blood flow.

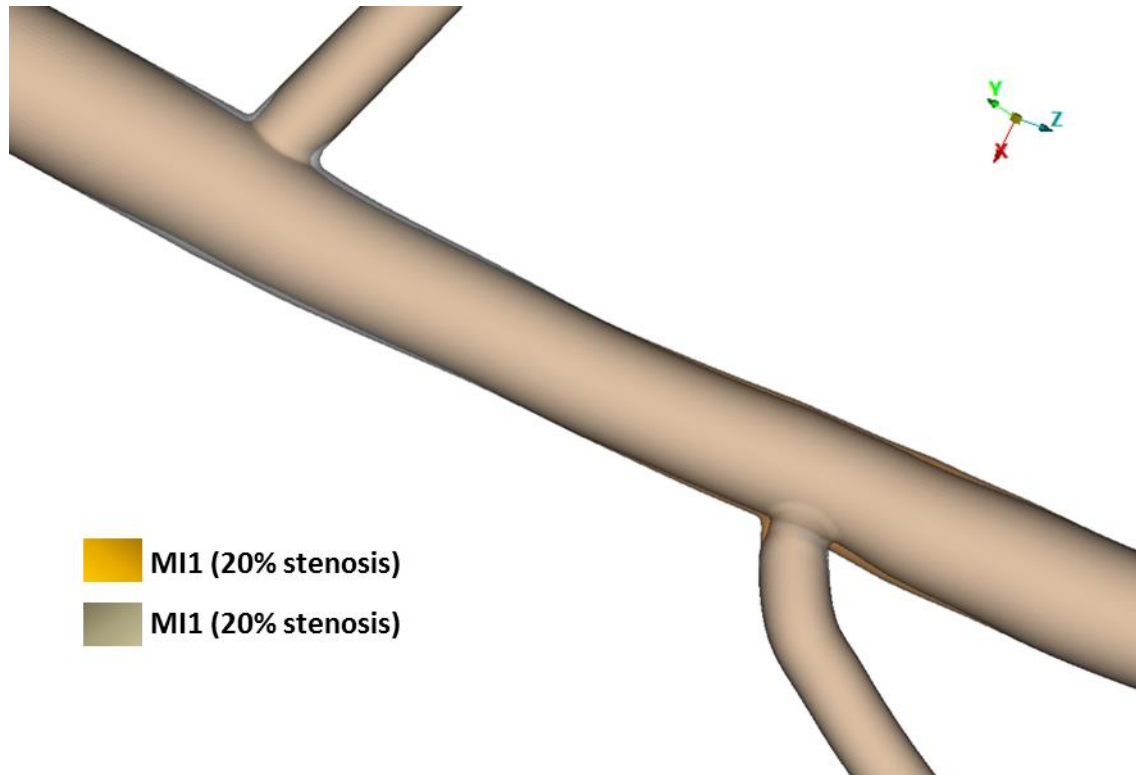


Figure 6-2: MI1 (orange) and MI2 (grey) models with 20% degree of stenosis. The differences between the two geometries are hard to distinguish and although these two models are supposed to be classified in different groups it is doubtful if a performed-from-scratch geometrical classification would make that distinction. The flow fields however have noticeable differences, as shown in chapter 4.

In all cases, the assessment based on flow simulation results is possible to overlap with assessment based purely on the geometrical characteristics of the coronary, similar to what is proposed by Wellenhoffer et al [230, 231]. It is also possible that in several cases the results of the two different methods of assessment might be similar, as the areas with extreme values of WSS and other quantities are actually determined by the shape of the vessel. To go one step further, **it is almost impossible to reproduce the exact flow conditions in an fully individual specific manner, as the heart cycle has variations, so even this so called flow based assessment is actually geometry assessment based on flow simulations, as it cannot be argued that the applied flow conditions can represent the real conditions in each individual.** Nevertheless, the use of flow

simulations in chapter 4 revealed that small differences between two geometries can lead to significant alterations on the characteristic quantities of the calculated flow field. For example, between the cases MI1 and MI2 with 20% of stenosis (Figure 6-2) and also the STABLE geometry with the same degree of stenosis (not shown), the differences in geometry are hard to distinct. On the other hand, the indexes related to low and high TAWSS are approximately one and two orders of magnitude higher respectively for MI2 model (the exact ratios are 7.22 and 99). This indicates –provided that we accept the relationship of flow with CAD progress and we trust the CFD results of course- that **geometrical assessment cannot substitute the assessment via flow simulation** as probably there is no geometrical criterion that would classify two real geometries with such small differences in different category. Indicative, the remodelling index $RI = 100 \cdot (D_s/D_{in})^2$ proposed by Wellenhofer et al [86] calculated for the models presented in Figure 6-2 with the use of the minimum diameter D_s in the stenotic lesion and the inlet diameter D_{in} is 21.43 for the MI1 geometry and 21,7 for the MI2 geometry.

The only justification for the fact that MI1 and MI2 geometries with 20% belong to different groups in this Thesis are the statistically derived criteria used for the reconstruction of the LAD geometrical models.

The main drawback of the method is that it was applied in a small number of geometries that additionally were derived using the same initial ‘average’ healthy model. The establishment of the physiological range of the risk indexes was thus based only on a number of simulations on a group of models with very similar geometrical characteristics (except for the stenosis location and degree). So, while based on the results it is demonstrated that it is possible to assess the risk of a LAD or coronary geometry based on CFD simulation, **the exact limits for the physiological range that we propose for the risk indexes except for CAI are rather indicative and further investigation in real coronary geometries with known progress is required** before they can be actually be used as diagnostic tools (from follow-up studies on CAD patients).

6.3 Thrombus model under transient flow conditions

In the last chapter the thrombus model was applied on the realistic models of stenosed LAD arteries under transient flow conditions. This part of the work exhibited certain (expected) difficulties. Obviously, there are no experimental data for the temporal and

spatial evolution of blood coagulation in vivo, so there is no way to validate the results of the simulations and perform any correction to the method. Besides that there are also additional information missing. The probable size and position of the reacting areas are unknown. The actual time scale of the phenomenon is also unknown and assumed to be in the order one day, and there is also big difference between the timescale of the heart pulse (approximately one second) and the time scale of thrombin and platelet aggregation sub-models (approximately five minutes). As one minute of simulation corresponded to 80 pulses or 8000 time instances of the flow, performing simulation for time interval of the order of days (about 10 million time instances) as a test was out of the question.

So we had to compromise in respect to the accuracy for all these aspects of the problem. We used a simplified pulse of 10 time instances (9 time intervals), and we restricted the simulation time up to 8 minutes. The simulation time was not the same for all cases, as we used as a criterion the downstream propagation of elevated thrombin concentration, and continued the simulation for two more minutes. As a reacting surface we used a part of the stenotic lesion, of the same stream-wise length for all cases, approximately 6mm. We made that choice, knowing that the total size of the reacting surface would be smaller for higher degrees of stenosis, because the experimental data used in Chapter 3 emphasized on the significance of the stream-wise length. As we applied the exact same method for all the cases we believe that our results can be trusted for a first comparison on how coagulation evolves in different cases, but we cannot guarantee that they depict the actual evolution of the process as it would be in *-vivo*. The results showed that:

- Similar to the flow simulations in Chapter 4, the model's behaviour was strongly influenced by the degree of stenosis and especially the models with 70% stenosis of all three groups exhibited similar but not identical results..
- Downstream propagation required more time and larger amount of bound activated platelets for higher degrees of stenosis. For the same degree of stenosis STABLE cases were the faster ones followed by MI1 cases with MI2 having the slowest evolution. Thrombin concentration downstream the reacting area reached concentrations much higher than threshold value, but lower than the typical peak concentration of the TGA.
- In order to distinguish the areas of higher risk for thrombus development we sought for sites where both thrombin concentration and thrombin production rate had elevated values. In MI2 cases those areas were small and localized,

while in STABLE group there were large areas with high thrombin concentration which in the 35% model also included some smaller areas with rapid thrombin production. MI1 models had an intermediate behaviour, with the geometries with low degree of stenosis behaving similarly to the STABLE model and the geometry with 70% similarly to the MI2 models. However as stated earlier the results' variation did not allow the extraction of some generalized conclusions on the behaviour of thrombus formation.

- A prolonged lag phase of thrombin generation in a thrombin generation assay is mainly related to hypocoagulable states. Increased lag time is observed in cases with reduced stimulation or increased inhibition of thrombin [232]. On the contrary, the application of the coagulation model under flow shows that a prolonged initiation phase leads to increased accumulation of a platelets at the reacting site. These bound platelets will become activated during the propagation phase and contribute locally to thrombin generation. The observed mechanism indicates that it is very possible that the prolonged lag phase indicates increased risk for thrombotic complications in vivo, provided that an initiation stimulus is present..

This work includes both zero dimensional simulation of thrombin production and simulation of thrombin production under flow. Modelling of thrombus formation, besides reproducing the clinical tests, can also be used for studying the formation of clot under flow conditions. Coagulation in vivo occurs under flow and this fact can change the importance of each parameter in respect to the steady state system. For example, it was demonstrated earlier while initial prothrombin concentration plays a major role in closed, zero dimensional systems, it is of minor importance under flow. Also, in all cases where the thrombus model was applied under transient flow conditions in the whole process was localized near the vessel wall. The vast majority of the related experimental data though, are derived from steady state experiments with the reactants being in solutions with uniform spatial concentrations. . This is probably due to the fact that the experiments under flow are more difficult to standardize and require much larger quantities of samples. Generally in the literature there is a lack of experimental data, especially quantitative, referring to the coagulation process under flow conditions. **In order for more reliable and accurate detailed or simplified models for coagulation under flow to be built, is required experimental data focusing on what happens under flow conditions (no depletion and stagnation of reactants) and paying special**

attention on the surface related processes near the vessel wall. A good example of the type of work required is the experimental study of Reininger et al [130], where material from human atheromatous plaques was exposed to blood and thrombin generation and platelet aggregation was measured under steady and flow. Performing a similar experiment for a larger variety of samples (TF, zymogen and platelet concentrations) and a wider range of flow conditions **can correlate the results of the currently used coagulation assays with coagulation under flow.**

To the best of my knowledge, this is the first attempt of applying even a simplified model of coagulation on a large number of realistic geometries under pulsating flow conditions. The comparison of the results, although they did not provide clear conclusions, showed that there are big differences in the behaviour of the model among different geometries. The huge volume of the result files is an additional obstacle in the process of extracting specific conclusions. As this study has mainly comparative character, as a next step I intend to apply the same method under average steady flow conditions, for different sizes and location of the reacting areas including the sites of low shear rate identified with the use of flow simulations. This might provide more clear differentiation of the results and maybe the extraction of some arithmetic indexes similar to the ones extracted for the flow conditions in chapter 4.

The supplementary character of the two methods used for the assessment of flow effect on thrombus formation must be emphasized. The flow-based assessment focuses both on the possibility of deterioration of the case and on the possibility of thrombus formation, as the progression of coronary artery disease is also related to wall shear rate and wall shear stress distribution. It deals with the possible growth of the atheromatus plaque and the identification of sites where pathological flow conditions may alter the behaviour of the endothelium, triggering the initiation of coagulation. On the other hand, the application of thrombus model is focusing on what happens after this triggering occurs, and whether the initiation leads to elevated thrombin concentration and thrombin production rate. Therefore an integrated assessment of a case requires the combined application of both methods, and the total risk for each patient should come from the co-estimation of the results.

Considering the differentiation of the conditions among patients (coronary shape diversity, blood coagulability and flow conditions) it is possible that the optimum treatment is not the same for all patients and that the problem cannot be answered using only the statistical approach. The use of different clinical scenarios cannot indicate the

preferable treatment for all cases where acute symptoms are absent. In this work it is supported that the problem can be approached in a more patient specific manner using computer simulations. A method that uses as input the images from coronary angiographies and the blood coagulation test of a patient and estimates the risk of thrombotic complications is presented. Unfortunately, the small number and variety of the geometrical models used does not allow a safe definition of the non-pathological values of the calculated quantities. However, this first application showed that the results of the simulations can be correlated with the complication risk. In order for these methods to be used in clinical practice, the application on a large number of real patient cases with known outcome is required, in order to have a statistical confirmation (and possibly correction) of the indices calculated for each case. The vision for the future of this work is to apply the developed method on a relatively small number (~20) of real cases including cases with stable CAD, ACS, wide range of TGA results and, if possible, cases, where acute syndromes 'were not expected'. After detailed examination of the results the non-pathological limits of the risk indices that are proposed here will be reconsidered and it will also be specified whether the risk is due to pathological flow or different coagulation potential for each case. After a final test on a larger number of patients I believe that the method will be appropriate to be used in clinical practice as an assessment tool.

References

1. Katritsis, D.G., et al., *Anatomic Characteristics of Culprit Sites in Acute Coronary Syndromes*. Journal of Interventional Cardiology, 2008. **21**(2): p. 140-150.
2. Badimon, L., et al., *Influence of arterial damage and wall shear rate on platelet deposition. Ex vivo study in a swine model*. Arteriosclerosis, Thrombosis, and Vascular Biology, 1986. **6**(3): p. 312-20.
3. Shen, F., et al., *Threshold Response of Initiation of Blood Coagulation by Tissue Factor in Patterned Microfluidic Capillaries Is Controlled by Shear Rate*. Arteriosclerosis, Thrombosis, and Vascular Biology, 2008. **28**(11): p. 2035-2041.
4. Go, A.S., et al., *Heart Disease and Stroke Statistics—2013 Update: A Report From the American Heart Association*. Circulation, 2013. **127**(1): p. e6-e245.
5. Rayner, M., et al., *Cardiovascular disease in Europe*. European Journal of Cardiovascular Prevention & Rehabilitation, 2009. **16**(2 suppl): p. S43-S47.
6. Allender, S., et al., *European cardiovascular disease statistics*. European Heart Network, 2008. **3**: p. 11-35.
7. Mozaffarian, D., et al., *Heart Disease and Stroke Statistics—2015 Update: A Report From the American Heart Association*. Circulation, 2015. **131**(4): p. e29-e322.
8. Uren, N.G., et al., *Relation between myocardial blood flow and the severity of coronary-artery stenosis*. New England Journal of Medicine, 1994. **330**(25): p. 1782-1788.
9. Head, S.J., et al., *The rationale for Heart Team decision-making for patients with stable complex coronary artery disease* 2013.
10. Simoons, M.L. and S. Windecker, *Controversies in Cardiovascular Medicine Chronic stable coronary artery disease: drugs vs. revascularization* 2010.
11. Yusuf, S., et al., *Effect of coronary artery bypass graft surgery on survival: overview of 10-year results from randomised trials by the Coronary Artery Bypass Graft Surgery Trialists Collaboration*.

- The Lancet, 1994. **344**(8922): p. 563-570.
12. Schömig, A., et al., *A Meta-Analysis of 17 Randomized Trials of a Percutaneous Coronary Intervention-Based Strategy in Patients With Stable Coronary Artery Disease*. Journal of the American College of Cardiology, 2008. **52**(11): p. 894-904.
 13. Trikalinos, T.A., et al., *Percutaneous coronary interventions for non-acute coronary artery disease: a quantitative 20-year synopsis and a network meta-analysis*. The Lancet, 2009. **373**(9667): p. 911-918.
 14. Boden, W.E., et al., *Impact of Optimal Medical Therapy With or Without Percutaneous Coronary Intervention on Long-Term Cardiovascular End Points in Patients With Stable Coronary Artery Disease (from the COURAGE Trial)*. The American Journal of Cardiology, 2009. **104**(1): p. 1-4.
 15. Boden, W., et al., Title LM, Gau G, Blaustein AS, Booth DC, Bates ER, Spertus JA, Berman DS, Mancini GB, Weintraub WS. *Optimal medical therapy with or without pci for stable coronary disease*. N Engl J Med, 2007. **356**(15): p. 1503-1516.
 16. Jeremias, A., et al., *The Impact of Revascularization on Mortality in Patients with Nonacute Coronary Artery Disease*. The American Journal of Medicine, 2009. **122**(2): p. 152-161.
 17. Hueb, W., et al., *Five-Year Follow-Up of the Medicine, Angioplasty, or Surgery Study (MASS II): A Randomized Controlled Clinical Trial of 3 Therapeutic Strategies for Multivessel Coronary Artery Disease*. Circulation, 2007. **115**(9): p. 1082-1089.
 18. Kappetein, A.P., et al., *Comparison of coronary bypass surgery with drug-eluting stenting for the treatment of left main and/or three-vessel disease: 3-year follow-up of the SYNTAX trial*. European Heart Journal, 2011. **32**(17): p. 2125-2134.
 19. Mohr, F.W., et al., *Coronary artery bypass graft surgery versus percutaneous coronary intervention in patients with three-vessel disease and left main coronary disease: 5-year follow-up of the randomised, clinical SYNTAX trial*. The Lancet, 2013. **381**(9867): p. 629-638.
 20. Hachamovitch, R., et al., *Comparison of the Short-Term Survival*

- Benefit Associated With Revascularization Compared With Medical Therapy in Patients With No Prior Coronary Artery Disease Undergoing Stress Myocardial Perfusion Single Photon Emission Computed Tomography.* *Circulation*, 2003. **107**(23): p. 2900-2907.
21. Stone, G.W., et al., *A Prospective Natural-History Study of Coronary Atherosclerosis.* *New England Journal of Medicine*, 2011. **364**(3): p. 226-235.
 22. Patel, M.R., et al., *ACCF/SCAI/STS/AATS/AHA/ASNC 2009 Appropriateness Criteria for Coronary Revascularization. A Report by the American College of Cardiology Foundation Appropriateness Criteria Task Force, Society for Cardiovascular Angiography and Interventions, Society of Thoracic Surgeons, American Association for Thoracic Surgery, American Heart Association, and the American Society of Nuclear Cardiology Endorsed by the American Society of Echocardiography, the Heart Failure Society of America, and the Society of Cardiovascular Computed Tomography.* *Journal of the American College of Cardiology*, 2009. **53**(6): p. 530-553.
 23. Patel, M.R., et al., *ACCF/SCAI/STS/AATS/AHA/ASNC/HFSA/SCCT 2012 Appropriate Use Criteria for Coronary Revascularization Focused Update A Report of the American College of Cardiology Foundation Appropriate Use Criteria Task Force, Society for Cardiovascular Angiography and Interventions, Society of Thoracic Surgeons, American Association for Thoracic Surgery, American Heart Association, American Society of Nuclear Cardiology, and the Society of Cardiovascular Computed Tomography.* *Journal of the American College of Cardiology*, 2012. **59**(9): p. 857-881.
 24. Ku, D.N., et al., *Pulsatile flow and atherosclerosis in the human carotid bifurcation. Positive correlation between plaque location and low oscillating shear stress.* *Arteriosclerosis, Thrombosis, and Vascular Biology*, 1985. **5**(3): p. 293-302.
 25. Asakura, T. and T. Karino, *Flow patterns and spatial distribution of atherosclerotic lesions in human coronary arteries.* *Circulation Research*, 1990. **66**(4): p. 1045-1066.
 26. Friedman, M.H., et al., *Relationship between the geometry and quantitative morphology of the left anterior descending coronary*

- artery. *Atherosclerosis*, 1996. **125**(2): p. 183-192.
27. Krams, R., et al., *Evaluation of Endothelial Shear Stress and 3D Geometry as Factors Determining the Development of Atherosclerosis and Remodeling in Human Coronary Arteries in Vivo: Combining 3D Reconstruction from Angiography and IVUS (ANGUS) with Computational Fluid Dynamics*. *Arteriosclerosis, Thrombosis, and Vascular Biology*, 1997. **17**(10): p. 2061-2065.
 28. Stary, H., et al., *A definition of the intima of human arteries and of its atherosclerosis-prone regions. A report from the Committee on Vascular Lesions of the Council on Arteriosclerosis, American Heart Association*. *Circulation*, 1992. **85**(1): p. 391.
 29. Zhu, H., et al., *Cataloguing the geometry of the human coronary arteries: a potential tool for predicting risk of coronary artery disease*. *International Journal of Cardiology*, 2009. **135**(1): p. 43-52.
 30. Katritsis, D.G., et al., *Ruptured versus stable plaques in human coronary arteries*. *Coronary Artery Disease*, 2011. **22**(5): p. 345-351 10.1097/MCA.0b013e3283471f95.
 31. Virmani, R., et al., *Lessons From Sudden Coronary Death: A Comprehensive Morphological Classification Scheme for Atherosclerotic Lesions*. *Arteriosclerosis, Thrombosis, and Vascular Biology*, 2000. **20**(5): p. 1262-1275.
 32. Caro, C.G., J.M. Fitz-Gerald, and R.C. Schroter, *Atheroma and Arterial Wall Shear Observation, Correlation and Proposal of a Shear Dependent Mass Transfer Mechanism for Atherogenesis*. *Proceedings of the Royal Society of London. Series B. Biological Sciences*, 1971. **177**(1046): p. 109-133.
 33. Tzima, E., et al., *Activation of integrins in endothelial cells by fluid shear stress mediates Rho-dependent cytoskeletal alignment*. *The EMBO Journal*, 2001. **20**(17): p. 4639-4647.
 34. Malek, A.M., S.L. Alper, and S. Izumo, *Hemodynamic shear stress and its role in atherosclerosis*. *JAMA: the journal of the American Medical Association*, 1999. **282**(21): p. 2035-2042.
 35. Davies, P.F. and S.C. Tripathi, *Mechanical stress mechanisms and the cell. An endothelial paradigm*. *Circulation Research*, 1993. **72**(2): p. 239-45.

36. Yin, W., S.K. Shanmugavelayudam, and D.A. Rubenstein, *The effect of physiologically relevant dynamic shear stress on platelet and endothelial cell activation*. *Thrombosis Research*, 2011. **127**(3): p. 235-241.
37. Hoffmann, U., et al., *Noninvasive Assessment of Plaque Morphology and Composition in Culprit and Stable Lesions in Acute Coronary Syndrome and Stable Lesions in Stable Angina by Multidetector Computed Tomography*. *Journal of the American College of Cardiology*, 2006. **47**(8): p. 1655-1662.
38. Motoyama, S., et al., *Computed Tomographic Angiography Characteristics of Atherosclerotic Plaques Subsequently Resulting in Acute Coronary Syndrome*. *Journal of the American College of Cardiology*, 2009. **54**(1): p. 49-57.
39. Schroeder, S., et al., *Noninvasive detection and evaluation of atherosclerotic coronary plaques with multislice computed tomography1*. *Journal of the American College of Cardiology*, 2001. **37**(5): p. 1430-1435.
40. Pundziute, G., et al., *Evaluation of plaque characteristics in acute coronary syndromes: non-invasive assessment with multi-slice computed tomography and invasive evaluation with intravascular ultrasound radiofrequency data analysis*. *European Heart Journal*, 2008. **29**(19): p. 2373-2381.
41. Motoyama, S., et al., *Multislice Computed Tomographic Characteristics of Coronary Lesions in Acute Coronary Syndromes*. *Journal of the American College of Cardiology*, 2007. **50**(4): p. 319-326.
42. Arbab-Zadeh, A., et al., *Acute coronary events*. *Circulation*, 2012. **125**(9): p. 1147-56.
43. Slager, C.J., et al., *The role of shear stress in the generation of rupture-prone vulnerable plaques*. *Nat Clin Pract Cardiovasc Med*, 2005. **2**(8): p. 401-407.
44. Samady, H., et al., *Coronary Artery Wall Shear Stress Is Associated With Progression and Transformation of Atherosclerotic Plaque and Arterial Remodeling in Patients With Coronary Artery Disease*. *Circulation*, 2011. **124**(7): p. 779-788.
45. Gibson, C.M., et al., *Relation of vessel wall shear stress to*

- atherosclerosis progression in human coronary arteries.* Arteriosclerosis, Thrombosis, and Vascular Biology, 1993. **13**(2): p. 310-5.
46. Jackson, S.P., W.S. Nesbitt, and E. Westein, *Dynamics of platelet thrombus formation.* Journal of thrombosis and haemostasis : JTH, 2009. **7 Suppl 1**: p. 17-20.
 47. Hathcock, J.J., *Flow Effects on Coagulation and Thrombosis.* Arteriosclerosis, Thrombosis, and Vascular Biology, 2006. **26**(8): p. 1729-1737.
 48. Siediecki, C., et al., *Shear-dependent changes in the three-dimensional structure of human von Willebrand factor.* Blood, 1996. **88**(8): p. 2939-2950.
 49. Nesbitt, W.S., et al., *A shear gradient-dependent platelet aggregation mechanism drives thrombus formation.* Natural Medicines, 2009. **15**(6): p. 665-673.
 50. Sheriff, J., et al., *High-Shear Stress Sensitizes Platelets to Subsequent Low-Shear Conditions.* Annals of Biomedical Engineering, 2010. **38**(4): p. 1442-1450.
 51. Peterson, D., et al., *Shear-induced platelet aggregation requires von Willebrand factor and platelet membrane glycoproteins Ib and IIb-IIIa.* Blood, 1987. **69**(2): p. 625-628.
 52. Moake, J., et al., *Shear-induced platelet aggregation can be mediated by vWF released from platelets, as well as by exogenous large or unusually large vWF multimers, requires adenosine diphosphate, and is resistant to aspirin.* Blood, 1988. **71**(5): p. 1366-1374.
 53. Chow, T., et al., *Shear stress-induced von Willebrand factor binding to platelet glycoprotein Ib initiates calcium influx associated with aggregation.* Blood, 1992. **80**(1): p. 113-120.
 54. Ruggeri, Z.M., et al., *Activation-independent platelet adhesion and aggregation under elevated shear stress.* Blood, 2006. **108**(6): p. 1903-1910.
 55. Taylor, C.A., T.A. Fonte, and J.K. Min, *Computational Fluid Dynamics Applied to Cardiac Computed Tomography for Noninvasive Quantification of Fractional Flow Reserve* Scientific

- Basis*. Journal of the American College of Cardiology, 2013. **61**(22): p. 2233-2241.
56. Morris, P.D., et al., *Virtual Fractional Flow Reserve From Coronary Angiography: Modeling the Significance of Coronary Lesions Results From the VIRTU-1 (VIRTUal Fractional Flow Reserve From Coronary Angiography) Study*. JACC: Cardiovascular Interventions, 2013. **6**(2): p. 149-157.
 57. Pijls, N.H.J., et al., *Fractional Flow Reserve: A Useful Index to Evaluate the Influence of an Epicardial Coronary Stenosis on Myocardial Blood Flow*. Circulation, 1995. **92**(11): p. 3183-3193.
 58. Baskurt, O.K. and H.J. Meiselman. *Blood rheology and hemodynamics*. in *Seminars in Thrombosis and Hemostasis*. 2003. New York: Stratton Intercontinental Medical Book Corporation, c1974-.
 59. Yilmaz, F. and M.Y. Gundogdu, *A critical review on blood flow in large arteries; relevance to blood rheology, viscosity models, and physiologic conditions*. Korea-Australia Rheology Journal, 2008. **20**(4): p. 197-211.
 60. Pries, A.R., T.W. Secomb, and P. Gaehtgens, *Biophysical aspects of blood flow in the microvasculature*. Cardiovascular Research, 1996. **32**(4): p. 654-667.
 61. Wells Jr, R.E. and E.W. Merrill, *Influence of flow properties of blood upon viscosity-hematocrit relationships*. Journal of Clinical Investigation, 1962. **41**(8): p. 1591.
 62. SCHMID-SCHÖNBEIN, H., R. Wells, and J. GOLDSTONE, *Influence of deformability of human red cells upon blood viscosity*. Circulation Research, 1969. **25**(2): p. 131-143.
 63. Berezina, T.L., et al., *Influence of Storage on Red Blood Cell Rheological Properties*. Journal of Surgical Research, 2002. **102**(1): p. 6-12.
 64. Pries, A.R., D. Neuhaus, and P. Gaehtgens, *Blood viscosity in tube flow: dependence on diameter and hematocrit*. American Journal of Physiology - Heart and Circulatory Physiology, 1992. **263**(6): p. H1770-H1778.

65. Picart, C., et al., *Human blood shear yield stress and its hematocrit dependence*. Journal of Rheology, 1998. **42**(1): p. 1-12.
66. Eckstein, E.C. and F. Belgacem, *Model of platelet transport in flowing blood with drift and diffusion terms*. Biophysical Journal, 1991. **60**(1): p. 53-69.
67. Aarts, P.A., et al., *Blood platelets are concentrated near the wall and red blood cells, in the center in flowing blood*. Arteriosclerosis, Thrombosis, and Vascular Biology, 1988. **8**(6): p. 819-24.
68. Heinrich Joist, J., J.E. Bauman, and S.P. Sutura, *Platelet adhesion and aggregation in pulsatile shear flow: Effects of red blood cells*. Thrombosis Research, 1998. **92**(6, Supplement 2): p. S47-S52.
69. Aarts, P., R. Heethaar, and J. Sixma, *Red blood cell deformability influences platelets--vessel wall interaction in flowing blood*. Blood, 1984. **64**(6): p. 1228-1233.
70. Goldsmith, H., et al., *Effect of red blood cells and their aggregates on platelets and white cells in flowing blood*. Biorheology, 1999. **36**(5-6): p. 461-468.
71. Turitto, V.T., A.M. Benis, and E.F. Leonard, *Platelet Diffusion in Flowing Blood*. Industrial & Engineering Chemistry Fundamentals, 1972. **11**(2): p. 216-223.
72. Xu, C. and D.M. Wootton, *Platelet near-wall excess in porcine whole blood in artery-sized tubes under steady and pulsatile flow conditions*. Biorheology, 2004. **41**(2): p. 113-125.
73. Tilles, A.W. and E.C. Eckstein, *The near-wall excess of platelet-sized particles in blood flow: its dependence on hematocrit and wall shear rate*. Microvascular research, 1987. **33**(2): p. 211-223.
74. Yeh, C. and E.C. Eckstein, *Transient lateral transport of platelet-sized particles in flowing blood suspensions*. Biophysical Journal, 1994. **66**(5): p. 1706-1716.
75. Lowe, G.D., et al., *Relation between extent of coronary artery disease and blood viscosity*. BMJ, 1980. **280**(6215): p. 673-674.
76. Yilmaz, F. and M.Y. Gundogdu, *Analysis of conventional drag and*

- lift models for multiphase CFD modeling of blood flow*. Korea-Australia Rheology Journal, 2009. **21**(3): p. 161-173.
77. Jonghwun Jung, A.H., *Three-phase CFD analytical modeling of blood flow*. 2006.
 78. Jung, J. and A. Hassanein, *Three-phase CFD analytical modeling of blood flow*. Medical Engineering & Physics, 2008. **30**(1): p. 91-103.
 79. Huang, J., R.W. Lyczkowski, and D. Gidaspow, *Pulsatile flow in a coronary artery using multiphase kinetic theory*. Journal of Biomechanics, 2009. **42**(6): p. 743-754.
 80. Johnston, B.M., et al., *Non-Newtonian blood flow in human right coronary arteries: steady state simulations*. Journal of Biomechanics, 2004. **37**(5): p. 709-720.
 81. Shibeshi, S.S. and W.E. Collins, *The rheology of blood flow in a branched arterial system*. Applied rheology (Lappersdorf, Germany: Online), 2005. **15**(6): p. 398.
 82. Razavi, A., E. Shirani, and M.R. Sadeghi, *Numerical simulation of blood pulsatile flow in a stenosed carotid artery using different rheological models*. Journal of Biomechanics, 2011. **44**(11): p. 2021-2030.
 83. Johnston, B.M., et al., *Non-Newtonian blood flow in human right coronary arteries: transient simulations*. Journal of Biomechanics, 2006. **39**(6): p. 1116-1128.
 84. Jonghwun Jung, R.W.L., Chandrakant B. Panchal, Ahmed Hassanein, *Multiphase hemodynamic simulation of pulsatile flow in a coronary artery*. 2005.
 85. Wellnhofer, E., et al., *Flow simulation studies in coronary arteries—Impact of side-branches*. Atherosclerosis, 2010. **213**(2): p. 475-481.
 86. Wellnhofer, E., et al., *Non-dimensional modeling in flow simulation studies of coronary arteries including side-branches: A novel diagnostic tool in coronary artery disease*. Atherosclerosis, 2011. **216**(2): p. 277-282.
 87. A. Theodorakakos, M.G., A. Andriotis, A. Zifan, P. Liatsis, and E.P.E. I. Pantos, D, Katritsis, *Simulation of cardiac motion on*

- non-Newtonian, pulsating flow development in the human left anterior descending coronary artery.* 2008.
88. Katritsis, D., et al., *Vortex formation and recirculation zones in left anterior descending artery stenoses: computational fluid dynamics analysis.* *Physics in Medicine and Biology*, 2010. **55**(5): p. 1395.
 89. Banerjee, R.K., et al., *Physiological Flow Simulation in Residual Human Stenoses After Coronary Angioplasty.* *Journal of biomechanical engineering*, 2000. **122**(4): p. 310-320.
 90. Boutsianis, E., et al., *Computational simulation of intracoronary flow based on real coronary geometry.* *European journal of Cardio-thoracic Surgery*, 2004. **26**(2): p. 248-256.
 91. Chen, M.C., et al., *Computational hemodynamics of an implanted coronary stent based on three-dimensional cine angiography reconstruction.* *ASAIO journal*, 2005. **51**(4): p. 313-320.
 92. Frauenfelder, T., et al., *In-vivo flow simulation in coronary arteries based on computed tomography datasets: feasibility and initial results.* *European radiology*, 2007. **17**(5): p. 1291-1300.
 93. Prosi, M., et al., *Influence of curvature dynamics on pulsatile coronary artery flow in a realistic bifurcation model.* *Journal of Biomechanics*, 2004. **37**(11): p. 1767-1775.
 94. Arslan, N., et al. *CFD modeling of blood flow inside human left coronary artery bifurcation with aneurysms.* in *IFMBE Proc.* 2005.
 95. Johnston, B.M.J.a.P.R., *Simulations of pulsatile blood flow in tapered S-shaped in-plane and out-of-plane coronary arteries.* 18th World IMACS / MODSIM Congress, Cairns, Australia, 2009.
 96. Kim, H., et al., *Patient-specific modeling of blood flow and pressure in human coronary arteries.* *Annals of Biomedical Engineering*, 2010. **38**(10): p. 3195-3209.
 97. Katritsis, D.G., et al., *Flow Patterns at Stented Coronary Bifurcations: Computational Fluid Dynamics Analysis.* *Circulation: Cardiovascular Interventions*, 2012. **5**(4): p. 530-539.
 98. Anand, M., K. Rajagopal, and K.R. Rajagopal, *A Model*

- Incorporating some of the Mechanical and Biochemical Factors Underlying Clot Formation and Dissolution in Flowing Blood.* Journal of Theoretical Medicine, 2003. **5**(3-4): p. 183-218.
99. Bodnár, T. and A. Sequeira, *Numerical simulation of the coagulation dynamics of blood.* Computational and Mathematical Methods in Medicine, 2008. **9**(2): p. 83-104.
 100. Ku, D.N., *BLOOD FLOW IN ARTERIES.* Annual Review of Fluid Mechanics, 1997. **29**(1): p. 399-434.
 101. Myers, J.G., et al., *Factors Influencing Blood Flow Patterns in the Human Right Coronary Artery.* Annals of Biomedical Engineering, 2001. **29**(2): p. 109-120.
 102. LaDisa, J., Jr., et al., *Three-Dimensional Computational Fluid Dynamics Modeling of Alterations in Coronary Wall Shear Stress Produced by Stent Implantation.* Annals of Biomedical Engineering, 2003. **31**(8): p. 972-980.
 103. Mittal, N., et al., *Analysis of blood flow in the entire coronary arterial tree.* American journal of physiology-Heart and circulatory physiology, 2005. **289**(1): p. H439-H446.
 104. Blondel, C., et al., *Reconstruction of coronary arteries from a single rotational X-ray projection sequence.* Medical Imaging, IEEE Transactions on, 2006. **25**(5): p. 653-663.
 105. Andriotis, A., et al., *A New method of three dimensional coronary artery reconstruction from x-ray angiography: Validation against a virtual phantom and multislice computed tomography.* Catheterization and Cardiovascular Interventions, 2008. **72**: p. 28-34.
 106. Perktold, K., et al., *Validated computation of physiologic flow in a realistic coronary artery branch.* Journal of Biomechanics, 1997. **31**(3): p. 217-228.
 107. Olufsen, M.S., *Structured tree outflow condition for blood flow in larger systemic arteries.* American journal of physiology-Heart and circulatory physiology, 1999. **276**(1): p. H257-H268.
 108. Stergiopoulos, N., J.-J. Meister, and N. Westerhof, *Simple and accurate way for estimating total and segmental arterial compliance: the pulse pressure method.* Annals of Biomedical

- Engineering, 1994. **22**(4): p. 392-397.
109. Stergiopoulos, N., P. Segers, and N. Westerhof, *Use of pulse pressure method for estimating total arterial compliance in vivo*. American journal of physiology-Heart and circulatory physiology, 1999. **276**(2): p. H424-H428.
 110. Pullan, A., N. Smith, and P. Hunter, *An anatomically based model of transient coronary blood flow in the heart*. SIAM Journal on Applied Mathematics, 2002. **62**(3): p. 990-1018.
 111. Vignon, I.E. and C.A. Taylor, *Outflow boundary conditions for one-dimensional finite element modeling of blood flow and pressure waves in arteries*. Wave Motion, 2004. **39**(4): p. 361-374.
 112. Vignon-Clementel, I.E., et al., *Outflow boundary conditions for three-dimensional finite element modeling of blood flow and pressure in arteries*. Computer Methods in Applied Mechanics and Engineering, 2006. **195**(29): p. 3776-3796.
 113. Rauch, U., et al., *Thrombus formation on atherosclerotic plaques: pathogenesis and clinical consequences*. Annals of Internal Medicine, 2001. **134**(3): p. 224-238.
 114. Lee, K.W. and G.Y. Lip, *Acute coronary syndromes: Virchow's triad revisited*. Blood coagulation & fibrinolysis, 2003. **14**(7): p. 605-625.
 115. Lowe, G.D.O., *Virchow's Triad Revisited: Abnormal Flow*. Pathophysiology of Haemostasis and Thrombosis, 2003. **33**(5-6): p. 455-457.
 116. Blann, A.D., *How a Damaged Blood Vessel Wall Contributes to Thrombosis and Hypertension*. Pathophysiology of Haemostasis and Thrombosis, 2003. **33**(5-6): p. 445-448.
 117. Chung, I. and G.Y.H. Lip, *Virchow's Triad Revisited: Blood Constituents*. Pathophysiology of Haemostasis and Thrombosis, 2003. **33**(5-6): p. 449-454.
 118. Watson, T., E. Shantsila, and G.Y.H. Lip, *Mechanisms of thrombogenesis in atrial fibrillation: Virchow's triad revisited*. The Lancet, 2009. **373**(9658): p. 155-166.
 119. Furie, B. and B.C. Furie, *Mechanisms of Thrombus Formation*.

- New England Journal of Medicine, 2008. **359**(9): p. 938-949.
120. Lawson, J.H., et al., *A model for the tissue factor pathway to thrombin. I. An empirical study.* Journal of Biological Chemistry, 1994. **269**(37): p. 23357-23366.
 121. Zarnitsina, V.I., A.V. Pokhilko, and F.I. Ataulakhanov, *A Mathematical model for the spatio-temporal dynamics of intrinsic pathway of blood coagulation. I. The model description.* Thrombosis Research, 1996. **84**(4): p. 225-236.
 122. Riddel, J.P., et al., *Theories of blood coagulation.* Journal of Pediatric Oncology Nursing, 2007. **24**(3): p. 123-131.
 123. Mackman, N., R.E. Tilley, and N.S. Key, *Role of the Extrinsic Pathway of Blood Coagulation in Hemostasis and Thrombosis.* Arteriosclerosis, Thrombosis, and Vascular Biology, 2007. **27**(8): p. 1687-1693.
 124. Kleinschnitz, C., et al., *Targeting coagulation factor XII provides protection from pathological thrombosis in cerebral ischemia without interfering with hemostasis.* The Journal Of Experimental Medicine, 2006. **203**(3): p. 513-518.
 125. Hoffman, M. and D.M. Monroe, *A cell-based model of hemostasis.* Thrombosis and Haemostasis, 2001. **85**(6): p. 958-965.
 126. Smith, S.A., *The cell-based model of coagulation.* Journal of Veterinary Emergency and Critical Care, 2009. **19**(1): p. 3-10.
 127. Mosesson, M.W., *Fibrinogen and fibrin structure and functions.* Journal of Thrombosis and Haemostasis, 2005. **3**(8): p. 1894-1904.
 128. Brass, L.F., *Thrombin and Platelet Activation**. CHEST Journal, 2003. **124**(3_suppl): p. 18S-25S.
 129. Fernández-Ortiz, A., et al., *Characterization of the relative thrombogenicity of atherosclerotic plaque components: Implications for consequences of plaque rupture.* Journal of the American College of Cardiology, 1994. **23**(7): p. 1562-1569.
 130. Reininger, A.J., et al., *A 2-Step Mechanism of Arterial Thrombus Formation Induced by Human Atherosclerotic Plaques.* Journal of the American College of Cardiology, 2010. **55**(11): p. 1147-1158.

131. Moroi, M., et al., *Analysis of platelet adhesion to a collagen-coated surface under flow conditions: the involvement of glycoprotein VI in the platelet adhesion*. *Blood*, 1996. **88**(6): p. 2081-2092.
132. Monroe, D.M., M. Hoffman, and H.R. Roberts, *Platelets and Thrombin Generation*. *Arteriosclerosis, Thrombosis, and Vascular Biology*, 2002. **22**(9): p. 1381-1389.
133. Rosing, J., et al., *The role of activated human platelets in prothrombin and factor X activation*. *Blood*, 1985. **65**(2): p. 319-332.
134. Jesty, J., et al., *Platelet activation in a circulating flow loop: combined effects of shear stress and exposure time*. *Platelets*, 2003. **14**(3): p. 143-149.
135. Rendu, F. and B. Brohard-Bohn, *The platelet release reaction: granules' constituents, secretion and functions*. *Platelets*, 2001. **12**(5): p. 261-273.
136. Butenas, S., K.G. Mann, and Butenas, *Blood Coagulation*. *Biochemistry (Moscow)*, 2002. **67**(1): p. 3-12.
137. Zwaal, R.F.A., P. Comfurius, and E.M. Bevers, *Lipid-protein interactions in blood coagulation*. *Biochimica et Biophysica Acta (BBA) - Reviews on Biomembranes*, 1998. **1376**(3): p. 433-453.
138. Esmon, C.T., *Cell mediated events that control blood coagulation and vascular injury*. *Annual review of cell biology*, 1993. **9**(1): p. 1-26.
139. Dahlbäck, B., *Blood coagulation*. *The Lancet*, 2000. **355**(9215): p. 1627-1632.
140. Esmon, C.T., *The roles of protein C and thrombomodulin in the regulation of blood coagulation*. *Journal of Biological Chemistry*, 1989. **264**(9): p. 4743-6.
141. Sadler, J.E., *Biochemistry and genetics of von Willebrand factor*. *Annual Review of Biochemistry*, 1998. **67**: p. 395-424.
142. Papadopoulos, K.P., M. Gavaises, and C. Atkin, *A simplified mathematical model for thrombin generation*. *Medical Engineering & Physics*, 2014. **36**(2): p. 196-204.

143. Michaelis, L. and M.L. Menten, *Kinetics of invertase action*. Biochem. z, 1913. **49**: p. 333-369.
144. Hockin, M.F., et al., *A Model for the Stoichiometric Regulation of Blood Coagulation*. Journal of Biological Chemistry, 2002. **277**(21): p. 18322-18333.
145. Zarnitsina, V.I., A.V. Pokhilko, and F.I. Ataulakhanov, *A Mathematical model for the spatio-temporal dynamics of intrinsic pathway of blood coagulation. II. Results*. Thrombosis Research, 1996. **84**(5): p. 333-344.
146. Xu, Z., et al., *Computational Approaches to Studying Thrombus Development*. Arteriosclerosis, Thrombosis, and Vascular Biology, 2011. **31**(3): p. 500-505.
147. Willems, G., et al., *Simulation Model for Thrombin Generation in Plasma*. Pathophysiology of Haemostasis and Thrombosis, 1991. **21**(4): p. 197-207.
148. Jones, K.C. and K.G. Mann, *A model for the tissue factor pathway to thrombin. II. A mathematical simulation*. Journal of Biological Chemistry, 1994. **269**(37): p. 23367-23373.
149. Lo, K., W.S. Denney, and S.L. Diamond, *Stochastic Modeling of Blood Coagulation Initiation*. Pathophysiology of Haemostasis and Thrombosis, 2005. **34**(2-3): p. 80-90.
150. Bungay, S.D., P.A. Gentry, and R.D. Gentry, *A mathematical model of lipid-mediated thrombin generation*. Mathematical Medicine and Biology, 2003. **20**(1): p. 105-129.
151. Beltrami, E. and J. Jesty, *Mathematical analysis of activation thresholds in enzyme-catalyzed positive feedbacks: application to the feedbacks of blood coagulation*. Proceedings of the National Academy of Sciences, 1995. **92**(19): p. 8744-8748.
152. Xu, C., et al., *Simulation of a mathematical model of the role of the TFPI in the extrinsic pathway of coagulation*. Computers in Biology and Medicine, 2005. **35**(5): p. 435-445.
153. Qiao, Y.H., et al., *The kinetic model and simulation of blood coagulation--the kinetic influence of activated protein C*. Medical Engineering & Physics, 2004. **26**(4): p. 341-347.
154. Wagenvoort, R., P.W. Hemker, and H.C. Hemker, *The limits of*

- simulation of the clotting system*. Journal of Thrombosis and Haemostasis, 2006. **4**(6): p. 1331-1338.
155. Huang, P.Y. and J.D. Hellums, *Aggregation and disaggregation kinetics of human blood platelets: Part I. Development and validation of a population balance method*. Biophysical Journal, 1993. **65**(1): p. 334-343.
 156. Huang, P.Y. and J.D. Hellums, *Aggregation and disaggregation kinetics of human blood platelets: Part II. Shear-induced platelet aggregation*. Biophysical Journal, 1993. **65**(1): p. 344-353.
 157. Huang, P.Y. and J.D. Hellums, *Aggregation and disaggregation kinetics of human blood platelets: Part III. The disaggregation under shear stress of platelet aggregates*. Biophysical Journal, 1993. **65**(1): p. 354-361.
 158. Tandon, P. and S.L. Diamond, *Hydrodynamic effects and receptor interactions of platelets and their aggregates in linear shear flow*. Biophysical Journal, 1997. **73**(5): p. 2819-2835.
 159. David, T., S. Thomas, and P.G. Walker, *Platelet deposition in stagnation point flow: an analytical and computational simulation*. Medical Engineering & Physics, 2001. **23**(5): p. 299-312.
 160. Wootton, D., et al., *A Mechanistic Model of Acute Platelet Accumulation in Thrombogenic Stenoses*. Annals of Biomedical Engineering, 2001. **29**(4): p. 321-329.
 161. Brash, J.L., J.M. Brophy, and I.A. Feuerstein, *Adhesion of platelets to artificial surfaces: Effect of red cells*. Journal of Biomedical Materials Research, 1976. **10**(3): p. 429-443.
 162. Mori, D., et al., *Computational study on effect of red blood cells on primary thrombus formation*. Thrombosis Research, 2008. **123**(1): p. 114-121.
 163. Sorensen, E.N., et al., *Computational Simulation of Platelet Deposition and Activation: I. Model Development and Properties*. Annals of Biomedical Engineering, 1999. **27**(4): p. 436-448.
 164. Sorensen, E., et al., *Computational Simulation of Platelet Deposition and Activation: II. Results for Poiseuille Flow over Collagen*. Annals of Biomedical Engineering, 1999. **27**(4): p.

449-458.

165. David, T., P.G. de Groot, and P.G. Walker, *Boundary-layer Type Solutions for Initial Platelet Activation and Deposition*. Journal of Theoretical Medicine, 2002. **4**(2): p. 95-108.
166. Worth Longest, P. and C. Kleinstreuer, *Comparison of blood particle deposition models for non-parallel flow domains*. Journal of Biomechanics, 2003. **36**(3): p. 421-430.
167. Ruggeri, Z.M. and G.L. Mendolicchio, *Adhesion Mechanisms in Platelet Function*. Circulation Research, 2007. **100**(12): p. 1673-1685.
168. Pivkin, I.V., P.D. Richardson, and G. Karniadakis, *Blood flow velocity effects and role of activation delay time on growth and form of platelet thrombi*. Proceedings of the National Academy of Sciences, 2006. **103**(46): p. 17164-17169.
169. Pivkin, I., P. Richardson, and G.E. Karniadakis, *Effect of red blood cells on platelet aggregation*. Engineering in Medicine and Biology Magazine, IEEE, 2009. **28**(2): p. 32-37.
170. Hubbell, J.A. and L.V. McIntire, *Platelet active concentration profiles near growing thrombi. A mathematical consideration*. Biophysical Journal, 1986. **50**(5): p. 937-945.
171. Folie, B.J. and L.V. McIntire, *Mathematical analysis of mural thrombogenesis. Concentration profiles of platelet-activating agents and effects of viscous shear flow*. Biophysical Journal, 1989. **56**(6): p. 1121-1141.
172. Lobanov, A.I. and T.K. Starozhilova, *The Effect of Convective Flows on Blood Coagulation Processes*. Pathophysiology of Haemostasis and Thrombosis, 2005. **34**(2-3): p. 121-134.
173. Kuharsky, A.L. and A.L. Fogelson, *Surface-Mediated Control of Blood Coagulation: The Role of Binding Site Densities and Platelet Deposition*. Biophysical Journal, 2001. **80**(3): p. 1050-1074.
174. Fogelson, A.L. and R.D. Guy, *Platelet-wall interactions in continuum models of platelet thrombosis: formulation and numerical solution*. Mathematical Medicine and Biology, 2004. **21**(4): p. 293-334.

175. Fogelson, A.L. and N. Tania, *Coagulation under Flow: The Influence of Flow-Mediated Transport on the Initiation and Inhibition of Coagulation*. Pathophysiology of Haemostasis and Thrombosis, 2005. **34**(2-3): p. 91-108.
176. Lai, M.-C. and C.S. Peskin, *An Immersed Boundary Method with Formal Second-Order Accuracy and Reduced Numerical Viscosity*. Journal of Computational Physics, 2000. **160**(2): p. 705-719.
177. Peskin, C.S., *The immersed boundary method*. Acta Numerica, 2002. **11**: p. 479-517.
178. Fogelson, A.L. and R.D. Guy, *Immersed-boundary-type models of intravascular platelet aggregation*. Computer Methods in Applied Mechanics and Engineering, 2008. **197**(25-28): p. 2087-2104.
179. Yang, X.S., R.W. Lewis, and H.Y. Zhang, *Finite Element Analysis of Fogelson's Model for Platelet Aggregation*. 2004.
180. Leiderman, K. and A.L. Fogelson, *Grow with the flow: a spatial-temporal model of platelet deposition and blood coagulation under flow*. Mathematical Medicine and Biology, 2011. **28**(1): p. 47-84.
181. Xu, Z., et al., *A multiscale model of thrombus development*. Journal of The Royal Society Interface, 2008. **5**(24): p. 705-722.
182. Marée, A.M., V. Grieneisen, and P. Hogeweg, *The Cellular Potts Model and Biophysical Properties of Cells, Tissues and Morphogenesis*, in *Single-Cell-Based Models in Biology and Medicine*, A.A. Anderson, M.J. Chaplain, and K. Rejniak, Editors. 2007, Birkhäuser Basel. p. 107-136.
183. Xu, Z., et al., *A Multiscale Model of Venous Thrombus Formation with Surface-Mediated Control of Blood Coagulation Cascade*. Biophysical Journal, 2010. **98**(9): p. 1723-1732.
184. Xu, Z., et al., *Study of blood flow impact on growth of thrombi using a multiscale model*. Soft Matter, 2009. **5**(4): p. 769-779.
185. Anand, M., K. Rajagopal, and K.R. Rajagopal, *A Model for the Formation and Lysis of Blood Clots*. Pathophysiology of Haemostasis and Thrombosis, 2005. **34**(2-3): p. 109-120.
186. Oliver, J.A., et al., *Thrombin Activates Factor XI on Activated*

- Platelets in the Absence of Factor XII. Arteriosclerosis, Thrombosis, and Vascular Biology*, 1999. **19**(1): p. 170-177.
187. McCormick, S.M., et al., *DNA microarray reveals changes in gene expression of shear stressed human umbilical vein endothelial cells*. Proceedings of the National Academy of Sciences, 2001. **98**(16): p. 8955-8960.
188. Sakariassen, K., et al., *A perfusion chamber developed to investigate platelet interaction in flowing blood with human vessel wall cells, their extracellular matrix, and purified components*. The Journal of laboratory and clinical medicine, 1983. **102**(4): p. 522.
189. Van Veen, J.J., A. Gatt, and M. Makris, *Thrombin generation testing in routine clinical practice: are we there yet?* British Journal of Haematology, 2008. **142**(6): p. 889-903.
190. Baglin, T., *The measurement and application of thrombin generation*. British Journal of Haematology, 2005. **130**(5): p. 653-661.
191. Gerotziafas, G.T., et al., *Towards a standardization of thrombin generation assessment: The influence of tissue factor, platelets and phospholipids concentration on the normal values of Thrombogram-Trombinoscope assay*. Thrombosis Journal, 2005. **3**(16).
192. van't Veer, C. and K.G. Mann, *Regulation of Tissue Factor Initiated Thrombin Generation by the Stoichiometric Inhibitors Tissue Factor Pathway Inhibitor, Antithrombin-III, and Heparin Cofactor-II*. Journal of Biological Chemistry, 1997. **272**(7): p. 4367-4377.
193. Hemker, H.C. and S. Béguin, *Thrombin generation in plasma: its assessment via the endogenous thrombin potential*. Thrombosis and Haemostasis, 1995. **74**(1): p. 134-138.
194. Okorie, U.M., et al., *Determination of surface tissue factor thresholds that trigger coagulation at venous and arterial shear rates: amplification of 100 fM circulating tissue factor requires flow*. Blood, 2008. **111**(7): p. 3507-3513.
195. Liu, L., et al., *Thrombin binding to platelets and their activation in plasma*. British Journal of Haematology, 1994. **88**(3): p. 592-

600.

196. Frojmovic, M.M., R.F. Mooney, and T. Wong, *Dynamics of platelet glycoprotein IIb-IIIa receptor expression and fibrinogen binding. I. Quantal activation of platelet subpopulations varies with adenosine diphosphate concentration*. Biophysical Journal, 1994. **67**(5): p. 2060-2068.
197. Hemker, H.C., et al., *Calibrated automated thrombin generation measurement in clotting plasma*. Pathophysiology of Haemostasis and Thrombosis, 2003. **33**(1): p. 4-15.
198. Allen, G., et al., *Impact of procoagulant concentration on rate, peak and total thrombin generation in a model system*. Journal of Thrombosis and Haemostasis, 2004. **2**(3): p. 402-413.
199. *Systems Biology Toolbox for MATLAB: A computational platform for research in Systems Biology* Bioinformatics and Biology Insights, 2006. **22**(4): p. 514-515.
200. Ninivaggi, M., et al., *Whole-Blood Thrombin Generation Monitored with a Calibrated Automated Thrombogram-Based Assay*. Clinical Chemistry, 2012. **58**(8): p. 1252-1259.
201. Whelihan, M.F. and K.G. Mann, *The role of the red cell membrane in thrombin generation*. Thrombosis Research, 2013.
202. van Dijk, K., et al., *Factor VIII half-life and clinical phenotype of severe hemophilia A*. Haematologica, 2005. **90**(4): p. 494-498.
203. Brummel-Ziedins, K., *Models for thrombin generation and risk of disease*. Journal of Thrombosis and Haemostasis, 2013. **11**: p. 212-223.
204. Bonderman, D., et al., *Coronary no-reflow is caused by shedding of active tissue factor from dissected atherosclerotic plaque*. Blood, 2002. **99**(8): p. 2794-2800.
205. Arabinda Guha, R.B., William Konigsberg and Yale Nemerson, *Affinity purification of human tissue factor: Interaction of factor VII and tissue factor in detergent micelles*. Biochemistry, 1986. **83**: p. 299-302.
206. Kulkarni, S., et al., *A revised model of platelet aggregation*. Journal of Clinical Investigation, 2000. **105**(6): p. 783-791.

207. Ikeda, Y., et al., *The role of von Willebrand factor and fibrinogen in platelet aggregation under varying shear stress*. Journal of Clinical Investigation, 1991. **87**(4): p. 1234.
208. Louvard, Y., et al., *Classification of coronary artery bifurcation lesions and treatments: time for a consensus!* Catheter Cardiovasc Interv, 2008. **71**(2): p. 175-83.
209. Finet, G., et al., *Fractal geometry of arterial coronary bifurcations: a quantitative coronary angiography and intravascular ultrasound analysis*. EuroIntervention, 2008. **3**(4): p. 490-8.
210. A Mailhac, J.B., JT Fallon, A Fernandez-Ortiz, B Meyer, JH Chesebro, V Fuster and L Badimon, *Effect of an eccentric severe stenosis on fibrin(ogen) deposition on severely damaged vessel wall in arterial thrombosis. Relative contribution of fibrin(ogen) and platelets*. Circulation, 1994. **90**(2): p. 988-996.
211. MYUNGJIN KANG, H.S.J.a.K.C.K., *In-vitro investigation of RBCs' flow characteristics and hemodynamic feature through a microchannel with a micro-stenosis*. INTERNATIONAL JOURNAL OF BIOLOGY AND BIOMEDICAL ENGINEERING, 2008. **2**(1).
212. Nurullah Arslan, V.T., Selman Nas, Ayse Durukan, *CFD modeling of blood flow inside human left coronary artery bifurcation with aneurysms*. 2005.
213. Mounter C. Y. Chen, P.-C.L., James S. Y. Chen, Ned H.C. Hwang, *Computational hemodynamics of an implanted coronary stent based on three dimensional cine angiography reconstruction*. 2005.
214. Crampin, E.J., et al., *Computational physiology and the physiome project*. Experimental Physiology, 2004. **89**(1): p. 1-26.
215. D. Katritsis, A.T., A. Andriotis, I. Pantos, E. P. Efstathopoulos, G. Siontis, N. Karcanias, S. Redwood, M. Gavaises *Vortex formation and recirculation zones in left anterior descending artery stenoses: Computational fluid dynamics analysis*. 2010.
216. Theodorakakos, A., et al., *Simulation of cardiac motion on non-Newtonian, pulsating flow development in the human left anterior descending coronary artery*. Physics in Medicine and Biology, 2008. **53**(18): p. 4875.

217. Kamiya, A. and T. Togawa, *Adaptive regulation of wall shear stress to flow change in the canine carotid artery*. Am J Physiol, 1980. **239**(1): p. H14-21.
218. Min, J.K., et al., *Diagnostic accuracy of fractional flow reserve from anatomic ct angiography*. JAMA, 2012. **308**(12): p. 1237-1245.
219. BETA-CAE, S.S.A., *META PostProcessor version 6.2.0. User's Guide*. 2008.
220. Soulis, J.V., et al. *Relative residence time and oscillatory shear index of non-Newtonian flow models in aorta*. in *Biomedical Engineering, 2011 10th International Workshop on*. 2011. IEEE.
221. Holme, P.A., et al., *Shear-Induced Platelet Activation and Platelet Microparticle Formation at Blood Flow Conditions as in Arteries With a Severe Stenosis*. Arteriosclerosis, Thrombosis, and Vascular Biology, 1997. **17**(4): p. 646-653.
222. Doriot, P.-A., et al., *In-vivo measurements of wall shear stress in human coronary arteries*. Coronary Artery Disease, 2000. **11**(6): p. 495-502.
223. Shaaban, A.M. and A.J. Duerinckx, *Wall shear stress and early atherosclerosis: a review*. American Journal of Roentgenology, 2000. **174**(6): p. 1657-1665.
224. Li, Z.Y., et al., *The mechanical triggers of plaque rupture: shear stress vs pressure gradient*. Br J Radiol, 2009. **82 Spec No 1**: p. S39-45.
225. Katriasis, D.G., J. Pantos, and E. Efstathopoulos, *Hemodynamic factors and atheromatic plaque rupture in the coronary arteries: from vulnerable plaque to vulnerable coronary segment*. Coronary Artery Disease, 2007. **18**(3): p. 229-37.
226. Feldman, C.L., et al., *Determination of in vivo velocity and endothelial shear stress patterns with phasic flow in human coronary arteries: a methodology to predict progression of coronary atherosclerosis*. American Heart Journal, 2002. **143**(6): p. 931-9.
227. Wurzinger, L.J., P. Blasberg, and H. Schmid-Schonbein, *Towards a concept of thrombosis in accelerated flow: rheology, fluid*

- dynamics, and biochemistry*. Biorheology, 1985. **22**(5): p. 437-50.
228. Bath, P. and R. Butterworth, *Platelet size: measurement, physiology and vascular disease*. Blood coagulation & fibrinolysis, 1996. **7**(2): p. 157-161.
229. Wolberg, A.S., *Thrombin generation and fibrin clot structure*. Blood Reviews, 2007. **21**(3): p. 131-142.
230. Hamdan, A., et al., *A prospective study for comparison of MR and CT imaging for detection of coronary artery stenosis*. JACC: Cardiovascular Imaging, 2011. **4**(1): p. 50-61.
231. Wellnhofer, E., et al., *In-vivo coronary flow profiling based on biplane angiograms: influence of geometric simplifications on the three-dimensional reconstruction and wall shear stress calculation*. Biomed Eng Online, 2006. **5**(39): p. 39.
232. Castoldi, E. and J. Rosing, *Thrombin generation tests*. Thrombosis Research, 2011. **127**, **Supplement 3**(0): p. S21-S25.